Forschungszentrum Jülich

Institut für Chemie und Dynamik der Geosphäre 3:
Atmosphärische Chemie

On the Global Distribution of Tropospheric NO_x: A Three-Dimensional Model Study

Annette B. Kraus

Jül-3352

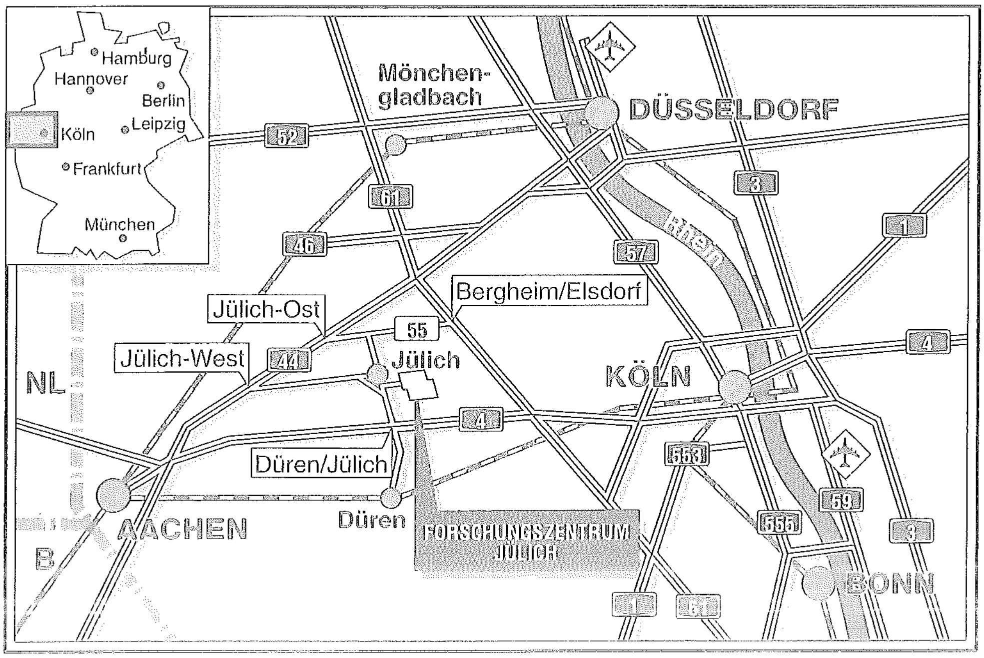

Berichte des Forschungszentrums Jülich ; 3352
ISSN 0944-2952
Institut für Chemie und Dynamik der Geosphäre 3:
Atmosphärische Chemie Jül-3352
D 38 (Diss. Universität Köln)

Zu beziehen durch: Forschungszentrum Jülich GmbH · Zentralbibliothek
D-52425 Jülich · Bundesrepublik Deutschland
☎ 02461/61-6102 · Telefax: 02461/61-6103 · e-mail: zb-publikation@fz-juelich.de

On the Global Distribution of Tropospheric NO_x: A Three-Dimensional Model Study

Annette B. Kraus

Zusammenfassung

Die Stickoxide NO und NO_2, die man als NO_X zusammenfaßt, spielen zwei wichtige Rollen in der Chemie der Troposphäre. Zum einen sind sie die Substanz, die den größten Einfluß auf die Nettoproduktion von troposphärischem Ozon hat, zum anderen steuern sie die Konzentration der Hydroxylradikale. Um Aussagen über die Verteilung einer dieser beiden Substanzen machen zu können, muß man deshalb die NO_X-Verteilung kennen. Durch Messungen ist letztere, zumindest global, aufgrund der kurzen chemischen Lebensdauer von NO_X und seiner daraus resultierenden hohen zeitlichen und räumlichen Variabilität schwer zu bestimmen.

Um die globale Verteilung von troposphärischem NO_X dennoch zu charakterisieren, wurde im Rahmen dieser Arbeit ein bestehendes, dreidimensionales Modell zur Berechnung von Spurenstoffverteilungen entsprechend erweitert. Dazu wurden ein bekanntes, lineares Schema für die NO_X-Chemie implementiert und folgende sechs Quellen troposphärischer Stickoxide berücksichtigt: Verbrennung fossiler Energieträger, mikrobielle Aktivität im Erdboden, Blitze, Verbrennung von Biomasse, Transport aus der Stratosphäre sowie Flugzeugemissionen. Da man die Emissionsraten jeder einzelnen dieser Quellen nur höchstens auf einen Faktor 2 genau kennt, sind auch die resultierenden globalen NO_X-Verteilungen mit entsprechenden Unsicherheiten behaftet.

Für die Blitzquelle wurde eine speziell auf das Modell zugeschnittene Parametrisierung entwickelt. Diese Parametrisierung geht von der relativen Verteilung der globaler Gewitteraktivität aus, die von der im Modell enthaltenen Konvektionsstatistik abgeleitet und anhand von entsprechenden, für die einzelnen Monate zeitlich gemittelten Beobachtungsdaten modifiziert wird. Die relativen Verteilungen werden mit einer aus globalen Schätzungen abgeleiteten Emissionsrate skaliert.

Insgesamt ist die globale Verteilung von troposphärischem NO_X gekennzeichnet durch Mischungsverhältnisse von bis zu mehreren ppbv in der planetaren Grenzschicht über Kontinenten, nur maximal 50-100 pptv in der mittleren und bis 500 pptv in der oberen Troposphäre. Nördlich von 30°N dominiert der Anteil von NO_X aus Verbrennung fossiler Energieträger deutlich, während in den Tropen und in südlichen mittleren Breiten durch Blitze erzeugtes NO_X bei weitem überwiegt. Flugzeugemissionen spielen nur in der oberen Troposphäre in nördlichen mittleren Breiten eine nennenswerte Rolle. Auch dort erreichen sie Beiträge von über 50% ausschließlich im Winter, wenn die Intensität der vertikalen Durchmischung der Troposphäre ihr jährliches Minimum erreicht.

Um die mit dem Modell berechneten NO-Mischungsverhältnisse zu überprüfen, wurden sie mit entsprechenden Messungen aus Flugkampagnen verglichen. Dieser Vergleich zeigt, daß das Modell in allen untersuchten Gegenden, zu allen Jahreszeiten und in allen troposphärischen Höhen, für die Meßdaten vorhanden sind, die richtige Größenordnung des NO-Mischungsverhältnisses liefert. Da es überdies auch die Hauptstrukturmerkmale der gemessenen NO-Verteilungen wiedergibt, bzw. die Diskrepanzen zwischen beiden Datensätzen im Einzelnen erklärt werden können, dürften die wichtigsten Eigenschaften der globalen Verteilung troposphärischer Stickoxide somit verstanden sein.

Darüberhinaus zeigt dieser Vergleich von gemessenen und berechneten NO-Mischungsverhältnissen, daß abgesehen von seiner geringen räumlichen und zeitlichen Auflösung das Konvektionsschema die Hauptschwäche des Modells ist. Zumindest in den Tropen ist die vertikale Umverteilung kurzlebiger Spurenstoffe zu stark vereinfacht. Dies zeigt zusätzlich auch ein Vergleich von Verteilungen des chemisch inerten Spurengases Radon, die einerseits mit dem hier verwendenten Modell und andererseits mit zwei anderen globalen Modellen berechnet wurden.

Abstract

The nitrogen oxides NO and NO_2, which are lumped into NO_X, play a dual role in tropospheric chemistry. On the one hand they are the most important species with respect to the net tropospheric ozone production, on the other hand they control the concentration of the hydroxyl radical. Thus, the distribution of NO_X must be known before distributions of these two species can be calculated. However, because of the short chemical lifetime and the resulting high temporal and spatial variability of NO_X, this distribution is difficult to determine by measurements, at least on a global scale.

In the present study an existing three-dimensional chemical tracer model was extended in order to characterize the global distribution of tropospheric NO_X. This was done by implementing a known, linear NO_X chemistry scheme and emission scenarios for the following six sources of tropospheric NO_X: fossil fuel combustion, soil microbial activity, lightning discharges, biomass burning, downward transport from the stratosphere, and aircraft emissions. Since the uncertainty of each of these sources is a factor of 2 at least, the resulting global NO_X distributions are associated with corresponding uncertainties as well.

A new parametrization was developed for the lightning source in which the relative distribution of global lightning activity is derived from the convection statistics included in the present model. Two parameters are used to weight individual convection convection events according to observed monthly mean relative lightning distributions. The relative distributions are scaled by an absolute emission rate derived from global estimates.

The global distribution of tropospheric NO_X is characterized by mixing ratios of up to several ppbv in the continental planetary boundary layer, maximum values of only 50-100 pptv in the mid-troposphere, and up to 500 pptv in the upper troposphere. North of 30°N the contribution of NO_X from fossil fuel combustion is by far dominant. In the tropics and at southern mid-latitudes, NO_X from lightning discharges makes the largest contribution. Aircraft emissions play an important role in the upper troposphere at northern mid-latitudes. Even there they reach contributions of more than 50% only during winter, when the intensity of vertical mixing throughout the depth of the troposphere has its annual minimum.

The NO mixing ratios calculated by the model were compared with corresponding measurements obtained during aircraft campaigns in order to estimate how realistic the calculated data are. This comparison shows that the model is able to yield the observed order of magnitude of the NO mixing ratio in all regions, during all seasons, and at all altitudes for which measurement data are available. In addition, the model either reproduces the main features of the observed NO distributions or, in regions where this is not the case, the discrepancies between both data sets at least can be explained in detail. Thus, the most important characteristics of the global distribution of tropospheric NO_X seems to be understood.

Moreover, the comparison between measured and calculated NO mixing ratios reveals that the main weakness of the model used here is its convection scheme, apart from its low spatial and temporal resolution. At least in the tropics the vertical redistribution of short-living tracers is oversimplified. This feature is demonstrated additionally by a comparison of distributions of the passive tracer radon which were calculated by the model used here on the one hand and by two other global models on the other hand.

Contents

List of Symbols

Symbol	Meaning	Unit
a_{Rn}	equivalent ^{222}Rn concentration	pCi/SCM
$a_{\mathrm{Rn}^{\mathrm{X}}}$	a_{Rn} calculated by model X	pCi/SCM
$\overline{X}^{a}$	annual mean of the quantity X	same as X
c_l	linear correlation coefficient	–
$\overline{X}^{ca}$	temporal mean of the quantity X over the time period of a measurement campaign	same as X
$\overline{X}^{d}$	daily mean of the quantity X	same as X
$\overline{X}^{d}\vert_{max}$	maximum value of the quantity X during a time period	same as X
$\overline{X}^{d}\vert_{min}$	minimum value of the quantity X during a time period	same as X
E_f	energy of a lightning flash	J
$[X]_{eq}$	thermochemichal equilibrium concentration of X	molecules X/m^3
γ_o	parameter used in the lightning parametrization	–
$G(\mathrm{NO})$	global rate of NO production by lightning	Mt N/yr
h_{cl}	cloud height	m
J_X	photolysis frequency of X	s^{-1}
k_{O_3}	reaction constant of $\mathrm{NO} + \mathrm{O}_3 \rightarrow \mathrm{NO}_2 + \mathrm{O}_2$	molecules s^{-1} m^{-3}
λ	geographical longitude	°
$\langle X \rangle_\lambda$	zonal mean of the quantity X	same as X
μ_X	volume mixing ratio of the chemical species X	pptv
M	third body in a collision reaction	–
m	mass (of tracer)	kg
$\overline{X}^{m}$	monthly mean of the quantity X	same as X
ν_{dwc}	frequency of deep wet convection	s^{-1}
ν_{gf}	global lightning flash frequency	s^{-1}
ν_{lf}	local lightning flash frequency	s^{-1}
n_{CC}	total number of cloud-to-cloud flashes	flashes
n_{CG}	total number of cloud-to-ground flashes	flashes
φ	geographical latitude	°
$\langle X \rangle_\varphi$	meridional mean of the quantity X	same as X
$P(\mathrm{NO})$	molecular production of NO by one flash	molecules NO/flash
p	pressure	Pa
$p(\mathrm{NO})$	yield of NO per unit energy of discharge	molecules NO/J
ρ_X	mass mixing ratio of the chemical species X	kg/kg
$\rho_{\leadsto}(\lambda, \varphi)$	normalized horizontal lightning distribution	–
$\rho^{c}_{\leadsto}$	mean equivalent lightning occurrence in a continental region	counts m^{-2} s^{-1}
$\rho^{o}_{\leadsto}$	mean equivalent lightning occurrence in an oceanic region	counts m^{-2} s^{-1}
r_{Rn}	ratio $\overline{a_{\mathrm{Rn}^{\mathrm{C}}}}^{m}/0.5(\overline{a_{\mathrm{Rn}^{\mathrm{E}}}}^{m}+\overline{a_{\mathrm{Rn}^{\mathrm{T}}}}^{m})$	–
r_{NO}	ratio $\mu_{\mathrm{NO}}/\mu_{\mathrm{NOx}}$	–
Rn^{X}	^{222}Rn mixing ratio calculated by model X	pCi/SCM
σ	normalized pressure coordinate	–
$\sigma_{sd}(X)$	standard deviation of the quantity X	same as X

Symbol	Meaning	Unit
τ_{cool}	characteristic cooling time	s
τ_{eq}	characteristic time to reach an equilibrium state	s
τ_{NOx}	chemical lifetime of $\mathrm{NO_X}$	s
t	time	s
T	temperature	K or °C
T_{ct}	parameter used in the lightning parametrization	K
T_{fr}	freeze-out temperature	K
u	zonal component of the velocity vector	m/s
$V_{bb}(X)$	in-between box variance of the field X	same as X^2
$V_{ib}(X)$	in-box variance of the field X	same as X^2
$V_{tot}(X)$	total variance of the field X	same as X^2
v	meridional component of the velocity vector	m/s
w	vertical component of the velocity vector	m/s
w_{max}	maximum updraft speed in thunderclouds	m/s
x_n	individual sample from a field X in a calculation of variances	same as X
z	vertical coordinate	m

List of Abbreviations

Abbreviation	Meaning
CC	cloud-to-cloud flash
CG	cloud-to-ground flash
CTM	chemical tracer model
DJF	winter season (December, January, February)
ECHAM3	general circulation model
GCM	general circulation model
GISS	Goddard Institute for Space Studies
JJA	summer season (June, July, August)
MAM	spring season (March, April, May)
PBL	planetray boundary layer
PEM-West A	Pacific Exploratory Mission-West A
PEM-West B	Pacific Exploratory Mission-West B
SON	autumn season (September, October, November)
TMK	transport model
TROPOZ	Tropospheric Ozone Experiment
STRATOZ	Stratospheric Ozone Experiment

Chapter 1

Introduction

The Earth's atmosphere is a complex dynamical and chemical system. Both components of this system are driven by the sun. On the one hand, solar radiation heats the Earth's surface. This heating is different for different types of surfaces, e.g. land and ocean, and for different geographical latitudes and seasons. The temperature differences generated thereby are the basic reason of atmospheric as well as oceanic motions. Photochemical processes, on the other hand, initiate most of the chemical reactions in the atmosphere.

The troposphere is the lowest layer of the atmosphere which extends from the Earth's surface up to heights of 8-18 km depending on geographical latitude, season, and the actual weather conditions. The atmospheric layer above the troposphere is called the stratosphere, the transition region in between is the tropopause. The troposphere is characterized by, on average, decreasing temperatures with increasing height, whereas the opposite is true in the stratosphere. The latter feature is a consequence of absorption of solar ultraviolet radiation by, inter alia, molecules of ozone, O_3. The different vertical temperature stratification in troposphere and stratosphere is the reason for an important dynamical difference between both layers: rapid, thermally induced convection can occur in the troposphere, but not in the stratosphere.

Life on Earth would not be possible in the present form without a number of atmospheric trace gases being present, as carbon dioxide, CO_2, and ozone, O_3, for example. These trace gases act as natural greenhouse gases. They are able to absorb incoming solar radiation or outgoing infrared radiation emitted by the Earth. The energy absorbed thereby is used to warm the corresponding region of the atmosphere. Since thermal radiation of such warmed atmospheric regions partly is directed towards the Earth, there is a net warming at the Earth's surface. How large the greenhouse potential of a specific trace gas is, i.e. how much this trace gas contributes to the warming effect depends on various parameters like its vertical distribution.

In the troposphere, two chemical species are of particular relevance in this context: the hydroxyl radical, OH, and O_3. The former, OH, is the main oxidizing agent in the troposphere and, hence, the dominant chemical sink of many greenhouse gases. The latter, O_3, has a high greenhouse potential itself. The concentrations of both OH and O_3 strongly depend on the concentration of the nitrogen oxides, NO_X, which consist of two trace gases: nitric oxide, NO, and nitrogen dioxide, NO_2. Because of this strong dependence, NO_X indirectly affects the Earth's radiation budget, although its own greenhouse potential is irrelevant.

Nitrogen oxides occur in the Earth's atmosphere due to natural sources such as lightning or photochemical formation in the stratosphere. However, much of the NO_X present in the troposphere is a result of anthropogenic emissions, in particular combustion of fossil fuel. How the chemical system of the atmosphere reacts to anthropogenic emissions is known only partly at the moment, but it is known that the response of tropospheric chemistry is highly non-linear with respect to changes in the NO_X concentration. The predicted impact of anthropogenic NO_X emissions therefore strongly depends on the initial NO_X distribution. This distribution is poorly known.

Measurements provide important informations on the distribution of tropospheric NO_X. However, since the chemical lifetime of NO_X is only a few days, its distribution is highly variable in space and time. Numerous measurements are required therefore in order to characterize the global distribution of tropospheric NO_X correctly. Despite multiple efforts, an adequate data set still does not exist. To provide such a distribution is main purpose of the present model study.

Additional aim of this study is to estimate the contributions of individual sources to the total burden of tropospheric NO_X. Contrary to measurements, model calculations allow such a decomposition. In addition, future developments of the tropospheric NO_X distributions only can be estimated if this decomposition is known, because the emission rates of the individual sources will change differently with time. Furthermore, knowledge of the spatial and temporal distribution of the NO_X contributions from the individual sources may assist in planning measurement campaigns.

The time scale during which an atmospheric layer is mixed vertically depends on the vertical temperature stratification and, hence, on the presence of convection. In strongly convective regions of the troposphere, this time scale is on the order of 10 days, whereas in the stratosphere, vertical mixing is significantly slower. The chemical lifetime of tropospheric NO_X, on the other hand, is about 1 day near the Earth's surface and about 10 days at the tropopause. Thus, in the troposphere, both dynamical and chemical processes act on NO_X on comparable time scales and any attempt to understand tropospheric NO_X distributions must take into account both types of processes. In contrast, the photochemical equilibrium between NO and NO_2 is reached within a few minutes. Since this is much shorter than the time scale of tropospheric dynamics, both species can be lumped into NO_X. In the stratosphere, the concentration of NO_X is dominated by in-situ photochemical production from N_2O.

The tool chosen here to investigate distributions of tropospheric NO_X is a global chemical tracer model. To describe how the most important dynamical processes act on NO_X, such a model uses meteorological data generated by a general circulation model or obtained from observation analyses. In the present study, the chemical tracer model developed by *Prather et al.* [1987] is adopted. The NO_X chemistry scheme which the model needs in addition, also was used previously [*Ehhalt et al.*, 1992]. In fact, the study of *Ehhalt et al.* [1992] is extended here from a two-dimensional analysis of the sources contributing to the upper tropospheric NO_X distribution at northern mid-latitudes to three dimensions and the entire globe.

Other previous investigations of the tropospheric distributions of NO_X either are restricted to the contributions from individual sources [*Levy and Moxim*, 1989; *Kasibhatla et al.*, 1991; *Kasibhatla*, 1993], consider Lagrangian air parcels [*Penner et al.*, 1991], or are based on monthly mean dynamics [*Müller and Brasseur*, 1995]. However, since the present interest in this subject is quite large, results obtained by several additional approaches can be expected soon.

A description of the chemical tracer model and its main components transport, sources, sinks, and chemistry is given in Chapter 2 together with an overview of the various input data required to run the model. In particular, these data include emission scenarios for five of the six sources of tropospheric NO_X which are considered in the present study: fossil fuel combustion, soil microbial activity, biomass burning, downward transport of NO from the stratosphere, and aircraft emissions.

The sixth source of tropospheric NO_X considered here are lightning discharges. This source is the only one for which no suitable data base exists. In addition, the present knowledge of the processes leading to lightning flash formation within a thunderstorm is rather poor. The same is true for the net NO production initiated by the high amounts of energy released during an individual lightning discharge. An overview of processes is given in Chapter 3. Further, this chapter includes an estimate of the global annual mean NO production rate of lightning and an empirical parametrization of this source which was developed here for the chemical tracer model.

In order to test the tracer transport properties of the chemical tracer model, runs were made in which Radon-222, ^{222}Rn, is used as a passive tracer. Radon emissions can be described very simply. Furthermore, ^{222}Rn has an e-folding lifetime of 5.5 days which is comparable to the chemical lifetime of tropospheric NO_X. Comparisons between observed and calculated ^{222}Rn distributions therefore also allow a specification of the transport characteristics of NO_X, at least for the contribution from the surface sources. Such comparisons are discussed in Chapter 4 together with a summary of previous results on this subject. Since reliable ^{222}Rn observations are sparse, in particular in the tropics, additional comparisons with ^{222}Rn distributions obtained by different models are included in the last part of Chapter 4.

Results of the model calculations for the chemically active species NO_X are discussed in Chapter 5. This discussion is restricted to monthly mean tracer distributions for January and July, the two months which are expected to represent the extreme values of the annual cycle. To give an impression of the global structure of tropospheric NO_X distributions, horizontal maps of monthly mean NO_X mixing ratios are presented. Further, the calculated HNO_3 distributions and the ratio NO/NO_X are discussed. The absolute and relative contributions of each individual source are considered in terms of zonal mean values in Chapter 5. Corresponding horizontal maps are shown in Appendix B.

Finally, in Chapter 6, the calculated distributions of NO are compared with measurements obtained during four regional aircraft measurement campaigns. Although far from being global, these measurement data are the most actual and spatially most extended ones available at the moment. Observed and calculated regionally averaged vertical profiles and zonal mean distributions are investigated. This kind of data representation allows an evaluation of how realistic the NO distributions are which the CTM calculates.

Chapter 2

Description of the Model

The model used in the present study is a chemical tracer model, CTM, as it will referred to in the following. This CTM is a global, three-dimensional Eulerian model and was developed by *Prather et al.* [1987] to study distributions of chemically inert tracers like Radon or Fluorocarbons in the troposphere. In the presents study the CTM is extended in a way that distributions of chemically reactive nitrogen oxides can be calculated. In this case the CTM must solve the following set of n continuity equations:

$$\frac{\partial \rho_i}{\partial t} = \left(\frac{\partial \rho_i}{\partial t}\right)_{\text{transport}} + \left(\frac{\partial \rho_i}{\partial t}\right)_{\text{sources}} + \left(\frac{\partial \rho_i}{\partial t}\right)_{\text{sinks}} + \left(\frac{\partial \rho_i}{\partial t}\right)_{\text{chem. conversion}} , \qquad (2.1)$$

where ρ_i denotes the mass mixing ratio of a tracer labeled i, $i \in \{1, .., n\}$. How large n is depends on the complexity of the chemistry scheme used. Equation (2.1) contains the four processes that determine the temporal variation of the tracer i's mixing ratio in the model: transport, sources, sinks, and chemical conversion. These processes are explained in detail in the present chapter.

In general, Equation (2.1) is a partial differential equation which, however, is not solved directly by the CTM. Instead, a split-operator method is used. Thereby, Equation (2.1) is replaced by four individual differential equations, each of them containing the temporal variations of ρ_i due to one of the terms on the right-hand side of the original equation:

$$\left(\frac{\partial \rho_i}{\partial t}\right)_a = \left(\frac{\partial \rho_i}{\partial t}\right)_{\text{transport}} , \qquad \left(\frac{\partial \rho_i}{\partial t}\right)_b = \left(\frac{\partial \rho_i}{\partial t}\right)_{\text{sources}} , \qquad \ldots \qquad (2.2)$$

These four individual equations then are solved in sequence. The actual problem of running the CTM is not to solve Equations (2.2), but to provide suitable data and parametrizations for their right-hand sides. How these data are obtained for runs focusing on NO_X is discussed in the following. Section 2.1 describes how transport is treated in the CTM. The parametrizations of source and sink processes are presented in Sections 2.2 and 2.3, respectively. Finally, Section 2.4 explains the assumptions made on the model chemistry.

2.1 Transport

The CTM itself does not solve the equations of motion for the atmosphere. Instead, all meteorological data required to solve Equations (2.2) are calculated off-line by a dynamical model. This method has the advantage of making the CTM significantly faster and easier to handle than a dynamical model or even a coupled dynamical-chemical model. On the other hand, off-line meteorological input restricts the applicability of the CTM to the conditions prescribed by the dynamical model which, at least in the present case, cannot be modified. The missing feedback between chemistry and dynamics also implies that climate change studies cannot be carried out with the CTM.

The meteorological input for the CTM is calculated by version II of the general circulation model developed at the Goddard Institute for Space Studies, the GISS GCM [*Hansen et al.*, 1983]. Both the GCM and the CTM use the same model grid and the same vertical resolution of 9 layers between the Earth's surface and 10 hPa in a system of σ-coordinates. These coordinates are pressure coordinates which are normalized in a way that $\sigma = 0$ holds at the model's top and $\sigma = 1$ at the bottom, respectively [*Phillips*, 1957]. Advantage of the σ-coordinates is that orography can be included easily. When averaged globally, the σ-layers of the CTM are centered at the pressure levels 959, 894, 787, 635, 470, 322, 202, 110, and 40 hPa.

The GCM has a horizontal resolution of 5° in longitude, λ, and 4° in latitude, φ, whereas the grid boxes of the CTM cover elements of $d\lambda = 10°$ and $d\varphi = 8°$. This latter resolutions corresponds to an approximate size of 1100 km × 880 km for a grid box near the equator. To fit the coarser model grid of the CTM, all GCM data required are averaged over 4 horizontally adjacent boxes. These data are the horizontal mass fluxes, surface pressure, frequencies of dry and wet convection, temperature, and detailed convection statistics. The former three fields are available as 8-hour averages, the latter two are 5-day mean values. The vertical mass flux is determined in the CTM by evaluating the surface pressure tendency equation [e.g., *Holton*, 1979, p. 202]. Altogether, the meteorological input covers one full year. Initially, the GCM was developed exclusively for climate experiments. Hence, it does not include diurnal cycles. Ocean ice cover and surface temperatures are specified climatologically based on monthly mean values.

Like Equation (2.1), Equation (2.2a) also is split into several contributions:

$$\begin{aligned}\left(\frac{\partial\rho_i}{\partial t}\right)_{\text{transport}} &= -\nabla\cdot(\mathbf{u}\cdot\rho_i) + \left(\frac{\partial\rho_i}{\partial t}\right)_{\text{dry convection}} \\ &\quad + \left(\frac{\partial\rho_i}{\partial t}\right)_{\text{wet convection}} + \left(\frac{\partial\rho_i}{\partial t}\right)_{\text{large-scale diffusion}}, \end{aligned} \tag{2.3}$$

where $\mathbf{u} \equiv (u, v, w)$ denotes the three-dimensional velocity vector. As before, the individual contributions of Equation 2.3 are treated separately and the resulting four equations are solved in sequence, each of them with a time step of 8 hours.

The first term on the right-hand side of Equation (2.3) is the advection term. It is split into its 3 spatial components and is finally integrated in time by a method that conserves the second-order moments of the tracer distribution [*Prather*, 1986]. These moments are obtained by orthogonal transformations from the original tracer distribution which is a three-dimensional second-order polynomial. The time step for an individual temporal integration is 2 hours for u, 8/3 hours for v, and 4 hours for w. Altogether, one 8-hour time step contains a specific order of 4 integrations in zonal direction, 3 in meridional direction, and 2 in the vertical.

The second and the third term on the right-hand side of Equation (2.3) represent vertical redistribution of tracer due to dry and wet convective mixing. These subgrid-scale processes are parametrized in the GCM by simple adiabatic adjustment [*Manabe et al.*, 1965]. If the moisture content of an unstable layer is insufficient for condensation, vertical motion proceeds on a dry adiabat until the level of stability is reached. Complete mixing of layers is assumed along this path. If the moisture content of the unstable layer is large enough to allow condensation, half of the material of this layer is moved upward along a moist adiabat until its density reaches equilibrium with the environment. The transported mass is deposited in the upper layer and uniform subsidence is assumed anywhere else in the grid column to balance the upward mass flux.

The same convection mechanism acts in the CTM as well. The strength of convection in a certain CTM grid column is determined by sampling the GCM every hour and averaging the number of convective events counted within the corresponding grid columns of the GCM over a time period of 8 hours. A certain convective event in the CTM is characterized by its strength on the one hand side and by the 5-day mean values of the GCM convection statistics on the other hand side. The latter indicates which layers are involved in convection, i.e. where the cloud bases and tops are located.

In the CTM, dry convection is the main mixing process within the planetary boundary layer, PBL, whereas deep wet convection is the process which dominates exchange between the PBL and the free troposphere. Mixing by dry convection or by large-scale dynamics plays a minor role for this exchange.

The last term on the right-hand side of Equation (2.3), large-scale diffusion, was implemented by *Prather et al.* [1987] to make the inter-hemispheric exchange more efficient. This correction term is coupled with deep wet convection and is necessary if long living trace species are investigated. In the present study, it plays only a minor role.

2.2 Sources

Nitrogen oxides are released into the atmosphere, primarily as NO, from a variety of sources. Six of them are believed to add up to an almost complete representation of the total tropospheric burden of NO_X [*Logan*, 1983; *Ehhalt and Drummond*, 1988]. These six sources are listed in Table 2.1 together with the emission rates assumed in the present study. Table 2.1 also shows that the emission rate of each of the individual sources has an uncertainty of a factor of 2 at least. This uncertainty is low compared to the range of more than four orders of magnitude of NO_X mixing ratios observed in the troposphere. The emission rates of all sources except the purely anthropogenic ones are varying seasonally. A short description of each individual source is given in the following. The parametrization of the lightning source was developed during this study and is described in detail in Chapter 3.

Source	Emission Rate [Mt N/yr]	Annual Cycle	Reference
fossil fuel combustion	21.9 (13.1 - 28.9)[a]	no	*Dignon* [1992]
microbial activity in soils	4 (1 - 20)	yes	*Lee and Grobler* [1995]
lightning discharges	5 (2 - 10)	yes	this study, see Chap. 3
biomass burning	4.4 (2.5 - 16.5)	yes	*Müller* [1992]
downward transport from the stratosphere	0.65 (0.3 - 0.9)	yes	*Kasibhatla et al.* [1991]
aircraft emissions	0.45 (0.45 - 0.85)	no	*Wuebbles et al.* [1993]

[a] The figures in parentheses are estimated upper and lower limits [*Logan*, 1983; *Ehhalt and Drummond*, 1988].

Table 2.1: The sources and source strengths of tropospheric NO_X used in the CTM.

The oxidation of ammonia, NH_3, is neglected as a source of tropospheric NO_X in the present study. This process results in a net NO_X production - or net NO_X destruction, depending on the actual concentrations of NO_X and O_3. The total amounts of NO_X produced thereby are estimated to be 3 Mt N/yr [*IPCC*, 1995]. In a different study the main product of NH_3-oxidation is assumed to be N_2O [*Dentener and Crutzen*, 1994]. Via the stratosphere, this N_2O also could increase the tropospheric NO_X concentrations. However, the global N_2O emission rate by NH_3-oxidation is 0.4-1.8 Mt N/yr which is only about 5% of the current atmospheric N_2O emissions.

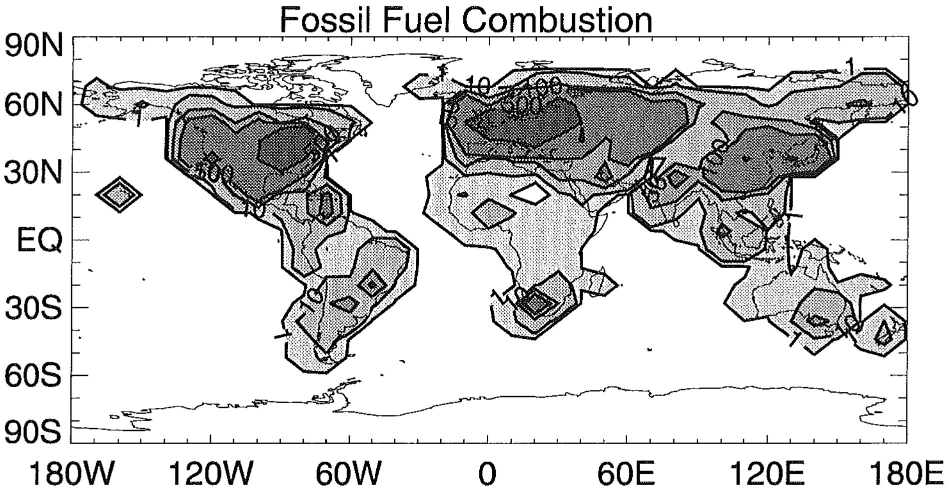

Figure 2.1: Monthly mean NO_X emission rate of the source fossil fuel combustion. Contours are displayed at 1, 10, 50, 100, and 500 mg N m^{-2} yr^{-1}.

2.2.1 Fossil Fuel Combustion

For the fossil fuel combustion source the emission scenario provided by *Dignon* [1992] is used. It is based on the assumption that within an individual country the distribution of the total fossil fuel consumption is given by the distribution of the population density of that country. The scenario has a resolution of $1° \times 1°$ and refers to the year 1980. Arithmetic mean values are used here for the coarser resolution of the CTM grid boxes. The resulting global emission pattern is shown in Figure 2.1. As much as 95% of the global fossil fuel consumption take place in the northern hemisphere. Peak values higher than 1 g N m^{-2} yr^{-1} are reached in the eastern United States, in central Europe and in East Asia. In the southern hemisphere emissions higher than 100 mg N m^{-2} yr^{-1} only occur in South Africa and southern Brazil. Altogether, more than half of the entire NO_X in the troposphere is emitted by fossil fuel combustion.

2.2.2 Microbial Activity in Soils [1]

Nitric oxide, NO, is produced in soils by nitrification under aerobic and denitrification under anaerobic conditions. It is released into the boundary layer and further transported into the free troposphere. *Williams et al.* [1992a] give NO release rates as a function of vegetation type, fertilization rates, and soil temperature. These rates together with the CTM's surface temperature and the global vegetation index distribution of *Matthews* [1983] are used to derive monthly mean patterns for microbial NO emission. Owing to the coarse grid of the CTM, the different kinds of vegetation zones are reduced to tropical forest, grassland, forest at mid-latitudes, agriculture regions (assumed to emit like soja beans), and emission-free surfaces (ice cover, water, desert). Growing periods of the agriculture regions are defined separately for the individual latitude bands of the model. This procedure results in a global emission of approximately 12 Mt N/yr, which is in reasonable agreement with previous estimates of this source [e.g., *Müller*, 1992].

However, the effective strength of soils as a source of atmospheric NO is much lower. In fact, a large fraction of the nitrogen oxides emitted is trapped by the vegetation canopy. To take account for this loss due to vegetation, the global strength of soil emissions is scaled down by a factor of 3 as it was estimated

---

[1] The parametrization of this source was developed by Ellen Grobler and Franz Rohrer and is documented in *Lee and Grobler* [1995] and *Grobler* [1996].

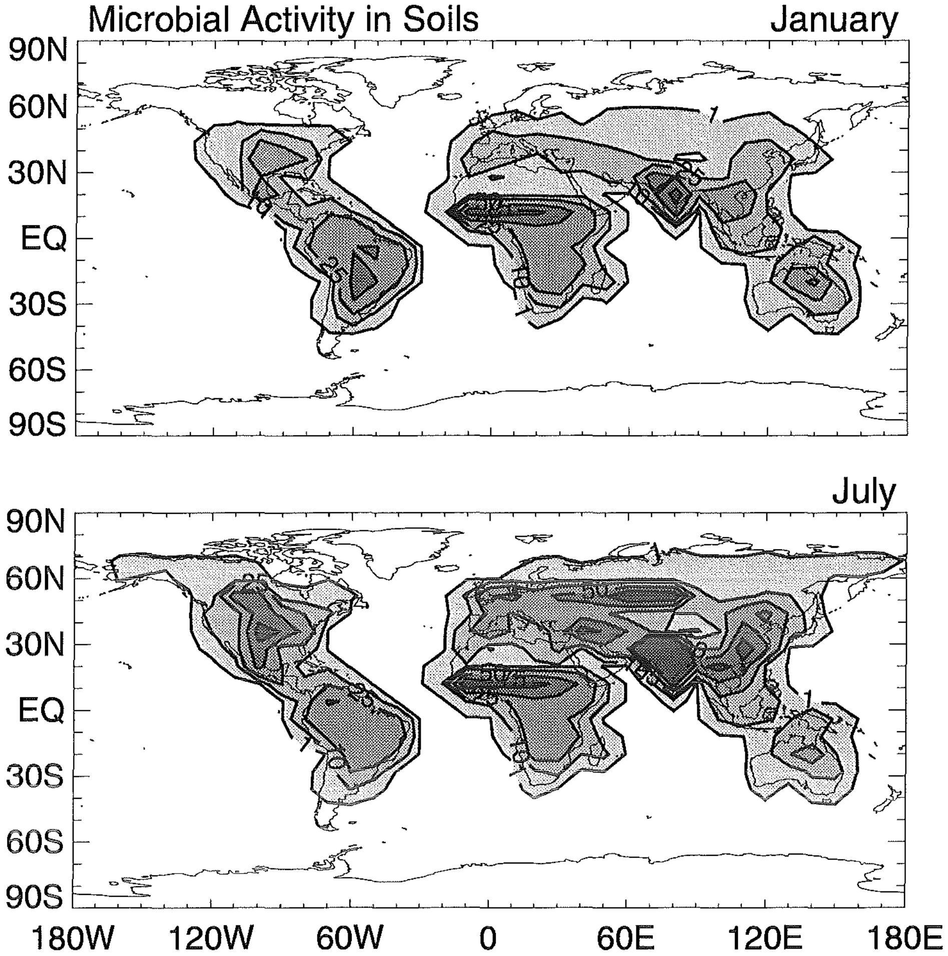

Figure 2.2: Monthly mean NO_X emission rates of microbial activity in soils for (upper panel) January and (lower panel) July. Contours are displayed at 1, 10, 25, 50, and 75 mg N m^{-2} yr^{-1}.

by *Jacob and Wofsy* [1990] for tropical forest. The resulting value of 4 Mt N/yr for the global emission rate of the source soil microbial activity is in close agreement with the recent estimate of 5.5 Mt N/yr for this quantitiy which was derived from a temperature and precipitation dependent emipirical model of soil-biogenic NO_X emissions [*Yienger and Levy*, 1995].

The resulting emission patterns of microbial activity in soils are shown in Figure 2.2 for January and July, respectively. Owing to the temperature dependence of this source the highest emission rates occur at low latitudes, in particular south of the Sahara and in India. In the lower panel of Figure 2.2, additional regions of emission rates higher than 50 mg N m^{-2} yr^{-1} are visible. These are the the main agricultural regions of the United States, Russia, and China, where large amounts of NO are released by fertilization. Altogether, the present estimate of NO emissions by microbial activity in soils reaches a global emission rate of 3.2 Mt N/yr for January and of 5.0 Mt N/yr for July.

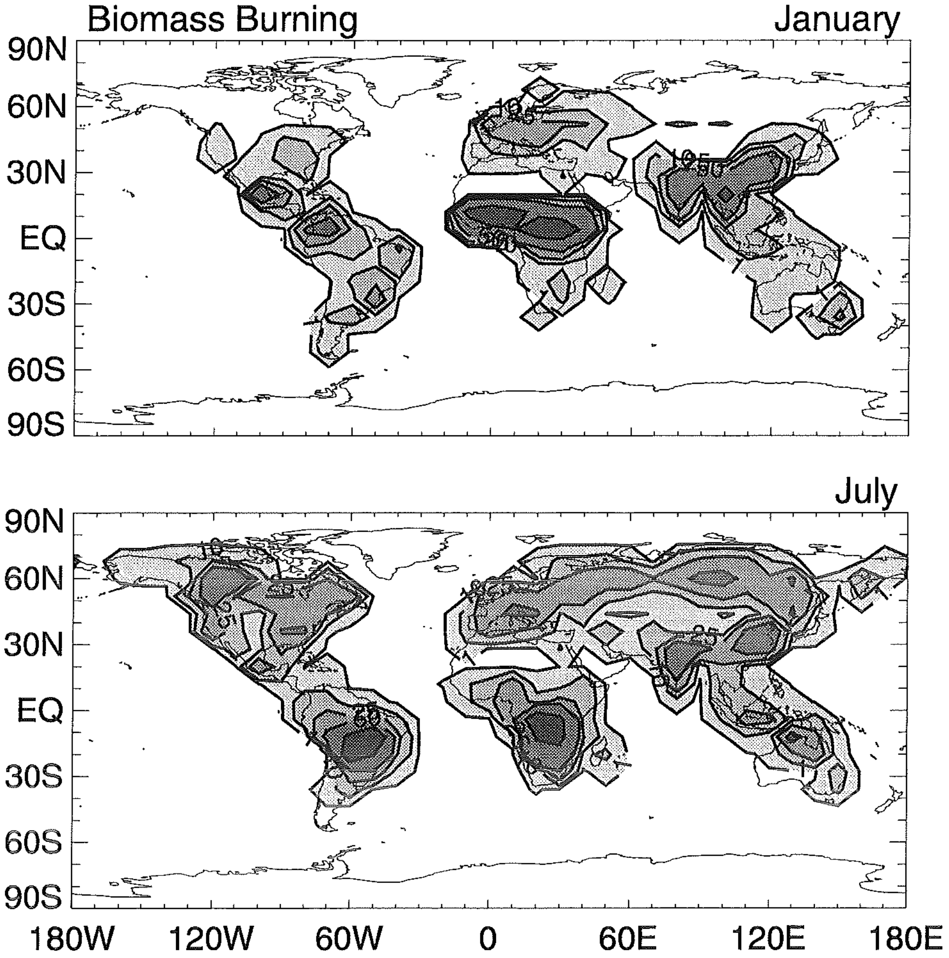

Figure 2.3: Monthly mean NO_X emission rates of biomass burning for (upper panel) January and (lower panel) July. Contours are displayed at 1, 10, 25, 50, and 150 mg N m^{-2} yr^{-1}.

2.2.3 Biomass Burning

Biomass burning is associated with deforestation, savannah burning, slash and burn agriculture, forest wildfires, wood used as fuel, and burning of agricultural wastes. Here, the monthly mean release estimates of *Müller* [1992] are adopted. They are mapped from their original resolution of 5° × 5° on the coarser grid of the CTM. The result is shown in Figure 2.3 for January and July, respectively, and averaged onto the CTM grid. Contrary to microbial activity in soils at low latitudes, biomass burning there mainly occurs during the dry season, which is the southern hemispheric winter. At higher northern latitudes, biomass burning also is largest in July. During this month it even is the largest individual source in northwestern Canada and parts of Siberia. The global emission rates of biomass burning used here are 4.0 Mt N/yr in January and 5.1 Mt N/yr in July.

2.2.4 Photochemical Production in the Stratosphere

Stratospheric NO is formed when highly reactive atomic oxygen, O(^{1}D), reacts with N_2O. The former species is generated by photolysis of O_3, the latter is emitted at the surface and reaches the stratosphere because it has no efficient sinks in the troposphere. From the lower stratosphere, NO can get back into the upper troposphere.
In the CTM, this source is taken into account by using the zonal mean stratospheric NO production rates calculated by *Kasibhatla et al.* [1991]. They are shown in Figure 2.4 for January and July, respectively. According to the annual cycle of the O_3 photolysis rate, the highest NO production rate occurs in the tropical summer hemisphere and decreases to zero over the winter pole. The stratospheric source in the CTM has an emission rate of 0.64 Mt N/yr in January and of 0.58 Mt N/yr July. It is assumed that 75% of the stratospheric NO react further to yield HNO_3 and that only 25% contribute to NO_X directly. Corresponding amounts of both tracers are added in the uppermost model layer at every time step. Since the time scale of vertical mixing in the stratosphere is much larger than the time scale of reaching photochemical equilibrium, the model's sensitivity with respect to the exact partitioning between NO_X and HNO_3 is very low.

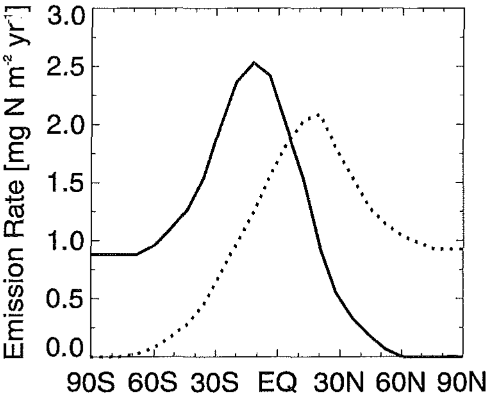

Figure 2.4: Monthly mean emission rate of the source stratospheric NO production for (solid line) January and (dotted line) July.

2.2.5 Aircraft Emissions

Strictly speaking, aircraft emissions are a component of fossil fuel combustion source. Moreover, their contribution to tropospheric NO_X is about 50 times smaller than that of the other fuel consuming processes. Despite this, aircraft emissions are treated here as a separate source. This is done because they inject NO_X directly into the upper troposphere, a region which is reached only by a few percent of the NO_X emitted at the surface. Further, air traffic increases at much higher rates than it does fossil fuel combustion at the surface. Hence, model calculations aiming at future emission scenarios require that both types of fossil fuel consumption are considered separately.

The aircraft emission scenario used here is based on the three-dimensional inventory compiled by Boeing and McDonnell Douglas [*Wuebbles et al.*, 1993] on a 1° x 1° grid. The scenario refers to the year 1990, for which an emission rate of 0.45 Mt N/yr is obtained. The corresponding emission pattern is shown in Figure 2.5. The regions of densest air traffic are reflected in high NO_X emissions over the United States and central Europe. In between, the flight corridor above the North Atlantic is clearly visible. Japan is another region of high aircraft emissions. Where air traffic is rare as over the Pacific, individual flight tracks can be distinguished which follow Great Circles.

2.2.6 Resolution of the Source Parametrizations

The emissions of the surface sources fossil fuel combustion, soil microbial activity, and biomass burning are treated as volume sources in the lowest model layer. The vertical resolution of the CTM with respect to volume sources can be improved if in addition to the total amount of tracer released in a grid box the mean slope of the tracer concentration in the box is adjusted also. This is done for fossil fuel combustion, the strongest surface source, and for aircraft emissions. The latter source needs a vertical resolution higher than the model's nine σ-layers in order to properly represent the vertical profile of the injections.

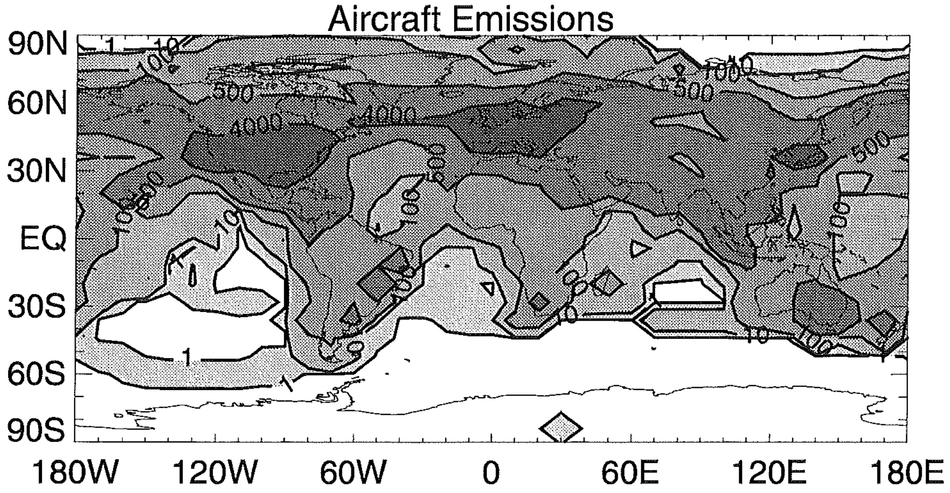

Figure 2.5: Monthly mean rates of NO_X emissions by aircraft. Contours are displayed at 1, 10, 100, 500, and 4000 μg N m^{-2} yr^{-1}.

Equations (2.2) are integrated in time one by one, each for the same time period of 8 hours. When the temporal integration of these four equations is completed, then a new set of meteorological data is read in before the temporal integration of the four equations is carried out again. However, it turned out that Equations (2.2b)-(2.2d) need shorter time steps in order to meet the requirement that mutation of the individual processes does not change the result. Therefore, each 8-hour time step of the processes sources, sinks, and chemical conversion is subdivided into 8 individual steps of 1 hour each. These three processes then are integrated in turn, each for 1 hour and each 8 times in total. Thus, the integration of the transport processes alternates with 24 (3 × 8) sub-integrations of 1 hour each for sources, sinks, and chemical conversion.

2.3 Sinks

Nitrogen compounds eventually are removed from the atmosphere by dry deposition at the Earth's surface as well as by the wet deposition processes rainout and washout. Dry deposition acts on NO_X and HNO_3, whereas wet deposition processes affect only the water soluble species, i.e. HNO_3. Following *Ehhalt et al.* [1992], the sink processes are parametrized in a very simple manner here.

2.3.1 Dry Deposition

Dry deposition is calculated from

$$\frac{dm(t)}{dt} = -m(t)\frac{v_d}{\Delta z}\,, \tag{2.4}$$

where $m(t)$ is the time dependent mass of tracer in a grid box of the lowest model layer, v_d is the deposition velocity, and Δz is the height of the grid box. The deposition velocity of HNO_3 is assumed to be 2 cm/s on all surfaces and that of NO_2 is 0.5 cm/s on land surfaces and zero over oceans. NO is not dry deposited at all. It should be noted that for HNO_3 v_d is rather high and may result in an overestimate of the dry deposition of this tracer.

Dry deposition essentially maps the surface source distribution, as Figure 2.6 indicates. This is the case since the rate of dry deposition is proportional to the tracer concentration in the lowest model layer which is dominated by the source processes. Horizontal transport velocities in this layer are rather low, up to a few meters per second only. In fact, most of the tracer emitted at the surface never leaves the lowest model layer, but is converted to HNO_3 and then removed by dry deposition close to the source.

2.3.2 Wet Deposition

Rainout summarizes all processes which remove HNO_3 from the troposphere except those acting within clouds. Such rainout processes are entrainment of air from outside a cloud, below-cloud scavenging or aerosol scavenging. Their mean effect is parametrized as a removal time which is a function of height only. The removal time is assumed to be 2 days in the lowest two σ-layers, 10 days in the free troposphere, and zero in the stratosphere.

Washout removes HNO_3 within clouds via scavenging by precipitation particles. It is coupled with the model's convection activity since cloud and precipitation processes are not resolved explicitly. If air is moved upwards in a cloud, a certain fraction of HNO_3 is removed. This fraction is 50%, a choice which is somewhat arbitrary. However, since in most regions the contribution of washout to the total HNO_3 removal is lower than 20%, the model is not very sensitive with respect to this parameter. Moreover, because of the slow back conversion rate of HNO_3 to NO_2, the resulting change in the NO_X mixing ratio is negligible, if this fraction is set to 25% or 75%, respectively. The corresponding change of the HNO_3 mixing ratio, of course, is higher, but is of little relevance in the present study, where interest is focused on NO_X.

The patterns of wet deposition are shown in Figure 2.7 for January and July. As dry deposition, wet deposition of HNO_3 is largest over the continents, simply because the tropospheric HNO_3 content is highest there. However, rainout acts across the entire depths of the troposphere and, hence, the zonal gradients in the wet deposition patterns are much weaker than that for dry deposition. At southern mid-latitudes, where hardly any dry deposition takes place, washout contributes 20-40% to the total removal of HNO_3. In northern mid-latitudes, this fraction is about 20%. In the tropics washout is even less important, since there the rising air is lifted from a less polluted boundary layer.

2.4 Model Chemistry

The chemical scheme used here is kept as simple as possible. It is a linear scheme and only 2 trace species are transported, NO_X and nitric acid, HNO_3. CTM calculations based on a more complex, nonlinear chemistry scheme including Carbon monoxide, CO, Methane, CH_4, and several other tracers are presented by *Kuhn* [1996].

2.4.1 The Tropospheric Chemistry Scheme

In the troposphere inter-conversion of the tracers NO_X and HNO_3 takes place according to the chemistry scheme adopted from *Ehhalt et al.* [1992]. This scheme represents the daytime conversion of NO_X to HNO_3 by the addition reaction of the hydroxyl radical, OH, to NO_2:

$$NO_2 + OH + M \rightarrow HNO_3 + M \,, \tag{2.5}$$

where M is any third body involved in collision. HNO_3 is converted back to NO_X via photolysis and reaction with OH:

$$HNO_3 + h\nu \rightarrow NO_2 + OH \tag{2.6}$$

$$HNO_3 + OH \rightarrow NO_3 + H_2O \,. \tag{2.7}$$

The NO_3 formed by Reaction (2.7) is assumed to photolyze to NO_2 immediately. Reactions (2.6) and (2.7) have relatively low rates and are not very important for the tropospheric model results.

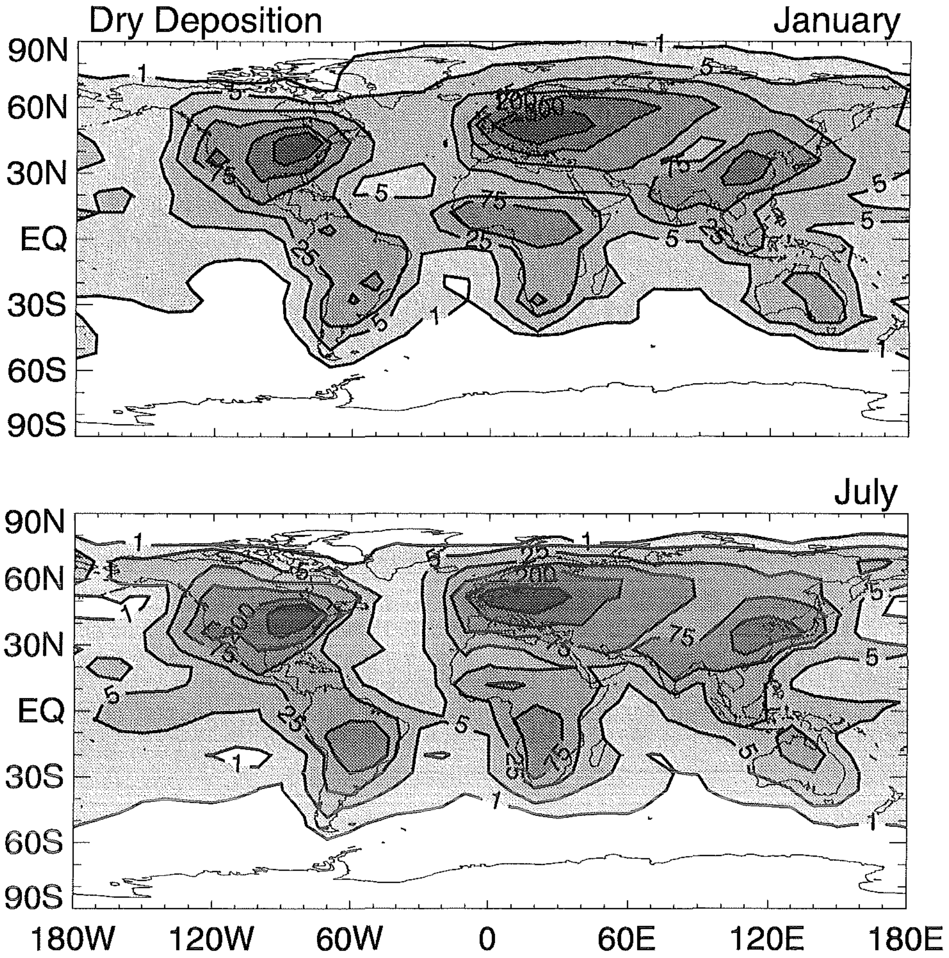

Figure 2.6: Monthly mean dry deposition rates of NO_X and HNO_3 for (upper panel) January and (lower panel) July. Contours are displayed at 1, 5, 25, 75, 200, and 500 mg N m^{-2} yr^{-1}.

Further, NO_2 is allowed to react with ozone, O_3:

$$NO_2 + O_3 \rightarrow NO_3 + O_2 \; . \tag{2.8}$$

Since NO_3 is photolysed back immediately in the presence of sunlight, Reaction (2.8) makes a net contribution during the night only. Then, however, all NO_3 formed by Reaction (2.8) is converted to HNO_3. Aqueous phase intermediate steps or formation of N_2O_5 are not resolved explicitly. This can be done, because Reaction (2.8) is assumed to be the rate limiting step for this reaction chain and, hence, determines the conversion rate of NO_3 to HNO_3.

The NO_2 concentrations needed for the conversion reactions are derived from the reactions

$$NO + O_3 \rightarrow NO_2 + O_2 \tag{2.9}$$

$$NO_2 + h\nu \rightarrow NO + O \; , \tag{2.10}$$

which establish a fast photochemical equilibrium between NO and NO_2 and, hence, between NO_X and NO_2.

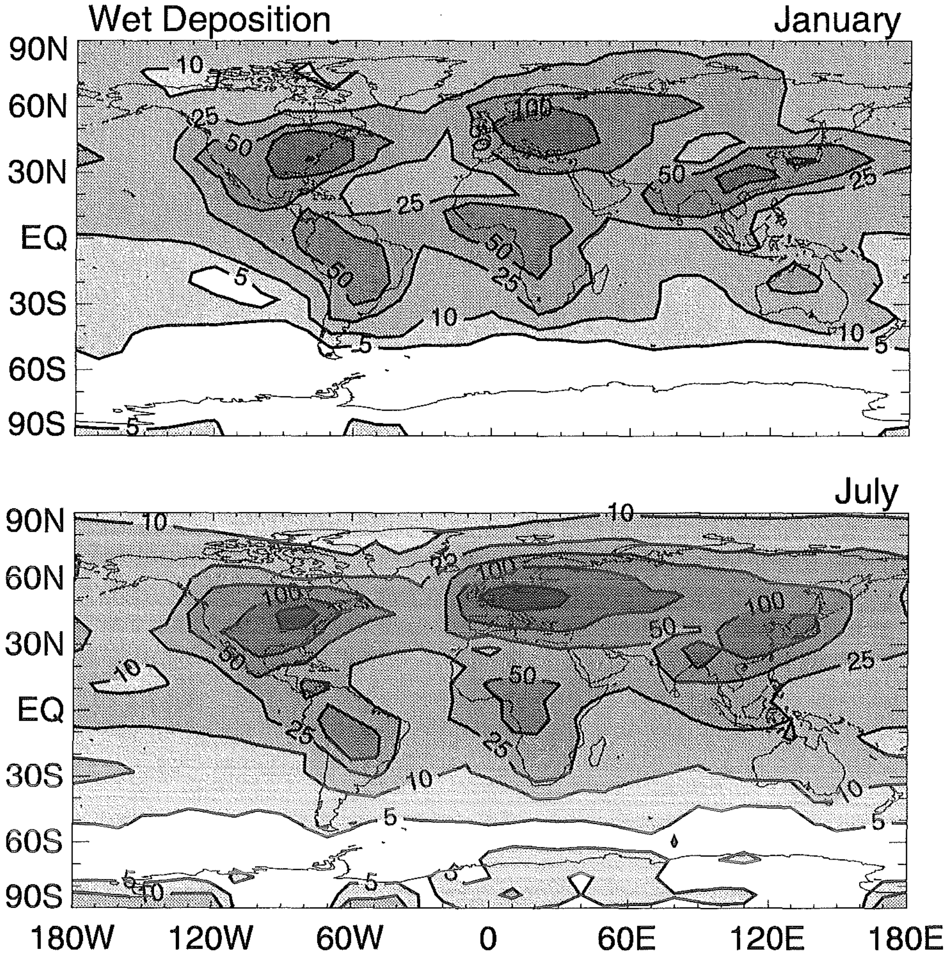

Figure 2.7: Monthly mean wet deposition rates of HNO_3 for (upper panel) January and (lower panel) July. Contours are displayed at 5, 10, 25, 50, 100, and 250 mg N m^{-2} yr^{-1}.

Consistent with the dynamical resolution of the CTM, the present chemistry scheme provides diurnal mean tracer mixing ratios. If necessary, as in Reaction (2.8), a weight factor is used which provides the percentage of nighttime per 24 hours as a function of latitude and Julian day.

2.4.2 OH, Ozone, and Photolysis Frequencies

The above chemistry scheme is linear, since the concentration fields of OH and O_3 are prescribed and held constant as 5-day averages. The same is true for the photolysis frequencies of NO_2 and HNO_3, J_{NO_2} and J_{HNO_3}, respectively.

The three-dimensional field of OH used here is provided by *Spivakovsky et al.* [1990]. It was calculated with a version of CTM where 24-hour average concentrations of OH from a detailed chemical model are approximated by a high-order polynomial fit. Zonal and monthly mean values of the resulting OH field are shown in Figure 2.9 for January and July. Peak concentrations of more than 2×10^6 molecules/cm^2 occur in the sub-tropical free troposphere of the summer hemisphere. In the upper troposphere, *Spivakovsky et al.*

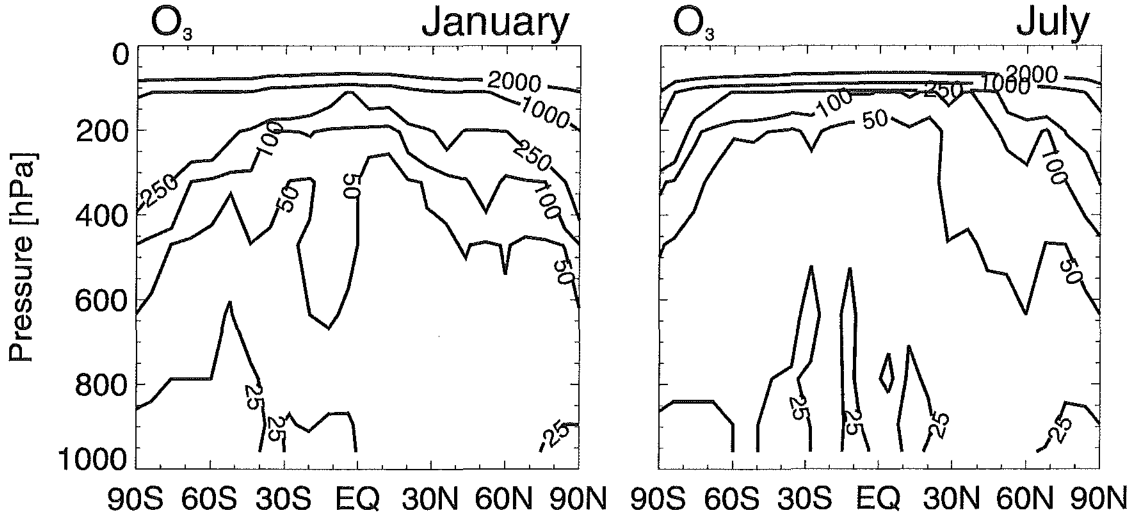

Figure 2.8: Monthly mean values of the O_3 mixing ratio for (left panel) January and (right panel) July. Contours are displayed at 25, 50, 100, 250, 1000, and 2000 ppbv.

probably underestimate the concentration of OH since they did not take into account the effect of acetone. Except in the tropics, no OH concentration are available for σ-layers 8 and 9.

The O_3 data used in the CTM's linear chemistry scheme are zonal and monthly mean mixing ratios. They have been compiled by Ellen Grobler and Franz Rohrer from the experimental studies cited in *Spivakovsky et al.* [1990] and a number of more recently published data [*Komhyr et al.*, 1989; *London and Liu*, 1992; *Marenco and Said*, 1989; *Pyle et al.*, 1994; *Seiler and Fishman*, 1981; *Smit et al.*, 1991; *Weller et al.*, 1996]. For January and July, the resulting O_3 data are shown in Figure 2.8. The troposphere is characterized by O_3 mixing ratios well below 100 ppbv, whereas in the stratosphere several ppmv O_3 occur. The small scale structure in Figure 2.8 reflect inconsistencies between the individual measurement techniques, natural variability, and the the fact that even the relatively large amount of measurements on which this figure is based is far from being sufficient for a climatological mean which is what one would prefer to use. However, one must keep in mind that corresponding O_3 distributions calculated by different models deviate from each other by about a factor of 2 [e.g., *WMO*, 1995]. The O_3 distributions shown in Figure 2.8 lie well in between these model results. The three-dimensional calculations of *Müller and Brasseur* [1995] show that in the lower troposhpere, where the zonal gradients of the O_3 mixing ratio are expected to be largest, the zonal variation of O_3 is a factor of 2 at most.

The photolysis frequencies J_{NO_2} and J_{HNO_3} are obtained as two-dimensional fields by interpolating the output of a one-dimensional, height-resolving model with fully treated chemistry [*Roeth*, 1986]. The aerosol distributions assumed in this model are based on *WMO* [1996]. Runs have been made for 4 different seasons and with solar UV radiation conditions for latitude $\varphi = 0°, 15°, 30°, ..., 90°$, each for continental and marine aerosol profiles separately. Cloud effects are not taken into account, all photolysis frequencies used in this study refer to clear-sky conditions. Altogether, the uncertainty of the photolysis frequencies is estimated to be a factor of 2.

Monthly mean values of the photolysis frequencies J_{NO_2} and J_{HNO_3} are shown in Figures 2.10 and 2.11 for January and July, respectively. The slight difference in these photolysis frequencies between the two summer hemispheres reflects the unequal distribution of aerosol induced by the unequal distribution of continents in both hemispheres. The different values of the surface albedo are of minor importance. In the

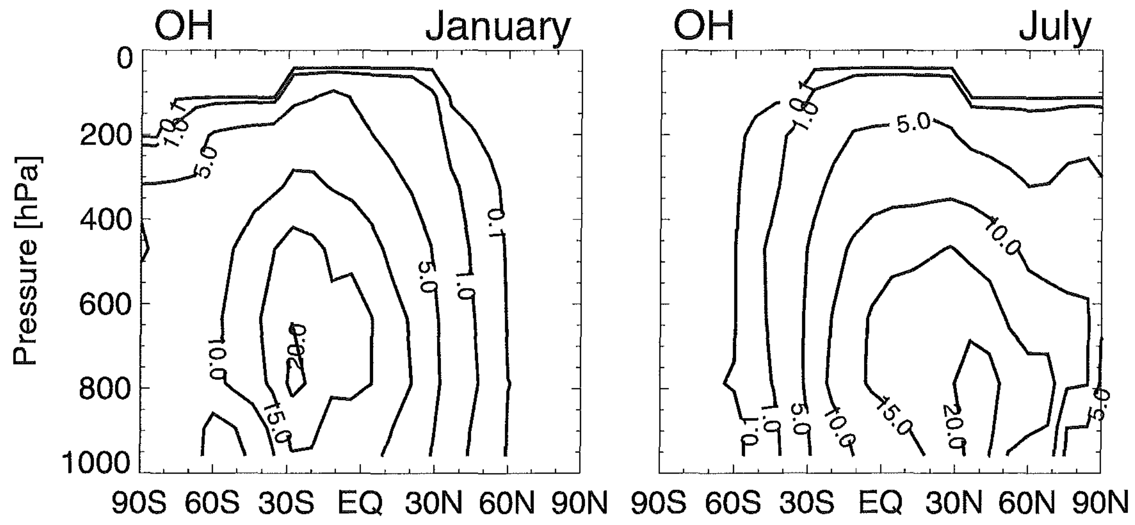

Figure 2.9: Monthly mean values of the OH concentration for (left panel) January and (right panel) July [redrawn from *Spivakovsky et al.*, 1990]. Contours are displayed at 1×10^4, 1×10^5, 5×10^5, 1×10^6, 1.5×10^6, and 2×10^6 molecules cm^{-2}.

winter hemispheres, where the photolysis frequencies generally are weaker, the dependence on the type of surface hardly is visible.

2.4.3 The Stratospheric Chemistry Scheme

The stratospheric chemistry is even simpler than the tropospheric one. Its sole function is to provide the proper partitioning between NO_X and $NO_Y \equiv NO_X + HNO_3$ for the stratospheric input at the tropopause, the height of which is defined by the lower rim of the grid box in which the vertical temperature gradient, $\partial T/\partial z$, is lower than $\partial T/\partial z\ |_{tropop.} \equiv -0.05$ K/hPa. [2] Above the tropopause, NO_X is converted to HNO_3 everywhere with a time constant of 13 days. HNO_3 is converted back to NO_2 by photolysis, Reaction (2.6), with a photolysis frequency of up to 3×10^{-7}. This choice of parameters yields a NO_X/NO_Y ratio of 0.3 at 40°N and 12 km altitude in January in good agreement with experimental observations of *Carroll et al.* [1990]. In addition, the strong latitude gradient of the NO_X/NO_Y ratio in the lower stratosphere, which decreases from 0.08 at about 60°N to 0.02 at about 70°N in winter [*Fahey et al.*, 1990], is described well by this simple parametrization. Examples of the CTM's stratospheric extent are shown below.

---

[2] A similar purely empirical, but convenient criterion is used by *Roelofs and Lelieveld* [1995] to distinguish between tropospheric and stratospheric chemistry in the ECHAM global circulation model. The exact value of $\partial T/\partial z\ |_{tropop.}$ depends on the model resolution. Here, it is set by comparing its zonal mean with corresponding climatological mean values [*Holton*, 1979; *Liljequist and Cehak*, 1979]. The criterion $\partial T/\partial z = \partial T/\partial z\ |_{tropop.}$, however, is applied in each grid column separately in order to allow variations with longitude.

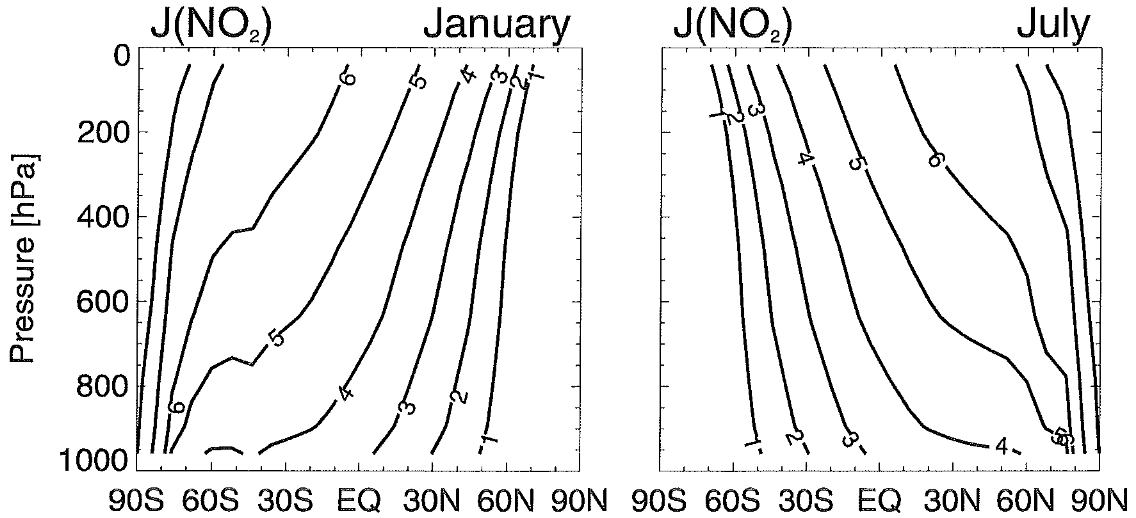

Figure 2.10: Monthly mean values of the photolysis frequency $J_{\mathrm{NO_2}}$ for (left panel) January and (right panel) July. Contours are displayed at 1×10^{-3}, 2×10^{-3}, 3×10^{-3}, 4×10^{-3}, 5×10^{-3}, 6×10^{-3}, 8×10^{-3}, and 1×10^{-2} s^{-1}.

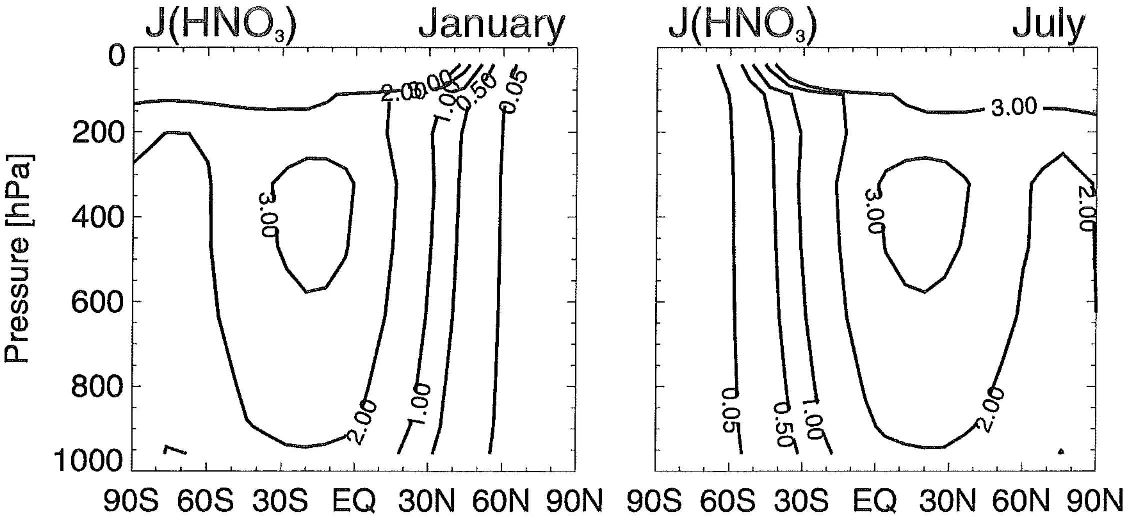

Figure 2.11: Monthly mean values of the photolysis frequency $J_{\mathrm{HNO_3}}$ for (left panel) January and (right panel) July. Contours are displayed at 5×10^{-9}, 5×10^{-8}, 1×10^{-7}, 2×10^{-7}, and 3×10^{-7} s^{-1}.

Chapter 3

Lightning Discharges as a Source of Tropospheric NO_X

Lightning is a transient, high-current electric discharge that occurs in the atmosphere of the Earth and of other planets. A lightning flash in principle is an enormous spark with a length of tens of kilometres or more. In the present study, lightning events are assumed to be generated exclusively by thunderclouds. Those rare events of lightning associated with other mechanism like sand storms, volcano eruptions, or discharges within the stratosphere are neglected.

The global rate of NO production by lightning discharges is highly uncertain because neither the processes leading to a discharge within a thundercloud nor the subsequent net NO formation are understood completely. For this reason the parametrization of lightning as a source of tropospheric NO_X is separated into two subproblems which are solved independently. The first problem is to estimate how much NO_X is produced globally by thunderstorms. Second, a global distribution of lightning occurrence is required which should be consistent with the meteorological conditions covered by the CTM. Since the amount of NO emitted by an individual lightning discharge depends on its energy, this problem is associated with the question of how to weight an individual discharge occurring at a specific location and during a specific season. This, in turn, depends on the vertical profile of the net NO_X production caused by a lightning discharge. Contrary to the solution of the second problem, the solution of the first one does not depend on the model one is using.

Before these two problems are addressed, the present knowledge about the processes leading to lightning and the formation of NO are explained briefly in Section 3.1. Section 3.2 describes how the global NO_X production rate of thunderstorms can be estimated. The actual parametrization of the lightning distribution consists of two steps, each covering different physical processes at different scales. First, in Section 3.3, the seasonally varying global horizontal distribution of lightning occurrence is determined. Then, in Section 3.4, NO emissions are distributed vertically within the grid columns that contain lightning. The result of the lightning source parametrization and an overview of all six sources of NO_X are given in Sections 3.5 and 3.6, respectively.

3.1 Phenomenology and Physical Basics

The most recent and probably most comprehensive overview of the present knowledge on atmospheric electricity is given by *Volland* [1995]. Another, somewhat less detailed collection on this subject was edited by *Krider and Roble* [1986]. Dynamical aspects of thunderstorms are discussed by *Cotton and Anthes* [1989] or in the August issue of Monthly Weather Review [*AMS*, 1994], whereas a variety of papers on electrical phenomena in the atmosphere can be found in special sections of the Journal of Geophysical Research [*AGU*, 1989; *AGU*, 1994; *AGU*, 1995].

3.1.1 Thunderstorms and Lightning Discharges

Convective clouds that succeed in producing lightning are thunderstorms by definition. They occur under a variety of meteorological situations as within one air mass that is heated inhomogeneously, at cold or warm fronts, associated with monsoon convection, in tropical cyclones, or in winter snow storms. Common to all these situations is that moist convection is triggered in a way that large concentrations of ice *and* liquid water particles coexist at temperatures well below -20°C. The presence of both types of particles is a necessary condition for charge separation to take place. In most cases this condition requires vigorous updrafts and downdrafts, but occasionally vertical motions of tens of centimetres per second can be sufficient to generate a lightning discharge [*Williams*, 1995].

Individual thunderstorm cells often occur embedded in meso-scale systems: in cloud clusters covering areas of several tens or sometimes hundreds kilometres in diameter, along squall lines with lengths of 100 km or more, or within meso-scale convective complexes. Such systems live between several hours and up to 2-3 days, whereas the individual cells have lifetimes of about 30 minutes. A comprehensive overview on the dynamics of such systems is can be found in *Cotton and Anthes* [1989].

The most frequent kind of thunderclouds are cumulonimbus clouds. They are the longest living convective clouds and the highest reaching ones. Their lifetimes range from 45 min to several hours. Often they extend from the level of condensation, the cloud base, up to the tropopause or even overshoot into the stratosphere. The typical horizontal dimension of such a thundercloud is about 30 km. Many cumulonimbus clouds consist of several individual cells which evolve successively. The updraft and downdraft structure of cumulonimbus clouds are highly variable in nature, as it are the related transport phenomena. References of recent observational and theoretical studies on this subject are provided by *Hauf et al.* [1995].

Cloud electrification processes are understood only roughly. They are assumed as acting over 2 spatial scales, a micro-scale separation that ultimately leads to charged ice and water particles, and a cloud-scale separation that produces large volumes of net positive and negative charge and eventually lightning [e.g., *Krider and Roble*, 1986; *Saunders*, 1995]. The micro-scale separation includes the creation of ion pairs, ion attachment, and charge that may be separated by collision between individual cloud and precipitation particles. This separation may be caused by gravitational forces acting on oppositely charged particles of different size and by aerodynamic drag. The cloud-scale separation is closely associated with the development of precipitation, although the space charge centre appears to be displaced both vertically and horizontally form the main precipitation core. The most likely case is that for the generation of a lightning discharge several of these processes must act simultaneously.

In most cumulonimbus clouds negative charges are centred at altitudes between 6 and 8 km above mean sea level where the ambient air temperature is about -10 to -20°C. The positive charge is more diffuse than the negative one and most of it at higher altitudes. A secondary pocket of positive charge is occasionally found in precipitation near the cloud base [*Williams*, 1989]. In meso-scale convective systems, up to 5 layers of charge with alternating sign are observed [*Stolzenburg et al.*, 1994].

The actual discharge can be initiated when the electric field in a thundercloud locally exceeds 400 kV/m. This initiating process is not well understood. The discharge channel usually is highly branched and propagates stepwise horizontally and downward. When one of the branches gets close to the ground, the first *return stroke* begins, a discharge that starts at the Earth's surface and propagates upwards. The peak power dissipated by the return stroke is on the order of 10^8 watts per meter of channel, the peak channel temperature is 30,000 K at least. Details of these processes are discussed by *Krider* [1986] or in the review of *Ogawa* [1995].

Many lightning discharges do not reach the Earth's surface, but remain within the cloud. Such discharges are called *cloud-to-cloud discharges*, CC for brevity, in contrast to *cloud-to-ground discharges*, CG, which touch the ground. Cloud-to-cloud discharges have no return stroke, whereas usually there are 2-4 return strokes associated with a CG discharge, each of them affecting a different volume of cloud charge.

3.1.2 Location of Discharges within Thunderclouds

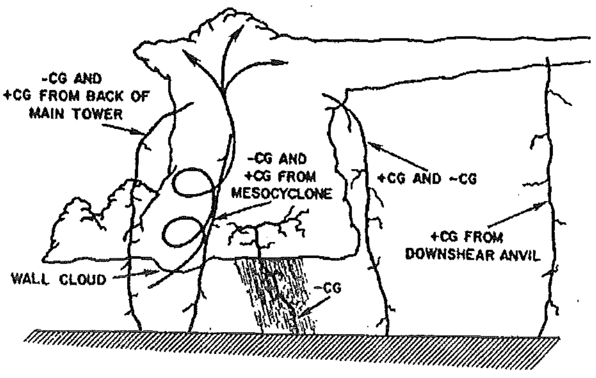

Figure 3.1: Sketch of observed locations of CG flashes from severe thunderstorms. The horizontal scale of this storm sketch is greatly compressed [adopted from *Rust et al.*, 1981].

The dynamical conditions in a thundercloud strongly depend on its type and on the meso-scale environment. Hence, they are quite variable and a general theory how individual flashes are distributed within a thunderstorm cannot be propounded. Moreover, even within the same general meso-scale environment distinctly different CG lightning signatures are observed [*Nielsen et al.*, 1994].

Observations relating dynamical properties of a thundercloud with lightning flash rates are inconsistent. *Krehbiel et al.* [1983], for example, report from thunderstorms observed in New Mexico that lightning discharges formed throughout the precipitation region of the storm. Moreover, the discharges appeared to be bounded by the precipitation region. *Williams* [1985], however, summarized a number of observations of lightning source regions and the locations of precipitation. He concluded that in many cases the regions of intense precipitation are not regions of maximum space charge density. *Rust et al.* [1981] report observations of +CG[1] starting at different regions within a thundercloud: on the back of the main storm tower, within the wall cloud, and from the down-shear anvil. A summarizing sketch of their observations is shown in Figure 3.1. Other, more recent observations also confirm a nonlocal distribution of individual lightning flashes as sketched in this figure [e.g., *MacGorman and Burgess*, 1994].

Meso-scale convective systems (MCS) tend to produce +CG lightning associated with stratiform precipitation [e.g., *Petersen and Rutledge*, 1992; *Rutledge and Petersen*, 1994], but, at least in the MCS observation reported by *Stolzenburg et al.* [1994], a relation between the spatial charge structure and the actual occurrence of +GC flashes was not found.

Grandt [1991] compares infrared synoptic-scale satellite observations of cloud top temperatures with measurements of sferic[2] activity. He finds that in the tropics, the cloud top temperatures vary considerably without much effect on the thunderstorm activity.

Reliable statistics on the vertical distribution of lightning flash occurrence are rare. Probably the best data set with respect to discharge origins within thunderclouds is provided by *Proctor* [1991]. He evaluated 773 flashes observed during 13 thunderstorms over South Africa and found a bimodal distribution of lightning origin regions with peaks at 5.3 ±0.2 km (mainly CG flashes) and 9.2 ±0.2 km (mainly CC flashes) above mean sea level.

---

[1] In general, CG flashes bring down negative charge to the positively charged ground. Such flashes are called negative, −CG, for brevity. Positive CG lightning, +CG, is observed also, in particular in winter thunderstorms [for references, see *MacGorman and Burgess*, 1994]. The dominant polarity of lightning is strongly depended on meso-scale properties of the atmosphere.

[2] Atmospherics, or sferics for short, are electro-magnetic pulses radiated by lightning discharges. They can be detected over distances of more than 10,000 km.

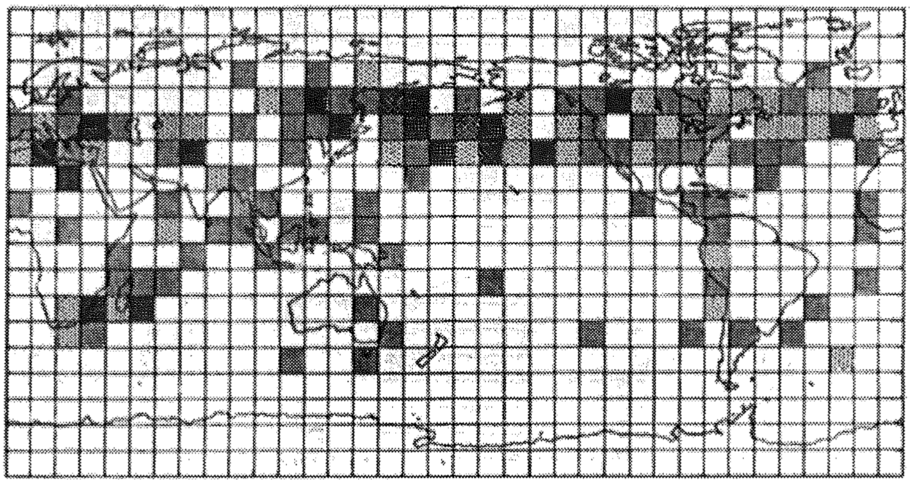

Figure 3.2: Lightning recorded by satellite in April 1978 at local dawn [*Turman and Edgar*, 1982]. For legend, see Figure 3.3.

Mackerras and Darveniza [1994] evaluated observations made between 1987 and 1991 at 14 continental sites with respect to the total numbers of CC and CG flashes, n_{CC} and n_{CG}, respectively. They found ratios of n_{CC}/n_{CG} between 1 and 3.8, but no significant dependence of this ratio on latitude. The fractions of +CG from total CG they report for the individual sites range between 0.02 and 0.28. *Prentice and Mackerras* [1977] use ratios of n_{CC}/n_{CG} between 3 and, in the tropics, up to 6.

3.1.3 Observed Global-Scale Lightning Distributions

The only global climatology of thunderstorm activity available at the moment are the thunderstorm day maps edited by *WMO*, 1953. These maps are based on counts of the number of days per month when thunder is audible at a given location. Since this criterion requires that thunder actually is heard, the figures given for uninhabited regions are quite uncertain. Further, this report provides no information about the number of lightning strokes per recorded thunderstorm or about their intensity. This means that a tropical thunderstorm with hours of strong lightning activity is not distinguished from a single thunderclap, as it might occur associated with a winterly cold front at mid-latitudes. Despite these restrictions, the WMO report probably is the most reliable data base on this subject until today [*Volland*, 1994].

Satellite observations provide a chance to study lightning activities without the geographical bias associated with most of the ground observations. Lightning activity has been observed from space since the 1960s using both optical and radio frequency sensors[3]. However, only a few of these satellite data sets base on at least several months of continuous observations. These are *Orville and Spencer* [1979], *Turman and Edgar* [1982], *Orville and Henderson* [1986], *Goodman and Christian* [1993], and *Kotaki and Katoh* [1983]. In the former four studies, measurements were made with optical detectors, whereas the latter one is based on radio frequency measurements. Since the satellites used for optical lightning detection fly sun-synchronous, the corresponding data refer to a short time of the day only. The data evaluated by *Kotaki and Katoh* [1983] do cover entire days, but results are presented for the interval 22 to 2 h local time exclusively.

A principal problem of satellite observations is their low detection limit. The optical sensors flown by satellites can only detect what is visible at the top of the atmosphere. Hence, lightning occurring in the low-

---

[3] *Goodman and Christian* [1993] present an overview of the more than a dozen satellites that have flown instruments to record signals from lightning discharges.

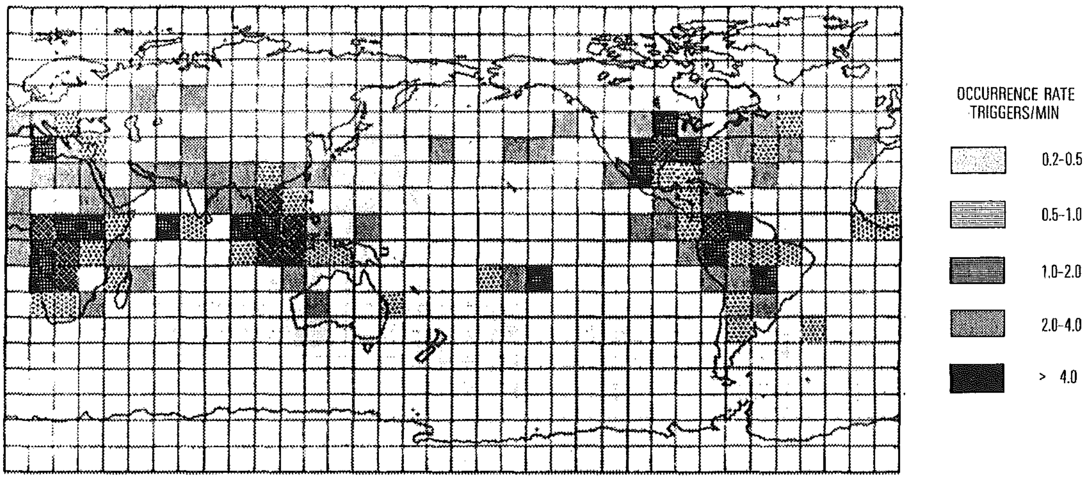

Figure 3.3: Lightning recorded by satellite in April 1978 at local dusk [*Turman and Edgar*, 1982].

er troposphere may not be detected if it is covered by high clouds. Also, a single stroke cannot be distinguished from several ones occurring at the same time at different altitudes. Besides these principal problems, satellite observations are restricted by the spatial and temporal resolution of the sensors used. *Turman and Edgar* [1982] estimate that their data capture about 2% of the global lightning activity, whereas the corresponding yield given by *Orville and Henderson* [1986] is one in 10^5 of all flashes occurring on Earth. There is no information available whether the systematic error associated with the low optical detection limit is homogeneous in time and space, or whether, for example, different latitudes are resolved differently well. Of the radio frequency measurements, about 30% are affected by interference from transmitters on the ground. Locally, this effect makes up to 70% of the signal [*Kotaki and Katoh*, 1983].

The lightning distributions presented by *Turman and Edgar* [1982] were recorded between August 1977 and June 1978 at dawn and dusk and have a temporal resolution of 2 month on average. As an example, the April distributions are shown in Figures 3.2 and 3.3. At dawn, highest lightning rates are reached between 30°N and 60°N, associated with the northern hemispheric polar front. In the tropics and in the southern hemisphere, the patches of detected lightning activity are rather scattered. At dusk, in contrary, lightning is restricted almost completely to continental regions. Further, at dusk there is much more lightning over continents than over oceans, whereas at dawn, the difference is weaker. This difference also is much more obvious in the tropics than at mid-latitudes. In fact, the lightning activity over continents decreases towards the poles, whereas it has no obvious dependence on latitude over oceans.

Since in the tropics deep convection over oceans reaches similar frequencies as over continents, at least within the inter-tropical convergence zone, the ITCZ, or in monsoon regions [e.g., *Rossow*, 1993], the low oceanic lightning activity cannot be explained by lower convection frequencies alone. Further, the vertical extent of tropical wet convection is similar over both types of surfaces [*Rossow*, 1993; *Williams et al.*, 1992b]. The question why in the tropics an oceanic convection event produces so much less lightning than continental convection is not answered completely. A well known fact is that oceanic convective vertical motions are much weaker than those over continents [*LeMone and Zipser*, 1980; *Zipser and LeMone*, 1980]. These authors and numerous others [e.g., *Jorgensen et al.*, 1985; *Williams et al.*, 1992b] speculate that the low oceanic updraft rates are related to the low convective available potential energy, CAPE, relative to continental locations. Since CAPE is a measure of the amount of buoyant energy available in the environment to drive updrafts, it is small if at the time scale of convection there is only weak warming of the surface, like over oceans. Ignoring these purely dynamical arguments, *Laube* [1994] assumes that over continents more different and larger condensation nuclei are available. Thus, the size distribution of cloud droplets or ice particles, respectively, is broader. In his opinion this is responsible for the fact that charging processes are much more efficient over continents than they are at oceanic region. *Laube*'s assumption is confirmed by *Takahashi* [1990], who explains the near absence of lightning in convective, torrential rainfall producing clouds over Micronesia by the observation that the concentration of frozen particles was one order of magnitude less than that required to trigger lightning.

At mid-latitudes, the contrast in heating and, hence, in convection activity between continental and oceanic surfaces is weaker than in the tropics. Consequently, the same is true for the lightning activity over both types of surfaces. Over warm currents as the Gulf stream, oceanic lightning can even be more frequent than over adjacent continental regions [*Biswas and Hobbs*, 1990]. The dependence on the type of surface also is weak for lightning associated with frontal passages.

3.1.4 Diurnal Cycles

Lightning rates observed at dusk are often assumed to be representative for the entire day [e.g., *Kowalczyk and Bauer*, 1981; *Crutzen and Zimmermann*, 1991; *Müller and Brasseur*, 1995; *Brasseur et al.*, 1996]. This assumption holds for regions where thunderstorms triggered by convection within one airmass are prevailing. Other thunderstorm generation mechanisms, however, are not necessarily most active in the late afternoon (see Figures 3.2 and 3.3).

Reliable, diurnal cycles resolving measurements are presented by *Grandt* [1991], who recorded sferics radiated by CG flash pulses between 1983 and 1987 near Pretoria. He finds no significant diurnal cycle in the oceanic region southeast of the African continent. Other oceanic regions have, depending on season, enhanced lightning rates in the morning, in the early afternoon, or no diurnal cycle at all. Over continental southern Africa, the number of observed lightning pulses peaks in the early afternoon, at dawn, and at dusk. Which one of these peaks is highest varies with season.

3.1.5 The Process of NO Formation

The mechanism by which lightning discharges produce NO is assumed to be similar to that expounded by *Zel'dovich and Raizer* [1966] for explosions [*Chameides*, 1986; *Lawrence et al.*, 1995; *Stark et al.*, 1996]. The lightning bolt and the associated shock wave produce a cylinder of very hot air (about 30,000 K) within which the gas is completely ionized plasma. As the gas cools by hydrodynamic expansion and turbulent mixing, the equilibrium composition of the gas changes from plasma to a mixture of neutral atoms such as N and O, then to a mixture of molecular species, and, ultimately, as the temperature returns to ambient, to a mixture much like the background composition of the atmosphere. Most species remain in thermochemical equilibrium throughout the cooling process so that there is no net effect on the bulk composition of air by the lightning discharge.

For a few minor species like NO, however, the high temperatures in and close to the discharge channel give rise to a net production via a sequence of reactions that both produce and destroy NO. The thermochemical equilibrium concentration, $[\mathrm{NO}]_{eq}(T)$, is the NO concentration at which the production and the destruction reactions balance each other. This concentration is strongly temperature dependent and reaches a maximum value of about 10% around 4000 K [*Borucki and Chameides*, 1984]. If the gas mixture maintained chemical equilibrium as it cools down to ambient temperatures, the amount of net NO production would be insignificant since $[\mathrm{NO}]_{eq}(T = 300\mathrm{K})$ is very low. However, the time required to establish thermochemical equilibrium, $\tau_{eq}(T)$, also is strongly temperature dependent. This time increases from a few milliseconds at 2500 K to about 1000 years at 1000 K. Thus, as long as the cooling process is slow enough for the characteristic cooling time of the heated air, τ_{cool}, to be larger than $\tau_{eq}(T)$, the NO concentration follows $[\mathrm{NO}]_{eq}(T)$. When the gas has cooled to the extent that $\tau_{cool}(T) \approx \tau_{eq}(T)$, then the equilibrium NO concentration for this temperature is "frozen-out". This is the case since, as the gas cools further, $\tau_{eq}(T)$ becomes so large that the new equilibrium concentration cannot be established within the time τ_{cool}. The freeze-out temperature, T_{fr}, is determined by the condition $\tau_{cool}(T_{fr}) \approx \tau_{eq}(T_{fr})$. The net amount of

NO produced by a discharge then simply is given by the volume of gas heated to temperatures above T_{fr} multiplied by $[\mathrm{NO}]_{eq}(T_{fr})$.

3.2 Estimate of the Global NO Production Rate

Most of the previous estimates of the annual rate of nitrogen fixation by lightning discharges base on the assumption that the global rate of NO production, $G(\mathrm{NO})$, is determined by

$$G(\mathrm{NO}) = \nu_{gf} P(\mathrm{NO}) \, , \tag{3.1}$$

where ν_{gf} denotes the global lightning flash frequency and $P(\mathrm{NO})$ is the molecular production of NO by a single, "typical" lightning flash. Because of the highly variable conditions under which lightning occurs, one typical lightning flash cannot be defined. Hence, it is not surprising to find estimates of $G(\mathrm{NO})$ which all are based on this approach, but deviate from each other by orders of magnitude. *Liaw et al.* [1990] and *Lawrence et al.* [1995] present tables summarizing previous estimates of global NO production rates by lightning. These tables, however, show some figures which are not consistent with the original papers.

The global flash rate is one of the more certain parameters in Equation (3.1). A common value of ν_{gf} is about 100 s^{-1} [e.g., *Orville and Spencer*, 1979; *Dawson*, 1980; *Hill et al.*, 1980], the lowest estimates are 63 s^{-1} [*Kotaki and Katoh*, 1983] and at least 40 s^{-1} [*Turman and Edgar*, 1982], whereas values as high as 300 s^{-1} are assumed by *Kowalczyk and Bauer* [1981]. Several authors distinguish between CC and CG flashes. *Peyrous and Lapeyre* [1982], for example, assume a global CC flash rate of 300 s^{-1} and, in addition, a CG rate of 100 s^{-1}.

The term $P(\mathrm{NO})$ can be determined either directly from measurements close to thunderstorms, or from laboratory or theoretical studies. The existing data gained by measurements under atmospheric conditions refer to the net effect of an entire thunderstorm [*Noxon*, 1976], are obtained at a distance of about 1.2 km from a flash [*Drapcho et al.*, 1983], or result in unrealistic NO production rates of 220 Mt N/yr [*Franzblau and Popp*, 1989]. Altogether, direct measurements provide order of magnitude estimates at best.

Theoretical estimates of $P(\mathrm{NO})$ invoke the freeze-out mechanism described on page 24. *Chameides et al.* [1977] assume that the energy dissipation process which determines the freeze-out temperature is dominated by the hydrodynamic rapid expansion of the discharge tube by a shock wave. They calculate $P(\mathrm{NO})$ from

$$P(\mathrm{NO}) = p(\mathrm{NO}) E_f \, , \tag{3.2}$$

where $p(\mathrm{NO})$ is the yield of NO per unit energy of discharge and E_f denotes the energy of a lightning flash. Using 3-7 $\times 10^{16}$ molecules NO/J for $p(\mathrm{NO})$ and and 2×10^9 J/flash for E_f, they obtain $P(\mathrm{NO})$ = 6-14 $\times 10^{25}$ molecules NO/flash. *Hill et al.* [1980] make different assumptions, but also get $P(\mathrm{NO}) \approx 6\times 10^{25}$ molecules NO/flash. They argue that, because of the long duration of the discharge, the resulting shock wave never travels sufficiently fast for the gas just behind the front to get hot enough to fix nitrogen. Instead, NO is formed when hot air from the discharge channel cools by turbulent mixing with surrounding ambient air.

A potential problem of laboratory experiments is that electrical discharges generated there have energy depositions of typically 10^3 to 10^4 J/m, while atmospheric lightning deposits 10^4 to 10^5 J/m [*Stark et al.*, 1996]. It is not clear whether results gained in the laboratory simply can be extrapolated for atmospheric conditions, or whether the NO production mechanism varies nonlinearly with discharge characteristics such as the energy deposit or discharge gap. *Chameides et al.* [1977], for example, measured $p(\mathrm{NO}) = 8\pm 4 \times 10^{16}$ molecules NO/J for a discharge gap of 1 m, whereas *Levine et al.* [1981] find $p(\mathrm{NO}) = 5\pm 2 \times 10^{16}$ molecules NO/J for a gap of 12 cm.

Probably the most reliable value for E_f is that proposed by *Borucki and Chameides* [1984]. Evaluating six studies of electrical and six of optical measurements, they obtain $4\pm 2 \times 10^8$ J/flash and $4\pm 3 \times 10^8$ J/flash, respectively. Because one lightning flash often has 4 return strokes, several authors assume the

4 times higher value of 2×10^9 J/flash for E_f [e.g., *Chameides et al.*, 1977; *Peyrous and Lapeyre*, 1982]. However, there is no reason to weight all strokes equally. First, CC flashes have no return stroke and, second, strokes go along the same discharge channel, partly at least [*Dawson*, 1980]. During the short interval between the individual strokes, there is no time for diffusive loss of NO from a previous stroke. Instead of producing new NO with every single stroke, the freeze-out mechanism acts on essentially the same molecules several times in succession.

Table 3.1 summarizes the values of the various quantities occurring in Equations (3.1) and (3.2) which are assumed to be most reliable. They yield a global NO production rate by lightning discharges of 4.4 Mt N/yr. Because each of these quantities is associated with an uncertainty of a factor 2 at least, $G(\mathrm{NO}) = 5$ Mt N/yr is assumed for simplicity. This value will be used below to scale the yield of NO_X per lightning event in the CTM. Several previous studies also base on the same value of 5 Mt N/yr for the global production of NO_X by lightning discharges [*Crutzen and Zimmermann*, 1991; *IPCC*, 1995; *Toumi et al.*, 1996].

Also shown in Table 3.1 is the range of all available estimates made previously for $G(\mathrm{NO})$: 2-220 Mt N/yr. A more realistic range of this quantity, however, is 2-10 Mt N/yr, as can be derived from nitrate deposition measurements [e.g., *Böttger et al.*, 1978]. This order of magnitude for $G(\mathrm{NO})$ is confirmed by an estimate which is not based on the extrapolated NO production rate of an individual lightning flash, but on the difference in NO mixing ratios measured inside and outside the anvils of 2 cumulonimbus clouds [*Chameides et al.*, 1987]. With the observed values of about 440 pptv inside and 20 pptv outside, a global NO production rate of 7 Mt N/yr is obtained. In addition, there is the recent study of *Ridley et al.* [1996] in which the NO production rates derived from measurements made within New Mexican thunderstorms are extrapolated to a global scale. For the generation at or transport to altitudes above 8 km, *Ridley et al.* obtain global production rates of 2.0-2.7 Mt N/yr or 4.1-4.9 Mt N/yr, respectively, depending on whether they assume a certain flash distribution between CC and CG discharges or just use the globally averaged number of thunderstorms per day. Finally, most of the previous studies and probably all recent three-dimensional global model calculations on tropospheric chemistry assume values of $G(\mathrm{NO})$ between 2 and 10 Mt N/yr [e.g., *Logan*, 1983; *Ehhalt and Drummond*, 1988; *Penner et al.*, 1991; *Kumar et al.*, 1995; *Müller and Brasseur*, 1995; *Brasseur et al.*, 1996].

$p(\mathrm{NO})$ $\times 10^{16}$ molecules NO/J	E_f $\times 10^8$ J/flash	$P(\mathrm{NO})$ $\times 10^{25}$ molecules NO/flash	ν_{gf} flashes/s	$G(\mathrm{NO})$ Mt N/yr
5 (3^a - 9^b)	4 (1^c - $20^{a,d}$)	6 (0.5^c - 300^e)	100 (40^f - 400^d)	5 (2^g - 220^e)

[a] *Chameides et al.* [1977]
[b] *Borucki and Chameides* [1984]
[c] *Levine et al.* [1981]
[d] *Peyrous and Lapeyre* [1982]
[e] *Franzblau and Popp* [1989]
[f] *Turman and Edgar* [1982]
[g] *Lawrence et al.* [1995]

Table 3.1: Quantities used to estimate the global NO production rate by lightning discharges. In addition to the values assumed in the present study, lower and upper limits are given.

3.3 Horizontal Distribution of Global Lightning Activity

In the following it is discussed how the 5 Mt N which are emitted annually by lightning discharges are distributed within the CTM's thunderstorms. This distribution requires a parametrization of the subgrid-scale process lightning in terms of the meteorological data included in the CTM.

The simplest way to parametrize the net result of a subgrid-scale process is to use climatological mean values. For the lightning source, however, such attempts are stopped by the lack of a suitable data base.

Several authors of previous model studies [e.g., *Kowalczyk and Bauer*, 1981; *Crutzen and Zimmermann*, 1991; *Müller and Brasseur*, 1995] simply adopt the dusk satellite observations of *Turman and Edgar* [1982] instead (see Figure 3.3). Since these dusk observations do not generally represent the diurnal mean lightning activity, have a rather low temporal resolution (6 maps for 11 months), and are associated with considerable experimental uncertainties (see p. 23 and p. 24), this approach is just a rough approximation of the true horizontal distribution of global lightning activity. Moreover, since the global-scale distribution of thunderstorms is affected by the general circulation, its inter-annual variability is considerable. This variability includes both different lightning activity at a given location and different geographical distributions. Thus, because the CTM is not designed to reproduce observed weather situations, the simple assumption that lightning occurs in the CTM where it was detected by *Turman and Edgar* [1982] leads to the situation that the model has to produce lightning in grid columns in which there is no deep wet convection. The uncertainty of the *Turman and Edgar* [1982] satellite observations could be diminished by using an averaged data set which includes the other long-time satellite observations as well. However, these other data are available to the public only in a form that makes mapping on a model grid rather difficult.

3.3.1 The Lightning Parametrization of Price and Rind

The parametrization of lightning distributions of *Price and Rind* [1992, 1994] is the only one suggested up to now for global models. *Price and Rind* assume $\nu_{lf} \propto h_{cl}^5$ over continents and $\nu_{lf} \propto h_{cl}^{1.7}$ over oceans, where ν_{lf} denotes the local flash frequency and h_{cl} is the cloud height. These assumptions are based on empirical relationships between the maximum updraft speed, w_{max}, and h_{cl} on the one hand and between w_{max} and ν_{lf} on the other hand. The uncertainty of the relationship between w_{max} and ν_{lf} is quite large for oceanic thunderstorms since it is based on a total of ten observations only. In addition to the horizontal distributions, *Price and Rind* [1993] present an empirical formula which yields the fraction of CC and CG flashes (see page 21) as a function of the vertical extent of the temperature region below 0°C within the model cloud.

Although *Price and Rind* seem to provide exactly what is missing for the present NO_X calculation, their results are not applied here, in contrast to the recently developed lightning source parametrization of *Levy et al.* [1996]. There is no doubt that for some thunderstorms h_{cl}^5 correlates very well with observed values of ν_{lf} [*Williams*, 1985; *Stolzenburg*, 1994], as derived from simple scaling relationships regarding a thundercloud as a steady state electrical dipole [*Vonnegut*, 1963]. However, these assumptions do not hold in general, as confirmed by various other observations [e.g., *Goodman et al.*, 1988; *Williams et al.*, 1989; *MacGorman and Burgess*, 1994; *Zipser*, 1994].

A principal problem of the parametrization of *Price and Rind* [1992] is its dependence on observations made at length scales which are several orders of magnitude below the size of their model grid boxes. For any model in which h_{cl} is an average value for a grid column containing clouds as well as clear sky regions, this value is far lower than that of an individual cloud. *Price and Rind* therefore adjusted h_{cl} in a way that it fits satellite observations. Is not clear, however, whether the relationships assumed between h_{cl}, w_{max}, and ν_{lf} still hold when transferred to the scale of a GCM grid box.

3.3.2 Lightning in the CTM

The parametrization of global horizontal lightning distributions presented in the following is even simpler than that of *Price and Rind*. It does not base on relationships derived from cloud-scale observations, but just tries to capture the structure of the available observations of large-scale lightning distribution. The parametrization consists of two parts: some straightforward assumptions of where lightning in the CTM may not occur and the introduction of two parameters. These parameters help to provide a lighting distribution in terms of the physical quantities available in the CTM.

Straightforward Assumptions

The only information about cloud formation given by the CTM are the convection statistics. Since most of the lightning discharges occurring in the real atmosphere are associated with deep wet convection, only this type of convection is taken into account for the lightning parametrization. The two other types of convection included in the CTM are assumed to make no contribution to the lightning source. For shallow wet convection on the one hand, the vertical extent of the updraft is too small to produce charge separation efficient enough for a discharge. Dry convection on the other hand occurs at moisture contents which are below condensation level and, hence, cloud droplets do not form at all.

Any event of deep wet convection is associated with the occurrence of lightning under one condition: the temperature in the grid box containing the cloud base must be above 10°C. For real clouds, this temperature criterion ensures the presence of amounts of liquid water in saturated cloud air which allow efficient charge separation. In the model, it prevents deep wet convection occurring at polar regions to produce lightning. As a consequence, there is no lightning in the CTM south of 56°S and north of 72°N, in good agreement with observations [e.g., *WMO*, 1953]. Further, it is assumed that for each event of deep wet convection the lightning activity is proportional to the strength of this event, which is defined by the number of convective events sampled by the GCM every hour and averaged over a period of 8 hours.

The Actual Parametrization

So far, the parametrization of the horizontal lightning distribution in the CTM just excludes situations where lightning is very unlikely to form. If no further assumptions are made, then the contribution of deep wet convection at mid-latitudes is larger than what one would expected from observations and that of tropical convection is smaller, respectively, over tropical oceans in particular. More realistic lightning distributions are obtained by two additional assumptions which further restrict the probability of lightning formation for certain events of deep wet convection in the CTM. These assumptions are guided by observations, but they cannot be derived thereof directly. Instead, each of them consist of a parameter which is adjusted in a way that the CTM reproduces observed lightning distributions as well as possible. They are:

1. At latitudes $\varphi \leq 24°$, an event of oceanic deep wet convection produces γ_o times as much lightning than an event of the same strength which occurs over tropical continents or at higher latitudes.

2. Lightning only occurs, if the corresponding event of deep wet convection reaches a grid box in which the temperature drops below a certain value T_{ct}.

The parameter $\gamma_o(\varphi)$ has to be introduced, because in the tropics the strong difference in lightning occurrence observed between continental and oceanic surfaces cannot be derived exclusively from the physical quantities included in the CTM. Partly, this difference is associated with corresponding differences in the frequency of deep wet convection, ν_{dwc}, and in the height reached by the convection events. However, a major cause of the low lightning activity over tropical oceans are processes which act at scales far below that of a model grid box (see page 22). Their net effect is obtained by setting $\gamma_o = 0.1$ in the tropics. For simplicity, γ_o is discontinuous between the tropics and the subtropics. i.e. at the latitude where $d\nu_{dwc}/d\varphi$ is largest. The reason for these choices is explained below.

A second parameter is necessary, because in the CTM the difference in strength between tropical deep wet convection and deep wet convection at mid-latitudes is much smaller than the observed meridional variations of lightning occurrence. Further, coupled with the height of the tropopause, the vertical extent of observed thunderclouds is significantly lower at mid-latitudes than it is in the tropics. In the CTM, there is some decrease in cloud height with increasing φ, but this decrease is underestimated because of the model's low vertical resolution and, in particular, the subsequent lack of a dynamical tropopause.

The idea of applying a cloud top temperature criterion, T_{ct}, as a second parameter is based on results of *Grandt* [1991]. He compared sferics measurements with cloud top temperatures obtained from METEOSAT pictures and finds that major thunderstorm activity is correlated with minimum cloud top temperatures of 225-245 K in temperate regions and 225-195 K in the tropics. Moreover, at mid-latitudes, minimum cloud top temperatures below 235 K generally were associated with thunderstorm activity.

The spatial and temporal scales of the sferics data *Grandt* evaluated, 200 km × 200 km and 30 min, are about one order of magnitude lower than the corresponding scales in the CTM. The satellite images have a resolution of about 200 km × 200 km and 6 hours. Since the result of a comparison between thunderstorm activity and cloud top temperatures depends on the scale at which it is carried out, the results of *Grandt* [1991] should not be applicable directly in the CTM. Despite this, 238 K turned out to be a suitable value of T_{ct} in the lightning source parametrization, as shown below. The reason why this value of T_{ct} is well within the range given by *Grandt* [1991] might be that both the resolution of the METEOSAT pictures and that of the CTM are significantly larger than the scales of a typical thundercloud.

A single, global cloud top temperature criterion is defined here because of the low vertical resolution of the model. Since the CTM underestimates the meridional gradient of the typical height of deep wet convection, it underestimates the corresponding gradient of cloud top temperatures as well. Thus, in the tropics, there are hardly any convection events in the CTM which reach heights corresponding to temperatures below 220 K, whereas at higher latitudes, rather low cloud top temperatures are reached. Despite this, T_{ct} sharpens the meridional gradient of lightning occurrence by excluding a larger number of convection events at higher latitudes than in the tropics. This is possible, because in the tropics most events of deep wet convection reach σ-layer 7. At mid-latitudes, in contrary, the uppermost layer involved in wet convection is quite variable. It is emphasized that the lowest σ-layer in which the temperature drops below 238 K in the CTM does vary with latitude. Otherwise T_{ct} simply could be replaced by the requirement that events of deep wet convection must reach σ-layer 6 or 7 if they produce lightning.

3.3.3 Comparison with Observations

The values of γ_o and T_{ct} chosen in the standard case are $\gamma_o(\varphi \leq 24°) = 0.1$, $\gamma_o(\varphi > 24°) = 1$, and $T_{ct} = 238$ K. These values are obtained empirically by comparison with various large-scale lightning flash observations: the WMO maps of thunderstorm days [*WMO*, 1953], three sets of midnight satellite data [*Orville and Spencer*, 1979; *Kotaki and Katoh*, 1983; *Orville and Henderson*, 1986], the dawn and dusk satellite data of *Turman and Edgar* [1982], and the sferics measurements of *Grandt* [1991]. It is emphasized that the values of γ_o and T_{ct} are adjusted in a way that the parametrization of global lightning distribution fits these different observational data sets simultaneously. This is done in order to eliminate the uncertainties associated with each individual data set (see page 22). However, since there are considerable differences between the the individual observational data sets, the lightning distribution calculated by the CTM may locally deviate significantly from an individual observation.

The lightning parametrization described above gives relative lightning distributions, but no absolute flash frequencies. As far as lightning is concerned as a source of NO_X, relative distributions are sufficient if the global emission rate is prescribed, as it is done in the present study. However, comparisons with observed absolute flash frequencies only can be done quantitatively. Such comparisons are discussed in the following. Because some of the observational data are lightning trigger rates, whereas others give flash counts or radio noise measurements, all lightning distributions, $\rho_{\rightsquigarrow}$, discussed here are normalized over all longitudes and all latitudes in a way that $\int_{-180°}^{+180°}\int_{-90°}^{+90°} \rho_{\rightsquigarrow}(\lambda,\varphi)d\lambda\, d\varphi = 1$.

The WMO Maps of Thunderstorm Days

A first impression of the reliability of the CTM's relative lightning distributions is gained when these patterns are compared with the corresponding WMO maps of thunderstorm days. Examples of both data sets are shown in Figures 3.4 and 3.5, respectively. These figures give monthly mean lightning distributions, $\overline{\rho_{\rightsquigarrow}}^{m}$, for January and July. It is emphasized that the contours in Figure 3.4 represent relative units scaled linearly in a way that orders of magnitudes similar to those occurring in the WMO maps are obtained.

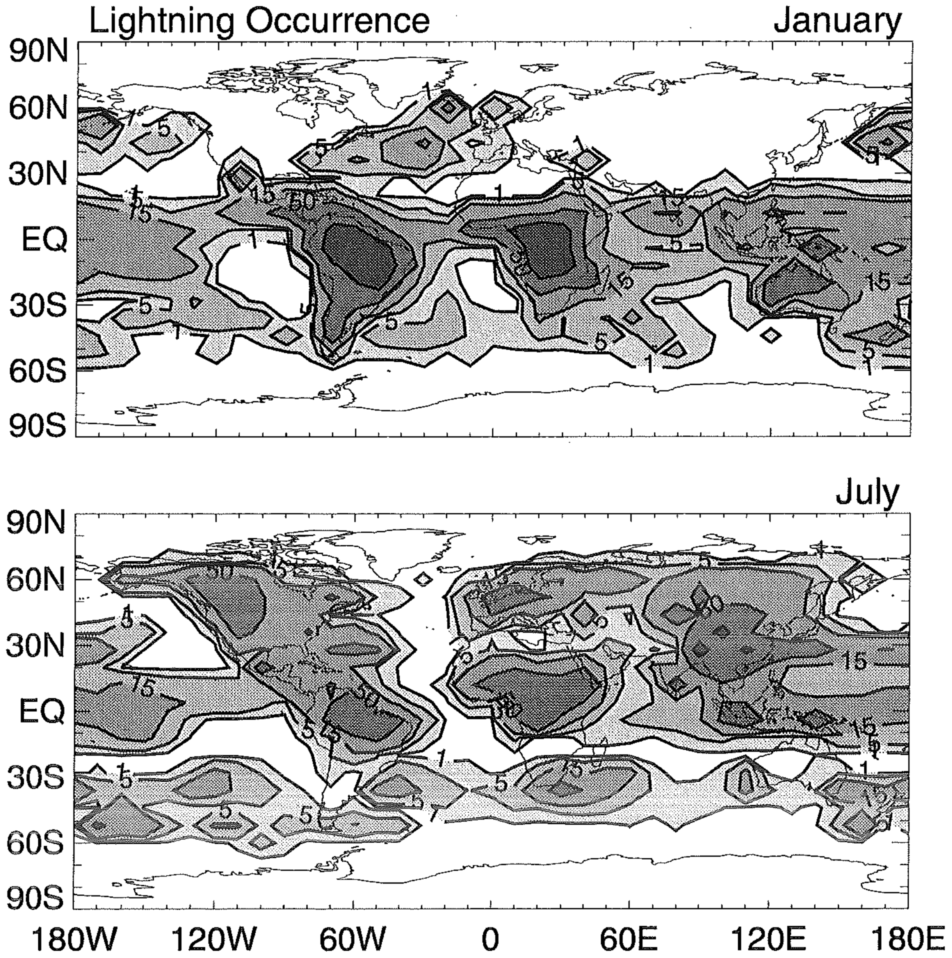

Figure 3.4: Monthly mean horizontal lightning distribution calculated by the CTM with the standard values of the lightning parametrization ($\gamma_o(\varphi \leq 24°) = 0.1$, $\gamma_o(\varphi > 24°) = 1$, $T_{ct} = 238$ K) for (upper panel) January and (lower panel) July. Contours are displayed at 1, 5, 15, 50, and 150 relative units.

In January, most thunderstorms occur over southern hemispheric tropical and subtropical continents both in the calculation and in the observation. Over South America and Africa, the position of these maxima is nearly the same for the two data sets. In the Asian tropics, however, the spatial agreement of the maxima is worse. In the CTM, $\overline{p_{\leadsto}}^{m}$ is large over Papua New Guinea and northern Australia, whereas in the WMO map, $\overline{p_{\leadsto}}^{m}$ has a peak over Indonesia. In the upper panels of both Figure 3.4 and Figure 3.5, the only northern hemispheric regions with enhanced values of $\overline{p_{\leadsto}}^{m}$ are the North Atlantic, where the warm Gulf current triggers convection, and a relatively small oceanic area north of Hawaii. The small maximum of $\overline{p_{\leadsto}}^{m}$ over the tropical Pacific is much more widespread in the model calculation than it is in the thunderstorm day observations.

In July, the main thunderstorm activity is less restricted to tropical continents than it is in January, as the lower panels of Figures 3.4 and 3.5 show. During the northern summer a considerable number of thunderstorm days is counted for North America and Europe. Enhanced lightning activity in these regions is obtained also from the model calculation, but the positions of these relative maxima do not match exactly for

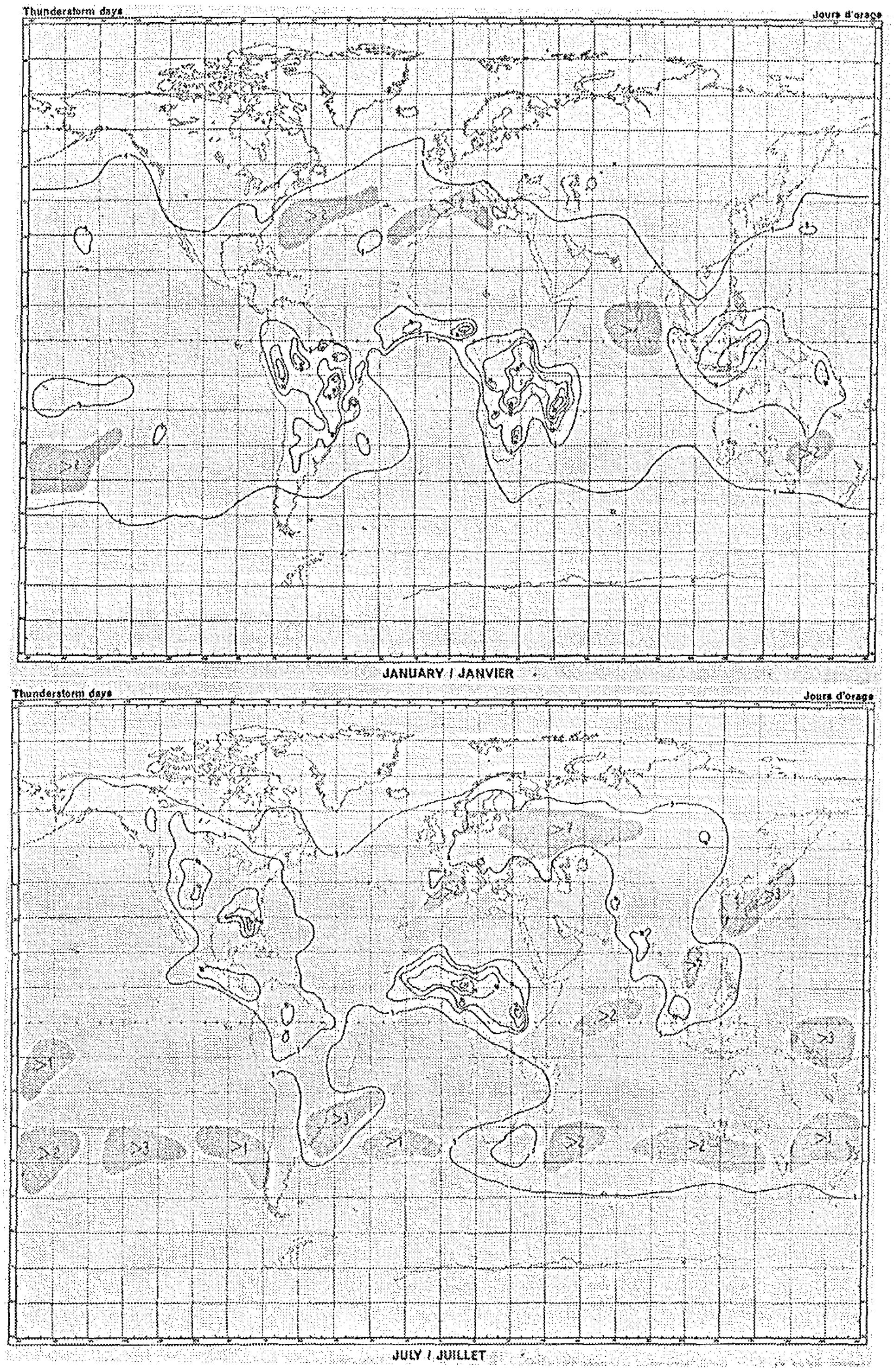

Figure 3.5: Global distribution of thunderstorm days for (upper panel) January and (lower panel) July [*WMO*, 1953].

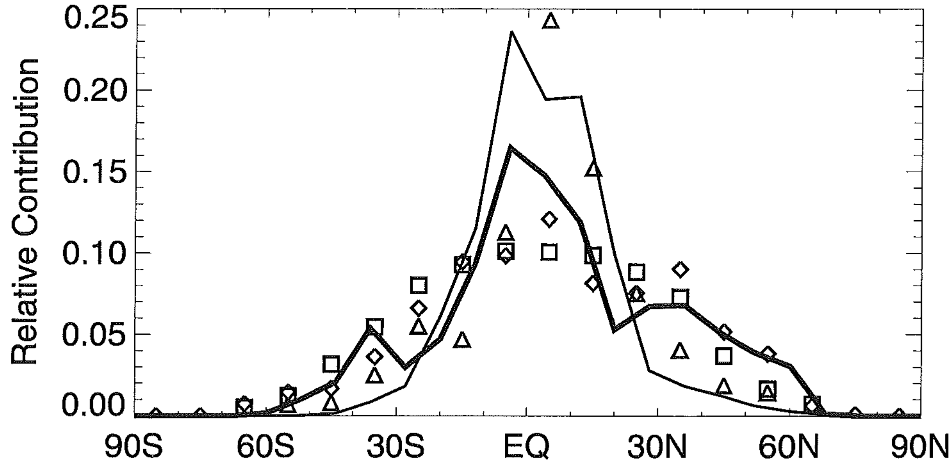

Figure 3.6: Zonally averaged annual mean relative lightning distribution, $\langle\overline{p_{\rightsquigarrow}}^{a}\rangle_{\lambda}$. CTM calculations with (thick line) the standard values of the lightning parametrization ($\gamma_o(\varphi \leq 24°) = 0.1$, $\gamma_o(\varphi > 24°) = 1$, $T_{ct} = 238$ K) and (thin line) the parametrization of *Price and Rind* [1992]. Symbols represent the satellite observations of (triangles) *Orville and Spencer* [1979], (diamonds) *Turman and Edgar* [1982], and (squares) *Kotaki and Katoh* [1983].

the two data sets. The model predicts higher values of $\overline{p_{\rightsquigarrow}}^{m}$ over the Caribbean Sea and over western Europe than are given in the lower panel of Figure 3.5, and less over Florida and western Russia, respectively. Similarly, both data sets agree in high thunderstorm activity over southeastern Asia, but differ in the exact position of the corresponding maxima. In the lower panel of Figure 3.4, there is a band of high lightning activity over the subtropical Pacific, which is missing completely in the lower panel of Figure 3.5. Between 30°S and 40°S, however, both figures show a band of enhanced thunderstorm activity with a maximum in the southeast of South Africa. There, the warm Agulhas current triggers convection in a similar way as it does the Gulf current over the Atlantic during northern winter.

For the months not shown here, the degree of agreement between WMO thunderstorm day observations and the CTM calculation is similar to that given for January and July. The main features of the observed lightning distribution are reproduced well by the CTM, whereas for individual grid boxes considerable deviations may be detected.

Satellite Observations

The standard values of the lightning parametrization result in the zonally and meridionally averaged annual mean relative distributions, $\langle\overline{p_{\rightsquigarrow}}^{a}\rangle_{\lambda}$ and $\langle\overline{p_{\rightsquigarrow}}^{a}\rangle_{\varphi}$, shown in Figures 3.6 and 3.7, respectively. Both figures also give the corresponding averages gained from several global satellite observations[4] and $\langle\overline{p_{\rightsquigarrow}}^{a}\rangle_{\lambda}$ and $\langle\overline{p_{\rightsquigarrow}}^{a}\rangle_{\varphi}$ obtained from a CTM run using the lightning parametrization of *Price and Rind* [1992].

In all data sets shown in Figure 3.6, $\langle\overline{p_{\rightsquigarrow}}^{a}\rangle_{\lambda}$ peaks in the tropics. However, the amplitude of this maximum differs by about a factor of 2 between the individual observations. In the CTM the maximum of $\langle\overline{p_{\rightsquigarrow}}^{a}\rangle_{\lambda}$ occurs at 4°S, whereas the curves of $\langle\overline{p_{\rightsquigarrow}}^{a}\rangle_{\lambda}$ derived from satellite data either peak slightly north of the equator [*Orville and Spencer*, 1979; *Turman and Edgar*, 1982], or show no sharp peak at all [*Kotaki and Katoh*, 1983]. For most latitudes the calculated lightning distribution lies in between the observations.

---

[4] The curves representing the lightning distributions given by *Orville and Henderson* [1986] and *Kotaki and Katoh* [1983] have been compiled by *Williams and Heckman* [1993]. Here, the presentation of these data given by *Price and Rind* [1994] is adopted.

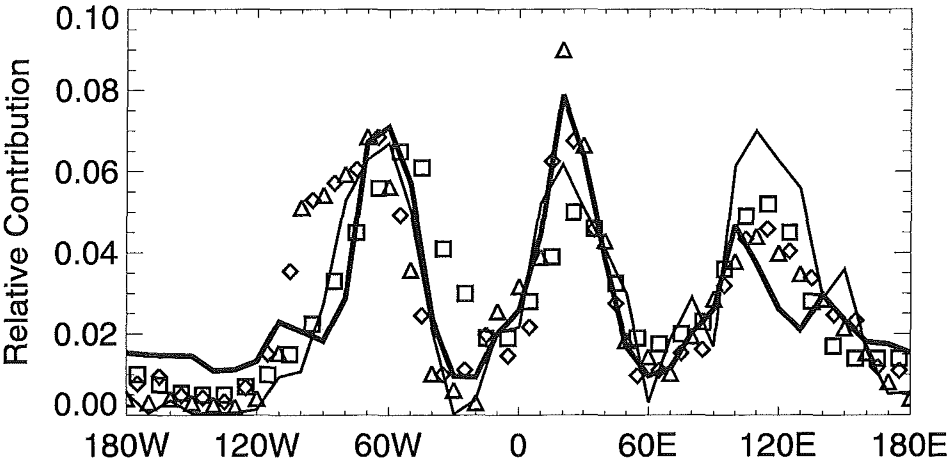

Figure 3.7: Meridionally averaged annual mean relative lightning distribution, $\langle\overline{p_{\rightsquigarrow}{}^{a}}\rangle_{\varphi}$. CTM calculations with (thick line) the standard values of the lightning parametrization ($\gamma_o(\varphi \leq 24°) = 0.1$, $\gamma_o(\varphi > 24°) = 1, T_{ct} = 238$ K) and (thin line) the parametrization of *Price and Rind* [1992]. Symbols represent the satellite observations of (triangles) *Orville and Henderson* [1986], (diamonds) *Turman and Edgar* [1982], and (squares) *Kotaki and Katoh* [1983].

Only at 20°N and between 20°S and 30°S, the CTM gives a smaller values of $\langle\overline{p_{\rightsquigarrow}{}^{a}}\rangle_{\lambda}$ than the observations. Main reason of these low values of $\langle\overline{p_{\rightsquigarrow}{}^{a}}\rangle_{\lambda}$ are low deep wet convection frequencies.

Figure 3.6 also shows that the agreement with observed distributions is worse when in the CTM the present parametrization is replaced by the parametrization of *Price and Rind* [1992]. This is the case mainly because the latter parametrization puts more weight on tropical convection and, as a consequence, lightning at mid-latitudes is underestimated.

Figure 3.7 shows meridionally averaged annual mean relative lightning distributions, $\langle\overline{p_{\rightsquigarrow}{}^{a}}\rangle_{\varphi}$. In general, there is good agreement between the observed and the calculated curves of $\langle\overline{p_{\rightsquigarrow}{}^{a}}\rangle_{\varphi}$. The observed ratio between continental maxima and oceanic minima is captured well by the CTM, except over the Pacific. The reason for this exception either is the fact that oceanic convection cannot be treated equally over all oceans or, as discussed in the next Chapter and more likely, the distribution and strength of convection in the GCM. The convection pattern also explains why the CTM produces less lightning between 105°E and 135°E than is observed. Between 80°W and 100°W, the calculated values of $\langle\overline{p_{\rightsquigarrow}{}^{a}}\rangle_{\varphi}$ are similarly low than those reported by *Kotaki and Katoh* [1983]. However, the exact position of the American peak of $\langle\overline{p_{\rightsquigarrow}{}^{a}}\rangle_{\varphi}$ is quite different for the individual observations, probably because of the large inter-annual variability of lightning off the Pacific coast associated with El Niño episodes.

Implementation of the lightning parametrization of *Price and Rind* [1992] in the CTM produces significantly higher values of $\langle\overline{p_{\rightsquigarrow}{}^{a}}\rangle_{\varphi}$ at longitudes $95°\mathrm{E} \leq \lambda \leq 135°\mathrm{E}$ than either the CTM calculation with the lightning parametrization developed here or any of the satellite observations. Reason for these high values is the fact that grid boxes containing coastal regions are considered as continental ones. As a result the entire Indonesian region is associated with continental lightning characteristics. A further consequence of the large difference which this parametrization makes between continental and oceanic convection are the very low lightning rates calculated for the Pacific.

Data Set \ Season	DJF	MAM	JJA	SON
sferics measurements of *Grandt* [1991]	1.52	0.46	0.21	1.22
CTM calculation with $\gamma_o(\varphi \leq 24°) = 0.1$, $\gamma_o(\varphi > 24°) = 1, T_{ct} = 238\,\mathrm{K}$	5.67	0.98	0.06	1.09
CTM calculation with the lightning parametrization of *Price and Rind* [1992]	18.57	6.94	0.13	5.23

Table 3.2: Ratio $\rho^o_{\leadsto}/\rho^c_{\leadsto}$, where $\rho^o_{\leadsto}$ is the seasonal mean equivalent lightning occurrence in the oceanic region 5°E $\leq \lambda \leq 25°$E, 32°S $\leq \varphi \leq 16°$S and $\rho^c_{\leadsto}$ denotes the corresponding value for the continental region $25°$E $\leq \lambda \leq 45°$E, $48°$S $\leq \varphi \leq 32°$S.

Data Set \ Month	Feb	Mar	Apr	Jun	Jul	Sep	Nov	Dec
sferics measurements of *Grandt* [1991]	1.52	0.86	0.73	1.69	0.28	0.23	0.35	4.09
CTM calculation with $\gamma_o(\varphi \leq 24°)$, $= 0.1, \gamma_o(\varphi > 24°) = 1, T_{ct} = 238\,\mathrm{K}$	0.75	0.80	0.06	$-^a$	$-^a$	1.00	1.24	3.90
CTM calculation with the lightning parametriz. of *Price and Rind* [1992]	0.07	0.07	0.01	$-^a$	$-^a$	0.03	0.03	0.06

^{a} no lightning in the oceanic region

Table 3.3: Ratio $\rho^o_{\leadsto}/\rho^c_{\leadsto}$, where $\rho^o_{\leadsto}$ is the monthly mean equivalent lightning occurrence in the oceanic region 35°W $\leq \lambda \leq 15°$W, $32°$N $\leq \varphi \leq 48°$N and $\rho^c_{\leadsto}$ denotes the corresponding value in the continental region 25°E $\leq \lambda \leq 45°$E, $24°$N $\leq \varphi \leq 40°$N.

The Sferics Measurements of Grandt [1991]

Grandt provides measurements of sferics distributions made within circles of about 10,000 km radius around Pretoria, South Africa, Bonn, Germany, and the Georg von Neumeyer station, Antarctica. Data from the former two sites are evaluated here to check the CTM's ability of producing a realistic ratio between continental and oceanic lightning frequencies at mid-latitudes. This is possible since sferics occurrence is a reliable measure of lightning occurrence. However, the probability of sferics detection decreases with increasing distance from the observation site. Each pair of regions selected for the following comparison therefore has approximately the same distance from Pretoria and Bonn, respectively.

For Pretoria, seasonal mean sferics data are available from the time period December 1985 to November 1986. These data have been averaged over the oceanic region at longitudes $25°$E $\leq \lambda \leq 45°$E and latitudes $48°$S $\leq \varphi \leq 32°$S on the other hand and at $5°$E $\leq \varphi \leq 25°$E and $32°$S $\leq \varphi \leq 16°$S on the other hand. The ratio $\rho^o_{\leadsto}/\rho^c_{\leadsto}$ of the sferics frequencies of the two regions is given in Table 3.2 together with the corresponding ratios obtained by CTM calculations using the lightning parametrization described on page 27 with the standard set of parameters and the parametrization of *Price and Rind* [1992], respectively. During southern winter, when only a small number of thunderstorms occurs over the continent $\rho^o_{\leadsto}/\rho^c_{\leadsto}$ is smallest and it is largest during southern summer. The CTM calculations also show this seasonal variability, but overestimate its amplitude. However, the values of $\rho^o_{\leadsto}/\rho^c_{\leadsto}$ derived from the sferics measurements agree

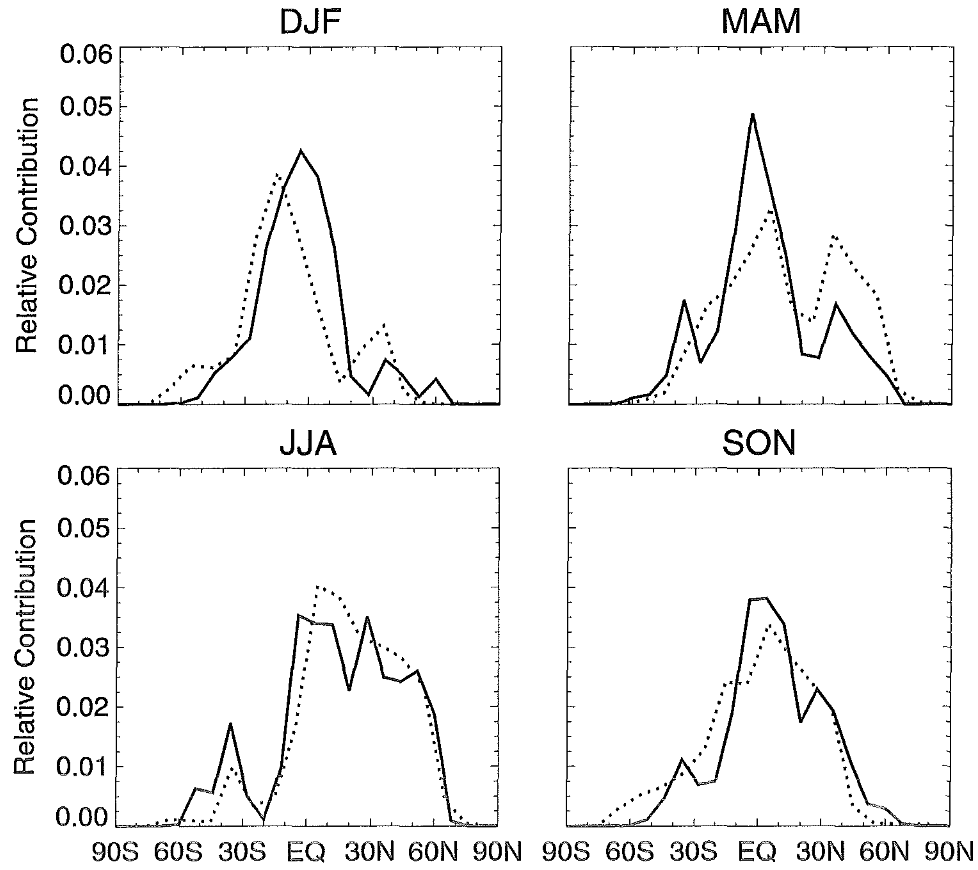

Figure 3.8: Zonal averages of the relative lightning distribution for the four seasons. Solid line in each panel: CTM calculation with the standard values of the lightning parametrization ($\gamma_o(\varphi \leq 24°) = 0.1$, $\gamma_o(\varphi > 24°) = 1$, $T_{ct} = 238$ K) and dotted line: dawn plus dusk satellite observations of [*Turman and Edgar*, 1982].

much better with the values obtained by the lightning parametrization developed here than they agree with the values from the parametrization of *Price and Rind* [1992].

The sferics data measured between March 1989 and February 1990 in Bonn are provided as a set of 8 monthly mean values. For the oceanic region at $35°\mathrm{W} \leq \lambda \leq 15°\mathrm{W}$ and $32°\mathrm{N} \leq \varphi \leq 48°\mathrm{N}$ and the continental one at $25°\mathrm{E} \leq \lambda \leq 45°\mathrm{E}$ and $24°\mathrm{N} \leq \varphi \leq 40°\mathrm{N}$, $\rho^o_{\rightsquigarrow}/\rho^c_{\rightsquigarrow}$ is shown in Table 3.3. Again, the present lightning parametrization gives values of $\rho^o_{\rightsquigarrow}/\rho^c_{\rightsquigarrow}$ much closer to those derived from the measurements than the parametrization of *Price and Rind* [1992]. However, the ratios derived from the measurements do not show an unambiguous seasonal cycle in this case. In summary, Tables 3.2 and 3.3 confirm an equal treatment of oceanic and continental convection at mid-latitudes as in the present lightning parametrization.

Seasonal Variability

A first check of the model's ability to reproduce seasonal variations of the lightning distribution correctly was the comparison with WMO maps of thunderstorm days for January and July. In addition, Figure 3.8

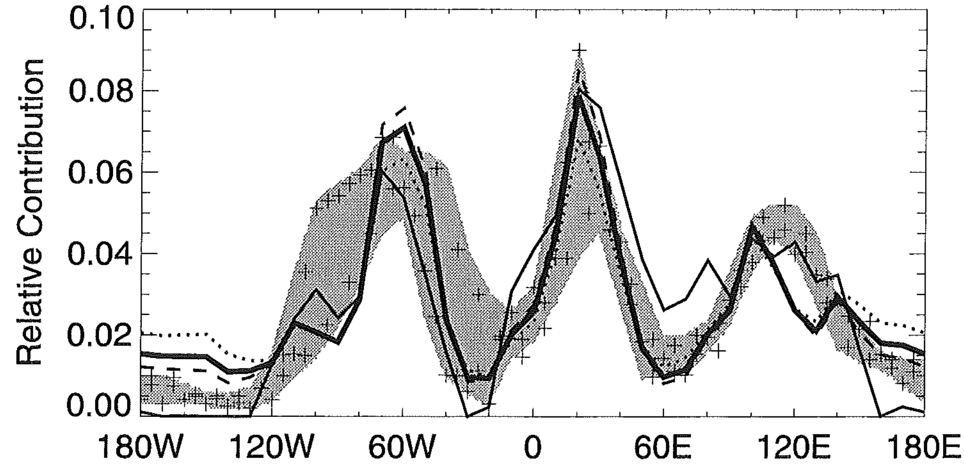

Figure 3.9: Meridional averages of the annual mean relative lightning distribution, $\langle\overline{p_{\leadsto}{}^{a}}\rangle_{\varphi}$, with $\gamma_o(\varphi > 24°) = 1$, $T_{ct} = 238$ K, and different values of $\gamma_o(\varphi > 24°)$: thick solid line 0.1, dotted line 0.2, and dashed line 0.05. The grey shading denotes the range of the values given by the satellite observations shown in Figure 3.7. These values are shown here as plus signs. The thin solid line is the normalized land fraction of each longitude belt in the CTM for latitudes $\varphi \leq 48°$.

shows seasonal averages of zonal mean lightning distributions obtained from the CTM as well as from the only satellite data set available with that temporal resolution [*Turman and Edgar*, 1982, dawn plus dusk]. The distribution of lightning over the four seasons in the CTM is very close to the corresponding observation. Moreover, the dependence of lightning on latitude is reproduced well during all seasons. The relatively large discrepancies between calculated and observed lightning rates which occur in the tropics and at northern mid-latitudes during spring are of the same order of magnitude as the deviations of the individual observations from each other (see Figure 3.6). At northern high latitudes the CTM reproduces the observed northward extent of lightning occurrence almost exactly, whereas the corresponding southward extent is slightly too small during all seasons. Further, the CTM underestimates by how much the tropical lightning maximum is shifted towards the northern hemisphere during northern summer and towards the southern hemisphere during southern summer. The seasonal variation of the meridional mean lightning distribution is much smaller than that of the zonal mean distribution.

3.3.4 Sensitivity Tests

Since most lightning occurs in the tropics, it is the oceanic attenuation factor γ_o, which mainly determines the meridional distribution of lightning in the CTM. For the zonal distribution, on the other hand, essentially T_{ct} is responsible. As a consequence, it is sufficient to discuss the sensitivity of the CTM with respect to variations of γ_o in terms of zonal means and, correspondingly, in terms of meridional means with respect to variations of T_{ct}.

Figure 3.9 shows the meridional average of the annual mean relative lightning distribution, $\langle\overline{p_{\leadsto}{}^{a}}\rangle_{\varphi}$, for three different values of γ_o: the standard value (γ_o = 0.1), half of this value, and the double thereof. The main effect of varying γ_o is to determine the ratio of the relative amplitudes of $\langle\overline{p_{\leadsto}{}^{a}}\rangle_{\varphi}$ between the Pacific on the one hand and South America and Africa on the other hand. For γ_o = 0.05, the CTM produces about 10% more lightning over Africa and America and up to 30% less over the Pacific than for $\gamma_o = 0.1$. Over the Atlantic and the Indian Ocean, the corresponding change of $\langle\overline{p_{\leadsto}{}^{a}}\rangle_{\varphi}$ is a decrease of up to 20%. At the

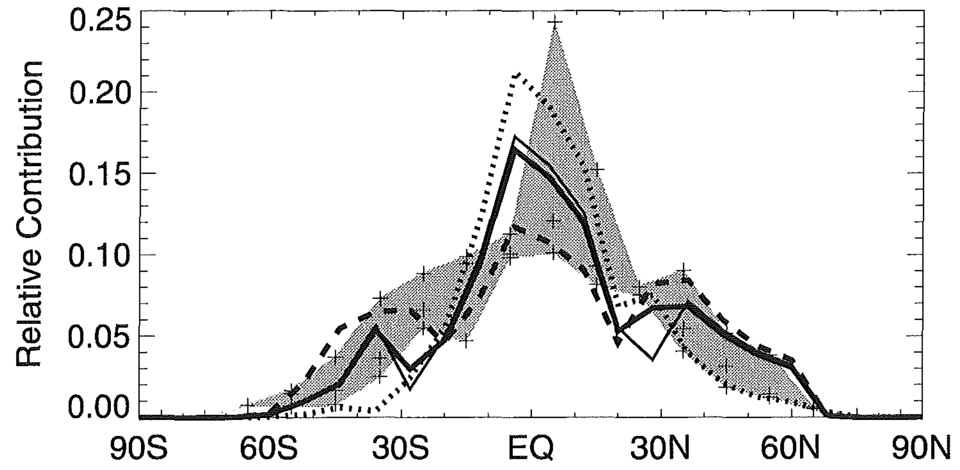

Figure 3.10: Zonal averages of the annual mean relative lightning distribution, $\langle\overline{\rho_{\leadsto}{}^{a}}\rangle_\lambda$, with $\gamma_o(\varphi \leq 24°) = 0.1$, $\gamma_o(\varphi > 24°) = 1$, and different values of T_{ct}: thick solid line 238 K, dotted line 228 K, and dashed line 248 K. The grey shading denotes the range of the values given by the satellite observations shown in Figure 3.7. These values are shown here as plus signs. The thin solid line gives $\langle\overline{\rho_{\leadsto}{}^{a}}\rangle_\lambda$ calculated with $\gamma_o(\varphi \leq 32°) = 0.1$, $\gamma_o(\varphi > 32°) = 1$, and $T_{ct} = 238$ K.

longitudes in between these sensitive regions, both model runs differ only slightly from each other. Inverse changes are obtained for $\gamma_o = 0.2$. In this case, $\langle\overline{\rho_{\leadsto}{}^{a}}\rangle_\varphi$ increased by up to 50% over the Pacific when compared to the run with $\gamma_o = 0.1$, whereas the continental peaks over America and Africa are decreased by 10-15%. Between 80°E and 140°E, variation of γ_o has hardly any effect on $\langle\overline{\rho_{\leadsto}{}^{a}}\rangle_\varphi$ due to counteracting changes of $\rho_{\leadsto}$ over land and over oceans.

In July, the CTM's convection activity at continental regions of northern mid-latitudes is quite strong. Hence, $\rho_{\leadsto}$ there probably is overestimated in the standard case, in particular over China, as Figure 3.5 indicates. Since $\gamma_o = 0.05$ increases $\rho_{\leadsto}$ over continents even further, the standard value of γ_o is set to 0.1, although Figure 3.9 gives the impression that $\gamma_o = 0.05$ results in a better fit of the satellite data. In summary, however, the changes of $\langle\overline{\rho_{\leadsto}{}^{a}}\rangle_\varphi$ in the CTM due to halving or doubling of γ_o are smaller than the deviations of the individual satellite observations from each other.

For comparison, Figure 3.9 also shows the meridional normalized mean land fraction of the latitudes $\varphi \leq 48°$ for each of the CTM's longitude belts. Since most of the global lightning activity occurs over continents at $\varphi \leq 48°$, this curve is the zero order approximation of the global, meridionally averaged annual mean lightning activity. For most longitudes, the relative land fraction agrees well with the relative lightning rate. The three clearly visible peaks reflect the increased lightning activity over the continents America, Africa plus Europe, and southeastern Asia, respectively. However, for the longitudes $60°\text{E} \leq \lambda \leq 90°\text{E}$, where the monsoon over Indian with it's low lightning rates plays an important role, much less lightning occurs than expected from the zero order approximation.

Figure 3.10 shows the zonally averaged annual mean relative lightning distribution, $\langle\overline{\rho_{\leadsto}{}^{a}}\rangle_\lambda$, for different values of T_{ct}. This parameter determines the ratio of the amplitudes which $\langle\overline{\rho_{\leadsto}{}^{a}}\rangle_\lambda$ has in the tropics and at mid-latitudes, respectively. When T_{ct} is set to 228 K, that is 10 K lower than the original value, then $\langle\overline{\rho_{\leadsto}{}^{a}}\rangle_\lambda$ is very similar to that obtained with the parametrization suggested by *Price and Rind* [1992] (see Figure 3.6). This change of T_{ct} corresponds with an increase of the tropical peak of $\langle\overline{\rho_{\leadsto}{}^{a}}\rangle_\lambda$ by 30% and a decrease of $\langle\overline{\rho_{\leadsto}{}^{a}}\rangle_\lambda$ by 58% at 44°N and of 80% at 44°S. When T_{ct} is increased by 10 K to 248 K, then the amplitude of the tropical maximum $\langle\overline{\rho_{\leadsto}{}^{a}}\rangle_\lambda$ decreases by 28%. At mid-latitudes, $\langle\overline{\rho_{\leadsto}{}^{a}}\rangle_\lambda$ is increased by about 20% in this case, whereas its amplitude is more than doubled at southern mid-latitudes. There, T_{ct} = 248 K results in unrealistically high lightning rates during southern winter. At 20°S and 20°N, neither increasing nor decreasing T_{ct} by 10 K makes an effect of more than a few percent.

Both Figures 3.9 and 3.10 show that in the present lightning parametrization there is no strong dependence of the zonally or meridionally averaged annual mean relative lightning distributions on the exact values of γ_o and T_{ct}. In fact, realistic distributions are obtained for a range of values. Even if $\gamma_o = 0.1$ is assumed for latitudes $\varphi \leq 32°$, $\langle \overline{\rho_{\rightsquigarrow}{}^{a}} \rangle_\lambda$ differs only slightly from the result obtained by the standard set of parameters, as shown in Figure 3.10. Locally or seasonally, however, the agreement between observed lightning distributions and the model results is sensitive with respect to changes of γ_o and T_{ct}.

3.4 Vertical Distribution of NO Emissions within a Thundercloud

Because of the highly variable nature of thunderstorms it is difficult to extract globally reliable characteristics both of the vertical distribution of lightning flashes within a thundercloud and of the NO yield per flash from the observations available at the moment. This is true even more for attempts to treat the NO production for CC and CG flashes separately, which nevertheless have been made [e.g., *Kowalczyk and Bauer*, 1981; *Köhler et al.*, 1995]. An additional difficulty for a realistic lightning parametrization is the low vertical resolution of the CTM.

3.4.1 The Emission Profile in the CTM

To avoid the problems just mentioned, the most simple of all approaches is made here: If a grid column in the CTM produces lightning during a certain time step, then an amount of NO_X proportional to the actual air density is emitted in every box between the Earth's surface and the highest level involved in deep wet convection. Thus, the net effect of a thunderstorm is parametrized as a height-independent increase of the NO_X mixing ratio in the corresponding grid column. The amplitude of this increase is scaled in a way that the sum over all thunderstorms occurring in the CTM during one year produce 5 Mt N (see Section 3.2).

The assumption of a density-weighted vertical distribution of NO_X emissions is consistent with equilibrium calculations at elevated atmospheric temperatures, which show an equivalent mole fraction of NO below 3000 K for all tropospheric air densities [*Kowalczyk and Bauer* 1981, referring to *Gilmore* 1975]. Another justification of this simple approach is the fact that an air parcel lifted by the updraft of a cumulonimbus cloud needs on the order of 10 min from the PBL to the tropopause. Thus, the time scale of vertical mixing within a cumulonimbus cloud is much smaller than the 8-hour time step for convection in the CTM and it makes no sense to resolve more than the net effect of a thunderstorm.

3.4.2 Sensitivity Tests

To test the CTM's sensibility with respect to variations of the vertical profile of NO_X emissions caused by lightning discharges, three model runs have been made in which lightning is the only source of NO_X. Transport, chemical conversion, and deposition processes take place as described in the previous chapter. The horizontal distribution of lightning is obtained from the parametrization given in Section 3.3 with the standard set of parameters in these three runs. Two additional runs are evaluated here which were made to estimate the effect of changes in the horizontal lightning distribution.

In the standard case, NO_X is added density-weighted as described above. The standard emission, E0, results in the standard distribution of NO_X mixing ratios, M0. In the variation case 1, more weight is put on emissions at higher altitudes than on emissions at lower altitudes: $E1(k) = k\ E0/\tilde{E1}$, where k denotes the index of the σ-layer (k = 1 is the lowest model layer) and $\tilde{E1} = 0.2 \sum_1^9 E1(k)$ is a scaling factor ensuring a global emission rate of 5 Mt N/yr. Reverse weights are put in the variation case 2: $E2(k) = (9\text{-}k)\ E0/\ \tilde{E2}$,

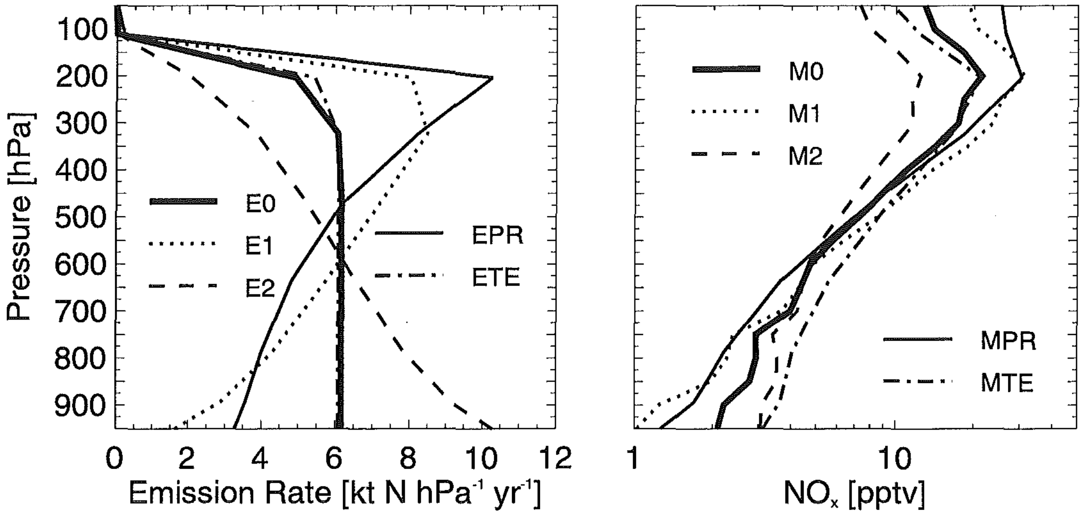

Figure 3.11: Vertical profiles of (left panel) NO_X emissions and (right panel) the resulting zonally, meridionally, and annually averaged mixing ratios for different CTM runs. The cases 0-2 are based on the standard lightning parametrization (see p. 27), the case PR on the lightning parametrization of *Price and Rind* [1992], and the case TE on the satellite observations of *Turman and Edgar* [1982]. See text for details.

where $\tilde{E2} = 0.2 \sum_1^9 E2(k)$ again ensures a global emission rate of 5 Mt N/yr. The mixing ratios obtained from the emission profiles E1 and E2 are M1 and M2, respectively.

Figure 3.11 shows the emission profiles for the three cases together with the resulting zonally, meridionally, and annually averaged mixing ratios. The decrease of E0 above 322 hPa reflects the decreasing number of lightning events reaching those levels. Corresponding changes of the slope are visible above 322 hPa for for E1 and E2 as well. The vertical profiles M0, M1, and M2 are characterized by mixing ratios below 5 pptv NO_X in the lower troposphere and a significant increase up to 200 hPa. Above, the mixing ratio again decreases since the amount of NO_X injected at that altitude is very low. In fact, most of the NO_X present there is emitted at lower altitudes.

The profile M0 peaks at 200 hPa, although neither E0 depends on altitude nor is there a change in the mixing ratio of an air parcel due to vertical motion. However, the chemical lifetime of NO_X, τ_{NOx}, does depend on altitude. It decreases from 1-2 days in the lowest model layer to about 10 days in the upper troposphere. Thus, once NO_X reaches the upper troposphere either by direct injection or by transport from below, it can accumulate there during τ_{NOx}, if it is not mixed downward again. Vertical mixing by convection also is the reason why the large differences between the three emission profiles are weakened in the resulting NO_X profiles. For example, the ratio E1/E0 is 0.24 at the surface, whereas M1/M0 there is 0.49. At 200 hPa, E1/E0 and M1/M0 are 1.63 and 1.46, respectively. However, despite this smoothing effect, the CTM is quite sensible with respect to variations of vertical NO emission profile.

In addition to the cases 0-2, Figure 3.11 also shows emission profiles EPR and ETE and corresponding averaged mixing ratios MPR and MTE, respectively. Case PR is added for completeness, since it was used by *Kraus et al.* [1996]. It is based on the lightning distribution of *Price and Rind* [1992] and the assumption of a constant emission of NO_X per meter of lightning channel with one channel from the Earth's surface up to the highest level involved in convection. Thus, both the horizontal lightning distribution and the vertical profile of NO emissions differ from the standard case.

The emissions EPR result in averaged stratospheric NO_X mixing ratios which are even higher by 35%

than those calculated in the variation case 1, whereas they are about 30% lower at altitudes of about 500 hPa. At 200 hPa, both cases yield the same mixing ratio although EPR is 27% larger there than E1. However, this coincidence is a result of averaging. In fact, M1 is higher than MPR at mid-latitudes and vice versa in the tropics. Since the highest exchange rates between the troposphere and the stratosphere are reached in the tropics, the latter also is the reason why MPR is higher than M1 above 200 hPa.

In the case TE, lightning is distributed horizontally as given by the satellite observations of *Turman and Edgar* [1982]. In this case lightning events may occur in model grid columns in which no deep wet convection takes place. This has two consequences: First, NO_X has to be emitted at a constant rate during each time step, monthly mean values, since no individual lightning event can be defined. Second, the vertical profile of NO emissions can be assumed density-weighted as in the standard case, but, due to the lack of cloud tops, extend from the Earth's surface up to the tropopause.

The difference between the emission profiles ETE and E0 is as small as 2% at all altitudes except at 200 hPa where it is 10%. Despite this, MTE is significantly larger than M0 below 600 hPa. This effect is mainly caused by, on the one hand, the temporal dependence of the emissions due to the coupling with deep convection events in the standard case and, on the other hand, emission rates based on a monthly mean values. Although the temporally averaged net emissions are equal in both cases, the resulting mixing ratios are different, because both deposition and conversion into HNO_3 remove amounts of NO_X proportional to the actual concentration. Hence, spikes in the NO emission by individual lightning events are associated with a subsequent e-folding decay of the excess amount of tracer. Since apart from dynamical dilution, this decay is characterized by the chemical lifetime of NO_X, it is much faster in the lower troposphere than in the upper troposphere.

An important consequence of the comparison between the case TE and the standard case is that using an observed, i.e. "correct" lightning distribution is not sufficient to improve the lightning source of the model. In general, an observed lightning distribution is not consistent with the dynamics of the CTM and, consequently, the same also is true for the resulting NO_X distribution.

Finally, the result of recent aircraft measurements is mentioned in this context which indicate that a local increase of NO in the vicinity of a thunderstorm is found in the upper troposphere, but not below the cloud [*Ridley et al.*, 1996; *Tuck*, 1996].

3.5 Result of the Lightning Source Parametrization

The results of the present parametrization of lightning as a source of NO_X is shown in Figure 3.12 for January and July. Since most lightning events have the same vertical extent of 7 σ-layers and, hence, approximately equal amounts of NO_X are emitted per event, the patterns of Figure 3.12 resemble those of Figure 3.4. However, there is a slight dependence of the convection height on latitude in the CTM so that a lightning event occurring at high altitudes emits less NO_X than a tropical one. Consequently, the poleward extent of NO_X emissions is usually smaller than the corresponding meridional distribution of lightning occurrence. At northern mid-latitudes this is not true in summer, when the large area covered by land causes high-reaching convection. The global NO_X emission rates of lightning are 4.6 Mt N/yr in January and 5.8 Mt N/yr in July. Figure 3.12 is the supplement to Figures 2.1-2.5 which show the emission patterns of the first five sources.

3.6 Overview of All Sources

Comparison of all six figures allows to summarize the most important features of the sources of NO_X in the CTM: Fossil fuel combustion causes more than 80% of the NO_X emissions in all continental regions north of 30°N except Greenland and the northernmost islands of Canada in January. In July, this fraction is reached only at central Europe, Japan, the east coast of Siberia, and the United States except the Rocky

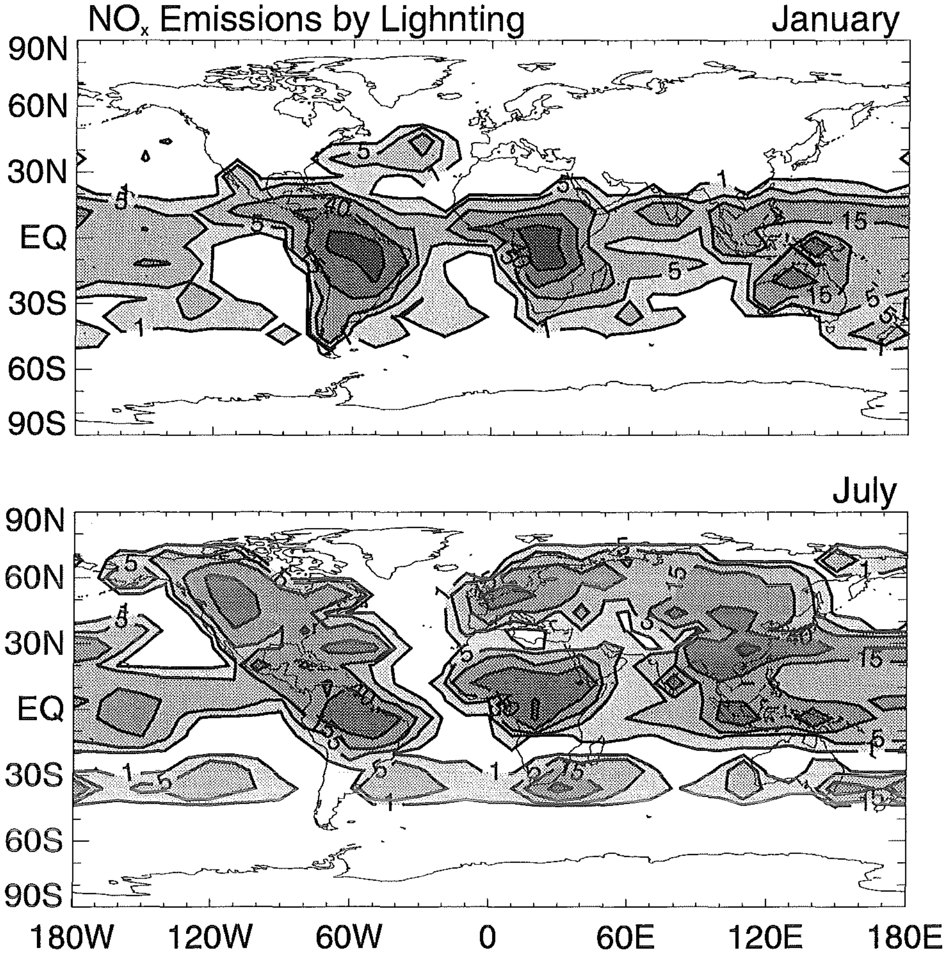

Figure 3.12: Monthly mean emission rates of the source lightning discharges for (upper panel) January and (lower panel) July. Contours are displayed at 1, 5, 15, 40, and 100 mg N m^{-2} yr^{-1}.

Mountains. In the southern hemisphere, fossil fuel combustion reach fractions of more than 80% during both months in Chile, South Africa, the Sydney region and, only in July, in New Zealand.

Microbial activity in soils contributes 20-40% to the NO_X emissions at almost all continental regions between 60°S and 20°N both in January and in July. This source reaches a fraction of more than 60% over the Sahara, but the absolute emission rate there is as small as 1-10 mg N m^{-2} yr^{-1}.

Lightning discharges are the source of more than 80% of the NO_X emissions at most of the oceanic regions between 50°S and and 40°N throughout the year. Over continents, this source makes contributions of more than 60% near the equator and of 20-40% in the southern hemisphere in January. In July, the corresponding contributions are about 40% near the equator and less than 20% south of 10°S. In addition, fractions of 20-40% are reached in July at western Alaska and at central Siberia.

Biomass burning contributes fractions of 40-60% of the total NO_X emission where the emission rates of this source are higher than 50 mg N m^{-2} yr^{-1}, i.e. in January in Africa between the equator and 20°N and in July in Brazil and in Africa between the equator and 30°S. Further, this source contributes 20-40% in India, southeastern Asia, and central America in January and similar fractions in Indonesia and northern

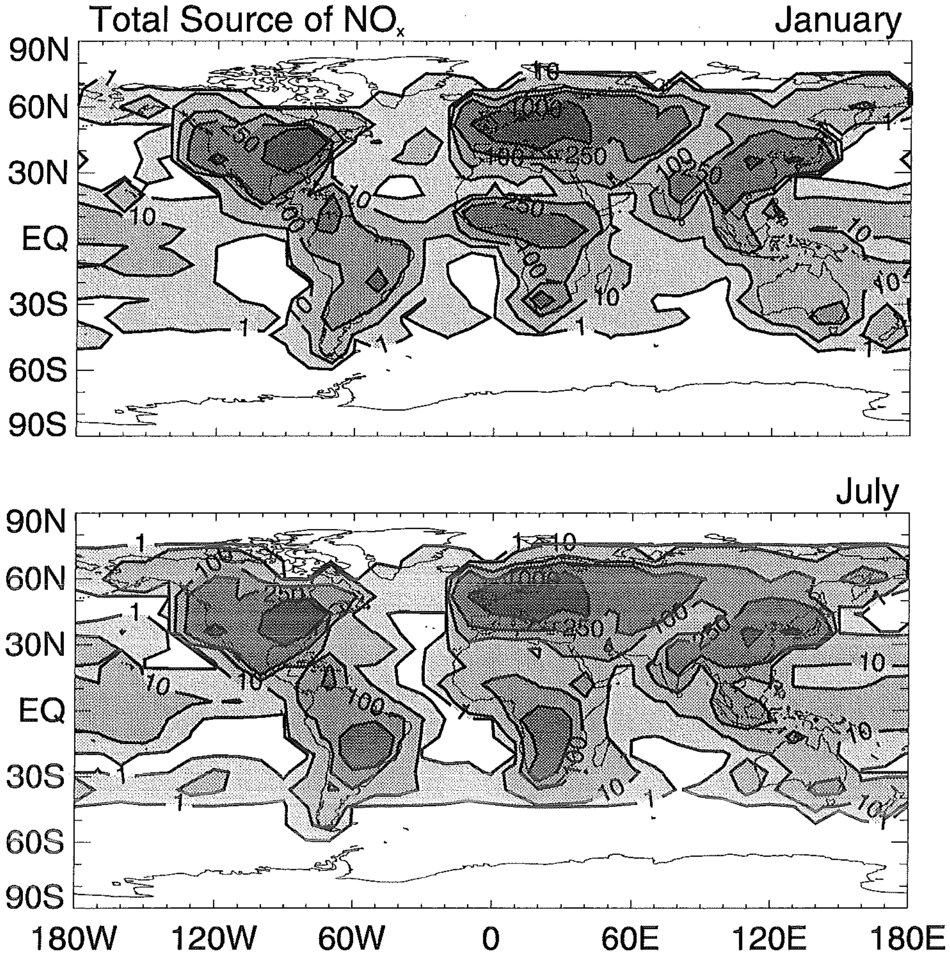

Figure 3.13: Total monthly mean emission rates of all 6 sources for (upper panel) January and (lower panel) July. Contours are displayed at 1, 10, 100, 250, and 1000 mg N m^{-2} yr^{-1}.

Australia in July.

Production of NO_X in the stratosphere is the by far dominant source south of 40°S in January north of 70°N in July. Furthermore, this source reaches fractions of more than 80% in oceanic regions which are little active with respect to deep wet convection so that lightning is missing as a source of NO_X. These regions are the oceans off the western coasts of South America, southern Africa, and Australia both in January and in July and, in addition in January, the entire latitude belt around 50°S.

Aircraft emissions are an important source of NO_X only in oceanic regions north of 30°N. Because of the annual cycle of the stratospheric source, they reach contributions of more than 80% there in January and of 40-60% in July.

For completeness, the CTM's total source of NO_X is shown in Figure 3.13. The patterns given there are simply obtained by linear superposition of the contributions from the six individual sources. Main purpose of Figure 3.13 is to facilitate the comparison with NO_X emission scenarios used in other model studies.

Chapter 4

Tracer Transport Properties of the Model

In the present CTM, realistic transport of tracer is only possible when three conditions are satisfied: First, the meteorological data used as input for the CTM have to be realistic, i.e. they must contain typical weather situations or represent climatological mean values. Second, the parametrizations of the dynamical processes included in the CTM itself must reproduce the dominant features of tracer transport correctly. Third, a realistic spatial and temporal distribution of the source of tracer is required. The last of these conditions was discussed in the previous two chapters. Previous results about the first two conditions are summarized in Section 4.1.

In addition, model runs are presented in this chapter in which Radon-222, ^{222}Rn, is used as a passive tracer. Such a tracer is chemically inert, it is moved according to the local flow conditions and, eventually, it decays after a certain lifetime. The purpose of passive tracer calculations is to check whether the model one is using is able to transport tracers in a way similar to what is expected from measurements. The same is true for comparisons between different models. Since the chemical lifetimes of ^{222}Rn and tropospheric NO_X are of the same order of magnitude, calculation of ^{222}Rn distributions as a preliminary step towards NO_X distributions also helps to interpret the latter ones, at least their contribution from the surface sources. An additional purpose of the ^{222}Rn runs is to provide a more detailed overview of the global-scale ^{222}Rn distributions than is given by *IPCC* [1995].

In Section 4.2, a ^{222}Rn emission scenario is defined. Results of ^{222}Rn calculations carried out with the CTM are compared with corresponding observations in Section 4.3. Suitable measurements for such comparisons are rare, but additional information about the model's tracer transport properties can be obtained by comparison with corresponding results from other global models. Such a model comparison is carried out in Section 4.4, where ^{222}Rn distributions calculated by the models ECHAM3 and TMK are evaluated.

4.1 Previous Results

Since several previous investigations use the same GISS GCM input data on which the present study is based, much knowledge about the quality of these data can be adopted here. Previous investigations of how the CTM distributes passive tracers also exist, but they provide only partial insight in the present problem. The reason for this is that either passive tracers with chemical lifetimes much longer than that of NO_X [*Prather et al.*, 1987; *Jacob et al.*, 1987], or passive tracers with short lifetimes, but then only specific regional aspects are considered. The most important results of the regional studies are summarized in the following, whereas the former two investigations are of limited relevance here. Slow transport processes like inter-hemispheric exchange play an important role for the tracers tracers CFC-11, CFC-12, and ^{85}Kr considered therein, which hardly affect the distribution of the short-living species NO_X.

4.1.1 The GISS GCM

The first discussion of the meteorological data calculated by the GISS GCM was provided by the authors of the model themselves [*Hansen et al.*, 1983]. Important with respect to the distribution of NO_X is their finding that the GCM does not reproduce the distribution and intensity of clouds and precipitation correctly. Despite the large uncertainties of cloud cover observations and the high inter-annual variability of this parameter, it is obvious that the GCM fails to produce the winter cloud minimum in eastern central Asia, although it generates realistic high pressure systems there. Also in winter, the model yields regions of anomalously high cloud cover and precipitation in the Bay of Bengal and off the west coast of central America. In summer, too many clouds occur in the GCM over northern Australia and over the central Pacific. In the latter region, the model generates a cloud cover of more than 70%, whereas 40-50% are observed. Since a deviation of the GCM's cloud cover from observations not necessarily is associated with a corresponding difference in the frequency of deep wet convection, the former deficiency is reflected only partly in the lightning distribution of the CTM. Over the central Pacific, however, it is the overestimate of deep wet convection in the GCM, which most likely explains the overestimate of lightning in that region in the CTM. Both dry convection and shallow wet convection are very small there. The assumption that the GCM overestimates the activity of deep wet convection over the central Pacific is additionally confirmed by recent satellite observations of global cloud distributions [*Rossow*, 1993].

Less important for distributions of the short-living tracers NO_X and ^{222}Rn is the fact that the intensity of the Hadley cell is about 10-20% too weak in the GCM and that the peak intensity of this cell occurs one grid box (8°) too far north. The winter hemispheric Ferrel cell is positioned correctly, but its intensity is less than half of the observed strength. Further, the zonal mean wind speed of the upper tropospheric tropical easterlies is too weak by about a factor of 2 in summer. During the same season, the northern hemispheric sub-tropical jet is about 20% weaker in the GCM than what is observed. Another minor weak point of the GCM is the underestimate of the surface temperature by up to 5 K in the Midwest of the United States during summer. This temperature deficiency results in an underestimate of the NO_X production by soil microbial activity.

4.1.2 CTM Calculations Using ^{222}Rn as a Passive Tracer

The radioactive noble gas ^{222}Rn constitutes a suitable tracer for tropospheric transport processes. It acts like a passive tracer, the only sink of which is radioactive decay with a half-life of 3.824 days or, correspondingly, an e-folding lifetime of 5.5 days. Thus, the lifetime of ^{222}Rn is comparable to the 1-10 days, during which NO_X typically lives in the troposphere. The primary source of ^{222}Rn is emanation out of soils as a daughter product of ^{226}Rn in the natural radioactive decay chain of ^{238}U. Oceans also emit some ^{222}Rn into the atmosphere, but their emanation rate is at least two orders of magnitude smaller than that of soils [*Broecker et al.*, 1967; *Wilkening and Clements*, 1975]. The continental emanation rates of ^{222}Rn depend strongly on soil conditions, as the ^{226}Rn content or soil porosity, and on meteorological factors such as heavy precipitation, snow- or ice-cover, and the strength of turbulent exchange in the boundary layer. Vegetation might play an additional role in increasing ^{222}Rn exhalation rates, but because of the low solubility of ^{222}Rn in water, emission from plant surfaces probably are negligible when compared with emissions from soils. Summarizing discussions of the processes which affect ^{222}Rn emanation as well as numerous references on this subject can be found in the studies of *Feichter and Crutzen* [1990] or *Jacob and Prather* [1990].

The previous studies in which transport properties of the CTM are tested by analyzing calculated ^{222}Rn distributions are *Jacob and Prather* [1990], *Balkanski and Jacob* [1990], and *Balkanski et al.* [1992]. The spatial and temporal resolution used there is $4^\circ \times 5^\circ$ and 4 hours, respectively, instead of the $8^\circ \times 10^\circ$ and 8 hours used here. The convection parametrization is the same in these studies and in the present one.

Jacob and Prather, 1990

Jacob and Prather investigate ^{222}Rn distributions over the North American continent and the adjacent oceans. They find that the equivalent ^{222}Rn concentrations[1], a_{Rn}, in the model are regulated primarily by dry convection. How well the CTM reproduces observed ^{222}Rn distributions therefore depends on the model's pattern of dry convection. In fact, the values of a_{Rn} they obtain over the northeastern United States are too low during spring, when excessive rainfall suppresses dry convection, and too high during autumn, when a severe drought allows dry convection to be considerable. This drought strongly is coupled with the fact that the Bermuda High is shifted north-eastward in the GCM. The shift, in turn, is associated with the parametrization of deep wet convection. It disappeared almost completely after a new scheme for moist convective mass transport was implemented in the GCM [*DelGenio and Yao*, 1988].

The higher temporal resolution used by *Jacob and Prather* allows a crude resolution of the diurnal cycle of a_{Rn}. During the day, the values of a_{Rn} calculated at four surface stations are in reasonable agreement with corresponding seasonally averaged measurements. At night, however, inversions may occur near the surface, which are associated with sharp gradients in tracer concentrations. Since the lowest model layer has a depth of about 700 m, these nocturnal inversions cannot be resolved.

Balkanski and Jacob, 1990

Balkanski and Jacob focus their interest on so-called radonic storms, which occur over the southern hemispheric part of the Indian Ocean. During these storms, ^{222}Rn-rich continental air is transported from the African continent towards the southeast. Usually, radonic storms are initiated by the simultaneous presence of a sub-tropical high pressure system located southeast of Madagascar and a low pressure system off the southern tip of the Africa.

The annual mean peak of a_{Rn} calculated by the CTM at the islands Crozet (46°S, 52°E), Kerguelen (49°S, 70°E), and Amsterdam (38°N, 77°E) during radonic storms is in good agreement with corresponding observations. However, the annual mean background equivalent ^{222}Rn concentrations *Balkanski and Jacob* obtain at these islands are 0.7-1.2 pCi/SCM, whereas 0.2-0.5 pCi/SCM are observed. Despite this, the calculated monthly mean values of a_{Rn} are lower between December and April than the lowest observations made during a period of 17 years at Kerguelen and Amsterdam. During the rest of the year, the CTM reproduces the observed monthly mean of a_{Rn} quite well there. At Crozet, the model results for southern hemispheric winter are too high by up to a factor of 3. However, *Balkanski and Jacob* find a prominent storm periodicity of 23 days in the CTM and a similar value, 27 days, in the observations during that time of the year. Further, model results and observations agree in a typical storm duration of 1-2 days. Since Crozet is the island located closest to the African continent, this might indicate that the decay of tropospheric a_{Rn} with increasing distance from Africa is overestimated in the CTM. A possible reason for such a too rapid decay might be an underestimate of horizontal mixing due to the lack of small-scale eddies in the CTM.

Balkanski and Jacob also find that within the PBL there are well defined plumes of continental air reaching the sub-antarctic Indian Ocean, but that these plumes account only for a minor fraction of the total ^{222}Rn advection. Most of the ^{222}Rn transport takes place in the free troposphere following deep convection over the continent.

---

[1] Amounts of atmospheric ^{222}Rn usually are given in pico-Curie per standard cubic meter, pCi/SCM, where 1 pCi/SCM is equal to a mixing ratio of 6.6×10^{-22} molecules of ^{222}Rn per molecules. Strictly speaking, pCi/SCM is a measure of activity per volume, but it is often called concentration. Here, such quantities are denoted by a_{Rn}.

Balkanski, Jacob, Arimoto, and Kritz, 1992

Balkanski et al. present CTM runs for the northern Pacific, where the equivalent ^{222}Rn concentration, a_{Rn}, mainly depends on advection of air from the Asian and American continents. The background value of a_{Rn} calculated by the CTM at sea level for approximately 30° west of the American west coast is about 1 pCi/SCM both during May and June 1986. This background value of a_{Rn} is in good agreement with corresponding measurements made aboard a vessel cruising between Alaska and Hawaii. Both the model calculation and the observations show similar frequencies and a similar duration of episodes with significantly enhanced values of a_{Rn}. During such episodes, a_{Rn} increases by about one order of magnitude at sea level. The CTM tends to produce peak values which are up to a factor of 2 higher than the highest values a_{Rn} observed. During some of these episodes horizontal plumes advect ^{222}Rn from Alaska directly within the PBL. If a_{Rn} is assumed to be correct over continents, then the overestimate of the ^{222}Rn peaks in the model can be explained either by the fact that the advecting processes are too fast or by an underestimate of horizontal diffusion and hence dilution of the plume.

Balkanski et al. also investigate a_{Rn} during July and August over the eastern Pacific at 200-300 hPa and 20°N-50°N. Most of the ^{222}Rn occurring there is lifted to the upper troposphere by deep convection over western and southeastern China from where it is advected quickly by the sub-tropical westerly jet. In the CTM, the average of a_{Rn} north of 25°N is 4 pCi/SCM, which is the same as the median of corresponding measurements. However, the standard deviation of the model result is about 1 pCi/SCM, whereas the observations are distributed bimodally with one mode centered below 1 pCi/SCM and the other at 11 pCi/SCM. Thus, instead of resolving individual episodes of continental influence at the upper troposphere, the CTM simply averages over both modes. Partly, this is a consequence of the fact that one grid box covers $4^\circ \times 5^\circ$, whereas significant variations of the upper tropospheric ^{222}Rn content are observed at distances as low as 150-300 km. Another reason for the low variability of CTM results is the representation of the sub-tropical jet in the GCM. In terms of monthly mean values, the GCM gives both the strength and the location of this jet correctly. However, since its day-to-day variability is underestimated, the instantaneous maximum speed of the jet systematically is too low [*Jacob et al.*, 1996]. In addition, the sub-tropical jet is located about 5° too far south and, more important, its wavy structure is resolved only weakly.

4.1.3 GISS GCM Calculations Using ^{222}Rn as a Passive Tracer

Since computing time becomes increasingly available, there are first studies which no longer use a CTM to solve the continuity equations for the tracers of interest. Instead, these equations are implemented directly in a general circulation model where the tracer concentrations are treated as a diagnostic variable like, for example, water vapor [e.g., *Roelofs and Lelieveld*, 1995; *Sausen*, 1995]. At the moment there are two studies, *Genthon and Armengaud* [1995] and *Rind and Lerner* [1996], in which ^{222}Rn is used as an on-line passive tracer in the GISS GCM.

Genthon and Armengaud, 1995

Genthon and Armengaud implemented a global ^{222}Rn cycle in the the original version of the GISS GCM, which is the version used here as well. The comparisons with observations they present are not essentially different from the results gained by the CTM calculations discussed above. In addition, *Genthon and Armengaud* compare the GISS GCM results with corresponding data calculated by the Laboratoire de Météorologie Dynamique model, LMD. Apart from various discrepancies between both models due to different source parametrizations, advection schemes, etc., there is a major difference caused by the finer model resolution of the LMD GCM. Compared with observations, the latter model is almost systematically better than the GISS GCM in reproducing seasonal cycles and rapid fluctuations of the equivalent ^{222}Rn concentration. Other large discrepancies between both models are consequences of the different parametrizations used for mixing within the PBL and for deep convection.

Rind and Lerner, 1996

Rind and Lerner give an overview of various changes of physics and parametrizations which have been made in the GISS GCM since the set up of the original version. They demonstrate the effects of these changes by comparing results of on-line CFC-11, ^{85}Kr, and ^{222}Rn calculations carried out with the different versions of the GCM. Most important with respect to the global distribution of tropospheric NO_X is the change of the convection parametrization, while the effect of altered numerical schemes for solving the momentum and energy equations have little influence on vertical mixing. The latter is true for the modified boundary layer physics and the new land surface parametrization also.

In the original version of the GCM, 50% of the mass of the lowest grid box involved in convection are raised whenever the moist static energy profile becomes unstable. The new scheme allows variable vertical mass fluxes proportional to the degree of instability. Entraining and non-entraining plumes are distinguished and, in addition, there are explicit downdrafts acting on 1/3 of the mass of the updraft [*DelGenio and Yao*, 1992]. As a result, the inner-tropical peak of the zonally averaged annual mean of a_{Rn} at 200 hPa decreases from 10.4 pCi/SCM in the original version to 5.6 pCi/SCM in the new version. The corresponding value is 7.3 pCi/SCM if the number of sigma layers is increased from 9 to 18. *Rind and Lerner* assume that the finer vertical resolution allows for more convection when stability is averaged over thiner levels. This substantial decrease of the upper tropospheric mean ^{222}Rn content extends from about 30°S to 30°N. At higher latitudes, the corresponding decrease is on the order of 10%.

The globally averaged annual mean vertical profile of a_{Rn} differs only slightly in the various versions of the GISS GCM below 6 km altitude. In the original version, a_{Rn} increases above that altitude up to a maximum of 4.7 pCi/SCM at 12 km, whereas in the newer versions, a_{Rn} between 6 and 12 km altitude is 3.3-3.9 pCi/SCM and more or less constant with hight. In the stratosphere, all versions show a similar decrease of a_{Rn} with altitude, but different absolute values of a_{Rn} . Unfortunately, *Rind and Lerner* provide their results of the ^{222}Rn experiments exclusively in terms of annual mean values and just shortly mention the differences between the various runs without explaining them.

The general lack of ^{222}Rn observations in the tropics prevents *Rind and Lerner* from drawing a conclusion which convection scheme is most realistic. The only data point available for an estimate of the zonal and annual mean of a_{Rn} in the tropical upper troposphere is an estimate derived from measurements made during January and February 1987 in the lower stratosphere over Darwin, Australia [*Kritz et al.*, 1993]. This estimate lies in between the the results of the original and the modified version of the GISS GCM and closest to the result from the newest GISS version with the increased vertical resolution of 18 σ-layers. *Rind and Lerner* note the model comparison included in *IPCC*, 1995 in this context, which shows that the ^{222}Rn distributions obtained from the newer parametrizations are more consistent with CTM results produced by other models.

4.2 Definition of a Simple ^{222}Rn Source

Because of the coarse resolution of the CTM version used here it is sufficient to assume the following very simple distribution of the ^{222}Rn emanation flux: 1.2 atoms ^{222}Rn cm^{-2} s^{-1} over the area covered by land in each grid box of the lowest model layer, if the actual temperature in the grid box is higher than 0°C. If this temperature is lower than 0°C, then there is no emission. Exhalation of ^{222}Rn from oceans is neglected. The total uncertainty associated with this ^{222}Rn emanation flux is a factor 2 at most [*Heimann et al.*, 1990]. A distinction is made in the definition of the ^{222}Rn source flux between frozen and non-frozen soil. This is done to take into account the results of observations which show that snow cover or ground temperatures below 0°C reduce the ^{222}Rn emanation considerably [e.g., *Dörr*, 1984].

The global mean ^{222}Rn emanation flux of 1.2 atoms ^{222}Rn cm^{-2} s^{-1} over continents is the value suggested by *Turekian et al.* [1977]. It is one of the higher estimates of this quantity, others are as low as 0.72 atoms cm^{-2} s^{-1} [*Lambert et al.*, 1982]. Most of the previous model studies use a source flux of 1.0

atoms ^{222}Rn cm^{-2} s^{-1} in between these estimates [*Balkanski and Jacob*, 1990; *Jacob and Prather*, 1990; *Heimann et al.*, 1990; *Balkanski et al.*, 1992; *Jacob et al.*, 1996]. The higher value of 1.2 atoms ^{222}Rn cm^{-2} s^{-1} is chosen here in order to allow a direct comparison between the ^{222}Rn distributions calculated by the CTM with corresponding results from two other global models (see below).

All CTM results shown in this chapter are obtained after one month of spin up time at least. After that time 99.6 % of the ^{222}Rn initially present have decayed and, hence, the dependence of the actual equivalent ^{222}Rn concentration on the initial conditions is negligible. To improve the resolution of the ^{222}Rn source, emissions are not just added to the mean of a_{Rn} in the corresponding grid boxes, but are decomposed spatially into orthogonal polynomials according to the second-order moments method [*Jacob and Prather*, 1990]. Thereby, the distribution of continents and oceans within a grid box can be taken into account to a certain degree. The major advantage of this decomposition, however, is that ^{222}Rn is not emitted in the middle of the lowest model layer, but at its lower edge, which is the Earth's surface. The latter feature considerably improves the agreement between model results and observations from surface stations.

4.3 Comparison of Calculated ^{222}Rn Distributions with Observations

The best way to check how realistic model results are is to compare them with observations. However, such a comparison often is difficult, because in general, the spatial and temporal resolution of the observed data does not match the resolution of the model. Furthermore, fluctuations of the concentration of an atmospheric trace gas often are larger than the actual concentration itself. Since the spatial and temporal resolution of the measurements has to be high enough to allow statistically reasonable averaging on the scales the model is resolving, it is all the more difficult to get suitable data from observations the coarser the model resolution is, or the shorter the lifetime of the considered trace gas. Most difficult, of course, it is to check calculations for a short-lived tracer against local observations.

With the resolution of the CTM used here, the atmospheric lifetime of ^{222}Rn is too short to extract more than order of magnitude estimates from observations. Nevertheless, a comparison between calculated and observed equivalent ^{222}Rn concentrations provides a useful tool to exclude unrealistic features from the model calculation. Unfortunately, however, only a few data sets of ^{222}Rn measurements are available. Some examples thereof are presented below, after a short sketch of how atmospheric ^{222}Rn is observed.

4.3.1 The Principle of ^{222}Rn Measurements

Measurements of atmospheric ^{222}Rn base on the following techniques: Sample air is pumped into a large decay volume after all progeny in the ^{222}Rn sub-series ^{218}Po - ^{214}Pb - ^{214}Bi - ^{214}Po have been removed by filters. The half lives of the daughter elements ^{218}Po, ^{214}Pb, and ^{214}Bi are shorter than 30 min. In the decay volume, some of the ^{222}Rn in the flow stream undergoes radioactive decay and produces new progeny. These progeny are collected on a second, downstream filter and are measured with an α-sensitive ZnS(Ag) scintillation detector. The equivalent ^{222}Rn concentration in the sample air then is derived from the resulting α activity counting rate. Instead of using a downstream filter, sub-micron particle condensation nuclei can be injected into the decay volume. The ^{222}Rn progeny then become attached to these nuclei and are filtered out onto a membrane which is monitored with a ZnS(Ag) scintillator. An alternative method to determine atmospheric values of a_{Rn} is to derived them from collection and assay of the short-lived ^{222}Rn progeny that are attached to aerosols in ambient air. This method assumes radioactive equilibrium between ^{222}Rn and its progeny.

The different ^{222}Rn measurement techniques usually alternate 1-2 hours of sample collection with 1-2 hours of scintillator measurements. The overall uncertainty of the individual techniques is ±20% or smaller, the detection limits are 0.01-3 pCi/SCM. A detailed comparison of different ^{222}Rn measurement techniques is given by *Collé et al.* [1995].

4.3.2 An Example of the Annual Cycle at a Ground Station: Bombay, India

Since the previous comparisons between equivalent ^{222}Rn concentrations calculated by the CTM and measurements do not include observations made at tropical or sub-tropical continental regions, the annual cycle of a_{Rn} in Bombay, India (18°N, 73°E) is chosen here as an example. Figure 4.1 shows monthly mean afternoon values of $\overline{a_{\mathrm{Rn}}}^m$ observed at that station during a period of 10 years [*Gesell*, 1983; redrawn from *Feichter and Crutzen*, 1990]. The corresponding values calculated by the CTM for the grid boxes centered at 12°N, 70°E and at 20°N, 70°E are shown also.

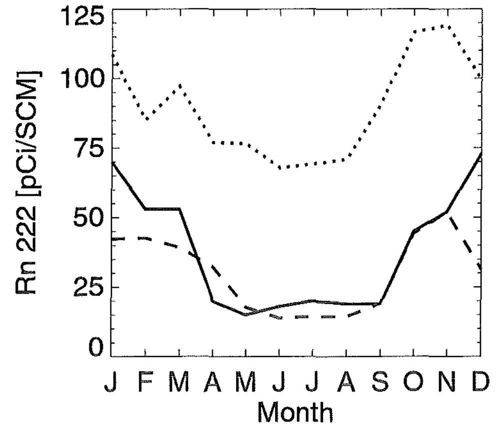

Figure 4.1: Monthly mean equivalent ^{222}Rn concentrations, $\overline{a_{\mathrm{Rn}}}^m$, calculated by the CTM for the grid boxes centered at (dotted line) 20°N, 70°E and (dashed line) 12°N, 70°E as well as (solid line) corresponding observations at Bombay, India 18°N, 73°E [*Gesell*, 1983].

Main purpose of Figure 4.1 is to demonstrate how the calculated value of $\overline{a_{\mathrm{Rn}}}^m$ of a grid box in the lowest model layer depends on the area covered by land in that box. The land fractions of the two examples chosen here are 31.3% and 2.1% for the more northern and the more southern grid box, respectively. Because the amount of ^{222}Rn emitted into a grid box is linearly proportional to the corresponding land fraction, the emission rates for the two grid boxes considered here differ by a factor of approximately 16. Despite this, $\overline{a_{\mathrm{Rn}}}^m$ in the more northern box is only roughly about a factor or 3 larger than in the more southern one. This is the case since vertical mixing, here in particular by dry convection, also is more efficient when the land fraction is larger. Horizontal wind speeds and directions are similar for both grid boxes boxes. In summer, oceanic air containing small amounts of ^{222}Rn is advected from the southwest or west to the western coast of India, whereas in winter, winds form the northeast or east are prevailing, which advect ^{222}Rn-rich continental air.

In general, the values of $\overline{a_{\mathrm{Rn}}}^m$ calculated for the two grid boxes show similar annual cycles, which are, however, much weaker than the annual cycle of the corresponding observation. This underestimate of seasonal variability mainly is caused by the coarse spatial resolution of the CTM, which does not allow to resolve strong gradients of a_{Rn} as they occur at coastal regions. Another consequence of the coarse model grid is the fact that regional circulation patterns as the monsoon cannot be resolved sufficiently.

4.3.3 The Annual Cycle at Other Ground Stations

Similar comparisons as shown in Figure 4.1 have been made for Crozet (46°S, 52°E), Kerguelen (49°S, 70°E), and Amsterdam (38°N, 77°E), three islands in the sub-antarctic Indian Ocean. These islands are too small to be resolved in the CTM's land cover map and, hence, a_{Rn} calculated for the corresponding grid boxes are determined by transport alone. The annual cycle of these values of a_{Rn} is almost identical to that calculated by *Balkanski and Jacob* [1990] with the CTM in a higher resolution version. *Balkanski and Jacob* assume a ^{222}Rn source flux of 1.0 atoms ^{222}Rn cm^{-2} s^{-1} over non-frozen land and decrease that flux by a factor of 3 if the 5-day mean temperature of a surface grid box is below 0°C. In addition, they allow modifications of the source flux associated with changes in the surface pressure.

When compared with values of a_{Rn} observed at Crozet, Kerguelen, and Amsterdam [*Polian*, 1984], the simpler source of ^{222}Rn used here yields results even slightly closer to the measurements than those of *Balkanski and Jacob* [1990]. More important, however, is the fact that there is no fundamental change in the calculated values of a_{Rn} when the input data provided by the GISS GCM are averaged to a resolution of

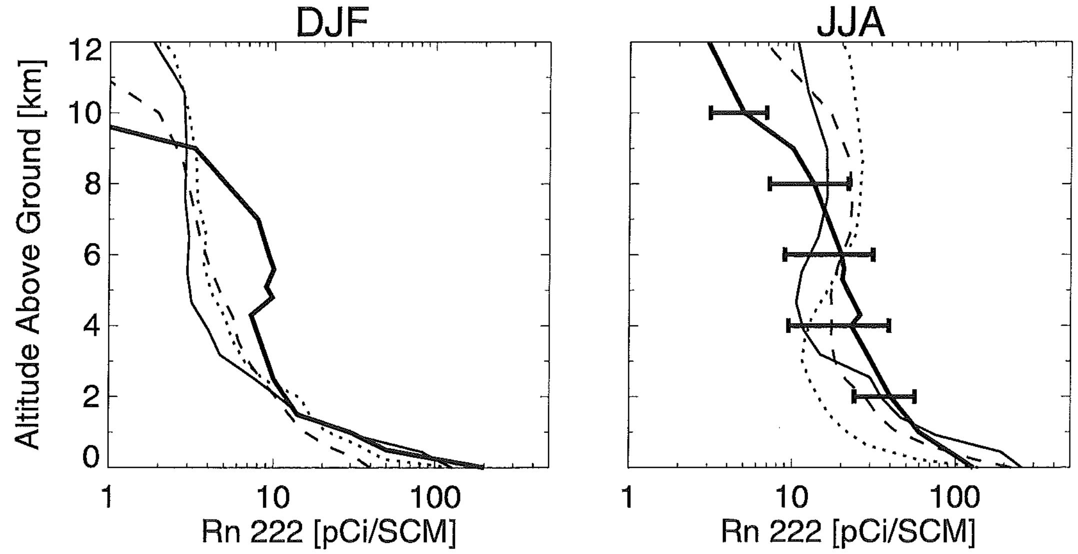

Figure 4.2: Seasonal mean vertical distribution of ^{222}Rn concentrations, a_{Rn}, for (left panel) winter and (right panel) summer. Thick solid lines are mean profiles compiled from various measurements at northern mid-latitudes [*Liu et al.*, 1984]. Thin lines are profiles calculated by the CTM for (solid lines) Socorro 34°N, 107°W, (dotted lines) Cincinnati 39°N, 84°W and (dashed lines) Kirov 58°N, 49°E. The solid bars in the right panel represent the standard deviation of the individual observations from the mean profile.

$8° \times 10°$. This insensitivity with respect to changes of the model resolution by averaging also is confirmed for the free troposphere. The calculated longitude-altitude a_{Rn} cross sections presented by *Jacob and Prather* [1990] and *Balkanski et al.* [1992] could be almost reproduced with the present version of the CTM.

At continental ground stations, however, there is much less agreement between the model calculations of *Jacob and Prather* [1990] and the present ones. For example, the monthly mean afternoon values of a_{Rn} they obtain for Washington D.C., Cincinnati, Socorro, and Livermore can be reproduced only roughly in the present study.

4.3.4 Vertical Profiles

Since long time observations of vertical ^{222}Rn distributions do not exist, the sporadic measurements collected by *Liu et al.* [1984] provide one of the few chances to compare model results with observations. The following comparison is given for completeness, not because it is believed to provide a real chance of evaluating model results.

Liu et al. [1984] analyzed previously published vertical profiles of a_{Rn} in order to derive seasonally averaged vertical eddy diffusion coefficients. The average profiles they present for summer and winter are based on 23 and 7 individual profiles, respectively, all of them observed over North America, the European part of Russia or over central Asia. Figure 4.2 shows these average profiles together with the standard deviation of the individual profiles from the average which *Liu et al.* determined for the summer case. The discontinuities in the averaged profiles are a result of the fact that the different individual profiles cover different ranges of altitude.

As in *Jacob et al.* [1996], three sites are chosen in Figure 4.2 for a comparison between seasonal mean vertical profiles calculated by the CTM and the averaged observations given by *Liu et al.*. They are Socorro (34°N, 107°W), Cincinnati (39°N, 84°W), and Kirov (58°N, 49°E). In winter, the calculated profiles at these sites are very similar. At the surface, a_{Rn} is dominated by the source flux, the net effect of which depends on whether there is snow cover, as in Kirov, or not, as in Cincinnati. At 2 km altitude, the calculated values of a_{Rn} have decreased to about 10 pCi/SCM at all three sites independent of the source flux. They continue to decrease above that altitude, but more slowly than near the surface due to the stronger vertical mixing within the free troposphere. Above the tropopause, which occurs at a lower altitude over Kirov than over Socorro and Cincinnati, a_{Rn} decreases rapidly with altitude.

The left panel of Figure 4.2 shows that within the lowest 4 km the calculated profiles agree well with the averaged observations. Above this altitude the value of a_{Rn} derived from the observations is larger by more than a factor of 2 than that calculated at any of the three sites, whereas above 9 km altitude, the opposite is true. This large discrepancy at altitudes higher than 4 km probably is caused by the small number of observations, which does not allow to determine a representative average. Thus, the bulge in the observed wintertime profile can be interpreted as an artifact of the averaging procedure [*Allen et al.*, 1996].

At all altitudes above 1 km both the averaged observed and the calculated values of a_{Rn} are higher in summer than they are in winter. The main reason for this is the stronger vertical mixing throughout the depth of the troposphere during that season. For the same reason the decrease of a_{Rn} with altitude also is weaker in summer than in winter, at least for the calculated profiles. The increased variation between the calculated profiles during summer arises, because in the model the frequencies of deep wet convection are quite different at the three sites. At Cincinnati, for example, deep wet convection is most frequent and, hence, the exchange of ^{222}Rn-rich air from low altitudes with relatively clean air from the upper troposphere is most efficient.

The three calculated profiles of a_{Rn} shown in the right panel of Figure 4.2 all have higher values in the upper troposphere than in the middle troposphere, whereas the averaged observed ^{222}Rn profile does not show such an increase with altitude. Moreover, at 2 km altitude, the model result for Cincinnati is lower than the lowest value within the 1σ standard deviation interval of the averaged observation, and it is higher than the highest value within that interval at 8 km altitude and above. The latter also is true for the profiles of Socorro and Kirov. This difference in structure between the calculated and the observed profiles points towards a weakness of the CTM. The parametrization of deep wet convection lifts air from the cloud base directly into the uppermost layer involved in convection. There, mixing with ambient air takes place, whereas during the upward motion of an air parcel entrainment or detrainment do not occur. The assumption that this is a weakness of the CTM and not an artifact associated with the averaging of observations is confirmed by inspection of the 23 individual ^{222}Rn profiles collected by *Liu et al.* [1984] for summer. Only a single one of these profiles shows an increase of a_{Rn} with altitude, as the three examples given in the right panel of Figure 4.2 do.

4.4 Comparison with Results from the Models ECHAM3 and TMK

Even if all ^{222}Rn measurements ever made were compared with the CTM calculation, these data would not be sufficient to make a reliable decision of how realistic the model results are. Comparison with ^{222}Rn distributions calculated by other models cannot guarantee realistic results either, because other models might be based on similar, possibly wrong assumptions as the CTM. Despite this, comparisons between different models provide helpful assistance in judging the individual results, in particular in the tropics, where hardly any ^{222}Rn measurements are available. The most important advantage of a model comparison is that data referring to similar spatial and temporal scales are compared with each other. Thus, extensive averaging is not required, as it is the case when calculated global distributions of a short-living tracer are compared with observations.

4.4.1 Description of the Models

In the following, ^{222}Rn distributions are compared which are calculated by the models ECHAM3, TMK, and the CTM used in the present study. ECHAM3 is a general circulation model in which ^{222}Rn is transported as an on-line tracer, whereas the transport model TMK is driven with observed meteorological input data from the European Centre for Medium Range Weather Forecasts (ECMWF). Short descriptions of the first two models are given below. Any difference between the ^{222}Rn distributions calculated by these three models can be attributed to differences in the model dynamics since the ^{222}Rn source parametrization described in Section 4.2 is implemented in all three models. The sink removing ^{222}Rn, radioactive decay with an e-folding lifetime of 5.5 days, also is identical in the three models.

The Atmospheric General Circulation Model ECHAM3

Based on a previous version of the numerical weather prediction model of the ECMWF (EC), the spectral model ECHAM was developed in Hamburg (HAM). The data evaluated here were generated and kindly provided by Robert Sausen and Ines Köhler with the modified ECHAM3 version used at the Deutsche Forschungsanstalt für Luft- und Raumfahrt (DLR), Oberpfaffenhofen. In this version, the prognostic variables vorticity, divergence, temperature and surface pressure are advected spectrally, whereas a semi-Lagrangian advection scheme is used for humidity, cloud water, and the passive tracer ^{222}Rn. The model is described comprehensively by *Roeckner et al.* [1992] and in *DKRZ* [1992]. The latter study also includes technical details of the parametrizations of radiation, cloud formation and precipitation, convection, and horizontal and vertical diffusion.

For the ^{222}Rn runs, ECHAM3 was operated in T21 resolution with an integration time step of 40 min. That means that the equivalent resolution for dynamical processes is approximately 1000 km. The corresponding Gaussian grid for calculating the non-linear and the diabatic terms has a resolution of about 5.6°. The vertical resolution of ECHAM3 is 19 layers in a hybrid σ-p-coordinate system, where σ-coordinates are used in the lower part of the atmosphere and pressure coordinates in the upper part. The model top is at 10 hPa. Diurnal cycles are included in the ^{222}Rn runs, but they are performed in perpetual January and July modes, respectively, with fixed insolation for the middle of the corresponding month and climatological sea surface temperatures. Some details of the DLR version of ECHAM3 as well as several references of climate sensitivity and climate change experiments, in which ECHAM participated, are given by *Sausen* [1995].

The Transport Model TMK

The three-dimensional chemical tracer model TMK is adapted from the global tracer transport model TM2 [*Heimann*, 1995]. It is run at the Koninklijk Nederlands Meteorologisch Instituut (KNMI) by Peter F. J. van Velthoven, who generously provided the ^{222}Rn data evaluated in this study, Wiel M. F. Wauben, and coworkers. The model TMK calculates the horizontal and vertical transport of tracers on the basis of 12-hourly output from the ECMWF model [cf. *Velders et al.*, 1992], which analyses and interpolates observations of wind, geopotential height, temperature, and humidity onto a grid with resolution of $2.5° \times 2.5°$. The vertical resolution of the TMK is 15 σ-layers up to 5 hPa. The ^{222}Rn runs were carried out with a coarser horizontal resolution, 5° in latitude × 4° in longitude, and a time step of 1 hour. Advection is parametrized in the TMK as in the present CTM, both models use similar split-operator methods. The convection parametrization implemented in the TMK is a simple Tiedtke scheme [*Tiedtke*, 1989], whereas in ECHAM3 a more sophisticated version of the Tiedtke scheme is used[2]. Some further characteristics of the TMK and addi-

---

[2] The Tiedtke scheme used in ECHAM3 [*Roeckner et al.*, 1992] has three types of convection, deep, shallow, and mid-level. In addition, an unsaturated downdraft is included. Deep and shallow convection are driven by moisture convergence in the entire column and in the boundary layer, respectively. Mid-level convection occurs when there is upward motion creating conditional instability. A bulk entraining plume-type cloud model is used for all types of convection, but with different rates of entrainment and detrainment. The updraft mass flux is proportional to boundary layer moisture convergence for the shallow and deep convection and proportional to the upward motion in the mid-level convection. The height of convection depends on the buoyancy of the plume.

tional references on this model are given by [*Velders et al.*, 1992; *van Velthoven and Wauben*, 1995; *van Velthoven and Kelder*, 1996].

4.4.2 Results of the Comparison

The following comparison of three different ^{222}Rn calculations is restricted to January and July because data from the models ECHAM3 and TMK are available for these two months only. Only monthly mean values of ^{222}Rn concentrations, $\overline{a_{\mathrm{Rn}}}^{m}$, are considered. Furthermore, horizontal distributions of ^{222}Rn are presented only for the 200 hPa level. This pressure level is chosen since the differences between the three models are largest there. At the surface, where ^{222}Rn is exclusively emitted, the distribution of this tracer is similar in all three models. The similarity decreases with increasing distance from the source, partly because of the differences in the meteorological data by which the models are driven, and partly because of differences in the transport parametrizations, in particular convection.

Upper Tropospheric Horizontal ^{222}Rn Distributions

The left panels of Figure 4.3 show the January monthly mean distributions of $\overline{a_{\mathrm{Rn}}}^{m}$ calculated by the models CTM, ECHAM3, and TMK at the 200 hPa level. The corresponding absolute differences between $\overline{a_{\mathrm{Rn}}}^{m}$ of each pair of models are given in the right panels of this figure. All three models agree in the main features of the upper tropospheric ^{222}Rn distribution, maxima over the tropical continents, background equivalent concentrations of 1-2 pCi/SCM over the tropical Pacific, and less than 1 pCi/SCM poleward of about 45° latitude. The general structure of the three distributions is very similar. However, the amplitudes of the maxima in the CTM distribution deviate considerably from that of the other two models. The values of $\overline{a_{\mathrm{Rn}}}^{m}$ calculated by the CTM, $\overline{a_{\mathrm{Rn_C}}}^{m}$ for short, reach peak values higher than 60 pCi/SCM, whereas the corresponding peaks of $\overline{a_{\mathrm{Rn}}}^{m}$ calculated by ECHAM3 and TMK, $\overline{a_{\mathrm{Rn_E}}}^{m}$ and $\overline{a_{\mathrm{Rn_T}}}^{m}$, respectively, are 20-40 pCi/SCM only[3]. The positions of the maxima also are different in the three ^{222}Rn distributions. The maxima of $\overline{a_{\mathrm{Rn_C}}}^{m}$ are shifted only slightly towards the southern hemisphere, about 5°, whereas the maxima of $\overline{a_{\mathrm{Rn_T}}}^{m}$ and $\overline{a_{\mathrm{Rn_E}}}^{m}$ are centered at about 10°S and 15°S, respectively. How far the maxima of the individual distributions extend into the northern hemisphere depends on where their centres are located and on their amplitude. The northward extent is largest in the CTM and smallest in ECHAM3.

Equatorial easterlies cause enhanced values of $\overline{a_{\mathrm{Rn}}}^{m}$ west of equatorial America and Africa in the CTM, but neither in ECHAM3 nor in the TMK. Partly, this can be explained by the northward shift of the tropical maxima in the CTM. Partly, however, this feature arises because the strength of the upper tropospheric easterlies is overestimated by the CTM during winter. In fact, the three different analyses of wind observations used by *WMO* [1991] to validate atmospheric general circulation models all agree in zonal wind speeds ranging from zero to -5 m/s at 200 hPa between the equator and 10°N for the season December to February. The corresponding wind speed in the CTM is about 8 m/s, which is roughly a factor of 2 too high.

The right panels of Figure 4.3 show the differences $\overline{a_{\mathrm{Rn_T}}}^{m}$-$\overline{a_{\mathrm{Rn_E}}}^{m}$, $\overline{a_{\mathrm{Rn_C}}}^{m}$-$\overline{a_{\mathrm{Rn_E}}}^{m}$, and $\overline{a_{\mathrm{Rn_C}}}^{m}$-$\overline{a_{\mathrm{Rn_T}}}^{m}$. These differences allow a direct comparison of the ^{222}Rn distributions calculated by the three different models. Discrepancies between ECHAM3 and TMK mainly are caused by the shift of about 5° in the position of the tropical maxima, whereas both models give almost identical amplitudes and a similar spatial extent of these maxima. Possible reason of this shift is the fact that the TMK is based on observations of specific years, 1989-1992, which may deviate from the situation simulated by the climate model ECHAM3.

The TMK version of the Tiedtke scheme [*Heimann*, 1995] includes deep and shallow convection only, but also has a downdraft. The mass fluxes and the plume height are determined as in the ECHAM3 version.

[3] The seasonally averaged horizontal distributions of ^{222}Rn calculated by the original version of the GISS GCM at 201 hPa and 468 hPa are very similar to the corresponding distributions calculated by the CTM [*Rind and Lerner*, 1996]. This is not necessarily the case as shown by the same authors for ^{85}Kr.

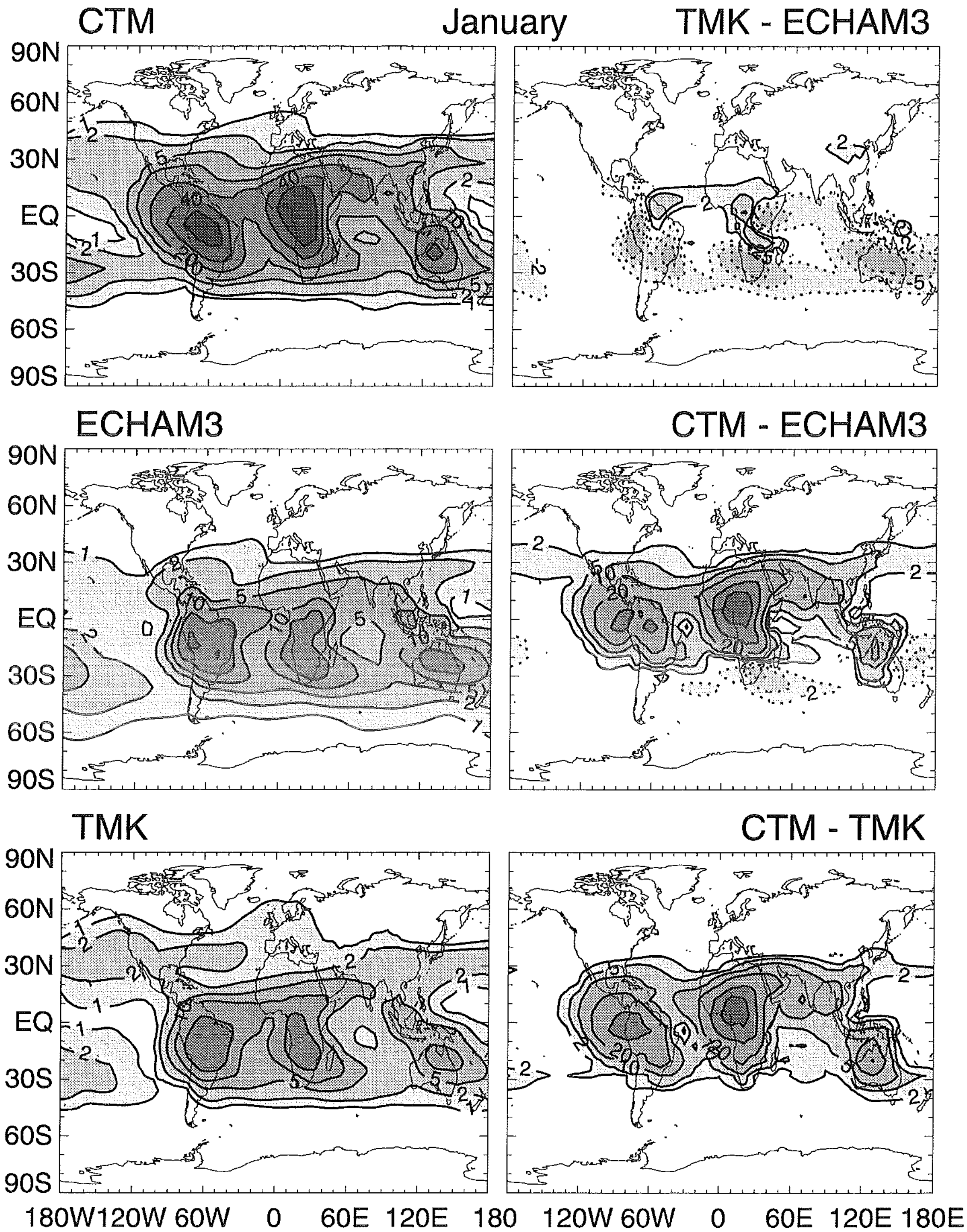

Figure 4.3: Left panels: January monthly mean values of the equivalent ^{222}Rn concentration, $\overline{a_{\mathrm{Rn}}}^{m}$, calculated by the different models at the 200 hPa level. Contours are displayed at 1, 2, 5, 10, 20, 40, and 60 pCi/SCM.
Right panels: Differences of the ^{222}Rn distributions shown in the left panels from each other. Contours are displayed at ±2, ±5, ±10, ±20, ±40, and ±60 pCi/SCM, solid for positive differences and dotted for negative ones.

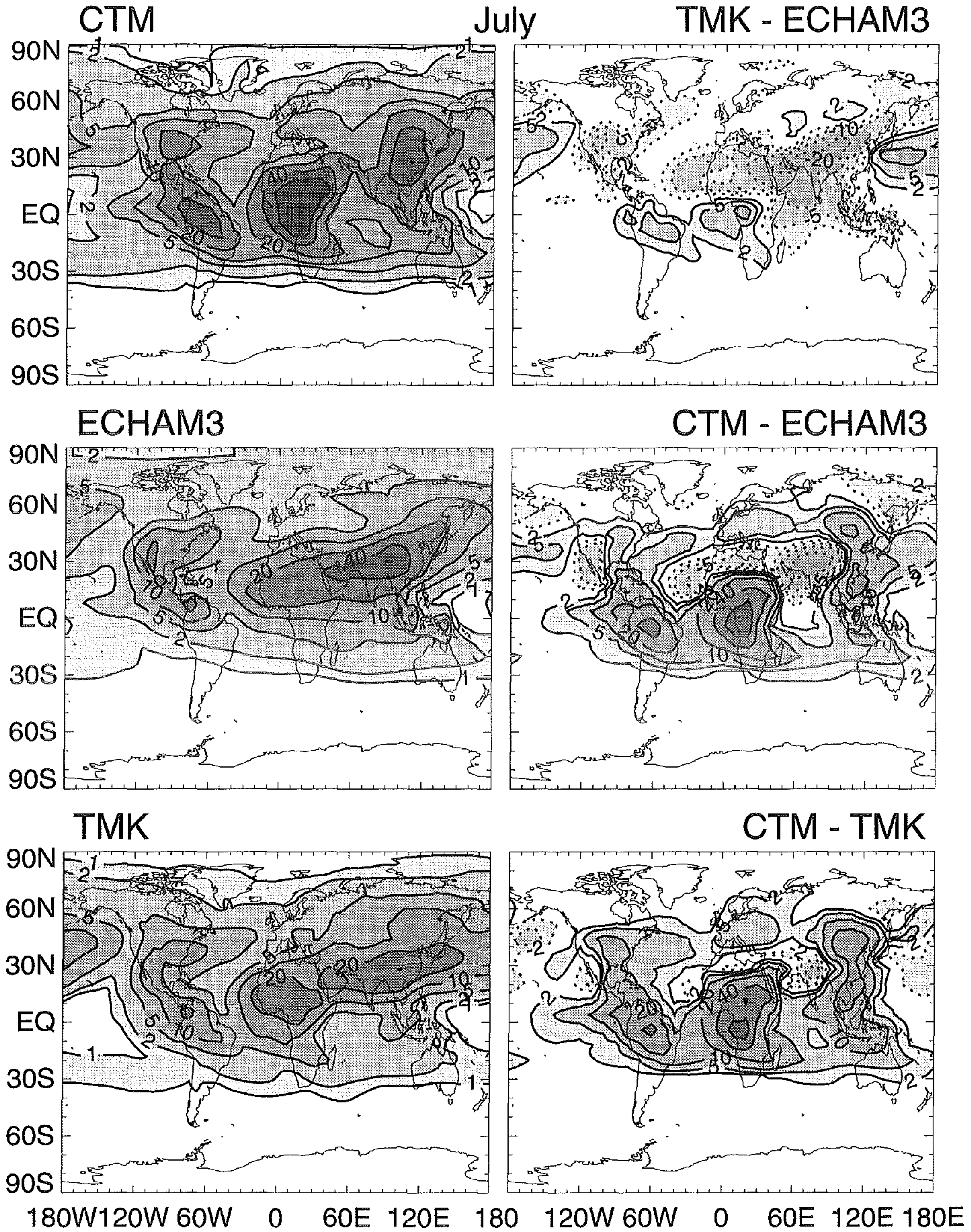

Figure 4.4: Left panels: July monthly mean values of the equivalent ^{222}Rn concentration, $\overline{a_{\mathrm{Rn}}}^{m}$, calculated by the different models at the 200 hPa level. Contours are displayed at 1, 2, 5, 10, 20, 40, and 60 pCi/SCM.
Right panels: Differences of the ^{222}Rn distributions shown in the left panels from each other. Contours are displayed at ±2, ±5, ±10, ±20, ±40, and ±60 pCi/SCM, solid for positive differences and dotted for negative ones.

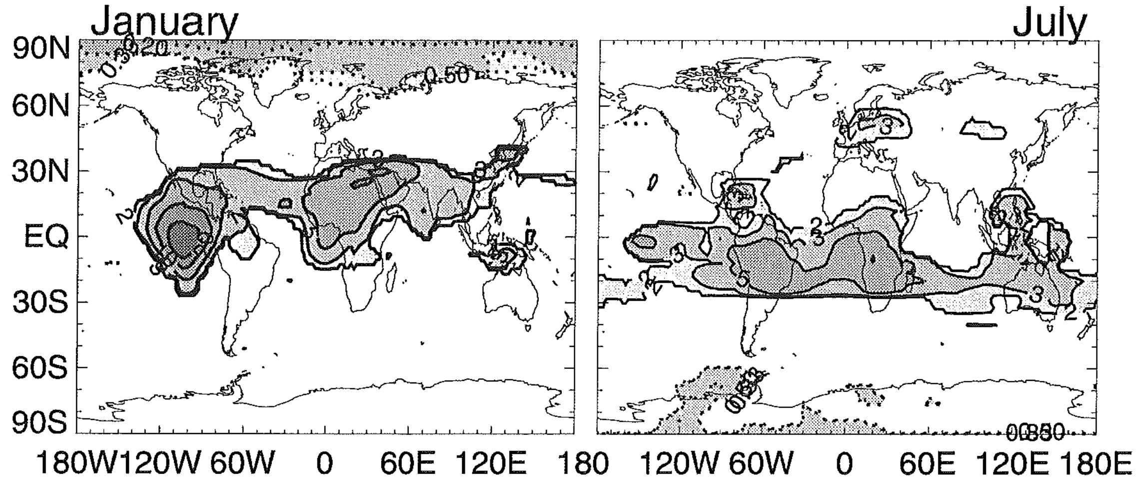

Figure 4.5: Ratio $r_{\mathrm{Rn}} = \overline{a_{\mathrm{Rn_C}}}^m/0.5(\overline{a_{\mathrm{Rn_E}}}^m+\overline{a_{\mathrm{Rn_T}}}^m)$ at the 200 hPa level. Only those regions are shaded grey, where both $\overline{a_{\mathrm{Rn_E}}}^m$ and $\overline{a_{\mathrm{Rn_T}}}^m$ separately differ from $\overline{a_{\mathrm{Rn_C}}}^m$ by more than a factor of 2. Solid contours are given at 2, 3, 5, 10, and 20, negative ones at 0.2, 0.333, and 0.5.

The difference $\overline{a_{\mathrm{Rn_T}}}^m$-$\overline{a_{\mathrm{Rn_E}}}^m$ is much smaller when compared to both $\overline{a_{\mathrm{Rn_C}}}^m$-$\overline{a_{\mathrm{Rn_E}}}^m$ and $\overline{a_{\mathrm{Rn_C}}}^m$-$\overline{a_{\mathrm{Rn_T}}}^m$, by about an order of magnitude at the location of the tropical maxima. Because of this smallness of the former difference, the panels of the latter two look similar with respect to position, spatial extent, and amplitudes of the maxima. The main reason for the large deviation of $\overline{a_{\mathrm{Rn_C}}}^m$ from both $\overline{a_{\mathrm{Rn_E}}}^m$ and $\overline{a_{\mathrm{Rn_T}}}^m$ is the convection parametrization of the CTM as discussed below.

For July, corresponding values of $\overline{a_{\mathrm{Rn}}}^m$ are shown in Figure 4.4. During this month, the upper tropospheric ^{222}Rn distributions are significantly asymmetric with respect to the equator. This is the case since in summer soil temperatures of more than 0°C are reached even at northern high latitudes, where then ^{222}Rn is emitted. Like in the tropics, this ^{222}Rn reaches the upper troposphere mainly via deep convection, which at high northern latitudes also is stronger in summer than it is in winter.

In the tropics, the results of the comparison shown in Figure 4.4 resemble those obtained for January. Again the tropical maxima of $\overline{a_{\mathrm{Rn_C}}}^m$ are more than a factor of 2 higher than the corresponding maxima of $\overline{a_{\mathrm{Rn_E}}}^m$ and $\overline{a_{\mathrm{Rn_T}}}^m$ and occur closer to the equator than in ECHAM3 or TMK. Over the Himalaya and southern China, however, all three models disagree considerably from each other. The amplitudes of $\overline{a_{\mathrm{Rn_C}}}^m$ are comparable to those of $\overline{a_{\mathrm{Rn_E}}}^m$ in this region, but the structure of the two tracer distributions is different. Instead of a band of enhanced values of $\overline{a_{\mathrm{Rn}}}^m$ extending from the western tip of Africa over the Arabian peninsula to Japan, the CTM produces two almost disjunct maxima, one over central Africa and the other over western China. The band probably is more realistic as July cloud cover observations or monthly mean global precipitation maps indicate [*Rossow*, 1993; *Jaeger*, 1976]. This is consistent with the note of *Hansen et al.* [1983] that in July the northward extent of the cloud cover over India is less in the GISS GCM than in corresponding observations.

At northern mid-latitudes, two additional local centres of strong convection occur in July in the CTM: the eastern part of the United States and central Europe. From there, ^{222}Rn-rich air lifted from the lower troposphere is transported downwind by the strong westerlies. This horizontal transport occurs rapidly enough for the downwind plumes to form a band of enhanced values of $\overline{a_{\mathrm{Rn}}}^m$. In the other two models, regions of enhanced convection activity at mid-latitudes are less localized and, hence, this band is much less distinct there.

Figure 4.5 shows the ratio $r_{\mathrm{Rn}} \equiv \overline{a_{\mathrm{Rn}^{\mathrm{C}}}}^{m}/0.5(\overline{a_{\mathrm{Rn}^{\mathrm{E}}}}^{m}+\overline{a_{\mathrm{Rn}^{\mathrm{T}}}}^{m})$ at the 200 hPa level for January and July. Purpose of this figure is to make those regions more clearly visible where $\overline{a_{\mathrm{Rn}^{\mathrm{C}}}}^{m}$ deviates by a factor of 2 or more from both $\overline{a_{\mathrm{Rn}^{\mathrm{E}}}}^{m}$ and $\overline{a_{\mathrm{Rn}^{\mathrm{T}}}}^{m}$. Smaller deviations are considered to indicate good agreement between the three models. Differences of that order of magnitude are expected since the models are driven by rather different meteorological input data. Moreover, the models are optimized with respect to their actual aims which are as different as episode studies or climate experiments, but not with respect to ^{222}Rn distributions.

The most important feature of Figure 4.5 is that r_{Rn} is larger than 2 approximately between the equator and 30° latitude of the winter hemisphere during both January and July. Thus, in this region the amounts of ^{222}Rn which reach the upper troposphere are substantially larger in the CTM than they are in the TMK or in ECHAM3. The symmetry of the two panels of Figure 4.5 with respect to the equator arises since in each of the three models the poleward shift of the maxima of deep convection is comparable during January and July, but is significantly less in the CTM than in the other two models.

In January, r_{Rn} is larger than 20 off the western coast of central America. Reason for this large value is the overestimate of the equatorial easterlies in the CTM together with the overestimate of the absolute value of $\overline{a_{\mathrm{Rn}}}^{m}$ at that altitude, as discussed above. In addition to the tropics, small patches where r_{Rn} is larger than 2 in July also occur over central Europe and over Siberia.

The small values of r_{Rn} over the poles probably are a consequence of how cross-polar transport is treated in the CTM. This feature is of little importance for the present study because the mixing ratios of the tracers considered here are expected to be low over the poles and, in addition, the poles are not within the main focus of interest.

Zonal Mean ^{222}Rn Distributions

The left panels of Figure 4.6 show the zonally averaged monthly mean January equivalent ^{222}Rn concentrations, $\langle\overline{a_{\mathrm{Rn}}}^{m}\rangle_{\lambda}$, calculated by the three models. Again, the absolute differences for each pair of models are included in the right panels of this figure. In all three models $\langle\overline{a_{\mathrm{Rn}}}^{m}\rangle_{\lambda}$ is at least 5 pCi/SCM between about 30°S and 45°N. Furthermore, the models agree quite well both in the absolute values of $\langle\overline{a_{\mathrm{Rn}}}^{m}\rangle_{\lambda}$ and in its meridional gradients at higher latitudes. There, the tropospheric ^{222}Rn content is almost independent of height because of the lack of a surface source. Close to the Earth's surface, the a_{Rn} is expected to be different in the three models due to their different resolution. A resolution effect occurs since the mean height of orography within a certain model grid box depends on the size of that box. Consequently, the same also is true for the exact vertical position of the ^{222}Rn source in the corresponding model.

The main discrepancy between the three models is the structure of the vertical profiles of $\langle\overline{a_{\mathrm{Rn}}}^{m}\rangle_{\lambda}$ within the region of enhanced concentrations. In the TMK, $\langle\overline{a_{\mathrm{Rn}}}^{m}\rangle_{\lambda}$ decreases monotonically with height whereby the decrease rate is lowest in the latitude belts of highest convection activity at 15°S and 30°N. In ECHAM3, the lower tropospheric decrease of $\langle\overline{a_{\mathrm{Rn}}}^{m}\rangle_{\lambda}$ with height is faster by about a factor of 2 than in the TMK. However, $\langle\overline{a_{\mathrm{Rn}^{\mathrm{E}}}}^{m}\rangle_{\lambda}$ shows a secondary maximum centred at 200 hPa and 20°S and reaching a peak value of 15 pCi/SCM. Such a maximum exists for $\langle\overline{a_{\mathrm{Rn}^{\mathrm{C}}}}^{m}\rangle_{\lambda}$ as well, but at 5°S and with an amplitude of almost 25 pCi/SCM. In the lower troposphere, $\langle\overline{a_{\mathrm{Rn}^{\mathrm{C}}}}^{m}\rangle_{\lambda}$ is significantly lower than $\langle\overline{a_{\mathrm{Rn}^{\mathrm{E}}}}^{m}\rangle_{\lambda}$ or $\langle\overline{a_{\mathrm{Rn}^{\mathrm{T}}}}^{m}\rangle_{\lambda}$. The structure of the CTM's vertical profiles with relatively high values of $\langle\overline{a_{\mathrm{Rn}}}^{m}\rangle_{\lambda}$ close to the Earth's surface and in the upper troposphere intersected by significantly lower values at mid-tropospheric levels often is called "C-like" or "C-shaped" [e.g., *Ehhalt et al.*, 1992].

Dominant feature of the zonal mean differences $\langle\overline{a_{\mathrm{Rn}^{\mathrm{C}}}}^{m} - \overline{a_{\mathrm{Rn}^{\mathrm{E}}}}^{m}\rangle_{\lambda}$ and $\langle\overline{a_{\mathrm{Rn}^{\mathrm{C}}}}^{m} - \overline{a_{\mathrm{Rn}^{\mathrm{T}}}}^{m}\rangle_{\lambda}$ are the large positive values, up to 15 pCi/SCM over the equator, which reflect the strong upper tropospheric maximum in the CTM. Origin of this large discrepancy is most likely the simple adjustment by which convection is parametrized in the CTM. Since this scheme includes neither entrainment nor downdrafts, too much air from the cloud base reaches the cloud top. In the tropics this means that too much air from the PBL is pumped directly into the upper troposphere. Missing entrainment and detrainment close to the cloud base

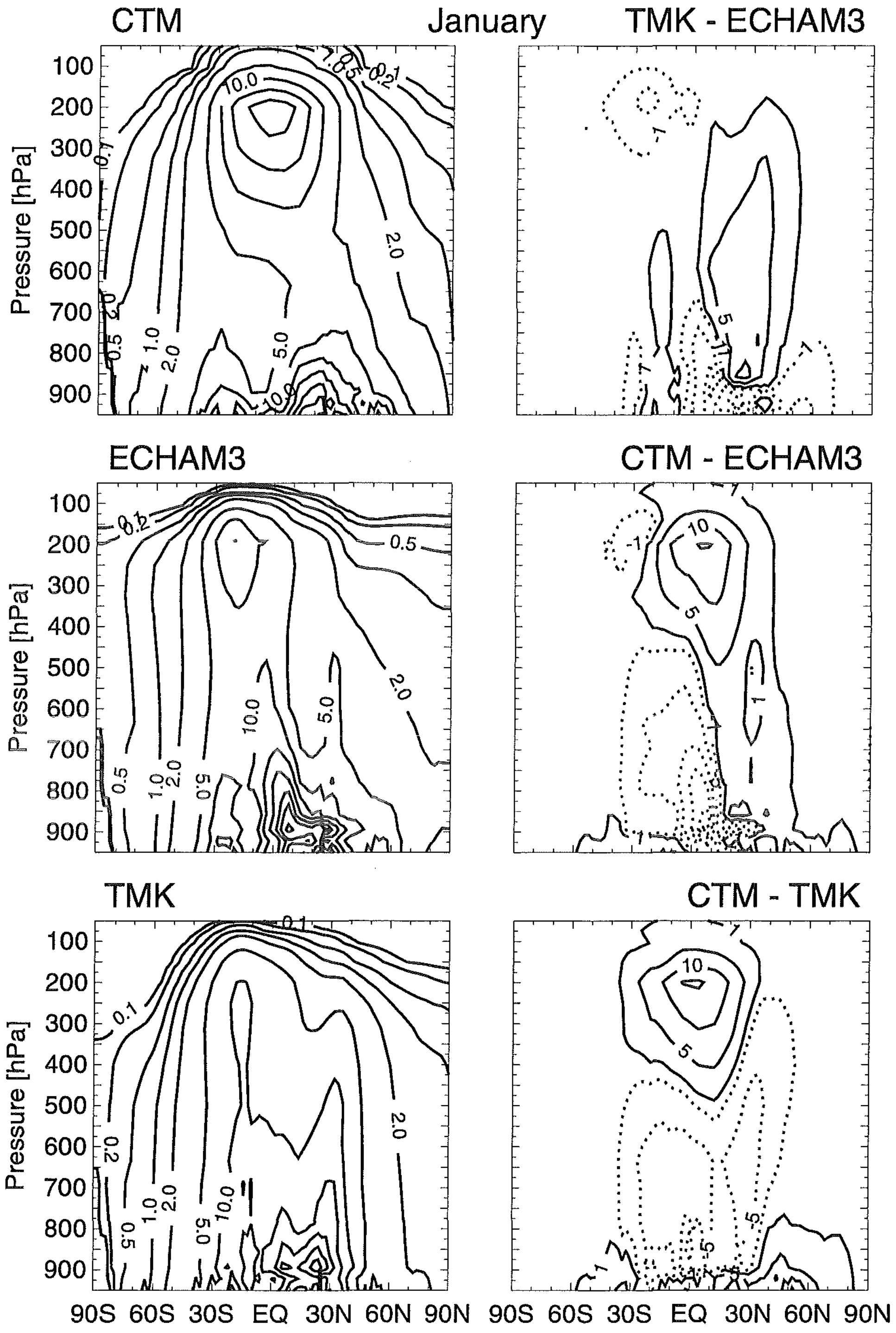

Figure 4.6: Left panels: January monthly mean values of the zonally averaged ^{222}Rn concentrations, $\langle\overline{a_{\mathrm{Rn}}}^{m}\rangle_{\lambda}$, calculated by the different models. Contours are displayed at 0.1, 0.2, 0.5, 1, 2, 5, 10, 15, 20, 25, 30, 40, 50, and 60 pCi/SCM.
Right panels: Differences of the ^{222}Rn distributions shown in the left panels from each other. Contours are displayed at ±1, ±5, ±10, ±15, ±20, ±25, and ±30 pCi/SCM, solid for positive differences and dotted for negative ones.

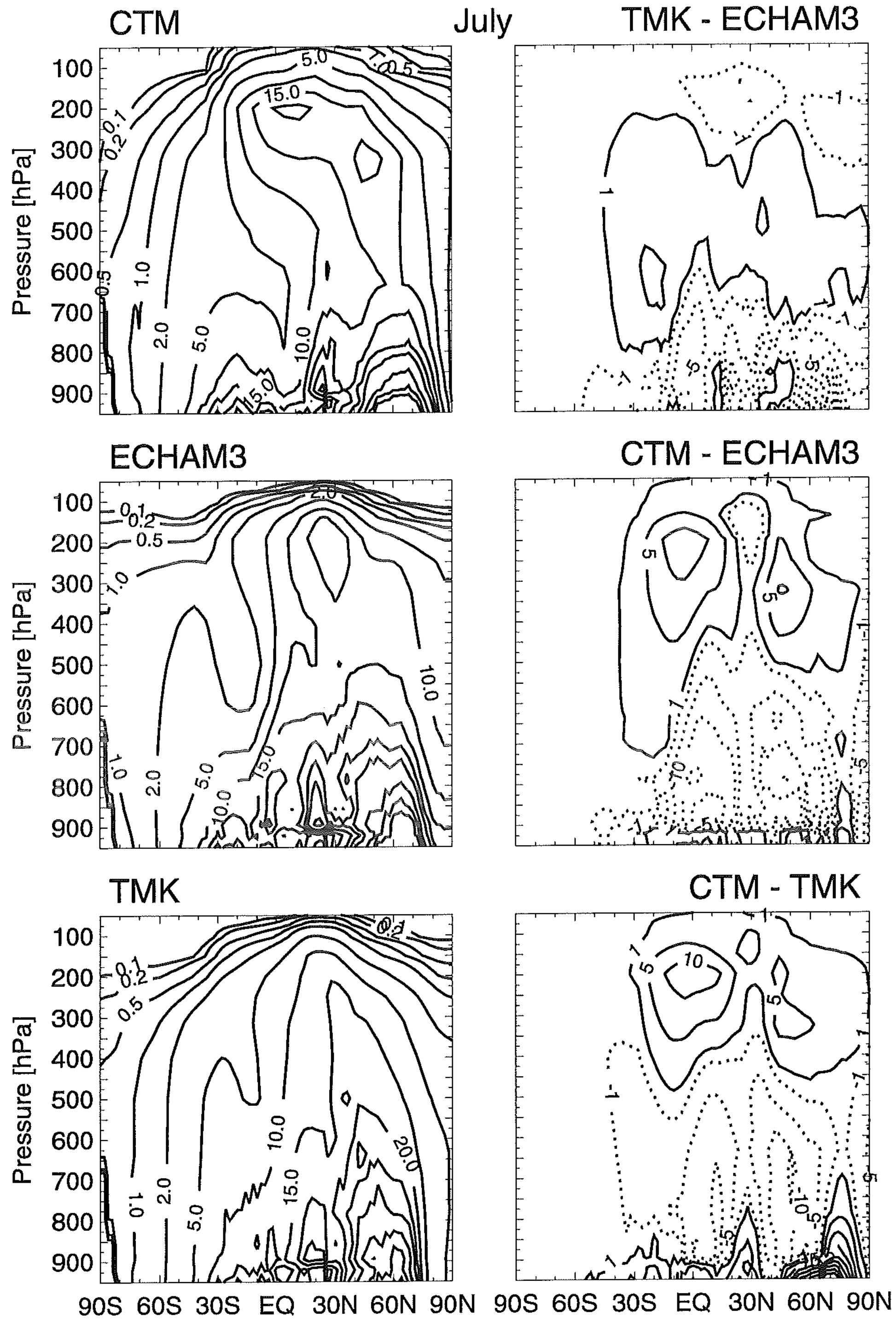

Figure 4.7: Left panels: July monthly mean values of the zonally averaged ^{222}Rn concentrations, $\langle \overline{a_{\mathrm{Rn}}}^{m} \rangle_{\lambda}$, calculated by the different models. Contours are displayed at 0.1, 0.2, 0.5, 1, 2, 5, 10, 15, 20, 25, 30, 40, 50, and 60 pCi/SCM.

Right panels: Differences of the ^{222}Rn distributions shown in the left panels from each other. Contours are displayed at ±1, ±5, ±10, ±15, ±20, ±25, and ±30 pCi/SCM, solid for positive differences and dotted for negative ones.

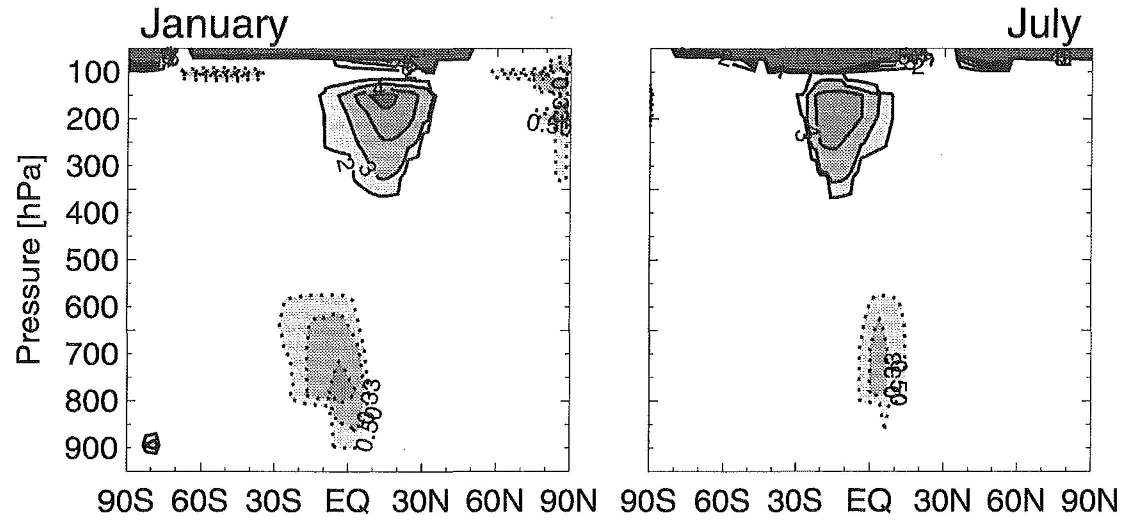

Figure 4.8: Zonal mean of the ratio $r_{\mathrm{Rn}} = \overline{a_{\mathrm{Rn^C}}}^{m}/0.5(\overline{a_{\mathrm{Rn^E}}}^{m}+\overline{a_{\mathrm{Rn^T}}}^{m})$. Only those regions are shaded grey, where both $\langle\overline{a_{\mathrm{Rn^E}}}^{m}\rangle_{\lambda}$ and $\langle\overline{a_{\mathrm{Rn^T}}}^{m}\rangle_{\lambda}$ separately differ from $\langle\overline{a_{\mathrm{Rn^C}}}^{m}\rangle_{\lambda}$ by more than a factor of 2. Solid contours are given at 2, 3, 4, and 5, negative ones at 0.25, 0.333, and 0.5.

also causes $\langle\overline{a_{\mathrm{Rn^C}}}^{m}\rangle_{\lambda}$ to be smaller than $\langle\overline{a_{\mathrm{Rn^E}}}^{m}\rangle_{\lambda}$ and $\langle\overline{a_{\mathrm{Rn^T}}}^{m}\rangle_{\lambda}$ by at least 5 pCi/SCM below the upper tropospheric maximum. Differences of similar magnitude occur at about 30°N as well. There, they are a result of the relatively high values of $\langle\overline{a_{\mathrm{Rn^T}}}^{m}\rangle_{\lambda}$ above the Himalaya, which neither are present in the CTM nor in ECHAM3. These high values of $\langle\overline{a_{\mathrm{Rn^T}}}^{m}\rangle_{\lambda}$ also explain most of the difference between $\langle\overline{a_{\mathrm{Rn^E}}}^{m}\rangle_{\lambda}$ and $\langle\overline{a_{\mathrm{Rn^T}}}^{m}\rangle_{\lambda}$. The rest of this difference is caused by the nearly absence of mid-level convection over India and southeastern Asia in ECHAM3.

Corresponding values of $\langle\overline{a_{\mathrm{Rn}}}^{m}\rangle_{\lambda}$ for July are shown in Figure 4.7. During this month, the region where $\langle\overline{a_{\mathrm{Rn}}}^{m}\rangle_{\lambda}$ exceed 5 pCi/SCM is shifted well into the northern hemisphere in all three models. Because of the larger source area available, $\langle\overline{a_{\mathrm{Rn}}}^{m}\rangle_{\lambda}$ generally is higher than in January, but the structure of the vertical profiles in the individual models keeps the same: monotonically decreasing in the TMK, faster decreasing in the lower troposphere and with a secondary maximum in the outer tropics in ECHAM3, and a strong upper tropospheric maximum centered at the inner tropics in the CTM. In the latter model there is a second upper tropospheric maximum centered at 45°N and 350 hPa. This corresponds with the band of enhanced values of $\langle\overline{a_{\mathrm{Rn}}}^{m}\rangle_{\lambda}$ discussed in the context of Figure 4.4. The reason why at 600 hPa the largest values of $\langle\overline{a_{\mathrm{Rn^C}}}^{m}\rangle_{\lambda}$ occur as high north as 60°N simply is the fact that the zonal mean land fraction reaches its maximum at that latitude.

In July, the difference $\langle\overline{a_{\mathrm{Rn^T}}}^{m} - \overline{a_{\mathrm{Rn^E}}}^{m}\rangle_{\lambda}$ is negligible, whereas strength and structure of $\langle\overline{a_{\mathrm{Rn^C}}}^{m} - \overline{a_{\mathrm{Rn^E}}}^{m}\rangle_{\lambda}$ and $\langle\overline{a_{\mathrm{Rn^C}}}^{m} - \overline{a_{\mathrm{Rn^T}}}^{m}\rangle_{\lambda}$ in the tropics are similar to January conditions. In addition, however, in July there is a second feature of the same structure and almost the same strength which occurs associated with the second upper tropospheric maximum of $\overline{a_{\mathrm{Rn^C}}}^{m}$ centered at 45°N.

Figure 4.8 shows the regions where the zonally averaged monthly mean values of r_{Rn} are less than 0.5 or larger than 2. Again, r_{Rn} is defined as $\overline{a_{\mathrm{Rn^C}}}^{m}/0.5(\overline{a_{\mathrm{Rn^E}}}^{m}+\overline{a_{\mathrm{Rn^T}}}^{m})$. These regions are the upper troposphere between 30° latitude of the winter hemisphere and the equator, and the lower troposphere in the tropics of the summer hemisphere. Although $\langle\overline{a_{\mathrm{Rn^C}}}^{m} - \overline{a_{\mathrm{Rn^E}}}^{m}\rangle_{\lambda}$ and $\langle\overline{a_{\mathrm{Rn^C}}}^{m} - \overline{a_{\mathrm{Rn^T}}}^{m}\rangle_{\lambda}$ are comparatively large at northern mid-latitudes during July, this region does not occur in the right panel of Figure 4.8. This is the case since $\langle \overline{a_{\mathrm{Rn}}}^{m} \rangle_\lambda$ itself is large in all three models and, hence r_{Rn} is close to 1. However, large values of r_{Rn} do occur in the stratosphere. They are caused mainly by convection events in the CTM which overshoot into the stratosphere and inject $^{222}\mathrm{Rn}$ there directly. For $\mathrm{NO_X}$, this effect is of little importance since NO is formed also directly at that altitudes.

4.4.3 Discussion

Comparisons with both observed vertical $^{222}\mathrm{Rn}$ profiles and with $^{222}\mathrm{Rn}$ distributions calculated by the models ECHAM3 and TMK show that the CTM gives realistic distributions of this short-living tracer at mid- and high latitudes. Only at northern mid-latitudes in summer, the upper tropospheric equivalent $^{222}\mathrm{Rn}$ concentrations probably are overestimated and the lower tropospheric ones are underestimated. Because the tropospheric lifetime of $\mathrm{NO_X}$ is similar to the lifetime of $^{222}\mathrm{Rn}$, the same should also hold for the calculated distributions of $\mathrm{NO_X}$ emitted in the lowest part of the troposphere.

In the tropics, reliable $^{222}\mathrm{Rn}$ measurements are not available. However, the model comparison reveals that there are large differences between the upper tropospheric equivalent $^{222}\mathrm{Rn}$ concentrations calculated by the CTM on the one hand and by ECHAM3 and TMK on the other hand. The structure of these differences is like at northern mid-latitudes in summer. This structure leads to the assumption that the main origin of these differences is the convective adjustment scheme used in the CTM to parametrize deep wet convection. This scheme neither includes entrainment and detrainment nor downdrafts, but simply injects a certain fraction of the air contained in the lowest grid box involved in convection directly into the uppermost grid box of the model cloud. The upward mass flux is balanced by uniform subsidence anywhere else in the grid column. Such subsidence of ambient air may not be confused with downdrafts which act on air parcels within the cloud.

One could argue that convective adjustment is a simpler parametrization of convective processes than it are the two different Tiedtke scheme implemented in ECHAM3 and TMK, respectively, but that it nevertheless reproduces the main features of observed tracer transport within clouds. This hypothesis neither can be proved nor disproved by comparison with observations, because reliable data for such a comparison are too scarce. However, there are several arguments which indicate that convective adjustment oversimplifies convective processes and lifts too large amount of tracer to the upper troposphere on the cost of the tracer concentration at lower and mid-tropospheric levels.

A first hint pointing into that direction was obtained from the comparison with $^{222}\mathrm{Rn}$ profiles observed during summer on continental sites at northern mid-latitudes (see right panel of Figure 4.2). Furthermore, clouds in the real world are entraining, and deep cumulus convection is in particular. If entrainment is neglected in a cloud model, i.e. if rising convective parcels are assumed not to mix with ambient air along their path upwards on a wet adiabat, then the cloud top height is overestimated. This is the case when the ambient air mixed in is unsaturated, which it usually is, because then some of the liquid water in the rising parcel must be evaporated to maintain saturation. This evaporative cooling caused by entrainment reduces the buoyancy of the convective parcel and, hence, the height of convection [for details see, e.g., *Holton*, 1979, p. 337].

Mahowald et al. [1995] implemented seven state-of-the-art moist convective parametrization schemes in the same column model in order to find out the most suitable one for a three-dimensional chemical tracer model. The Tiedtke schemes of ECHAM3 and TM2 are included in these tests, the convective adjustment of the CTM it is not. Three data sets of observations are used for a comparison with the model results: the averaged $^{222}\mathrm{Rn}$ profiles observed at northern mid-latitudes during summer [*Liu et al.*, 1984], the height of tropical oceanic convection observed during the Central Equatorial Pacific Experiment [*Wang et al.*, 1995], and the transport of the trace gas CO during a 6-hour period in tropical continental convection during the Amazon Boundary Layer Experiment 2A [*Garstang et al.*, 1988; *Pickering et al.*, 1992]. Although these tests are not sufficient to draw final conclusions, they indicate that the Tiedtke scheme used in ECHAM3 yields the most realistic results of all convection schemes investigated.

Finally, there is the fact the convective adjustment scheme in the GISS GCM has been replaced meanwhile by a more complex scheme which produces substantially smaller ^{222}Rn distributions in the tropical upper troposphere [*DelGenio and Yao*, 1992; *Rind and Lerner*, 1996].

Attempts to modify the convection scheme version of the CTM used for this study have been given up at an early stage. The upper tropospheric tracer concentrations do decrease if simply the fraction of mass involved in convection is reduced, but this causes a reduction of the tracer concentrations in the lower and mid-troposphere as well. Thus, the improvement in the upper troposphere is associated with even worse results at lower levels. Moreover, this way of correcting tracer profiles is based on empirical try and error tests rather than physical considerations.

Implementation of a modified, complete convection scheme would be the better alternative to improve vertical tracer profiles in the CTM. However, then the entire set of input data has to be replaced in order to avoid inconsistencies with the wind, pressure, and temperature fields. This requires support from the owners of a general circulation model but is in principle possible. Such a change is straightforward if just the resolution is increased. In the present case the largest immediate improvement probably could be achieved by increasing the vertical resolution. The input data presently used are averaged from a calculation on a grid with resolution of $4^\circ \times 5^\circ$ which is is comparable to the grid sizes applied in the ECHAM3 and TMK calculations discussed above. However, further improvement is possible if the horizontal resolution also is increased, as the ^{222}Rn distributions of *Heimann et al.* [1990] and *Balkanski and Jacob* [1990] show. The grid used in the latter, more realistic calculation is four times finer than that of the former, while transport processes are parametrized similarly in the two models.

The most promising, but most manpower consuming way to improve tracer transport in the CTM is to implement a convection scheme which is not based on simple convective adjustment. Then, however, additional difficulties arise since both the number and the type of the input parameters has to be changed by which the convection parametrization is driven. In this case the code of the general circulation model also has to be changed in order to provide these new set of input parameters. Such changes will be necessary for future investigations, but are beyond the scope of the present study.

Chapter 5

Results of the Model Calculation

This chapter shows results of CTM runs carried out for the chemically active tracers NO_X and HNO_3 and based on the parametrizations described in Chapters 2 and 3. Because of the linearity of the chemistry scheme used, the local chemical lifetimes of NO_X and HNO_3 do not depend on the local tracer concentration. As a consequence, the total tracer distributions may be generated by linear superposition of the six fields calculated individually for the individual sources. This ability of superposition is the most important advantage of the linear chemistry scheme. It allows a very simple separation of a total mixing ratio into the contributions from the individual sources, an option that would require considerable effort in a nonlinear chemistry scheme.

The results presented in the following either are gained from daily mean tracer mixing ratios stored in a run including all sources or from monthly mean tracer mixing ratios stored in six separate runs, each for one of the six sources. For most runs a spin-up time of 1 year is sufficient to reach a quasi steady state where the distributions of NO_X and HNO_3 are repeated in the next year. However, runs including the stratospheric source require a spin-up time of 4 years because of the slow transport times in σ-layers 8 and 9.

Section 5.1 gives an overview of the global, total distribution of NO_X calculated by the CTM. Summer and winter conditions are represented by monthly mean mixing ratios for January and July, respectively. Distributions of HNO_3 are discussed in Section 5.2 and the relation between NO and NO_X is analyzed in Section 5.3. In Section 5.4, the absolute and relative zonal mean contributions of the individual sources are presented. Finally, in Section 5.5, the calculated NO_X distributions are discussed in the context of the results of Chapter 4.

5.1 Global Distributions of NO_X

Figure 5.1 shows maps of the monthly mean NO_X mixing ratios, $\overline{\mu_{NOx}}^m$, calculated by the CTM for the lower PBL as well as for the middle and the upper troposphere in January. Corresponding maps of $\overline{\mu_{NOx}}^m$ for July are given in Figure 5.2. The values presented at the pressure levels 200 and 500 hPa are obtained by interpolation due to the second order moments scheme [*Prather*, 1986]. At high latitudes, the 200 hPa level reaches into the lower stratosphere (cf. Figure 5.3 below).

5.1.1 Lower PBL: The Lowest Model Layer

The highest tropospheric values of $\overline{\mu_{NOx}}^m$ occur in the lowest model layer. Particularly large values are reached over the eastern part of North America and over central Europe, where the peak emissions of the strongest source of NO_X, fossil fuel combustion, occur. In January, maximum values of 5-10 ppbv are obtained for $\overline{\mu_{NOx}}^m$ in these regions. In July, when upward transport by convection is stronger and the

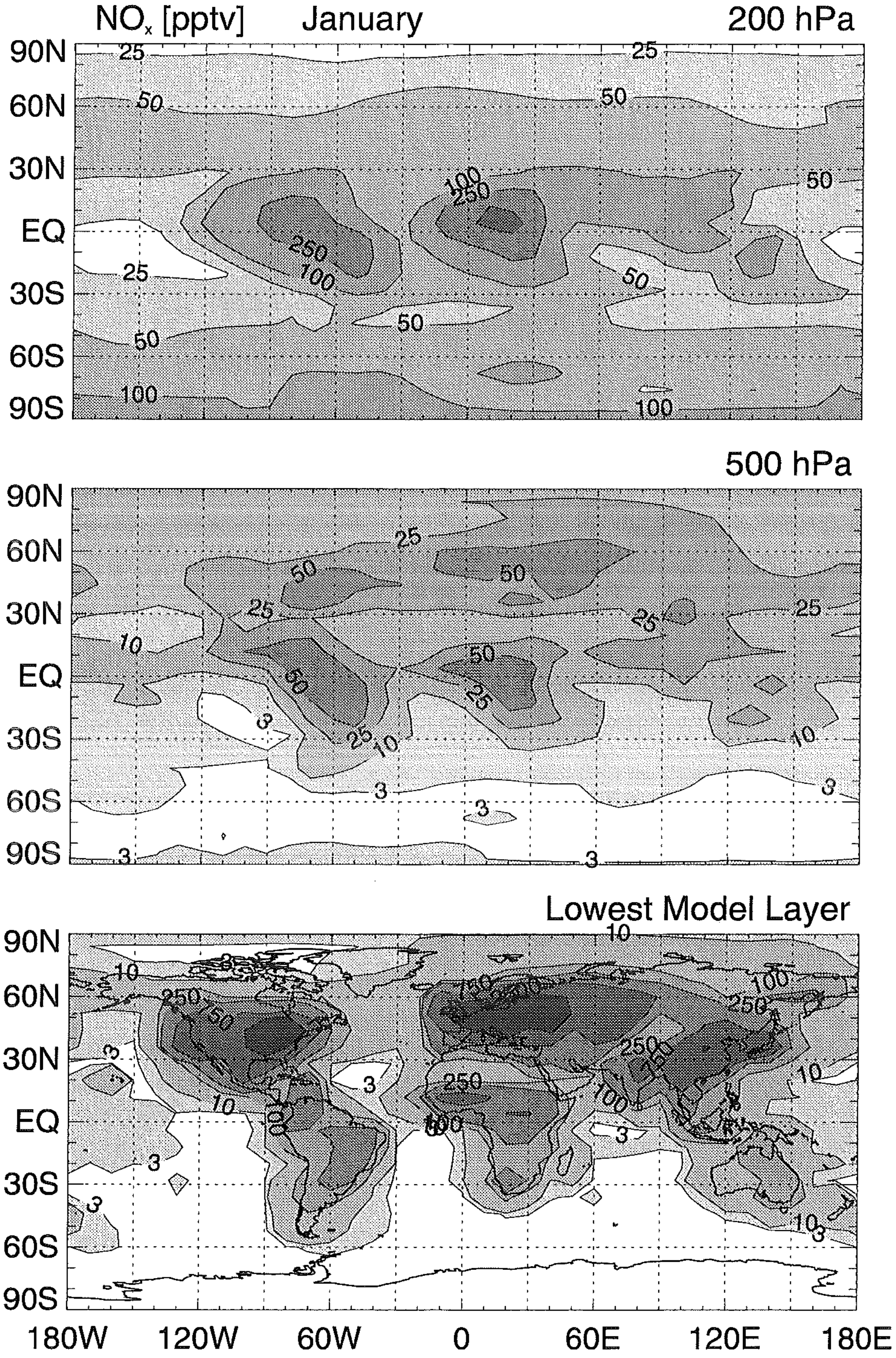

$\mathrm{NO_x}$ [pptv] January 200 hPa

500 hPa

Lowest Model Layer

Figure 5.1: January monthly mean distributions of $\mathrm{NO_X}$ mixing ratios, $\overline{\mu_{\mathrm{NOx}}}^{m}$, calculated with all sources included: (upper panel) 200 hPa level with contours at 25, 50, 100, 250, and 500 pptv, (middle panel) 500 hPa level with contours at 3, 10, 25, 50, and 100 pptv, and (lower panel) the lowest model layer with contours at 3, 10, 100, 250, 750, and 2500 pptv.

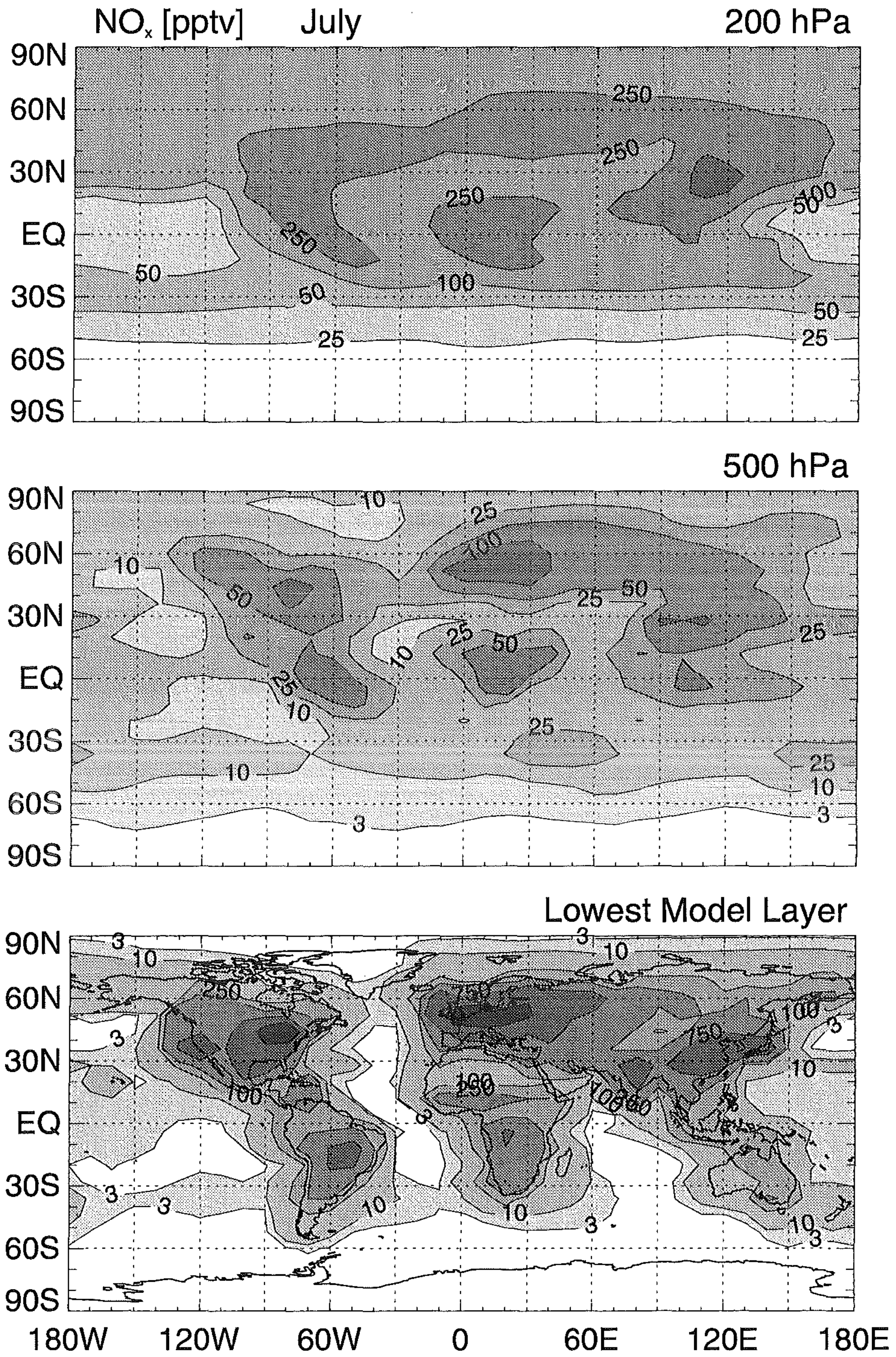

Figure 5.2: July monthly mean distributions of NO_X mixing ratios, $\overline{\mu_{NOx}}^m$, calculated with all sources included: (upper panel) 200 hPa level with contours at 25, 50, 100, 250, and 500 pptv, (middle panel) 500 hPa level with contours at 3, 10, 25, 50, and 100 pptv, and (lower panel) the lowest model layer with contours at 3, 10, 100, 250, 750, and 2500 pptv.

photochemical conversion of $\mathrm{NO_X}$ into $\mathrm{HNO_3}$ is faster than in winter, the corresponding peaks of $\overline{\mu_{\mathrm{NOx}}}^{m}$ are 3-5 ppbv. A second region where $\overline{\mu_{\mathrm{NOx}}}^{m}$ is high extends from the Indian subcontinent over the western part of China to Japan. In January, $\overline{\mu_{\mathrm{NOx}}}^{m}$ there reaches 1-2 ppbv and up to 1.5 ppbv in July. Values of $\overline{\mu_{\mathrm{NOx}}}^{m}$ around 1 ppbv also occur over western Africa in January and over Brazil and a small region in central Africa in July. At most other continental regions, $\overline{\mu_{\mathrm{NOx}}}^{m}$ ranges between 100 and 500 pptv during both January and July. Only in remote areas like Alaska or the Sahara desert, values of $\overline{\mu_{\mathrm{NOx}}}^{m}$ as small as 10 pptv are found in the continental PBL.

The contours of $\overline{\mu_{\mathrm{NOx}}}^{m}$ shown in the lower panels of Figures 5.1 and 5.2 closely follow the outline of the continents. In addition, the patterns for the lowest model layer are quite similar to that of the surface sources. This similarity is caused by the comparatively short lifetime of $\mathrm{NO_X}$, τ_{NOx}, in the PBL. At mid-latitudes, τ_{NOx} is about 10 hours in summer and more than 1 day in winter. Within times of that order of magnitude, horizontal advection typically carries $\mathrm{NO_X}$ over distances of less than 1000 km. Thus, most of the $\mathrm{NO_X}$ emitted at the Earth's surface is converted to $\mathrm{HNO_3}$ before it passes horizontally through more than 2 grid boxes. Because of the short lifetime in the PBL, $\mathrm{NO_X}$ reaches its lowest levels of less than 1 pptv also in the lowest model layer. Altogether, the total range of $\mathrm{NO_X}$ mixing ratios calculated for σ-layer 1 spans more than 5 orders of magnitude.

5.1.2 Middle Troposphere: The 500 hPa Level

At 500 hPa, mixing ratios $\overline{\mu_{\mathrm{NOx}}}^{m}$ higher than 50 pptv are obtained over the main surface sources at northern mid-latitudes and, in addition, over the tropical continents, as the middle panels of Figures 5.1 and 5.2 show. In the former region, upward transport of polluted air from lower levels is the main reason for the relatively high $\mathrm{NO_X}$ mixing ratios, whereas in the latter, most of the $\mathrm{NO_X}$ comes from in-situ production by lightning discharges. Over tropical continents, the enhanced values of $\overline{\mu_{\mathrm{NOx}}}^{m}$ show only slight variation with season both in their amplitude and in location. At the same altitude in northern mid-latitudes, the amplitude of the local continental maximum of $\overline{\mu_{\mathrm{NOx}}}^{m}$ is about a factor of 2 lower in January than it is in July. The reason for this difference is the annual cycle of the convection activity. For the same reason the area where $\overline{\mu_{\mathrm{NOx}}}^{m}$ is larger than 50 pptv also is much larger in summer than it is in winter. The region where $\overline{\mu_{\mathrm{NOx}}}^{m}$ is less than 3 pptv is confined almost completely to latitudes south of 60°S both in January and in July.

Comparison of the middle panels of Figures 5.1 and 5.2 with the lower ones shows that at 500 hPa the patterns of $\overline{\mu_{\mathrm{NOx}}}^{m}$ are much smoother than that of the lowest model layer. One reason for this is the chemical lifetime of $\mathrm{NO_X}$ which at 500 hPa is 20-30 hours in the tropics and in the summer hemisphere at mid-latitudes. At mid-latitudes in winter, τ_{NOx} is about 4 days. Another reason why at 500 hPa the zonal gradients of $\overline{\mu_{\mathrm{NOx}}}^{m}$ are weaker are the zonal wind speeds which are higher there than near the surface. The main surface source regions at continental mid-latitudes, however, still are clearly visible, both in the January and in the July contour maps. It is emphasized that $\overline{\mu_{\mathrm{NOx}}}^{m}$ is 1-2 orders of magnitudes lower there at 500 hPa than in the lowest model layer. Over the tropical continents, $\overline{\mu_{\mathrm{NOx}}}^{m}$ is a factor of 5-10 lower at 500 hPa than in the lowest model layer. In summary, the range of $\overline{\mu_{\mathrm{NOx}}}^{m}$ calculated for the 500 hPa level is 1-150 pptv, which is much narrower than the corresponding range in the lowest model layer.

5.1.3 Upper Troposphere: The 200 hPa Level

The upper panels of Figures 5.1 and 5.2 show that $\overline{\mu_{\mathrm{NOx}}}^{m}$ has only weak zonal gradients at 200 hPa in mid-latitudes. There, the zonal wind speeds even are faster than at 500 hPa. In the tropical upper troposphere, the continents are outlined mainly by direct injection of $\mathrm{NO_X}$ from lightning discharges. Contrary to January when the belt of elevated values of $\overline{\mu_{\mathrm{NOx}}}^{m}$ is limited to the tropics, in July it extends well into the northern hemisphere. There, it merges with the plumes of the main surface source regions. Because of the underestimate of the upper tropospheric zonal wind speeds at low latitudes in summer, the gradients in the corresponding $\mathrm{NO_X}$ distribution, the upper panel of Figure 5.2, probably still are slightly too weak (see p. 44).

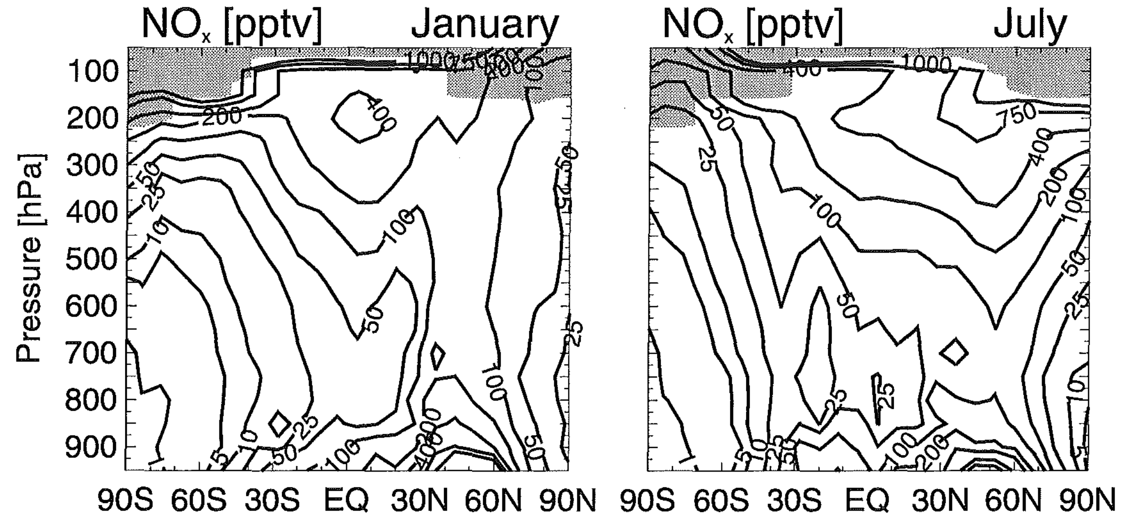

Figure 5.3: Zonally averaged monthly mean values of the NO_X mixing ratio calculated with all sources included: (left panel) January and (right panel) July. Contours are displayed at 1, 5, 10, 25, 50, 100, 200, 400, 750, and 1000 pptv. Stratospheric regions are shaded grey.

In general, the values of $\overline{\mu_{\mathrm{NO_X}}}^{m}$ shown in the upper panels of Figures 5.1 and 5.2 are higher than those of the 500 hPa level, up to a factor of 5 above the major source regions. This is a consequence of several factors. First, at 200 hPa only the low and mid-latitudes are part of the upper troposphere. The polar regions belong to the stratosphere and should not be compared directly with the levels below. Second, the upper troposphere is accessed directly by the sources lightning discharges, stratospheric input, aircraft emissions in northern mid-latitudes, and input by fast vertical transport from surface sources during summer to a much larger degree than the middle troposphere. Finally, the chemical lifetime of NO_X is larger at 200 hPa than at 500 hPa, partly because the ratio NO/NO_2 increases with height and partly because the OH mixing ratio decreases above its maximum which occurs between 800 and 600 hPa.

Above the winter hemispheric poles, $\overline{\mu_{\mathrm{NO_X}}}^{m}$ is very low. This is a result of the lacking daylight during the polar night, which inhibits HNO_3 to get photolyzed into NO_X (Reaction (2.6). This reaction, however, is the only chemical source of NO_X in the stratosphere.

5.1.4 Zonally Averaged NO_X Distributions

To provide a better feeling for the vertical structure of the global distribution of NO_X, Figure 5.3 shows the zonally averaged monthly mean total NO_X mixing ratio, $\langle \overline{\mu_{\mathrm{NO_X}}}^{m} \rangle_{\lambda}$, for January and July. In addition, this figure gives the zonally averaged altitude of the tropopause for the two months. The most important features of Figure 5.3 during both January and July are the significant difference between northern hemispheric and southern hemispheric values of $\langle \overline{\mu_{\mathrm{NO_X}}}^{m} \rangle_{\lambda}$ in the lower free troposphere as well as the increase of $\langle \overline{\mu_{\mathrm{NO_X}}}^{m} \rangle_{\lambda}$ with altitude above the PBL. In January, the highest upper tropospheric values of $\langle \overline{\mu_{\mathrm{NO_X}}}^{m} \rangle_{\lambda}$ occur in the tropics, whereas they peak at northern mid-latitudes in July. These features have been mentioned in the context of Figures 5.1 and 5.2 already, but are visible here more clearly.

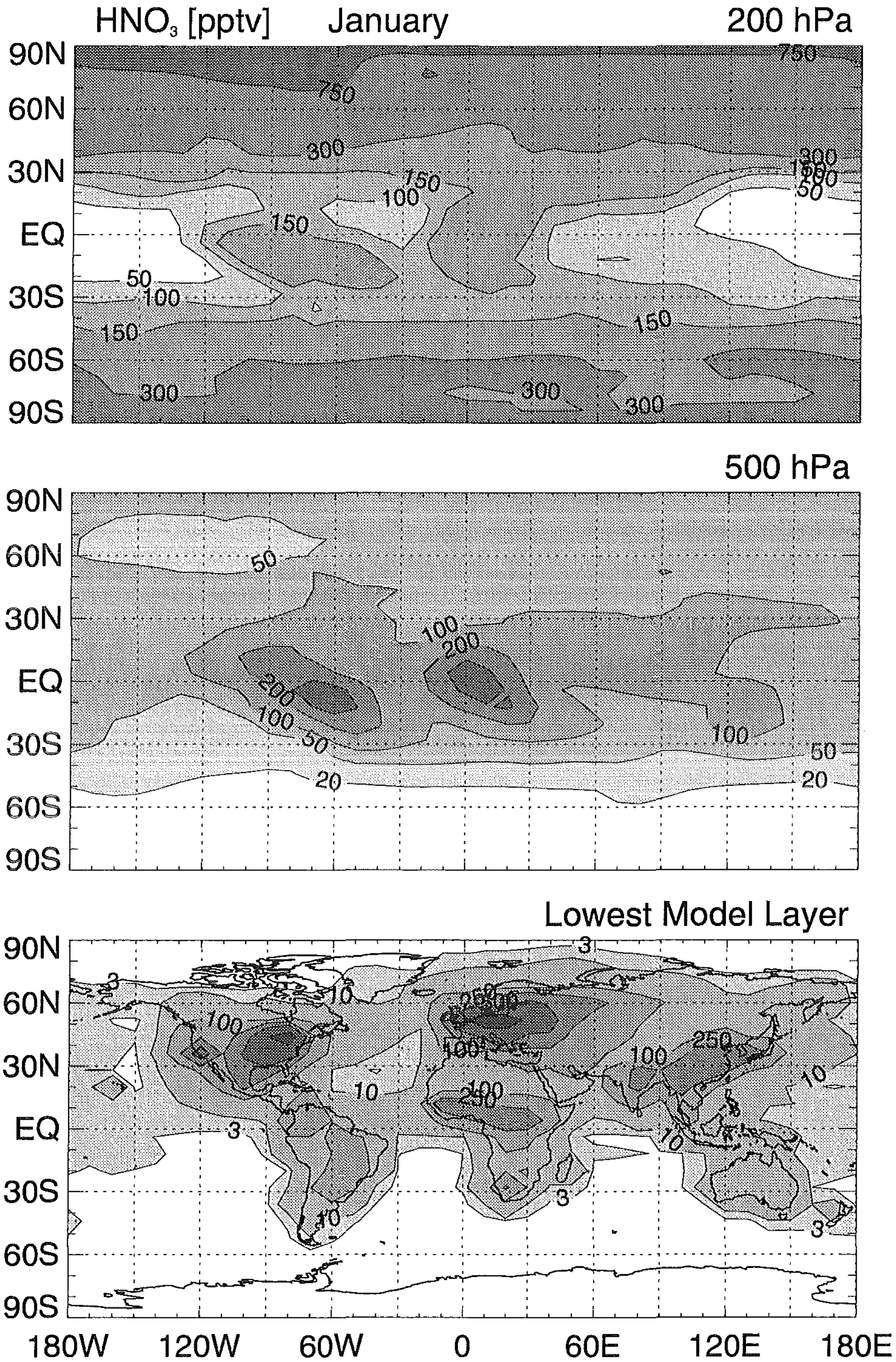

Figure 5.4: January monthly mean distributions of HNO_3 mixing ratios, $\overline{\mu_{HNO_3}}^m$, calculated with all sources included: (upper panel) 200 hPa level with contours at 50, 100, 150, 300, and 750 pptv, (middle panel) 500 hPa level with contours at 20, 50, 100, 200, and 300 pptv, and (lower panel) the lowest model layer with contours at 3, 10, 100, 250, 500, and 1000 pptv.

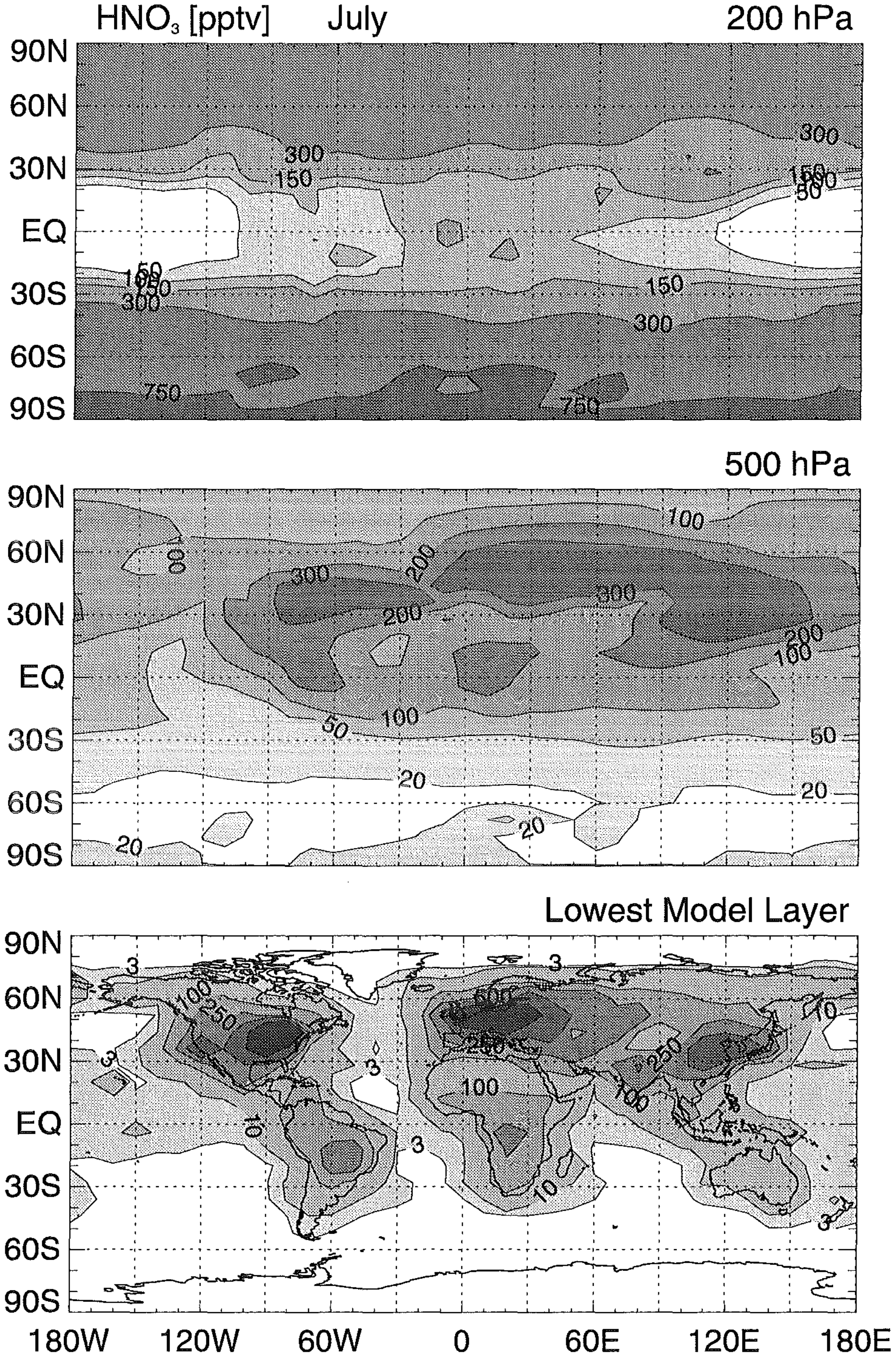

Figure 5.5: July monthly mean distributions of HNO$_3$ mixing ratios, $\overline{\mu_{\mathrm{HNO_3}}}^m$, calculated with all sources included: (upper panel) 200 hPa level with contours at 50, 100, 150, 300, and 750 pptv, (middle panel) 500 hPa level with contours at 20, 50, 100, 200, and 300 pptv, and (lower panel) the lowest model layer with contours at 3, 10, 100, 250, 500, and 1000 pptv.

5.2 Global Distributions of HNO_3

With the present simplified chemistry scheme, the tracer called HNO_3 bears only limited resemblance to the atmospheric molecule HNO_3 [*Ehhalt et al.*, 1992]. Monthly mean January and July HNO_3 mixing ratios, $\overline{\mu_{HNO_3}}^m$, are given in Figures 5.4 and 5.5 for completeness, but have to be considered as less realistic than those of NO_X. Nevertheless they are expected to show the salient features of atmospheric HNO_3. In absolute terms, μ_{HNO_3} probably is overestimated since in the atmosphere NO_Y is partitioned in a number of additional molecules, such as PAN, NO_3^--aerosol etc., which in the CTM all are summarized by a single tracer called HNO_3.

In the lowest model layer HNO_3 has a short lifetime, about 1 day, due to dry deposition and rainout. Since this lifetime is comparable to τ_{NO_X}, the contours of $\overline{\mu_{HNO_3}}^m$ near the surface closely follow the outlines of the continents also. Peak values of $\overline{\mu_{HNO_3}}^m$ are up to 1.5 ppbv in January and up to 3 ppbv in July, respectively.

At 500 hPa, the lifetime of HNO_3 is just below 10 days, mainly determined by rainout. Owing to this longer lifetime and, to a lesser extent, to the continued production of HNO_3 from NO_X, the zonal gradients of $\overline{\mu_{HNO_3}}^m$ are much weaker than that of $\overline{\mu_{NO_X}}^m$. The same is true at the 200 hPa level also. Within the troposphere, $\overline{\mu_{HNO_3}}^m$ decreases monotonically with altitude. The high stratospheric values of $\overline{\mu_{HNO_3}}^m$ are a consequence of the in-situ production of HNO_3 at that altitudes. In addition, there is no chemical sink of stratospheric HNO_3 during the polar night when Reaction (2.6) is suppressed.

5.3 The Ratio NO/NO_X

Contrary to the mixing ratio of HNO_3, which in the CTM is an individual tracer with its own chemical source and sink processes, the mixing ratio of the species NO, μ_{NO}, is a diagnostic variable. The concentration of NO, [NO], is determined locally by a combination of Reactions (2.9) and (2.10) giving [NO] as a function of the photolysis rate J_{NO_2} and the concentrations $[NO_X]$ and $[O_3]$:

$$[NO] = \frac{J_{NO_2}}{k_{O_3}[O_3] + J_{NO_2}}[NO_X] , \qquad (5.1)$$

where k_{O_3} is the rate coefficient of Reaction (2.9). Because both $[O_3]$ and J_{NO_2} are zonal mean values in the present study, the discussion of the ratio μ_{NO}/μ_{NO_X} is restricted to zonal mean values also. Locally, $\langle \mu_{NO}/\mu_{NO_X} \rangle_\lambda$ may deviate slightly from μ_{NO}/μ_{NO_X} due to the temperature dependence of k_{O_3}. However, this deviation is much smaller than the latitudinal and altitudinal variation of k_{O_3}. It is emphasized that the ratio μ_{NO}/μ_{NO_X} is determined exclusively by the assumptions made on $[O_3]$ and on J_{NO_2} since any feedback of $[NO_X]$ on $[O_3]$ is suppressed in the chemistry scheme used here.

The upper panels of Figure 5.6 show the zonally averaged monthly mean NO mixing ratio, $\langle \overline{\mu_{NO}}^m \rangle_\lambda$, calculated for January and July, whereas the lower panels of this figure give the corresponding ratios $r_{NO} \equiv \langle \overline{\mu_{NO}/\mu_{NO_X}}^m \rangle_\lambda$. For completeness, horizontal monthly mean distributions of NO are shown in Appendix A.

In the lower free troposphere in January, the inter-hemispheric gradient of $\langle \overline{\mu_{NO}}^m \rangle_\lambda$ is not as strong as it is for $\langle \overline{\mu_{NO_X}}^m \rangle_\lambda$. The main reason for this is the seasonal variation of J_{NO_2}. In January, r_{NO} is about 0.45 at 45°S and a pressure of 700 hPa, but only 0.2 at the same pressure and 45°N. In July, $k_{O_3}[O_3]$ and J_{NO_2} counteract in a way that r_{NO} is almost constant with latitude between 45°S and 60°N. Consequently, the structure of the distributions $\langle \overline{\mu_{NO}}^m \rangle_\lambda$ and $\langle \overline{\mu_{NO_X}}^m \rangle_\lambda$ is almost identical within this latitudes belt.

In the troposphere, both the rate coefficient k_{O_3} and $[O_3]$ decrease with increasing height. Since in addition J_{NO_2} increases with height, the same also is true for the ratio r_{NO}. In the tropical upper troposphere, r_{NO} is higher than 0.7 in January and higher than 0.8 in July. Towards the winter hemispheric pole, r_{NO} drops rapidly and almost independent of altitude, as does J_{NO_2}. In the upper troposphere, the gradients of $\langle \overline{\mu_{NO}}^m \rangle_\lambda$ therefore are even stronger than they are for $\langle \overline{\mu_{NO_X}}^m \rangle_\lambda$. In the stratosphere, where O_3 mixing

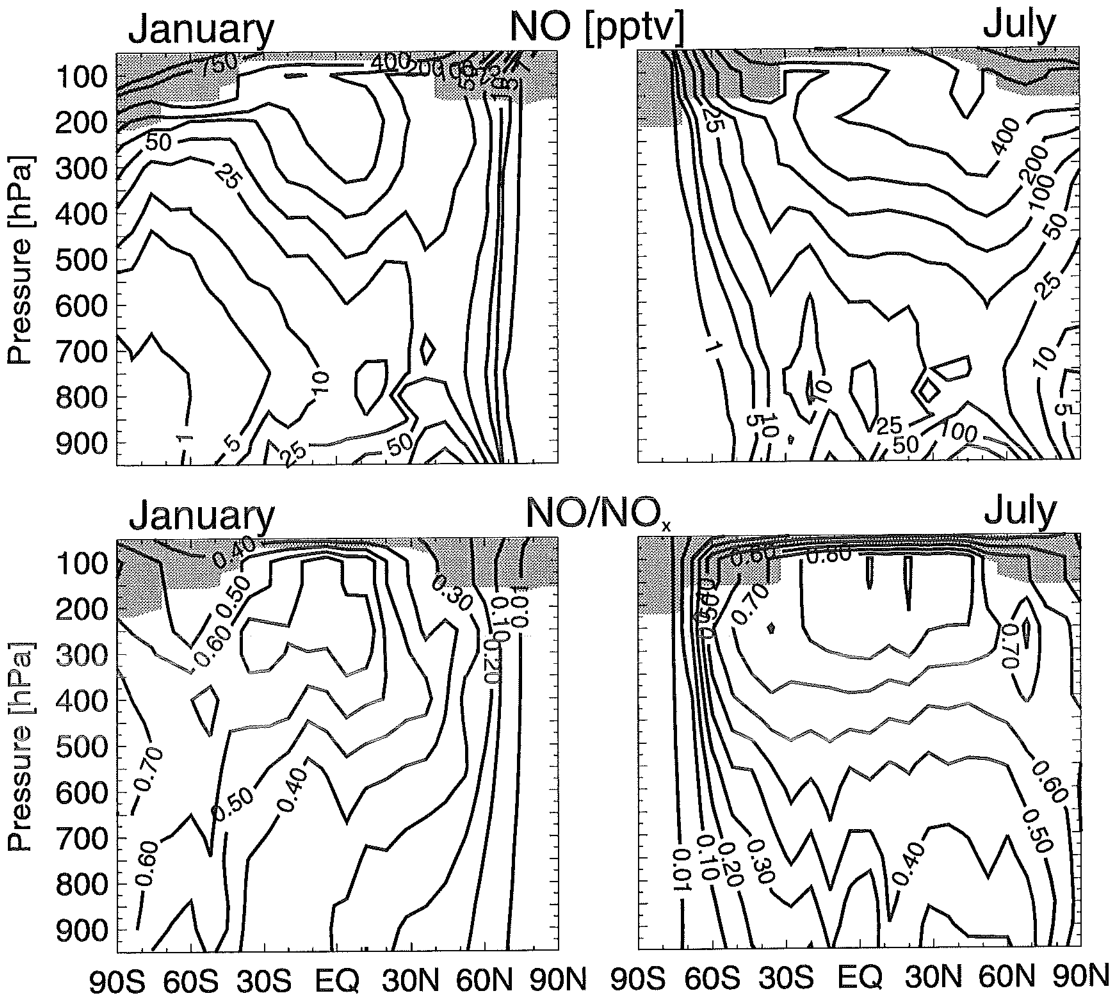

Figure 5.6: Upper panels: Zonal and monthly mean NO mixing ratio, $\langle\overline{\mathrm{NO}}^{m}\rangle_{\lambda}$, calculated with all sources included and contours at 1, 5, 10, 25, 50, 100, 200, 400, 750, and 1000 pptv.
Lower panels: corresponding ratio $r_{\mathrm{NO}} = \langle\overline{\mu_{\mathrm{NO}}/\mu_{\mathrm{NOx}}}^{m}\rangle_{\lambda}$ with contours at 0.01, 0.1, 0.2, 0.3, 0.4, 0.5, 0.6, 0.7, 0.8, 0.9.
Left panels are January values, right panels are July values. Stratospheric regions are shaded grey.

ratios on the order of ppm are reached, r_{NO} decreases with height. However, because of the simplicity of the present stratospheric chemistry scheme, the NO mixing ratios calculated for this part of the atmosphere are associated with quite large uncertainties.

The terms $J_{\mathrm{NO_2}}$, $[\mathrm{O_3}]$, and $[\mathrm{NO_X}]$ on the right-hand side of Equation (5.1) describe daily mean values, $\overline{J_{\mathrm{NO_2}}}^{d}$, $[\overline{\mathrm{O_3}}^{d}]$, and $[\overline{\mathrm{NO_X}}^{d}]$.Hence, [NO] on the left-hand side of this equation is an approximated daily mean value. The exact value of $[\overline{\mathrm{NO}}^{d}]$ is obtained when the diurnal cycles of $J_{\mathrm{NO_2}}$, $\mathrm{O_3}$, and $\mathrm{NO_X}$ are included in Equation (5.1) before its temporal average is calculated. However, these diurnal cycles are not available in the present version of the CTM.

The following estimate of the error, ϵ, can be made which is made by deriving the approximated daily mean value of [NO] from Equation (5.1) instead of the true one: First it is noted that the diurnal cycles of $k_{\mathrm{O_3}}[\mathrm{O_3}]$ and of $[\mathrm{NO_X}]$ are much weaker than the diurnal cycle of $J_{\mathrm{NO_2}}$. Hence, their contribution to ϵ can be neglected. Then $[\mathrm{NO}] = [\mathrm{NO}](J_{\mathrm{NO_2}}, \overline{k_{\mathrm{O_3}}[\mathrm{O_3}]}^{d}, [\overline{\mathrm{NO_X}}^{d}])$ is expanded around the point $\overline{J_{\mathrm{NO_2}}}^{d}$:

$$
\begin{aligned}
[\mathrm{NO}](J_{\mathrm{NO_2}}, \cdots) &= [\mathrm{NO}](J_{\mathrm{NO_2}}, \cdots) + \left.\frac{\partial\, [\mathrm{NO}]\left(\overline{J_{\mathrm{NO_2}}}^{d}, \cdots\right)}{\partial J_{\mathrm{NO_2}}}\right|_{\overline{J_{\mathrm{NO_2}}}^{d}} \left(J_{\mathrm{NO_2}} - \overline{J_{\mathrm{NO_2}}}^{d}\right) \\
&+ \mathcal{O}\left(\left(J_{\mathrm{NO_2}} - \overline{J_{\mathrm{NO_2}}}^{d}\right)^2\right) \\
&\approx [\mathrm{NO}]\left(\overline{J_{\mathrm{NO_2}}}^{d}, \cdots\right) + \frac{\overline{k_{\mathrm{O_3}}[\mathrm{O_3}]}^{d}\,[\overline{\mathrm{NO_X}}^{d}]}{\left(\overline{k_{\mathrm{O_3}}[\mathrm{O_3}]}^{d} + \overline{J_{\mathrm{NO_2}}}^{d}\right)^2} \left(J_{\mathrm{NO_2}} - \overline{J_{\mathrm{NO_2}}}^{d}\right) , \qquad (5.2)
\end{aligned}
$$

where the last term defines ϵ. During the night, when $J_{\mathrm{NO_2}} = 0$, the true value of $[\overline{\mathrm{NO}}^{d}]$ is overestimated by approximately $\epsilon = -(\overline{k_{\mathrm{O_3}}[\mathrm{O_3}]}^{d}\,[\overline{\mathrm{NO_X}}^{d}]\,\overline{J_{\mathrm{NO_2}}}^{d})/(\overline{k_{\mathrm{O_3}}[\mathrm{O_3}]}^{d} + \overline{J_{\mathrm{NO_2}}}^{d})^2$. At noon, when $J_{\mathrm{NO_2}} \gtrsim 2\,\overline{J_{\mathrm{NO_2}}}^{d}$, $[\overline{\mathrm{NO}}^{d}]$ is overestimated by about the same amount. In the upper troposphere, typical values of $\overline{k_{\mathrm{O_3}}[\mathrm{O_3}]}^{d}$ and $\overline{J_{\mathrm{NO_2}}}^{d}$ are $1 \times 10^{-3}\ \mathrm{s^{-1}}$ and $5 \times 10^{-3}\ \mathrm{s^{-1}}$, respectively (see Figures 2.8 and 2.10, $k_{\mathrm{O_3}} = 2.3 \times 10^{-12} \exp(-1450 K/T)\ \mathrm{cm^3\ molecules^{-1}\ s^{-1}}$) giving $\epsilon = 0.14\,[\overline{\mathrm{NO_X}}^{d}]$. With $\overline{k_{\mathrm{O_3}}[\mathrm{O_3}]}^{d} = 1 \times 10^{-2}\ \mathrm{s^{-1}}$ and $\overline{J_{\mathrm{NO_2}}}^{d} = 1 \times 10^{-3}\ \mathrm{s^{-1}}$ for mid-latitudinal conditions in the lower troposphere, $\epsilon \approx 0.08\,[\overline{\mathrm{NO_X}}^{d}]$ is obtained.

5.4 Contributions from the Individual Sources

The following discussion of the contributions from the individual sources to the total burden of tropospheric $\mathrm{NO_X}$ is restricted to zonal mean values. The dominant features of the distribution are maintained thereby. In general, the $\mathrm{NO_X}$ mixing ratios, $\mu_{\mathrm{NO_X}}$, depend much more on latitude and altitude than on longitude. Only within the PBL zonal gradients of $\mu_{\mathrm{NO_X}}$ also are substantial. There, however, the chemical lifetime of $\mathrm{NO_X}$ is short and wind speeds are low. Hence, the composition of the total $\mathrm{NO_X}$ content in the PBL is similar to the contributions from the individual sources to the total surface source. For completeness, longitude by latitude maps of the contributions from the individual sources are given in Appendix B for January and July, each for the lowest model layer, the 500 hPa level, and the 200 hPa level.

Figures 5.7 and 5.8 present the zonal mean $\mathrm{NO_X}$ distributions resulting from the individual sources for January and July. The six panels of each figure total up to the contours given in Figure 5.3. Because of the linearity of model's chemistry scheme, scaling up in the strength of one of the six sources results in a corresponding scale up in the $\mathrm{NO_X}$ contribution shown in Figures 5.7 and 5.8. In this way these figures can be used to construct zonal mean distributions of $\mu_{\mathrm{NO_X}}$ for other estimates of the global source strengths, as long as the geographical patterns of the individual sources stay the same. This is a useful feature considering the uncertainties associated with the global emission rates of the individual sources.

All six sources reach mixing ratios μ_{NO_X} of several tens of pptv at least locally and, hence, make a significant contribution to the tropospheric burden of this tracer. Above the PBL, all sources make their largest contributions to μ_{NO_X} in the upper troposphere. How much the CTM's upper tropospheric tracer composition is affected by convective transport of polluted air from the continental PBL is most obvious in the patterns of NO_X emitted by soil microbial activity and biomass burning, respectively.

Instead of deriving the answer of the question which source makes the largest contribution at which part of the atmosphere and during which season from Figures 5.7 and 5.8, it is easier to consider the relative contributions of the individual sources directly. For January and July, they are obtained by dividing the mixing ratios shown in the individual panels of Figures 5.7 and 5.8 by those of Figure 5.3. The result are six panels for each month which total up to 100% and which are given in Figures 5.9 and 5.10.

5.4.1 Fossil Fuel Combustion

In the PBL, the tracer distribution is dominated by the distribution of the surface sources, fossil fuel combustion in particular. At northern mid-latitudes in January, this source contributes more than 60% to μ_{NO_X} within the entire troposphere up to 500 hPa and at high latitudes even up to 300 hPa. In July, the relative importance of fossil fuel combustion in that region is somewhat lower because of in-situ production of NO_X by lightning discharges, but it still is the dominant source by far. In the upper troposphere at northern mid-latitudes, the contribution of fossil fuel combustion reaches a second maximum of more than 50% in summer. Owing to the lack of other sources, fossil fuel combustion also is the dominant source in the lower troposphere at southern mid-latitudes.

5.4.2 Soil Microbial Activity and Biomass Burning

Emissions due to microbial activity in soils are the dominant contribution of μ_{NO_X} in the tropical, continental PBL of the summer hemisphere, whereas biomass burning makes the largest contribution there in the winter hemisphere. Both these sources provide about 70-80% of μ_{NO_X} in the lowest model layer in central Africa. Further, this source reaches fractions of more than 50% in equatorial South America, northern Australia, and, only in July, in India. In Brazil, biomass burning contributes well above 50% of the NO within the PBL during January. In July, such relative contributions occur in the sparsely populated regions of Alaska, Northern Canada and Siberia. Like the main source regions of fossil fuel combustion, those of soil microbial activity and biomass burning are associated with relative maxima in the upper troposphere. In fact, more than 20% of the total NO_X present in the tropics at a pressure of about 200 hPa are emitted by these two surface sources.

5.4.3 Lightning Discharges

Emissions by lightning discharges dominate the NO_X distribution in the tropical free troposphere. On average, the zonal mean fractional contribution of this source reaches a maximum of more than 80% near the equator throughout the year. The location of this maximum is shifted seasonally by about 10° into the summer hemisphere. In addition, lightning discharges reach zonal mean relative contributions larger than 50% at mid-latitudes during southern winter. This secondary maximum arises due to the enhanced lightning activity around 40°S during this season (see, e.g., Figure 3.8) and the lack of other sources. Since convective clouds occasionally overshoot into the stratosphere, lightning discharges can act as a source of NO above the tropopause also. Remote from continental source regions, most of the NO_X near the surface also originates in lightning discharges. Their contribution to the total NO_X near the surface is higher than 75% over large parts of the the tropical Pacific and, locally, even higher than 95%. Contributions of more than 75% are reached by lightning discharges in January over the western part of the tropical Atlantic and in July off the American east coast. Over the eastern part of the tropical Atlantic, lightning discharges are less

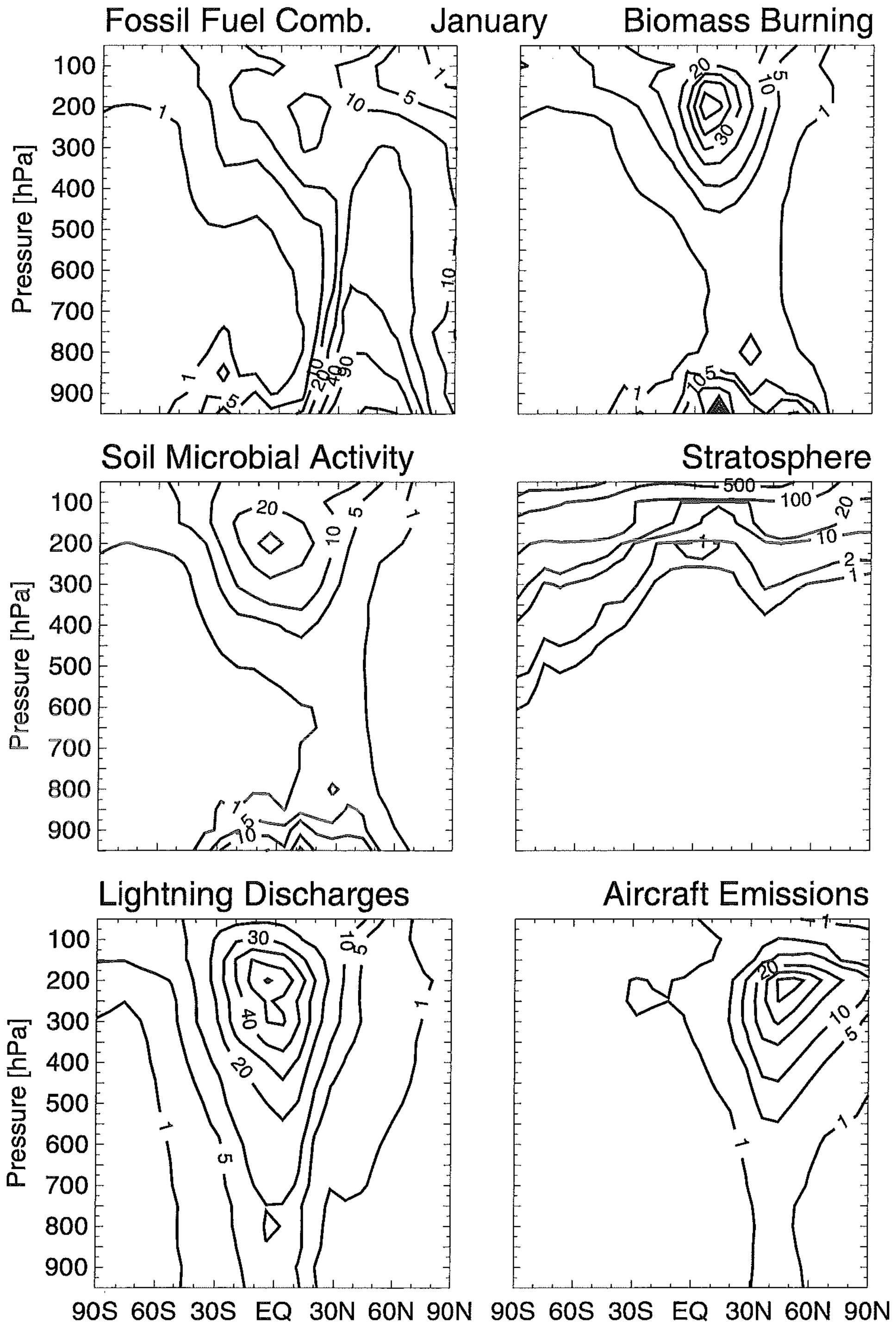

Figure 5.7: January monthly mean values of the zonal mean absolute contribution of NO_X from the individual sources. Contours are displayed at 1, 5, 10, 20, 40, 90, and 500 pptv for the source fossil fuel combustion, at 1, 2, 10, 20, 100, 500, and 1000 pptv for NO_X transported downwards from the stratosphere, and at 1, 5, 10, 20, 30, 40, 50, and 60 pptv for the other sources.

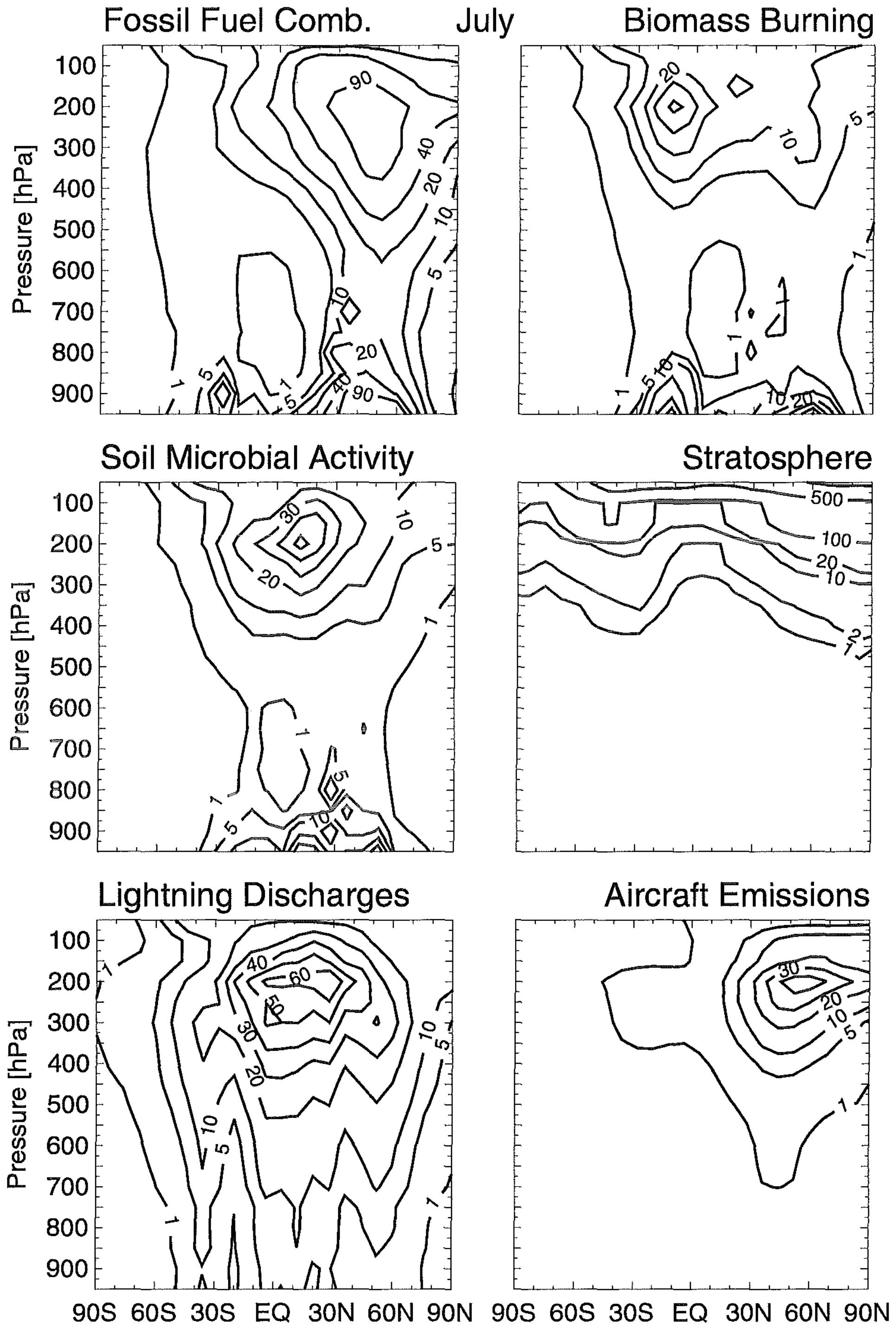

Figure 5.8: July monthly mean values of the zonal mean absolute contribution of NO_X from the individual sources. Contours are displayed at 1, 5, 10, 20, 40, 90, and 500 pptv for the source fossil fuel combustion, at 1, 2, 10, 20, 100, 500, and 1000 pptv for NO_X transported downwards from the stratosphere, and at 1, 5, 10, 20, 30, 40, 50, and 60 pptv for the other sources.

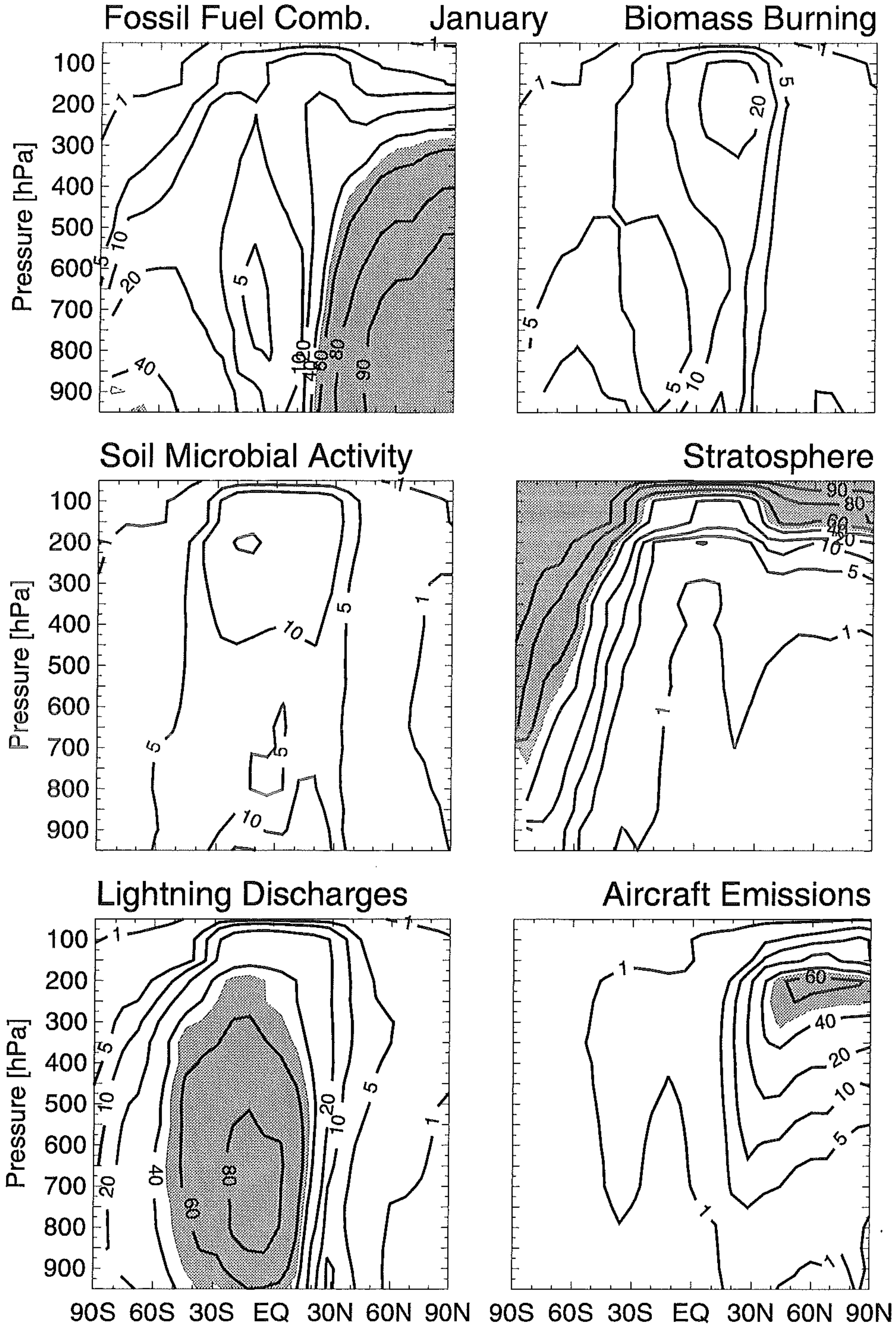

Figure 5.9: January monthly mean values of the zonal mean relative contribution of NO$_X$ from the individual sources. Contours are displayed at 1, 5, 10, 20, 40, 60, 80, and 90%. The shaded area denotes relative contributions larger than 50%.

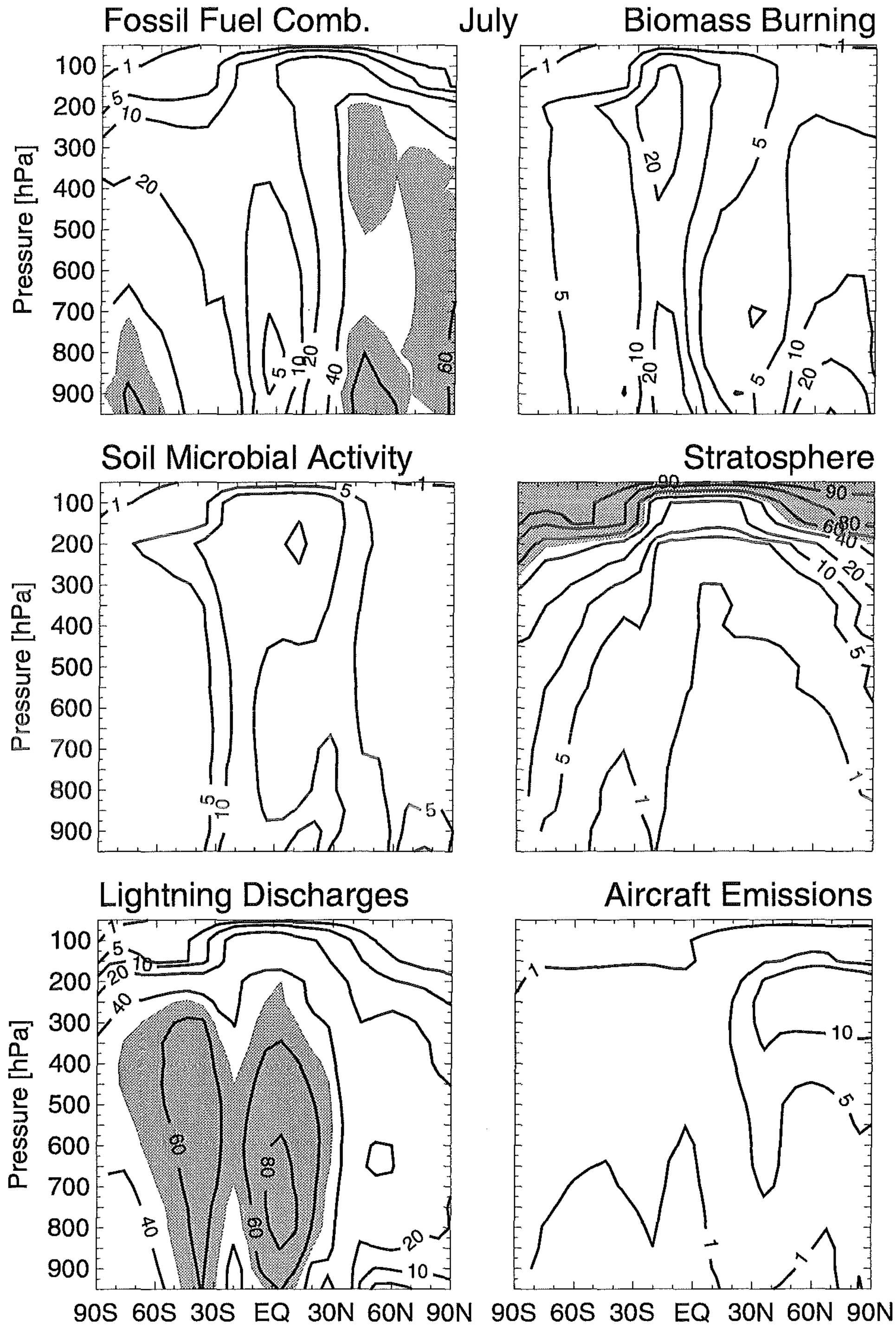

Figure 5.10: July monthly mean values of the zonal mean relative contribution of NO_X from the individual sources. Contours are displayed at 1, 5, 10, 20, 40, 60, 80, and 90%. The shaded area denotes relative contributions larger than 50%.

dominant. There, the tracer composition mainly is determined by the prevailing easterlies, which advect polluted air from the African continent.

5.4.4 NO_X Transported Downward from the Stratosphere

Owing to the lack of other sources in Antarctica, NO_X transported downward from the stratosphere is most important during the austral summer in that remote area. Everywhere else, except within the uppermost troposphere, this source is negligible. It is not clear how realistic the relative contribution of stratospheric input is close to the poles, because the CTM does not calculate tracer transport in the polar latitude bands, but assumes a uniform tracer distribution there. Further, the meridional exchange between the two columns of grid boxes closest to the poles is very small. Hence, due to the lack of surface sources, the main way how NO_X reaches the polar lower troposphere is by downward transport.

5.4.5 Aircraft Emissions

Aircraft emissions are among the most important sources of NO_X in the upper troposphere along the main flight tracks over North America, the Northern Atlantic, and Western Europe. All these regions are located at northern mid-latitudes. In winter, aircraft emissions occur right in between the regions of strong stratospheric influence on the one hand and substantial contributions from fossil fuel combustion on the other hand. At the height of the January tropopause, their zonally averaged contribution to μ_{NO_X} reaches almost 70%. In April and October, the corresponding contributions are 40% and 43%, respectively, whereas in July, a peak value of only 20% is reached. Thus, the relative importance of aircraft emissions shows a strong annual cycle, although the emission rate itself is constant throughout the year and so is their absolute contribution to μ_{NO_X}. The injection height also remains constant throughout the year. In summer, however, inner-tropospheric vertical mixing dilutes NO_X emitted by aircraft with NO_X coming from surface sources or from lightning discharges.

In summer, the zonal mean relative contribution of aircraft emissions calculated here are as low as 19% during July in the upper troposphere between 40°N and 50°N. This figure can be compared with results from previous model studies. *Ehhalt et al.* [1992], for example, obtain a contribution from this source of about 30% at northern mid-latitudes in the upper troposphere in June. There are several reasons for that difference, the main one being the larger contribution from upward transport of surface NO_X during July than during the period June to August. The contributions of the other sources are similar in both studies. *Kasibhatla* [1993] obtains a contribution of aircraft emissions of 30-40% between 30°N and 60°N in the upper troposphere for April. This figure is roughly consistent with that determined here, although the other sources differ considerably from the present model. *Brasseur et al.* [1996] give a value of 15-20% for the relative contribution of NO_X from aircraft emissions at northern mid-latitudes and 10 km altitude. This value refers the year 1990 and, probably, is the annual mean contribution.

5.4.6 Summary of the Most Important Contributions

To make those regions more clearly visible where one of the six sources contributes at least half of the total of μ_{NO_X}, these regions are shaded grey in Figures 5.9 and 5.10. It is emphasized that this is done only when the zonal average of a relative contribution is larger than 50%. In the troposphere, four sources reach such contributions:

1. Fossil fuel combustion in January in the lower and middle troposphere at northern mid-latitudes, in July in the lower troposphere at both northern and southern mid-latitudes, and, also in July, at northern high latitudes up to about 300 hPa.

2. Lightning discharges from above the PBL (or from the oceanic surface) to pressures of about 300 hPa, in January between 45°S and 10°N and in July between 60°S and 20°N.

3. Stratospheric NO_X in January at southern high latitudes.

4. Aircraft emissions in January north of 40°N between 150 and 250 hPa.

During both April and October, the patterns of the zonal mean relative contributions of NO_X from fossil fuel combustion and of stratospheric NO_X are similar to the corresponding distributions shown in Figure 5.9 for January. For the sources soil microbial activity and biomass burning, the April distribution differ only slightly from the January distribution. The same is true for these two sources during October and July. The relative contribution of lighting discharges reaches values of more than 50% in a similar region during April than during January. In October, however, such contributions occur only between 20° S and 20°N. The region where aircraft emissions play a significant role is the same throughout the year, only their relative importance varies with season.

Strongly simplified, the seasonal variation of the relative contributions from the individual sources can be summarized by the following 3 points: First, at the continents of the northern hemisphere, the convection activity is weak except when there is strong heating, i.e. from June to August. Frequent convection is associated with enhanced lightning activity, which diminishes the relative importance of NO_X from fossil fuel combustion at that region. Second, in the tropics, the NO_X composition is fairly constant throughout the year with a dominating contribution from lightning discharges. The seasonal variation of the minor contributions mainly is determined by the annual cycle of the corresponding sources. South of 45° S, finally, the tropospheric NO_X mixing ratios are below 10 pptv throughout the year. The composition of this low total should not be regarded as more than a first order approximation, since the major contributions in this region come from the stratosphere and from lightning discharges, which both are sources with comparatively high uncertainties.

5.5 Discussion

Uncertainties of the absolute NO_X distribution presented above arise due to uncertainties of the emission rates of the sources. This uncertainty is estimated to be a factor of 2 at least for each individual source. Because of the non-linear coupling between emission and transport, the geographical distribution of the sources also affects the distribution of tropospheric NO_X. Of particular importance for the free tropospheric NO_X distribution is in this context the relation between the distributions of the surface sources on the one hand and of deep convection on the other hand. The largest uncertainty of the geographical distribution of the surface sources probably arises as a result of the coarse model resolution, i.e. is comparatively small. More important is the fact that in the tropics the CTM seems to underestimate the annual cycle of deep convection activity and to overestimate the "C-like" structure of the vertical profiles, as the ^{222}Rn calculations show (see Chapter 4).

The results gained by the ^{222}Rn calculations cannot be transferred directly to the surface source contribution of the NO_X distribution because ^{222}Rn has a constant lifetime, whereas the lifetime of NO_X depends on altitude and on geographical latitude. Despite this, Figures 4.5 and 4.8 allow a rough estimate of which effect implementation of a Tiedtke convection scheme in the CTM would have. In the tropics, the zonal mean absolute contribution of biomass burning would increase in January by about a factor of 3 in the lower troposphere and decrease by a similar amount in the upper troposphere. The corresponding change in the relative contribution of this source is less, since by far the largest amount of NO_X present in the tropical free troposphere originates in lightning activity. A similar decrease would occur for the upper tropospheric tropical maximum of this source during July. The contributions of soil microbial activity also would be affected by such a change of the CTM's convection scheme, but, because of the latitudinal asymmetry of the convection correction, much less than the contribution of biomass burning.

A modification of the CTM's convection scheme hardly can affect the dominant role of NO_X generated by tropical lightning discharges. However, it would change the vertical distribution of the absolute NO_X

contribution of this source. If the assumption of NO emission proportional to the local air density is maintained, then inclusion of entrainment, up- and downdrafts weakens the strong vertical gradient obtained with the present version of the CTM. The consequence of such a smoother vertical profile is a lower total burden of NO_X of the tropical troposphere, because the chemical lifetime of NO_X is by about an order of magnitude lower in the lower troposphere than it is in the upper troposphere. However, this effect on the total burden is significantly less than the uncertainty associated with the global NO emission rate of lightning. A smoother vertical profile of the absolute contribution of NO_X from lightning discharges not necessarily is associated with lower relative contributions in the upper troposphere and higher ones in the lower troposphere since the absolute contributions of the surface sources are changed in the same way.

At mid-latitudes, replacement of the CTM's present convective scheme by a less simple one also would weaken the "C-like" shape of vertical NO_X profiles. The largest effect this would have on the July pattern of NO from fossil fuel combustion. However, apart from a decrease in the upper troposphere, it could only increase the lower tropospheric relative contribution of this source even further. The net effect of such a replacement would be similar small as for NO_X from lightning discharges in the tropics.

In summary, this transfer of the results gained by the ^{222}Rn runs to the NO_X distributions shows that the convection scheme used in the present study overestimates the vertical gradients of short-living tracers, in particular in the tropical troposphere. However, this overestimate has hardly any consequences for the composition of the total NO_X mixing ratio with respect to the individual sources.

Chapter 6

Comparison with NO Aircraft Measurements

The natural question arising subsequent to the previous discussion of global tropospheric distributions of NO_X is: How realistic are these distributions? This question is difficult to answer. In fact, it was the main purpose of this model study to provide a global overview of the tropospheric distribution of NO_X, *because* a corresponding data set based on observations is not yet available.

Since global observations of NO_X are still missing, the tracer distributions calculated by the CTM can be compared with measurements only locally. The most suitable data available at the moment for such a comparison are the NO measurements made during the four aircraft campaigns STRATOZ III, TROPOZ II, PEM-West A, and PEM-West B. These aircraft measurements provide a one-dimensional data set, but at least sample tropospheric NO mixing ratios within cubes covering almost 1000 model grid boxes each. Using observed mixing ratios of NO instead of NO_X is no restriction for the following comparison, because both tracers are uniquely connected in the present chemistry scheme. These aircraft measurements are far from providing representative mean values, but at least they cover large regions of the globe as well as four different seasons in the northern hemisphere. Moreover, they represent the actual composition of the troposphere and are gained by the present state-of-the-art measurement techniques.

The four aircraft measurement campaigns are described briefly in Section 6.1. Section 6.2 gives an overview of the NO mixing ratios measured and calculated for each of the four campaigns in terms of chronologically ordered data series. A detailed comparison of vertical profiles is carried out in Section 6.3. Similar profiles observed during subsequent flights are averaged for this purpose. Finally in Section 6.4, zonal mean latitude-altitude cross section are presented in order to give an overview of the spatial structure of the regional NO distributions.

6.1 The Aircraft Measurement Campaigns STRATOZ III, TROPOZ II, PEM-West A, and PEM-West B

The NO measurements evaluated here were made from June 4 to June 26, 1984 during the Stratospheric Ozone Experiment (STRATOZ) III, from January 9 to February 1, 1991 during the Tropospheric Ozone Experiment (TROPOZ) II, from September 12 to October 21, 1991 during the Pacific Exploratory Mission-West A (PEM-West A), and from February 4 to March 19, 1994 during the Pacific Exploratory Mission-West B (PEM-West B). Details of various aspects of these campaigns are provided by *Drummond et al.* [1988] for STRATOZ III, *Rohrer et al.* [1996] for TROPOZ II, *Gregory and Scott* [1995a] for PEM-West A, and *Gregory and Scott* [1995b] for PEM-West B. Additional information about PEM-West A is collected in a special section of the Journal of Geophysical Research [*AGU*, 1996]. The NO measurements made during this campaign are described by *Kondo et al.* [1996] and a detailed overview of the meteorological conditions is given by [*Bachmeier et al.*, 1996].

6.1.1 The Principle of NO Measurements

During the four aircraft campaigns, the principle of measuring NO is to count photons emitted subsequent to the chemilumminescent reaction between NO contained in the sampled air and added O_3:

$$\begin{aligned} NO + O_3 &\longrightarrow NO_2^* + O_2 \\ NO_2^* &\longrightarrow NO_2 + h\nu \,. \end{aligned} \tag{6.1}$$

The photons are monitored by a photo-multiplier in a low pressure detection volume. Since in addition to photons emitted by Reaction 6.1, the photo-multiplier has a dark current and chemiluminescence from other air-borne molecules is detected as well, the so-called zero mode and the measurement mode are used alternating. During the zero mode, NO is removed from the sample air before it passes the detection volume. Photon counts are integrated every 5-10 s and both modes are altered at times between 20 s (STRATOZ III) and 120 s (PEM-West A), respectively. The actual NO signal is obtained by subtracting the zero mode value from the measurement value. For this reason the measured NO mixing ratios may include some slightly negative values. Calibrations of each system were carried out during the flights by using air with a known NO mixing ratio. Figures characterizing resolution and experimental error of the four sets of instrumentation are summarized in Table 6.1.

campaign	temporal resolution	spatial resolution		accuracy	detection limit
		horizontal	vertical		
STRATOZ III	3 min	≈ 40 km	1.5 km	< 15 %	10-15 pptv
TROPOZ II	1 min	10-15 km	0.5 km	< 15 %	50 pptv
PEM-West A	1 min	10-15 km	0.5 km	7 %	5-10 pptv
PEM-West B	1 min	10-15 km	0.5 km	7 %[a]	5-10 pptv[a]

[a] estimated from PEM-West A

Table 6.1: Resolution and uncertainties of the NO measurements.

6.1.2 Overview of the Flight Tracks and Data Reduction

Figures 6.1 and 6.2 show maps of those portions of tracks flown during the four campaigns where NO measurements were made which are taken into account in the following. Along the missing portions of the flight tracks either NO was not measured correctly or the solar zenith angle was larger than 80° at the time of the measurement. The latter means that the data points gained during nighttime, at dawn, or at dusk are neglected here. The reason why this is done is that in the absence or almost absence of daylight the photolysis rate of NO_2 is very low or zero and, hence, the ratio NO/NO_X is very low.

Since the CTM determines daily mean values of μ_{NO}, it underestimates μ_{NO} in the presence of sunlight. The error made thereby is only about 15% of the daily mean NO_X concentration, as discussed in Section

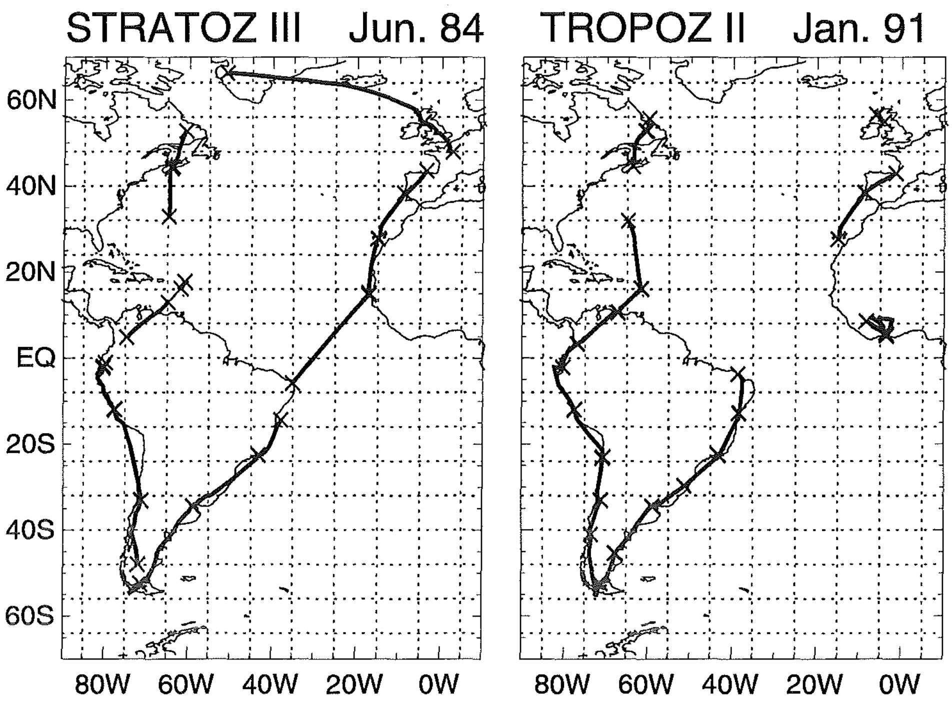

Figure 6.1: Portion of the flight track of the aircraft campaigns (left panel) STRATOZ III and (right panel) TROPOZ II along which the NO data evaluated here were measured. Crosses denote airports and the dashed lines show the grid of the CTM.

5.3. Thus, the underestimate of μ_{NO} made in the model calculation still could be quite large if there is a strong diurnal cycle in the NO_X concentration. However, the dependence of the daytime concentrations of NO and NO_X on the exact value of the solar zenith angle are small as the diurnal cycle resolving calculations of *Logan* [1983] show. A dependence of the NO measurements on the time of the day at which they were made therefore can be excluded as a possible reason for a bias between observed and calculated values of μ_{NO}.

Much more important than the error made by using diurnal averages of NO is the fact that an individual measurement data point refers to a volume of about 100 km^3, whereas in the tropics a single CTM grid cell covers approximately $1000 \times 800 \times 1.5 = 1.2 \times 10^6$ km^3. Even when the vertical resolution is increased to 50 hPa $\approx$ 0.5 km, a difference of three orders of magnitudes in the spatial resolution of both kinds of data is remaining. The corresponding difference in the temporal resolution is even larger. Since the measured NO mixing ratios vary significantly in time and space, it is not clear whether they are are sufficent to provide representative mean values on the scale of a CTM grid box.

6.2 Overview of the NO Data

An overview of the global NO distributions calculated by the CTM for January, April, July, and October is given in Figures A.1-A.4 in Appendix A, whereas Figures 6.3-6.6 give an overview of the complete aircraft measurement campaign data sets. The left parts of Figures 6.3-6.6 show the chronologically ordered series

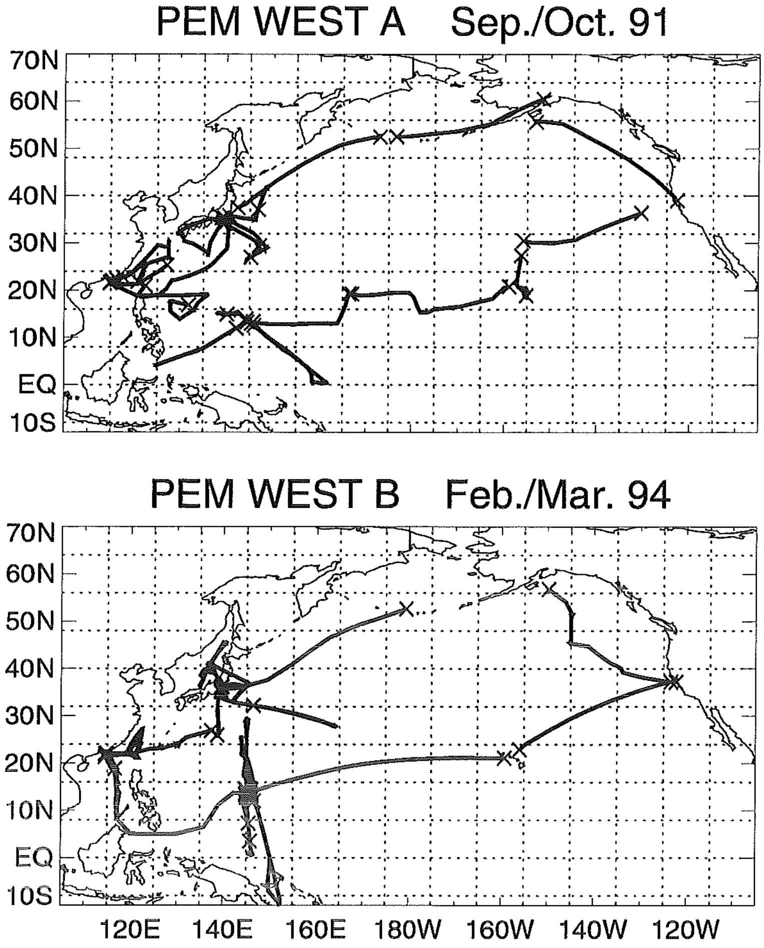

Figure 6.2: Portion of the flight track of the aircraft campaigns (upper panel) PEM-West A and (lower panel) PEM-West B along which the NO data evaluated here were measured. Crosses denote airports and the dashed lines show the grid of the CTM.

of all measured NO mixing ratios, $\mu_{\mathrm{NO}^{\mathrm{M}}}$. Spatial averages over the individual grid boxes of the CTM are shown here to reduce the high variability which $\mu_{\mathrm{NO}^{\mathrm{M}}}$ has on the scale of its resolution. Equal values of μ_{NO} for several subsequent samples therefore indicate that all these samples were taken in a volume corresponding to the same model grid box. Such cases occur during the traverse flights at constant altitude as comparison with the altitude coordinates of the flight tracks shows. These coordinates are given in the right parts of Figures 6.3-6.6, together with the longitude and latitude coordinates of the flight tracks.

In addition to the measured values $\mu_{\mathrm{NO}^{\mathrm{M}}}$, the middle parts of Figures 6.3-6.6 show the NO mixing ratios calculated along the flight track, $\mu_{\mathrm{NO}^{\mathrm{C}}}$, as a second series with a reversed ordinate. The values $\mu_{\mathrm{NO}^{\mathrm{C}}}$ are temporal averages over the entire time period of the corresponding campaign, i.e. roughly monthly mean values, if not noted otherwise. These temporal averages are calculated from daily mean CTM output and are denoted by $\overline{\mu_{\mathrm{NO}^{\mathrm{C}}}}^{ca}$ henceforth. In order to give an impression of the temporal variability of $\mu_{\mathrm{NO}^{\mathrm{C}}}$ during this time period, the range given by the lowest and highest daily mean values of $\mu_{\mathrm{NO}^{\mathrm{C}}}$, $\overline{\mu_{\mathrm{NO}^{\mathrm{C}}}}^{d}|_{max}$ and $\overline{\mu_{\mathrm{NO}^{\mathrm{C}}}}^{d}|_{min}$, respectively, are shown as well. The vertical resolution of $\mu_{\mathrm{NO}^{\mathrm{C}}}$ is 50 hPa achieved by interpolation due to the second-order moments method [*Prather*, 1986]. If both $\mu_{\mathrm{NO}^{\mathrm{M}}}$ and $\overline{\mu_{\mathrm{NO}^{\mathrm{C}}}}^{ca}$ were identical, each of these two data sets would be the mirror image of the other one with respect to the line $\mu_{\mathrm{NO}^{\mathrm{M}}} = \overline{\mu_{\mathrm{NO}^{\mathrm{C}}}}^{ca} = 0$. This kind of representation is chosen here to give an impression of the main features of both data sets, not to compare their exact values.

During STRATOZ III, $\mu_{\mathrm{NO}^{\mathrm{M}}}$ and $\overline{\mu_{\mathrm{NO}^{\mathrm{C}}}}^{ca}$ are low in the lower troposphere and significantly higher in the upper one, as Figure 6.3 shows. In addition, μ_{NO} clearly depends on latitude in both data sets. High values of μ_{NO} occur in the tropical upper troposphere and at northern mid-latitudes, in particular over Europe (flights 1 and 17). At southern mid-latitudes, μ_{NO} is very low even in the upper troposphere (flights 10-12). At low altitudes, $\mu_{\mathrm{NO}^{\mathrm{M}}}$ shows spikes of more than 0.3 ppbv which are missing in the calculated data. Local pollution close to airports not resolved by the model is the most likely reason for this discrepancy. During most flights, $\overline{\mu_{\mathrm{NO}^{\mathrm{C}}}}^{d}|_{min}$ agrees better with $\mu_{\mathrm{NO}^{\mathrm{M}}}$ than $\overline{\mu_{\mathrm{NO}^{\mathrm{C}}}}^{ca}$.

Figure 6.4 shows that during TROPOZ II the variability of $\mu_{\mathrm{NO}^{\mathrm{M}}}$ is higher than during STRATOZ III due to a larger number of ascends and descents and, hence, less spatial averaging. This is the case in particular for flights 19-21, during which vertical soundings were flown close to active bush-fires. In addition, the PBL was rather turbulent there and reached up to an altitude of 3 km. During flight 3, very high NO mixing ratios were observed, the origin of which is not yet understood, but might be a previous event of stratospheric intrusion. Relatively high values of $\mu_{\mathrm{NO}^{\mathrm{M}}}$ also occured in the downwind direction of the American continent (flight 4, 17, and 18), whereas the variation of $\overline{\mu_{\mathrm{NO}^{\mathrm{C}}}}^{ca}$ with latitude is similar to the corresponding variation during STRATOZ III. The temporal variability of $\mu_{\mathrm{NO}^{\mathrm{C}}}$ is small during TROPOZ II.

For PEM-West A, $\mu_{\mathrm{NO}^{\mathrm{M}}}$ is generally low, as Figure 6.5 shows. The only exceptions are flight 3, which took place in a strong westerly flow off the Asian continent between 35°N and 50°N and some spikes of very high NO mixing ratios encountered during flight 10. The dependence of $\mu_{\mathrm{NO}^{\mathrm{M}}}$ on altitude therefore is less striking than it is for the observations made at low latitudes during STRATOZ III and TROPOZ II. The values of $\overline{\mu_{\mathrm{NO}^{\mathrm{C}}}}^{ca}$ obtained for PEM-West A also are low far from the Asian continent. However, close to the east coast of this continent (flights 3-12), enhanced values of $\overline{\mu_{\mathrm{NO}^{\mathrm{C}}}}^{ca}$ occur in the upper troposphere. The different scales of the μ_{NO}-axes in Figures 6.3 and 6.4 on the one hand and in Figures 6.3 and 6.4 on the other hand should be noted in this context.

During PEM-West A, heavy biomass burning occured over western and central Indonesia, but had no effect on $\mu_{\mathrm{NO}^{\mathrm{M}}}$, despite southerlies prevailing during flights 12 and 14. Neither was there a significant increase of $\mu_{\mathrm{NO}^{\mathrm{M}}}$ during flights 7 and 12, when the aircraft passed close to the typhoons Mireille and Orchid, respectively. Flight 7 was specifically devoted to the sampling of boundary layer inflow and upper tropospheric outflow in the vicinity of Mireille. However, spikes of NO did occur during flight 10, probably because of local NO production by thunderstorms located above the East China Sea. As during STRATOZ III, the agreement between $\mu_{\mathrm{NO}^{\mathrm{M}}}$ and $\mu_{\mathrm{NO}^{\mathrm{C}}}$ is better for $\overline{\mu_{\mathrm{NO}^{\mathrm{C}}}}^{d}|_{min}$ than for $\overline{\mu_{\mathrm{NO}^{\mathrm{C}}}}^{ca}$.

Most of the NO mixing ratios measured during PEM-West B are similarly low as those of PEM-West A. Enhanced values of $\mu_{\mathrm{NO}^{\mathrm{M}}}$ occur in the upper troposphere of the tropical western Pacific and close to the Asian continent between 20°N and 35°N (flights 9-11). Apart from local peaks close to the ground, the corresponding calculated values $\overline{\mu_{\mathrm{NO}^{\mathrm{C}}}}^{ca}$ are very low during the entire period of the campaign. Since up to now the NO measurements made during PEM-West B are published only in a preliminary version, a detailed analysis of the meteorological conditions during this campaign is not yet available. Since the CTM tends to give NO mixing rations lower than $\mu_{\mathrm{NO}^{\mathrm{M}}}$, during most flights $\overline{\mu_{\mathrm{NO}^{\mathrm{C}}}}^{d}|_{max}$ is closer to $\mu_{\mathrm{NO}^{\mathrm{M}}}$ than is $\overline{\mu_{\mathrm{NO}^{\mathrm{C}}}}^{ca}$.

The representation of the observed and calculated NO mixing ratios chosen in Figures 6.3-6.6 indicates a certain correlation correlation between both data sets. However, if the linear correlation coefficient, c_l, is calculated from the series of $\mu_{\mathrm{NO}^{\mathrm{M}}}$ and $\overline{\mu_{\mathrm{NO}^{\mathrm{C}}}}^{ca}$, the values 0.09, 0.02, 0.40, and 0.23 are obtained for STRATOZ III, TROPOZ II, PEM-West A, and PEM-West B, respectively. These values are much lower than what one would expect from Figures 6.3-6.6, because individual events of very high NO mixing ratios,

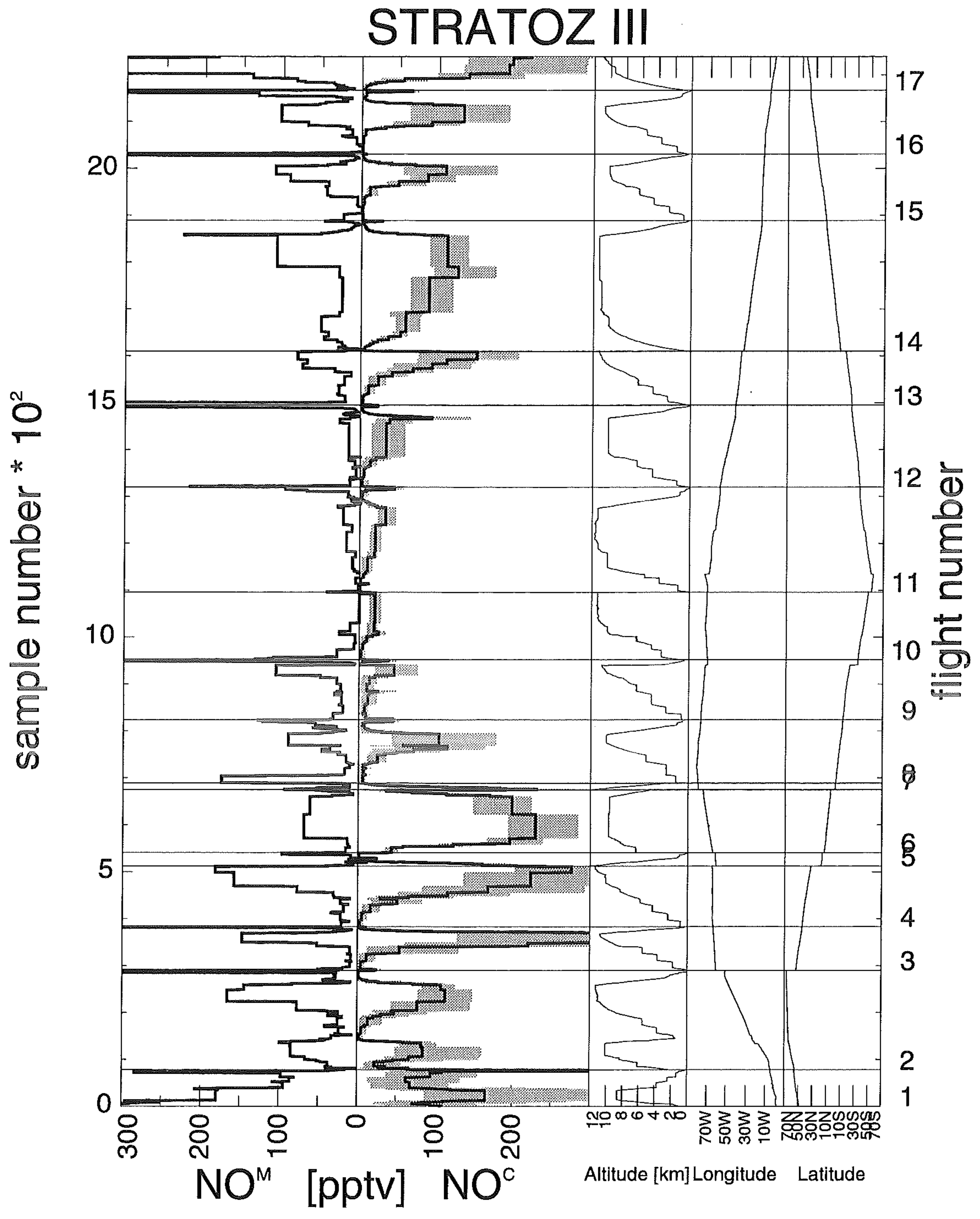

Figure 6.3: Time series of the NO mixing ratios (left part) $\mu_{\mathrm{NO^M}}$ measured during the STRATOZ III aircraft campaign and (middle part) temporal average $\overline{\mu_{\mathrm{NO^C}}}^{ca}$ calculated along the flight track. The grey shading denotes the range given by the highest and the lowest daily mean value achieved in the CTM during the time period of the campaign. The right part shows the spatial coordinates of the flight tracks.

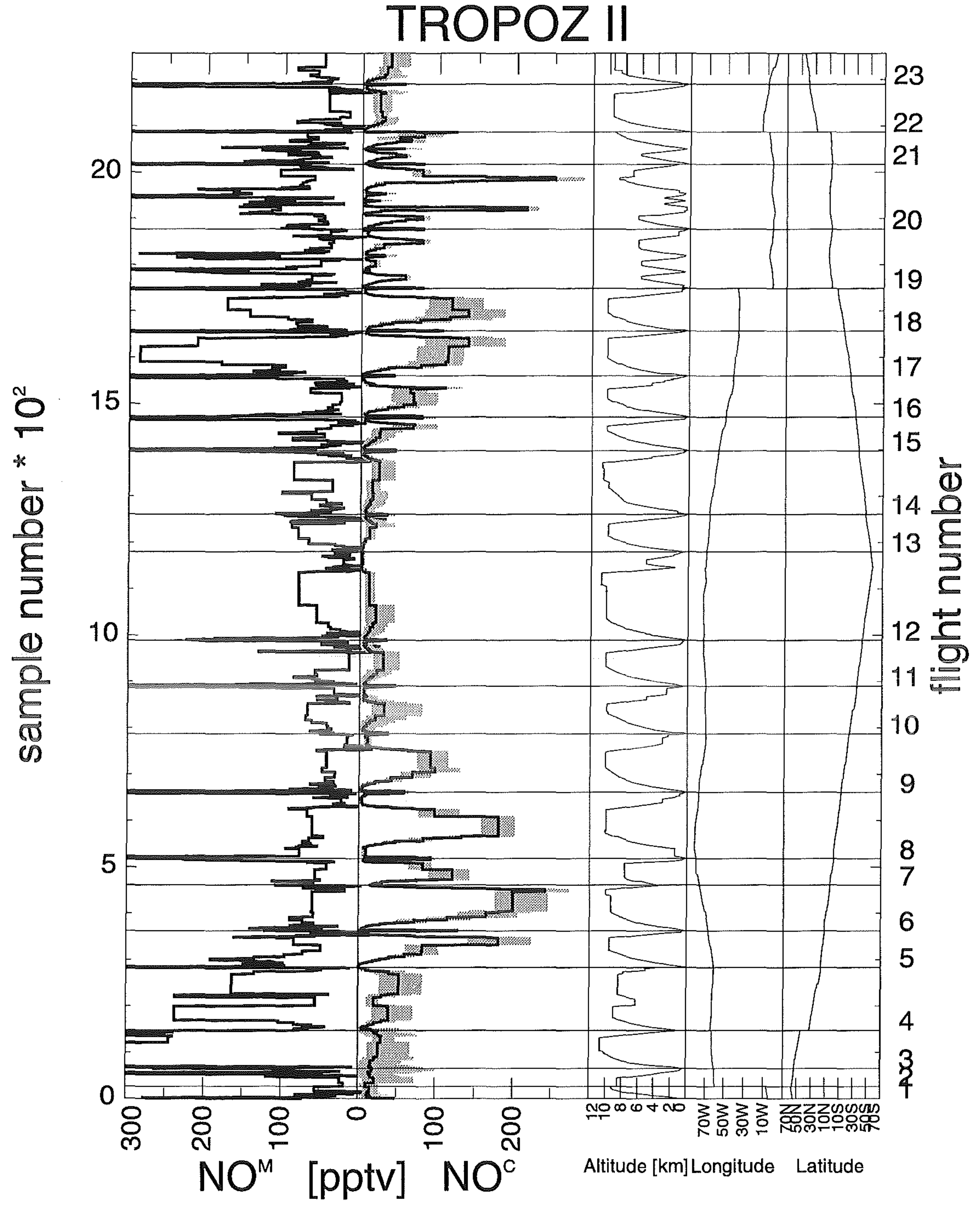

Figure 6.4: Time series of the NO mixing ratios (left part) $\mu_{\mathrm{NO^M}}$ measured during the TROPOZ II aircraft campaign and (middle part) temporal average $\overline{\mu_{\mathrm{NO^C}}}^{ca}$ calculated along the flight track. The grey shading denotes the range given by the highest and the lowest daily mean value achieved in the CTM during the time period of the campaign. The right part shows the spatial coordinates of the flight tracks.

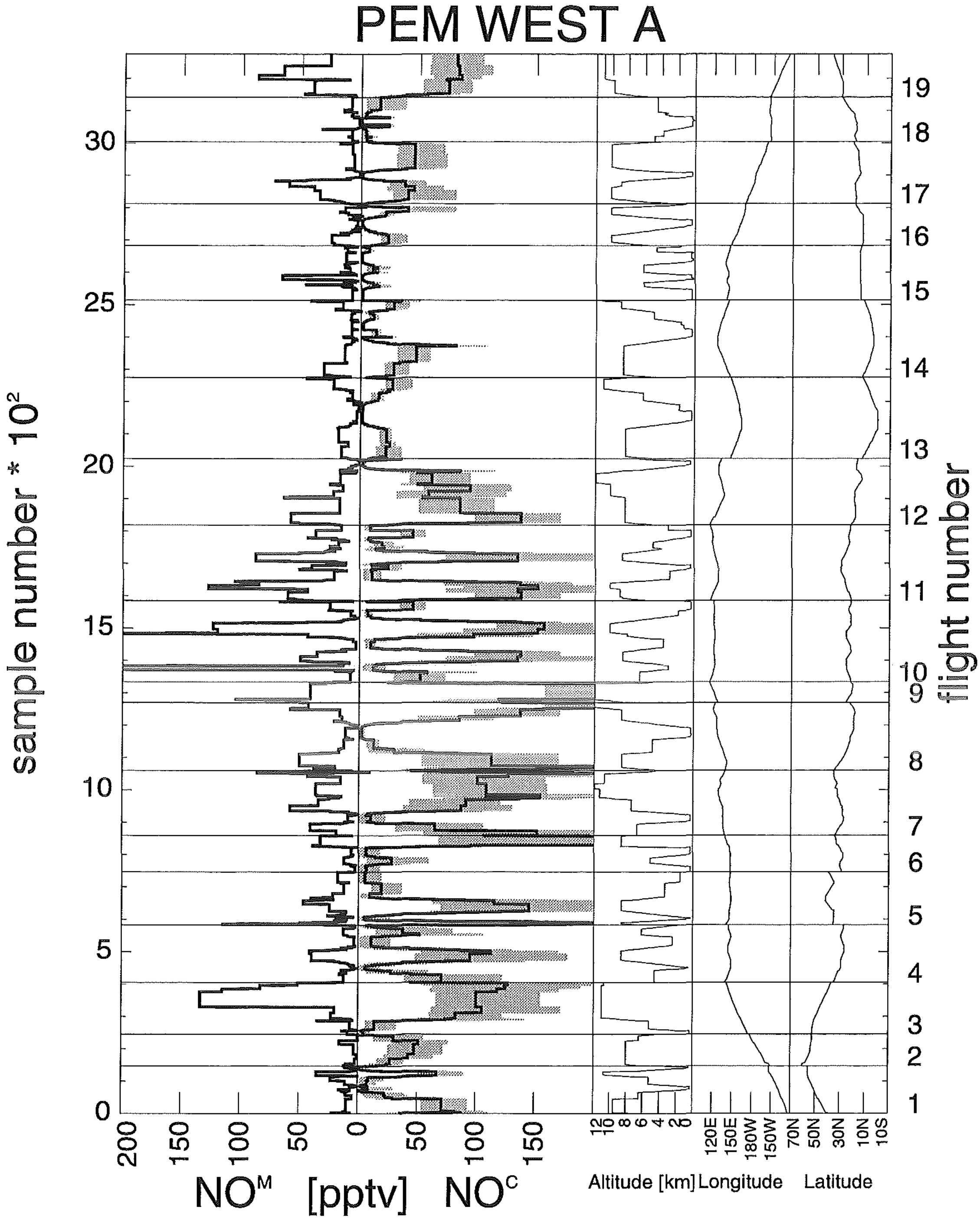

Figure 6.5: Time series of the NO mixing ratios (left part) μ_{NO^M} measured during the PEM-West A aircraft campaign and (middle part) temporal average $\overline{\mu_{NO^C}}^{ca}$ calculated along the flight track. The grey shading denotes the range given by the highest and the lowest daily mean value achieved in the CTM during the time period of the campaign. The right part shows the spatial coordinates of the flight tracks.

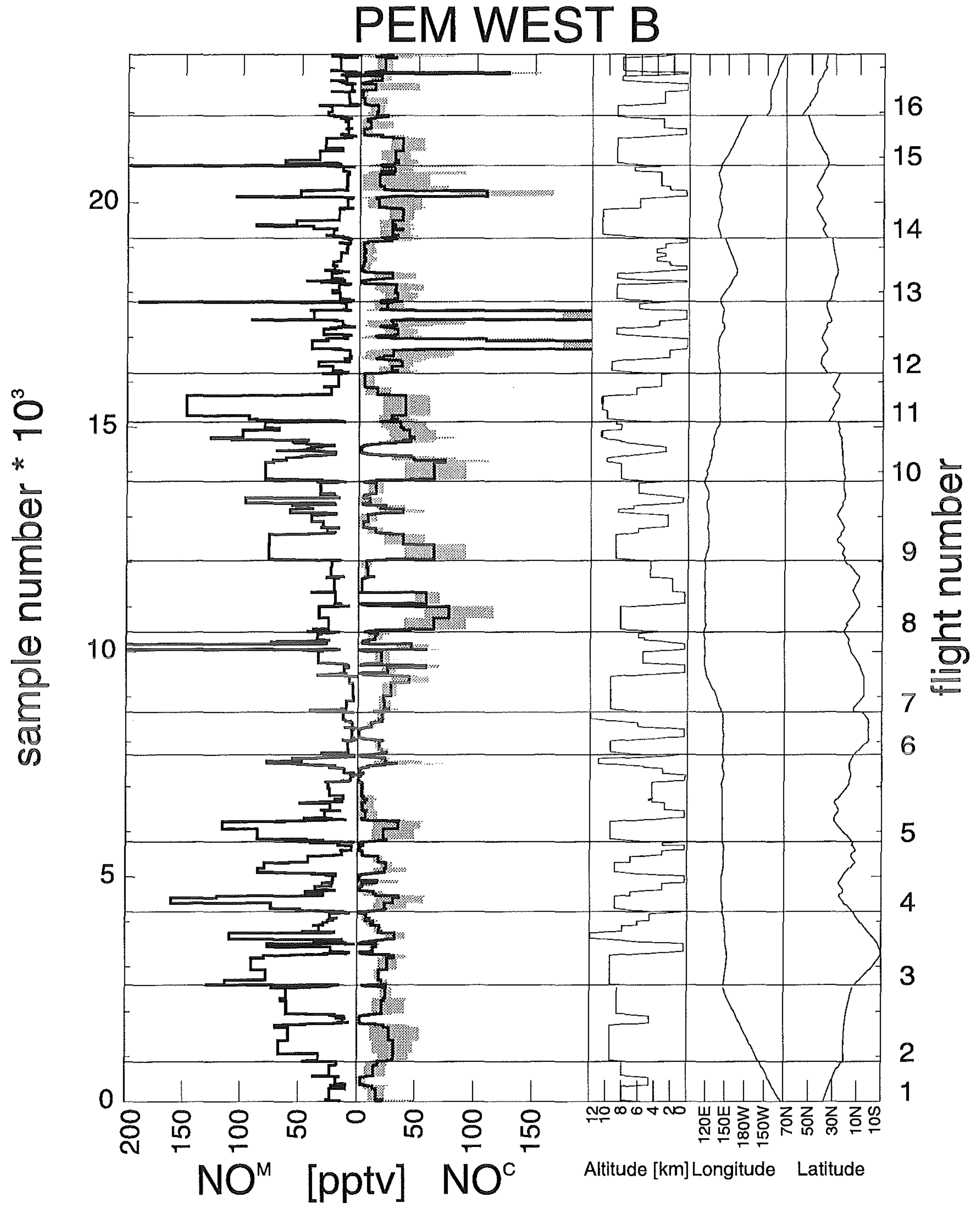

Figure 6.6: Time series of the NO mixing ratios (left part) $\mu_{\mathrm{NO^M}}$ measured during the PEM-West B aircraft campaign and (middle part) temporal average $\overline{\mu_{\mathrm{NO^C}}}^{ca}$ calculated along the flight track. The grey shading denotes the range given by the highest and the lowest daily mean value achieved in the CTM during the time period of the campaign. The right part shows the spatial coordinates of the flight tracks.

several ppbv, make substantial contributions to the mean values of $\mu_{\mathrm{NO^M}}$ and $\overline{\mu_{\mathrm{NO^C}}}^{ca}$. The values of c_l therefore increase to 0.58, 0.19, 0.65, and 0.37, respectively, when only those data points are taken into account, which are shown in Figures 6.3-6.6, i.e. $\mu_{\mathrm{NO^M}} < 300$ pptv and $\mu_{\mathrm{NO^C}} < 300$ pptv for STRATOZ III and TROPOZ II and $\mu_{\mathrm{NO^M}} < 200$ pptv and $\mu_{\mathrm{NO^C}} < 200$ pptv for PEM-West A and PEM-West B. In summary, the low values of c_l indicate that $\mu_{\mathrm{NO^M}}$ either is not well correlated with $\overline{\mu_{\mathrm{NO^C}}}^{ca}$, or that the correlation is not linear. These aspects are discussed in the following.

6.3 Regionally Averaged Vertical Profiles

In this section, the NO mixing ratios $\mu_{\mathrm{NO^M}}$ and $\mu_{\mathrm{NO^C}}$ shown in Figures 6.3-6.6 are represented as regionally averaged vertical profiles. This representation allows a detailed analysis of the degree of agreement between the model calculation and the measurements. Furthermore, this representation reveals possible reasons of discrepancies between both data sets in many regions.

Since it is not aim of the present model study to reproduce observed episodes, but to provide characteristic, mean tracer distributions, the vertical profiles investigated here are averages over the data obtained during several individual flights. On the one hand, averaging is necessary in order to suppress a possible bias due to data measured during untypical conditions. On the other hand, as little averaging as possible is desired in order to maintain the spatial resolution as high as possible. The decision whether data of two flights can be summarized or not was made by inspection of both the absolute values of μ_{NO} and the structure of its vertical profile. The results for each of the four data sets are discussed in the following. Possible reasons for systematic deviations of $\overline{\mu_{\mathrm{NO^C}}}^{ca}$ from $\mu_{\mathrm{NO^M}}$ are discussed at the end of this section.

6.3.1 STRATOZ III

Because of the large range of latitudes covered by the flight track during this campaign, an adequate representation of the corresponding NO data as mean vertical profiles requires as many as 7 regions. How the individual STRATOZ III flights are averaged is given in Table 6.2. The regionally averaged vertical profiles of $\mu_{\mathrm{NO^M}}$ and $\overline{\mu_{\mathrm{NO^C}}}^{ca}$ are shown in Figure 6.7 in terms of mean, maximum, and minimum values, medians, and standard deviations. For this purpose, all data are binned with a vertical resolution of 50 hPa. The medians of both data set are connected by thick lines to allow a direct comparison between $\mu_{\mathrm{NO^M}}$ and $\overline{\mu_{\mathrm{NO^C}}}^{ca}$. The reason why this is done for the medians, not for the mean values is a significant bias towards higher mean values when the data contain spikes of significantly enhanced values of μ_{NO}. The median, however, in general is affected only slightly by individual spikes. In the PBL, large differences between the median and mean value of $\mu_{\mathrm{NO^M}}$ are frequent due to strong local gradients in the vicinity of sources (see, e.g., the 950 hPa layer of the Northern Hemispheric American East Coast profile in Figure 6.7). In the upper troposphere, the difference between median and mean value usually is low. It is emphasized that the standard deviations shown for the calculated data are obtained from the temporal mean values $\overline{\mu_{\mathrm{NO^C}}}^{ca}$ and, hence, represent spatial variability exclusively. In order to give an impression of the temporal variability of $\mu_{\mathrm{NO^C}}$ in each region, the maximum and minimum daily mean values $\overline{\mu_{\mathrm{NO^C}}}^{d}$ are added in the right panels of Figure 6.7.

The main features of the comparison between the mean vertical profiles of $\mu_{\mathrm{NO^M}}$ and $\overline{\mu_{\mathrm{NO^C}}}^{ca}$ are summarized in Table 6.2. This table contains judgments of the agreement between both data sets like "good", "medium", or "poor". These classifications base on a visual inspection of how similar the vertical structure of both profiles is. In addition, the number of pressure levels is taken into account at which the interval $[\langle\mu_{\mathrm{NO^M}}\rangle - \sigma_{sd}, \langle\mu_{\mathrm{NO^M}}\rangle + \sigma_{sd}]$ includes the median of $\mu_{\mathrm{NO^C}}$, where $\langle\mu_{\mathrm{NO^M}}\rangle$ denotes the mean value of $\mu_{\mathrm{NO^M}}$ and σ_{sd} is the standard deviation.

The reason why the agreement between the regionally averaged vertical profiles is so poor for Great Britain probably is the unusual meteorological situation during which the measurements were made. Instead of the typical westerly winds advecting relatively clean oceanic air, easterlies associated with NO-rich air from the European continent were prevailing. This situation continued during the flight across the North Atlantic [*Ehhalt et al.*, 1993]. For the other five regions, the agreement between the vertical profiles of $\mu_{\mathrm{NO^M}}$ and $\overline{\mu_{\mathrm{NO^C}}}^{ca}$ is better.

In the West Atlantic region, the mean vertical profiles of $\mu_{\mathrm{NO^M}}$ and $\overline{\mu_{\mathrm{NO^C}}}^{ca}$ agree particularly well both in structure and in their absolute values. The large differences in the lowest two pressure layers are a result of measurements made in highly polluted air close to airports. This pollution partly is a consequence of local aircraft emissions. However, since most airports are situated in the vicinity of urban regions, a major fraction of the NO enhancement probably originates in fossil fuel combustion. The same effect occurs in other regions as well.

Apart from untypical meteorological conditions or events of local pollution which are not resolved by the CTM, the model generally underestimates the NO mixing ratios measured during STRATOZ III in the

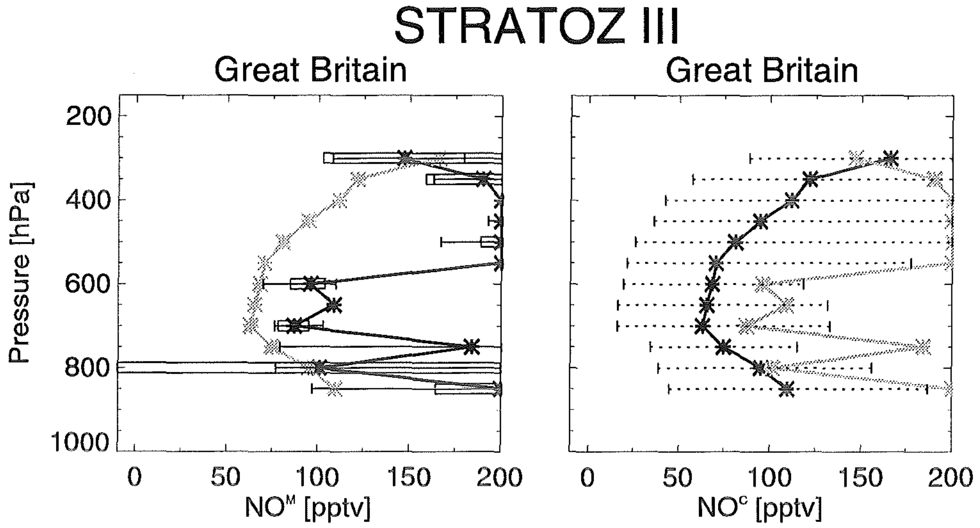

Figure 6.7: Left panels: regionally averaged vertical profiles of NO mixing ratios measured during STRATOZ III, $\mu_{\mathrm{NO^M}}$. The data are binned with a vertical resolution of 50 hPa. Black stars connected by a thick black line are medians of $\mu_{\mathrm{NO^M}}$. Stars positioned at the right rim of the panel denote medians of $\mu_{\mathrm{NO^M}}$ larger than the highest value shown on the NO-axis. Horizontal bars are centered around the mean value of $\mu_{\mathrm{NO^M}}$, $\langle\mu_{\mathrm{NO^M}}\rangle$, denoted by a small vertical tick. They give the range $[\langle\mu_{\mathrm{NO^M}}\rangle - \sigma_{sd}, \langle\mu_{\mathrm{NO^M}}\rangle + \sigma_{sd}]$, where σ_{sd} denotes the standard deviation. No horizontal bar is shown for bins containing less than three values. Horizontal thin solid lines extend from the minimum value of $\mu_{\mathrm{NO^M}}$ to the maximum value of $\mu_{\mathrm{NO^M}}$. Corresponding values outside the interval given by the NO-axis are suppressed. For comparison, medians of the temporal mean $\overline{\mu_{\mathrm{NO^C}}}^{ca}$ calculated along the flight track for the same region are shown as grey stars connected by a grey line.

Right panels: Medians, mean, maximum, and minimum values, and standard deviations as in the left panels, but for $\overline{\mu_{\mathrm{NO^C}}}^{ca}$. For comparison, the medians of $\mu_{\mathrm{NO^M}}$ shown in the left panels in black are redrawn here in grey. Horizontal thin dotted lines extend from the minimum daily mean value of $\mu_{\mathrm{NO^C}}$ calculated during the campaign, $\overline{\mu_{\mathrm{NO^C}}}^{d}|_{min}$, to the corresponding maximum daily mean value, $\overline{\mu_{\mathrm{NO^C}}}^{d}|_{max}$. In some of the right panels, as for Great Britain, $[\langle\overline{\mu_{\mathrm{NO^C}}}^{ca}\rangle - \sigma_{sd}, \langle\overline{\mu_{\mathrm{NO^C}}}^{ca}\rangle + \sigma_{sd}]$ and the maximum and minimum values of $\overline{\mu_{\mathrm{NO^C}}}^{ca}$ are too close to the median of $\overline{\mu_{\mathrm{NO^C}}}^{ca}$ to be distinguished from the black stars.

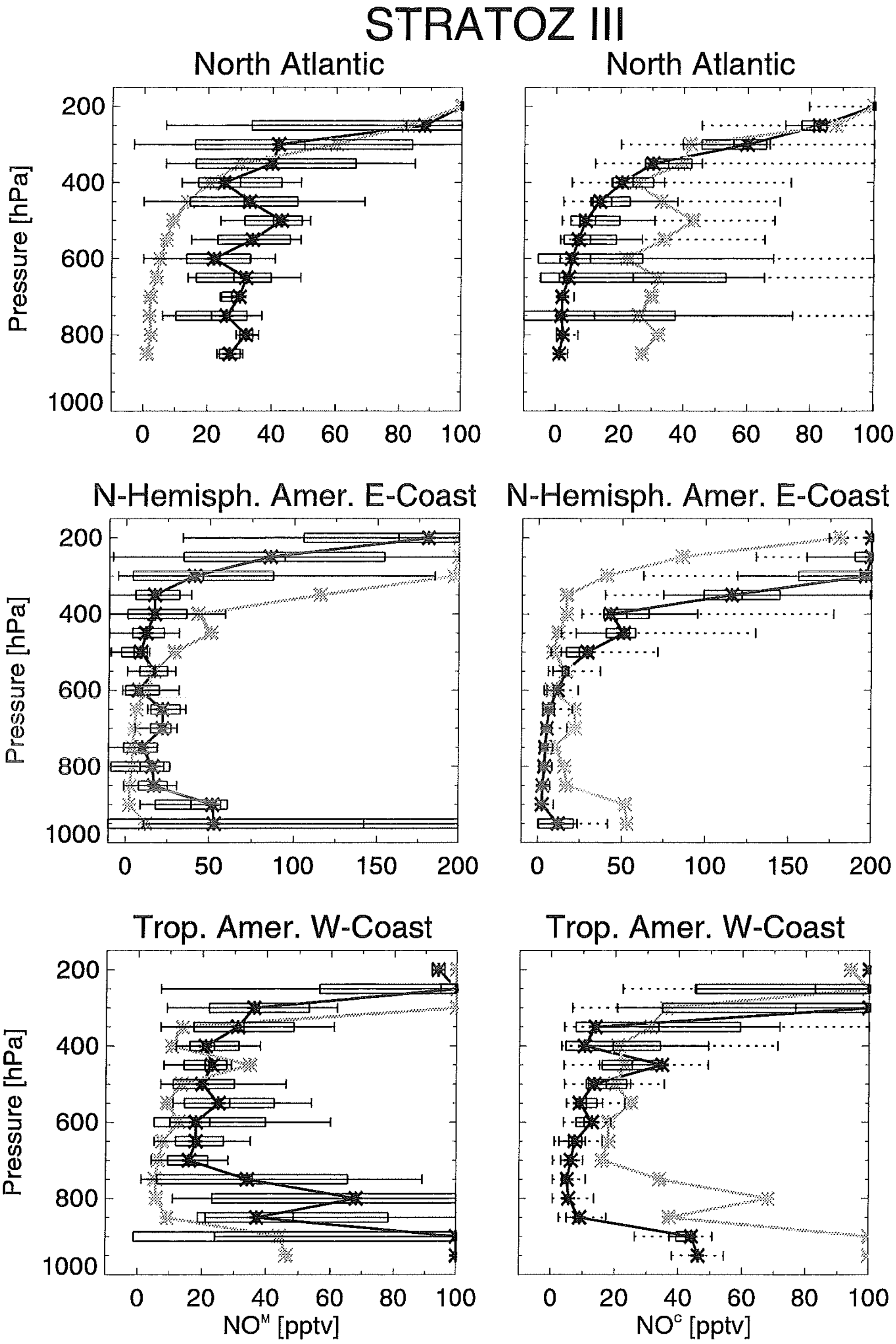

Figure 6.7: continued

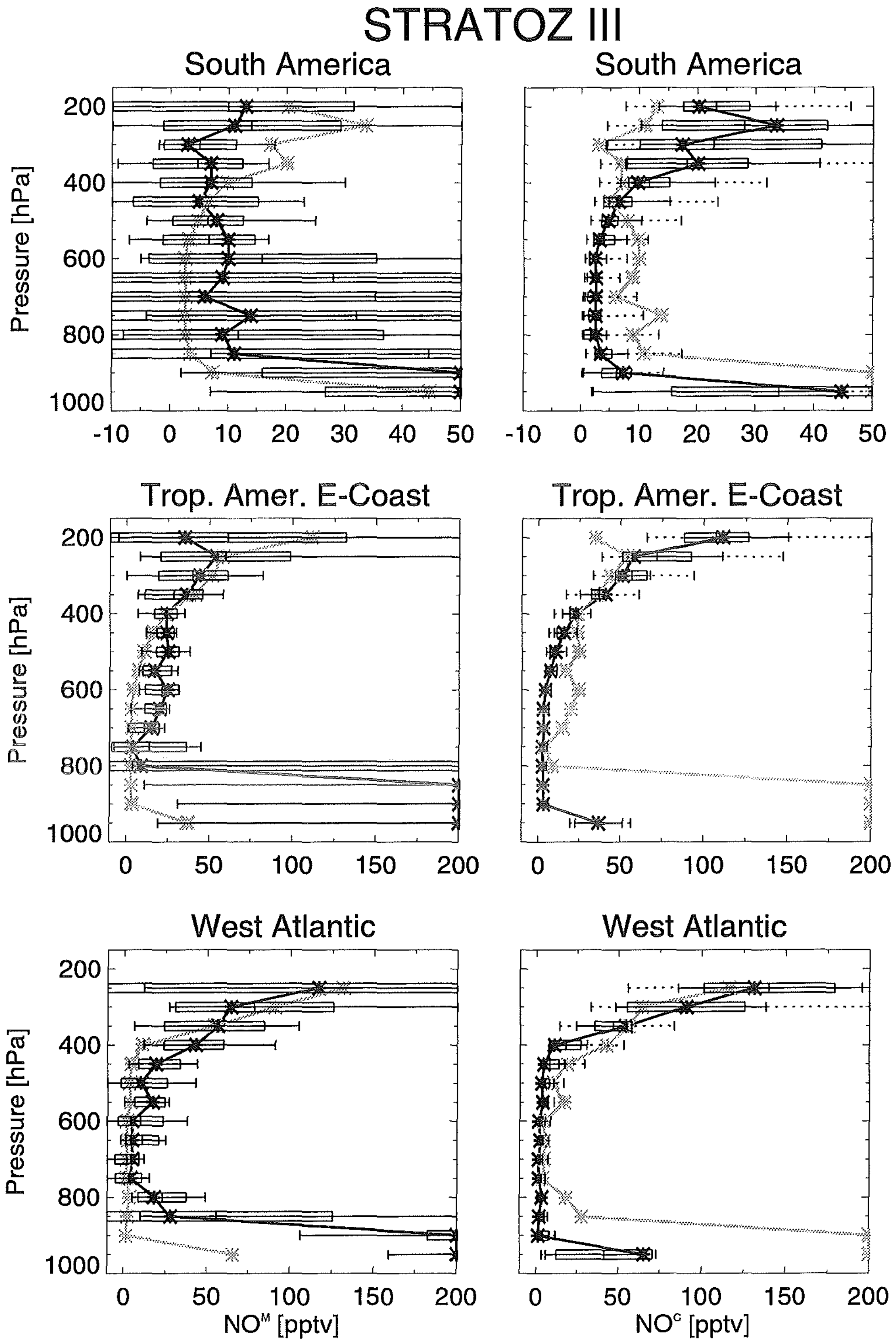

Figure 6.7: continued

region	flights	number of data points	agreement	discrepancy or comment
Great Britain	1	78	poor	p $\in$ [750 hPa, 350 hPa]: $\overline{\mu_{\mathrm{NO^C}}}^{ca} \ll \mu_{\mathrm{NO^M}}$
North Atlantic	2	212	p $\leq$ 400 hPa: good p $\geq$ 500 hPa: poor	p $\geq$ 500 hPa: $\overline{\mu_{\mathrm{NO^C}}}^{ca} \ll \mu_{\mathrm{NO^M}}$
Northern Hemispheric American East Coast	3-6	385	medium	p $\leq$ 350 hPa: $\overline{\mu_{\mathrm{NO^C}}}^{ca} \gg \mu_{\mathrm{NO^M}}$ p $\geq$ 650 hPa: $\overline{\mu_{\mathrm{NO^C}}}^{ca} \lesssim \mu_{\mathrm{NO^M}}$
Trop. Amer. West Coast	7-9	277	medium	p $\geq$ 550 hPa: $\overline{\mu_{\mathrm{NO^C}}}^{ca} \lesssim \mu_{\mathrm{NO^M}}$
South America	10-12	543	medium	σ_{sd} of $\mu_{\mathrm{NO^M}}$ very large
Trop. Amer. East Coast	13,14	394	medium-good	p $\geq$ 450 hPa: $\overline{\mu_{\mathrm{NO^C}}}^{ca} \lesssim \mu_{\mathrm{NO^M}}$
West Atlantic	15-17	351	good	

Table 6.2: Evaluation of the comparison between regionally averaged vertical STRATOZ III profiles of $\mu_{\mathrm{NO^M}}$ and $\overline{\mu_{\mathrm{NO^C}}}^{ca}$ (see Figure 6.7).

lower and mid-troposphere and overestimates μ_{NO} in the upper troposphere. There are four possible reasons for these discrepancies: an oversimplification of the convection processes by the convective adjustment scheme as discussed in Chapter 4, missing or insufficiently parametrized sources, an unrealistic vertical profile of the chemical lifetime of $\mathrm{NO_X}$, $\tau_{\mathrm{NO_X}}$, or a missing dynamical process like subgrid-scale eddy diffusion. The last of these reasons partly is associated with the convection scheme used here, but in addition might play an important role for horizontal tracer redistribution in regions with highly variable meteorological conditions as in mid-latitudes. Which one of these reasons is responsible for the deviation of $\overline{\mu_{\mathrm{NO^C}}}^{ca}$ from $\mu_{\mathrm{NO^M}}$ in each of the individual regions is discussed in the following.

In the regions Northern Hemispheric American East Coast, Tropical American West Coast, and Tropical American East Coast, an overestimate of $\overline{\mu_{\mathrm{NO^C}}}^{ca}$ in the upper troposphere due to the convection scheme is likely, as Figure 4.5 indicates. The relative contribution maps included in Appendix B (see Figures B.7-B.12) show that lightning contributes about 40% of the total $\mathrm{NO_X}$ present there at 200 hPa in July and that the remaining 60% originate in surface sources. The relative contributions of the individual sources are equal for NO and $\mathrm{NO_X}$ and their differences between June and July should be small. If now, guided by Figure 4.5, the upper tropospheric contribution of the surface sources is reduced by a factor of 3, then the total value of $\overline{\mu_{\mathrm{NO^C}}}^{ca}$ decreases by 40% in these regions. Strictly speaking, this decrease is even larger since the NO emission by lightning partly also takes place in the lower troposphere and, hence, is redistributed by convection. Thus, roughly a factor of 2 of the overestimate of the upper tropospheric NO mixing ratios during the STRATOZ III flights over tropical America is a result of the convection scheme used here. The corresponding effect for the mid-troposphere is smaller, as can be derived from Figures 4.7 and 4.8. In summary, these corrections modify $\overline{\mu_{\mathrm{NO^C}}}^{ca}$ in a way that better agreement with $\mu_{\mathrm{NO^M}}$ is obtained, but they are not sufficient to explain the entire discrepancy between both data sets.

At low latitudes during northern summer, an additional reason of high upper tropospheric values of $\overline{\mu_{\mathrm{NO^C}}}^{ca}$ might be the relatively long chemical lifetime $\tau_{\mathrm{NO_X}}$. In July, the zonal mean value of $\tau_{\mathrm{NO_X}}$ is 12.9 days at latitudes $\varphi \leq 8°$ and 200 hPa. In contrast, the corresponding January value of $\tau_{\mathrm{NO_X}}$ is 5.8 days.

Main reason of this large seasonal dependence of $\tau_{\mathrm{NO_X}}$ are variations of the O_3 mixing ratio in that part of the atmosphere. There, the present zonal mean ozone field gives values of 65 ppbv and 25 ppbv for January and July, respectively.

In the region South America, the upper tropospheric overestimate of $\mu_{\mathrm{NO^M}}$ by $\overline{\mu_{\mathrm{NO^C}}}^{ca}$ also might be a consequence of the relatively low O_3 mixing ratio of 40 ppbv at 44°S and 200 hPa in July. Since in addition the OH concentration is low there, $\tau_{\mathrm{NO_X}}$ is as long as 39 days. The mid-tropospheric values of $\overline{\mu_{\mathrm{NO^C}}}^{ca}$ are 2-3 pptv in this region, whereas $\mu_{\mathrm{NO^M}}$ is about 10 pptv. This discrepancy cannot be explained by the convection scheme, since convection only plays a minor role at winter hemispheric mid-latitudes. For the same reason possible errors due to the lightning source parametrization can be excluded. In contrast, the chemical lifetime of NO_X can be modified in a way that $\overline{\mu_{\mathrm{NO^C}}}^{ca}$ approximately fits $\mu_{\mathrm{NO^M}}$. However, such a modification requires that the error associated with each of the fields O_3, OH, $J_{\mathrm{NO_2}}$, and $J_{\mathrm{HNO_3}}$ is a factor of 2 at least and that all these errors add up in the same direction. This might be possible, but is not very likely. Apart from the lack of subgrid-scale eddy diffusion, the only other possibility why $\overline{\mu_{\mathrm{NO^C}}}^{ca}$ is so low in the South American mid-troposphere is a substantial underestimate of at least one of the sources. Such an underestimate can occur since in the real world the emission rates of the sources soil microbial activity and biomass burning strongly depend on the dryness of the soil and, hence, can vary considerably on the time scale of one or a few days. In the CTM, however, this dependence is suppressed and monthly mean emission rates are used instead. Thus, the model underestimates the NO emissions from these two sources during dry periods, but overestimates them if there is rain.

The above discussion referred to quantities derived from the temporally averaged values of $\mu_{\mathrm{NO^C}}$. The position of the minimum and maximum daily mean values shown in the right panels of Figure 6.7 indicates that in some cases as for the Great Britain profile or the upper troposphere of the profile for South America, the interval given by $[\overline{\mu_{\mathrm{NO^C}}}^{d}|_{min}, \overline{\mu_{\mathrm{NO^C}}}^{d}|_{max}]$ does include the median of $\mu_{\mathrm{NO^M}}$ at the corresponding pressure level, whereas the interval $[\langle\overline{\mu_{\mathrm{NO^C}}}^{ca}\rangle - \sigma_{sd}, \langle\overline{\mu_{\mathrm{NO^C}}}^{ca}\rangle + \sigma_{sd}]$ does not. In most cases, however, the median of $\mu_{\mathrm{NO^M}}$ lies either inside of both these intervals or outside of both. In addition, when $[\langle\overline{\mu_{\mathrm{NO^C}}}^{ca}\rangle - \sigma_{sd}, \langle\overline{\mu_{\mathrm{NO^C}}}^{ca}\rangle + \sigma_{sd}]$ is very small, the same is true usually for $[\overline{\mu_{\mathrm{NO^C}}}^{d}|_{min}, \overline{\mu_{\mathrm{NO^C}}}^{d}|_{max}]$ also, as for the Tropical American East Coast profile. Contrary to the exact value of median and standard deviation, the dominant features of the regionally averaged vertical profiles therefore do not depend on whether $\mu_{\mathrm{NO^C}}$ is averaged temporally over the time period of the campaign or not.

6.3.2 TROPOZ II

For TROPOZ II, the two data sets $\mu_{\mathrm{NO^M}}$ and $\overline{\mu_{\mathrm{NO^C}}}^{ca}$ are evaluated in the same way as done for the STRATOZ III data before. Table 6.3 shows how the individual flights are averaged, how $\mu_{\mathrm{NO^M}}$ and $\overline{\mu_{\mathrm{NO^C}}}^{ca}$ agree with each other, and where differences occur. The regionally averaged vertical profiles of $\mu_{\mathrm{NO^M}}$ and $\overline{\mu_{\mathrm{NO^C}}}^{ca}$ are shown in Figure 6.8.

During the entire campaign, the measured NO mixing ratios are higher than the corresponding values of $\overline{\mu_{\mathrm{NO^C}}}^{ca}$. The only exception are the upper troposphere in the regions Central America and Africa. In Canada and Africa, the agreement between $\mu_{\mathrm{NO^C}}$ and $\overline{\mu_{\mathrm{NO^C}}}^{ca}$ is poor because of local events which affect $\mu_{\mathrm{NO^M}}$, as noted on page 85. In the other regions, the structure of the vertical profiles is represented well by the CTM, despite the probable underestimate of μ_{NO}. As during STRATOZ III, the temporal variability of $\mu_{\mathrm{NO^C}}$ is very small in the regions Tropical American East Coast and West Atlantic and much smaller than the corresponding variability of $\mu_{\mathrm{NO^M}}$ in South America. This might indicate that the variability of possible meteorological conditions is underestimated in the CTM.

In the region Central America, similar arguments hold with respect to an effect of the convection scheme on the shape of the vertical profile of $\overline{\mu_{\mathrm{NO^C}}}^{ca}$ as those applied for the tropical American regions during STRATOZ III. In the lower and mid-troposphere of the TROPOZ II region Central America, the discrepancy between $\mu_{\mathrm{NO^M}}$ and $\overline{\mu_{\mathrm{NO^C}}}^{ca}$ is even significantly larger than it was in the corresponding region during

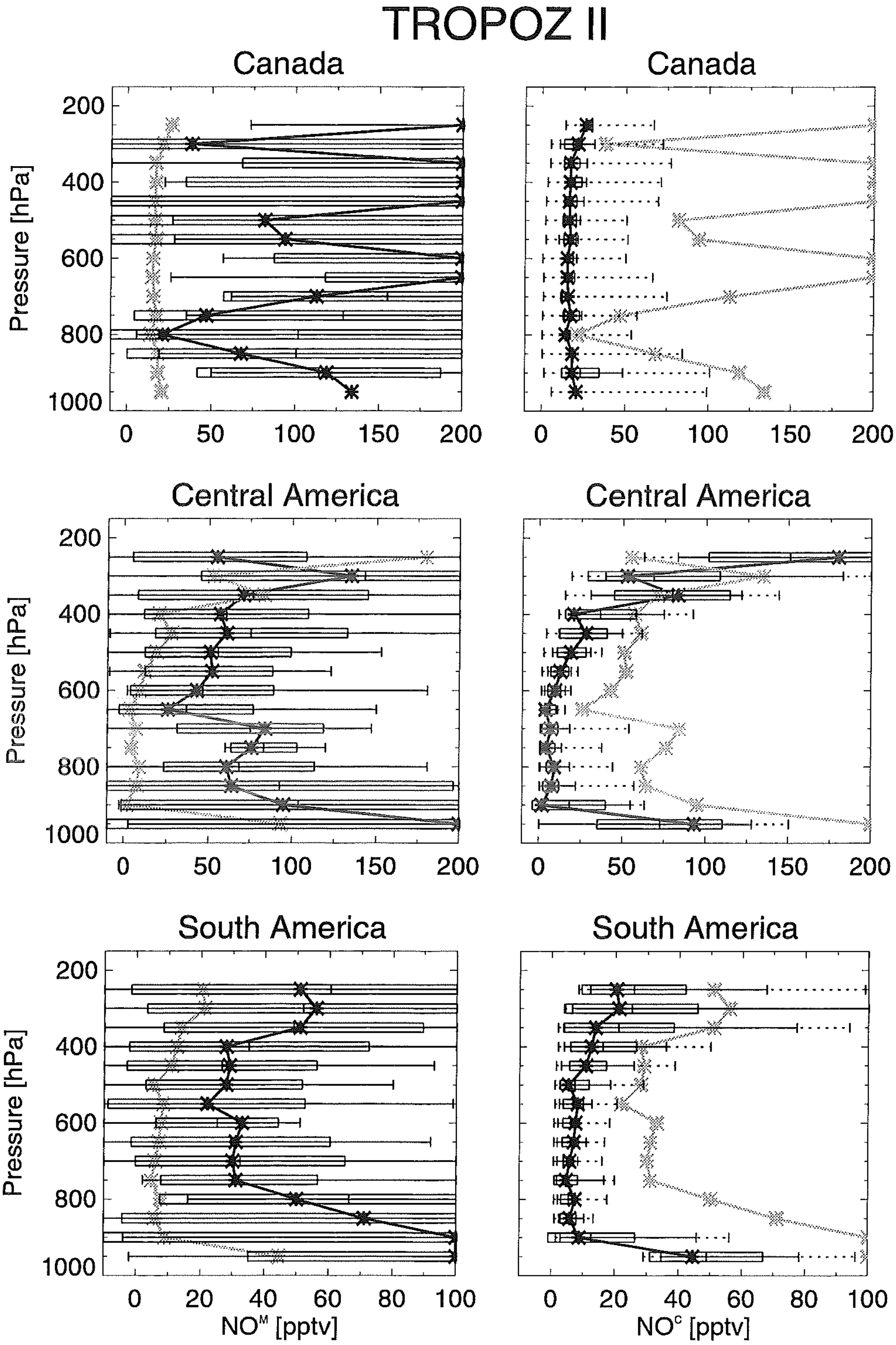

Figure 6.8: As Figure 6.7, but for TROPOZ II.

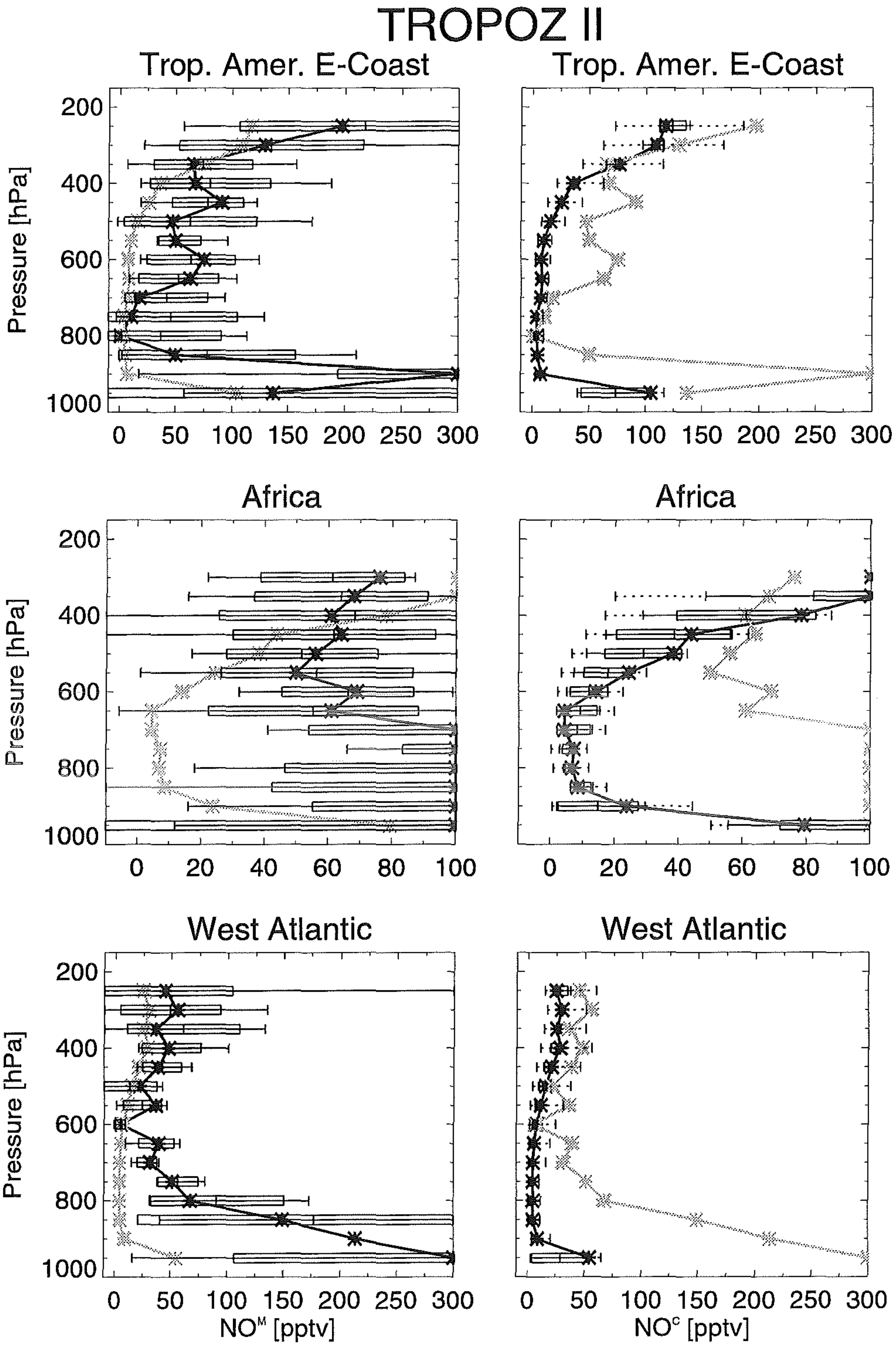

Figure 6.8: continued

region	flights	number of data points	agreement	discrepancy or comment
Canada	1-3	147	poor	$p \in [750\,\mathrm{hPa}, 350\,\mathrm{hPa}]$: $\overline{\mu_{\mathrm{NO^C}}}^{ca} \ll \mu_{\mathrm{NO^M}}$
Central America	4-9	641	medium-poor	$p \geq 400\,\mathrm{hPa}$: $\overline{\mu_{\mathrm{NO^C}}}^{ca} \lesssim \mu_{\mathrm{NO^M}}$
South America	10-16	772	structure: good	$\overline{\mu_{\mathrm{NO^C}}}^{ca} \ll \mu_{\mathrm{NO^M}}$
Trop. Amer. East Coast	17,18	189	medium-good	$p \in [650\,\mathrm{hPa}, 450\,\mathrm{hPa}]$: $\overline{\mu_{\mathrm{NO^C}}}^{ca} \ll \mu_{\mathrm{NO^M}}$
Africa	19-21	338	poor	$p \leq 350\,\mathrm{hPa}$: $\overline{\mu_{\mathrm{NO^C}}}^{ca} \gg \mu_{\mathrm{NO^M}}$ $p \geq 600\,\mathrm{hPa}$: $\overline{\mu_{\mathrm{NO^C}}}^{ca} \ll \mu_{\mathrm{NO^M}}$
West Atlantic	22,23	171	$p \leq 600\,\mathrm{hPa}$: good	$\overline{\mu_{\mathrm{NO^C}}}^{ca} \lesssim \mu_{\mathrm{NO^M}}$

Table 6.3: Evaluation of the comparison between regionally averaged vertical TROPOZ II profiles of $\mu_{\mathrm{NO^M}}$ and $\overline{\mu_{\mathrm{NO^C}}}^{ca}$ (see Figure 6.8).

STRATOZ III. Even the daily mean maximum values of $\overline{\mu_{\mathrm{NO^C}}}^{ca}$ are about a factor of 2 lower than the medians of $\mu_{\mathrm{NO^M}}$. However, the error probably made by using the convective adjustment scheme there also is significantly larger, up to a factor of 5 when averaged zonally, as Figures 4.6 and 4.8 indicate. Nevertheless such corrections are not sufficient to explain the order of magnitude difference between the observed and measured NO mixing ratios. Trajectory calculations show that the flow conditions during TROPOZ II flights 4-9 were not substantially different from those covered by the CTM [*Rohrer et al.*, 1996]. Thus, the remaining difference requires an unfortunate coupling of the errors associated with each of the prescribed fields OH, O_3, $J_{\mathrm{NO_2}}$, and $J_{\mathrm{HNO_3}}$, or a very poor representation of the sources.

The most uncertain of the sources of tropospheric $\mathrm{NO_X}$ is lightning. However, the thunderstorm activity is rather low in the region Central America during January [*Turman and Edgar*, 1982; *Orville and Henderson*, 1986; *Goodman and Christian*, 1993] and probably overestimated by the CTM. In addition, even when in the lightning source parametrization the rather unphysical case is assumed that, density-weighted, more NO is emitted in the lower than in the upper troposphere (see case E2 in Figure 3.11), the resulting change in the vertical profile of $\mu_{\mathrm{NO_X}}$ is only about a factor of 2. Implementation of a lightning source based on the satellite observations of *Turman and Edgar* [1982] does not improve the vertical μ_{NO} profile in the region Central America neither, since it further decreases the NO emission in the tropics, in favour of emissions at mid-latitudes.

Since fossil fuel combustion is the best known of the surface sources of tropospheric $\mathrm{NO_X}$, the only other possibility why $\overline{\mu_{\mathrm{NO^C}}}^{ca}$ is so low in the lower and mid-troposphere of the region Central America is a substantial local underestimate of the sources biomass burning and soil microbial activity. Such an underestimate is not unlikely because of the considerable temporal variability of their emission rates which is not resolved by the CTM. The same also is true for emissions from the the lightning source.

In the regions South America, Tropical American East Coast and West Atlantic, convection plays a less dominant role than in the region Central America. Consequently, $\overline{\mu_{\mathrm{NO^C}}}^{ca}$ increases only slightly with altitude and remains lower than $\mu_{\mathrm{NO^C}}$ even at 200 hPa. In the regions South America and Tropical American East Coast, some of the CTM's underestimate of μ_{NO} can be explained by the fact that, in the model, the centre of deep convection occurs too close to the equator and, hence, lightning is underestimated south of

region	flights	number of data points	agreement	discrepancy or comment
Extratrop. Pacific	1-3, 19	540	p $\leq$ 450 hPa: poor p$\geq$ 550 hPa: good	p $\leq$ 450 hPa: $\overline{\mu_{\mathrm{NO}^{\mathrm{C}}}}^{ca} \gg \mu_{\mathrm{NO}^{\mathrm{M}}}$
Japan	4-8	865	p $\leq$ 500 hPa: poor p$\geq$ 550 hPa: good	p $\leq$ 500 hPa: $\overline{\mu_{\mathrm{NO}^{\mathrm{C}}}}^{ca} \gg \mu_{\mathrm{NO}^{\mathrm{M}}}$
Hong Kong	9-12	754	p $\leq$ 450 hPa: poor p$\geq$ 500 hPa: good	p $\leq$ 450 hPa: $\overline{\mu_{\mathrm{NO}^{\mathrm{C}}}}^{ca} \gg \mu_{\mathrm{NO}^{\mathrm{M}}}$
Tropical Pacific	13-18	1118	medium-good	p $\leq$ 300 hPa: $\overline{\mu_{\mathrm{NO}^{\mathrm{C}}}}^{ca} \gg \mu_{\mathrm{NO}^{\mathrm{M}}}$

Table 6.4: Evaluation of the comparison between regionally averaged vertical PEM-West A profiles of $\mu_{\mathrm{NO}^{\mathrm{M}}}$ and $\overline{\mu_{\mathrm{NO}^{\mathrm{C}}}}^{ca}$ (see Figure 6.9).

20°S. However, because of the simultaneous underestimate if μ_{NO} at lower latitudes, an additional process is more likely to be the main reason of the low mid-tropospheric values of μ_{NO}.

During all TROPOZ II flights in the region South America, westerlies were prevailing. Hence, purely oceanic air was sampled on the southbound flights 10-12 and air that has been passing over South America on the northbound flights 13-16. Despite this, the observed NO mixing ratios are similar for both the southbound and the northbound flights. This might point towards a missing oceanic source of NO, not a continental one, at least at southern mid-latitudes. A slight underestimate of the chemical lifetime $\tau_{\mathrm{NO_X}}$ over oceans may arise because the O_3 mixing ratios are averaged zonally and, hence, are too high over oceans. However, the zonal variation of O_3 at southern mid-latitudes is not larger than a factor of 2 at most [*Müller and Brasseur*, 1995], and, much more important, it is OH which primarily determines the lower tropospheric lifetime of NO_X. The OH field used here was proved to result in realistic global lifetimes of CH_3CCl_3 [*Spivakovsky et al.*, 1990]. Despite this, the spatial distribution of OH still can be unrealistic and, maybe, there is an overestimate of southern hemispheric oceanic OH concentrations at mid-latitudes.

Finally, in the region West Atlantic, the CTM is able to reproduce both the structure and the order of magnitude of the mean vertical profile derived from the observed NO mixing ratios. The high values of $\mu_{\mathrm{NO}^{\mathrm{M}}}$ below 800 hPa probably are an effect of local pollution within the PBL and do not indicate basic disagreement between both vertical profiles, as in the same region during STRATOZ III.

6.3.3 PEM-West A

For PEM-West A, the distribution of the individual flights into regions is given in Table 6.4[1]. The corresponding regionally averaged vertical profiles of $\mu_{\mathrm{NO}^{\mathrm{M}}}$ and $\overline{\mu_{\mathrm{NO}^{\mathrm{C}}}}^{ca}$ are shown in Figure 6.9. Table 6.4 in addition classifies the agreement between both kinds of profiles and denotes pressure layers where discrepancies occur.

In the lower and mid-troposphere in all of the four PEM-West A regions, the CTM either reproduces the observed NO mixing ratios exactly or underestimates $\mu_{\mathrm{NO}^{\mathrm{M}}}$ slightly. Above 400 hPa, $\overline{\mu_{\mathrm{NO}^{\mathrm{C}}}}^{ca}$ is about

---

[1] Flights 3 and 19 are combined with flights 1 and 2 to the region Extratropical Pacific, although the upper tropospheric values of $\mu_{\mathrm{NO}^{\mathrm{M}}}$ are rather different for both groups, as Figure 6.5 shows. The reason why this combination nevertheless is possible is that the traverse parts of both pairs of flights, during which the largest number of data was gained, took place at different altitudes and, hence, contribute to different pressure layers in the corresponding panels of Figure 6.9. In fact, all data points of the pressure layer 200 hPa there are from flight 3, but only 2 of 57 in the layer 250 hPa. In the lower and mid-troposphere, the variability of $\mu_{\mathrm{NO}^{\mathrm{M}}}$ is small for the entire region.

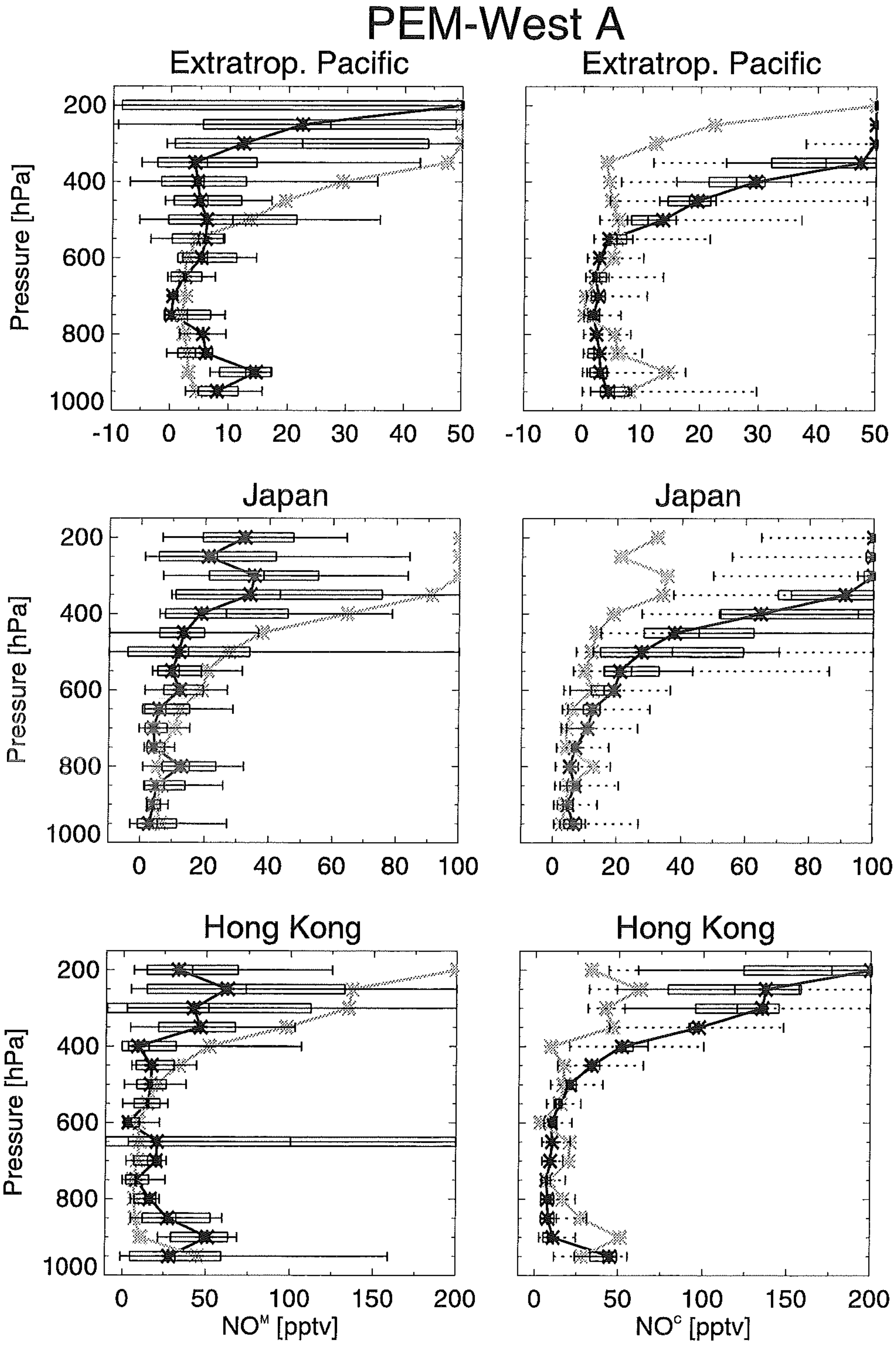

Figure 6.9: As Figure 6.7, but for PEM-West A.

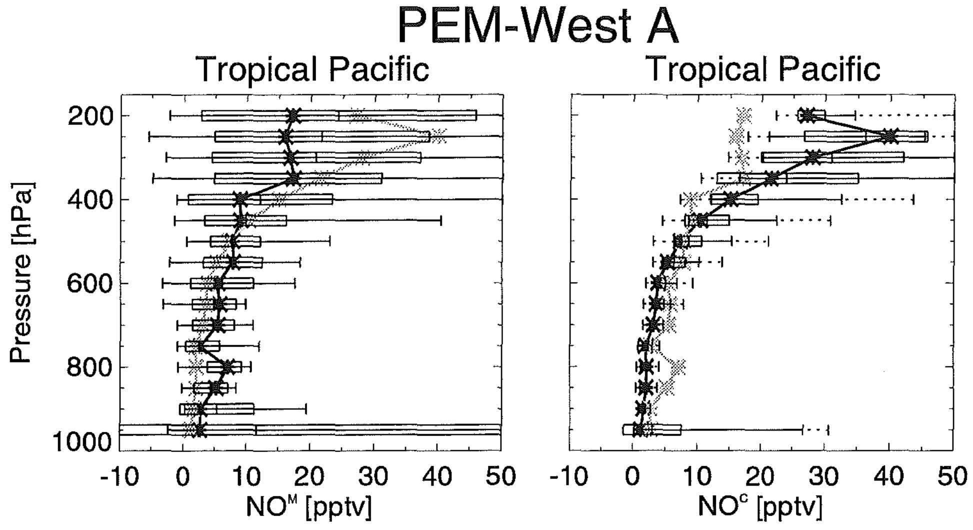

Figure 6.9: continued

two times larger than $\mu_{\mathrm{NO^M}}$, except in the region Japan, where this difference is even larger. The main reason for this poor agreement is the fact that, during flights 4, 6, and 7, an anticyclone off the Japanese east coast advected oceanic air of low NO content into the sampling region [for trajectory calculations, see *Merrill*, 1996]. Such anticyclones are no untypical feature, but persisted during the entire time period of the campaign [*Bachmeier et al.*, 1996]. In the CTM, however, their occurrence is suppressed due to the low model resolution. Instead, the region Japan is dominated by strong westerlies advecting air that has been passing over the entire Eurasian continent. Moreover, the NO content of the upper tropospheric westerlies probably is overestimated downwind the continent because of their low variability and, in addition, strong convection over China, as discussed on page 46. The overestimate of $\mu_{\mathrm{NO^M}}$ by $\overline{\mu_{\mathrm{NO^C}}}^{ca}$ in the region Extratropical Pacific presumably is caused by the same process.

In the regions Hong Kong and Tropical Pacific, the contribution of NO emitted by lightning discharges is 20-40 % and about 60%, respectively. Hence, an unrealistic vertical redistribution of these emissions by the present convective scheme can explain the overestimate of $\mu_{\mathrm{NO^M}}$ by $\overline{\mu_{\mathrm{NO^C}}}^{ca}$ above the Tropical Pacific, but only partly in the region Hong Kong. However, this effect is difficult to estimate since the comparsion of the ^{222}Rn distribution discussed in Chapter 4 is limited to January and July, whereas PEM-West A took place during September and October. If correction factor of 2 is assumed for the upper troposphere, then this is sufficient to explain the deviation of $\overline{\mu_{\mathrm{NO^C}}}^{ca}$ from $\mu_{\mathrm{NO^M}}$ in the region Tropical Pacific. In the region Hong Kong, the upper tropospheric values of $\mu_{\mathrm{NO^M}}$ are similar to those over the Tropical Pacific, as it is the chemical lifetime $\tau_{\mathrm{NO_X}}$ in the model. Hence, if the lack of a zonal gradient in the OH concentration between both regions is assumed to be realistic, an overestimate of the upper tropospheric westward transport of polluted air from the Asian continent remains as a possible explanation of the high values of $\overline{\mu_{\mathrm{NO^C}}}^{ca}$ in the region Hong Kong (see Figure A.4).

6.3.4 PEM-West B

For PEM-West B, the two data sets $\mu_{\mathrm{NO^M}}$ and $\overline{\mu_{\mathrm{NO^C}}}^{ca}$ are evaluated in the same way as before. Table 6.5 shows how the individual flights are averaged, classifies the agreement between $\mu_{\mathrm{NO^M}}$ and $\overline{\mu_{\mathrm{NO^C}}}^{ca}$, and denotes where differences occur. The regionally averaged vertical profiles of $\mu_{\mathrm{NO^M}}$ and $\overline{\mu_{\mathrm{NO^C}}}^{ca}$ are shown in Figure 6.10.

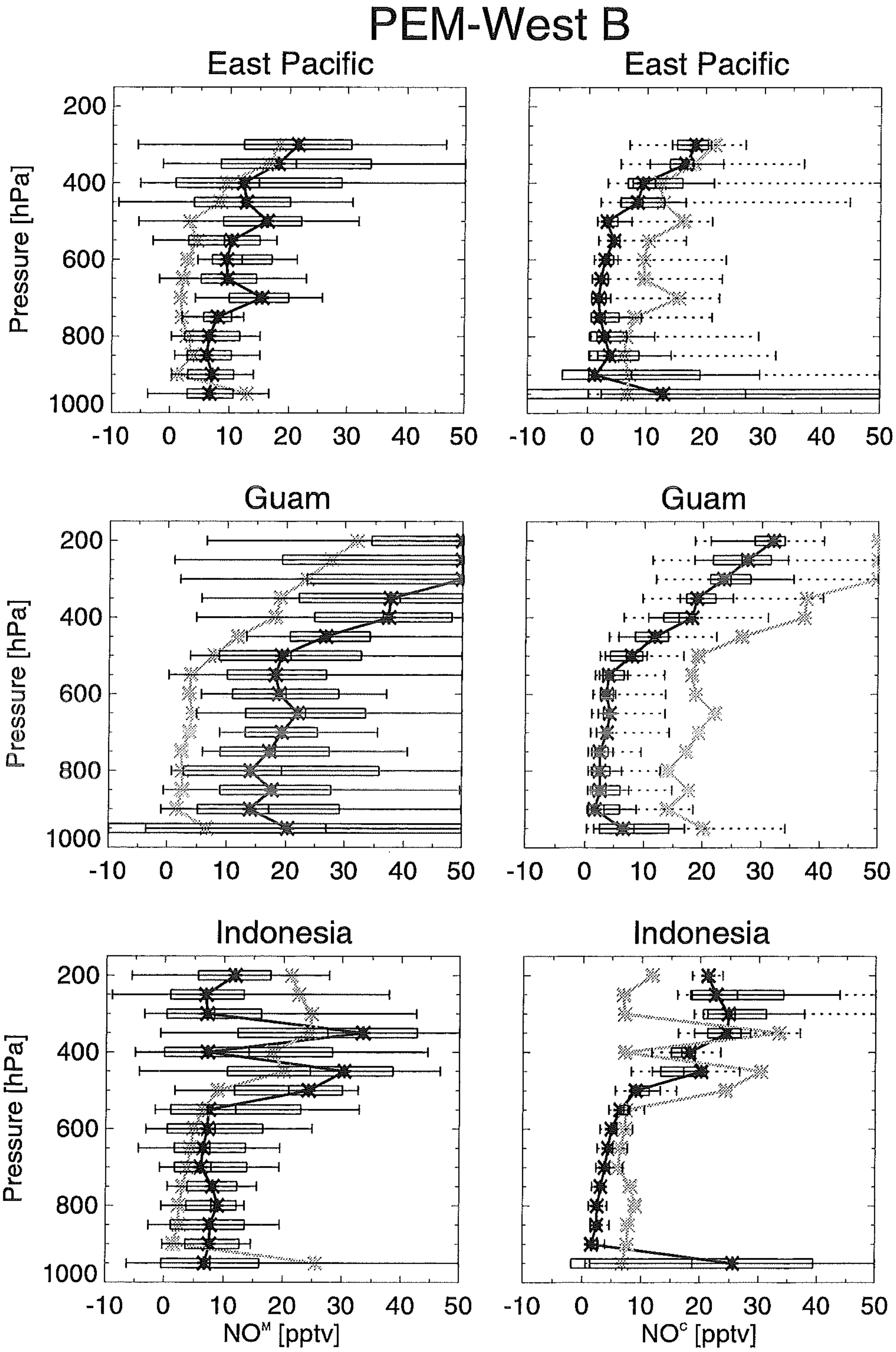

Figure 6.10: As Figure 6.7, but for PEM-West B.

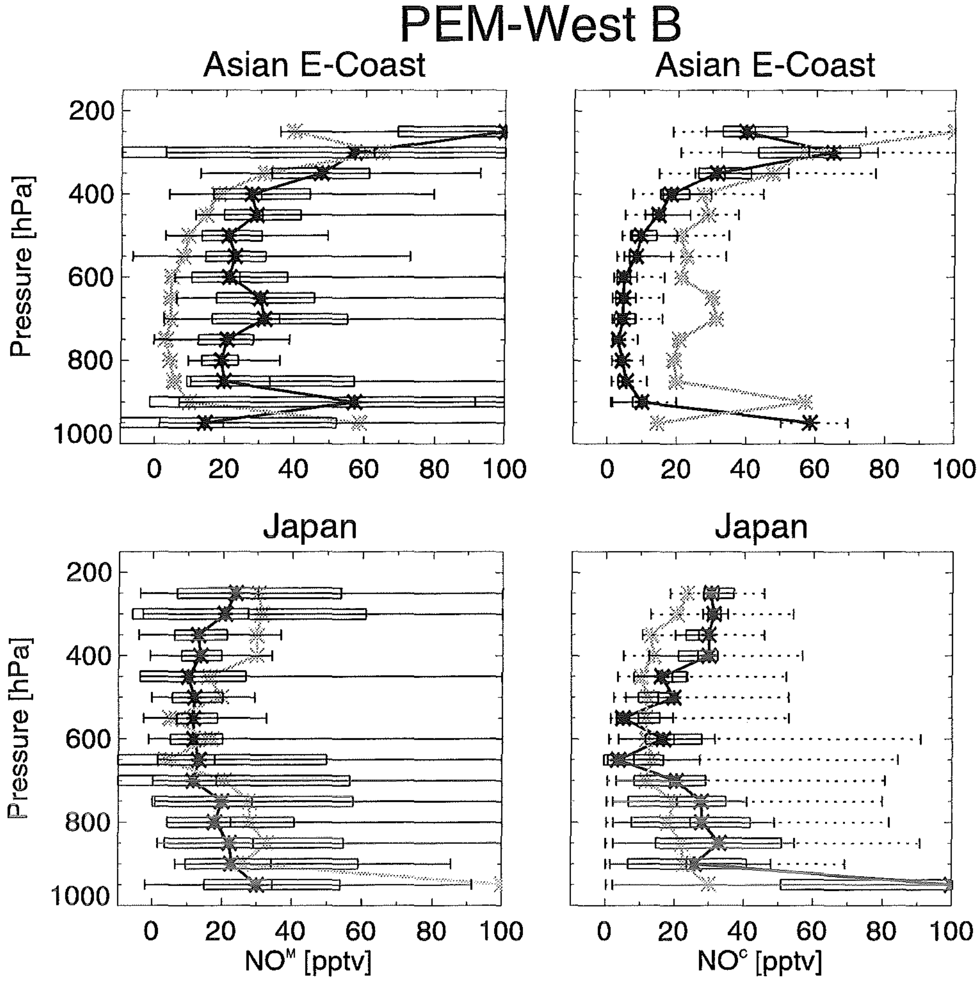

Figure 6.10: continued

Since for PEM-West B a detailed analysis of the prevailing meteorological conditions or of trajectory calculations is not yet published, an interpretation of the regionally averaged vertical profiles is more difficult than it was for the other campaigns. However, the profiles calculated for the regions East Pacific, Indonesia, and Japan agree well with the corresponding profiles of $\mu_{\mathrm{NO^M}}$. Apart from a factor of 2 overestimate of $\mu_{\mathrm{NO^M}}$ in the Indonesian upper troposphere, this good agreement includes both the structure and the absolute values of $\mu_{\mathrm{NO^M}}$. The increased values of $\mu_{\mathrm{NO^M}}$ at mid-tropospheric levels in the region East Pacific might be caused by local continental outflow from North America associated with an anticyclone not resolved by the CTM.

In the region Asian East Coast, there are three possibilities why the mid-tropospheric values of $\overline{\mu_{\mathrm{NO^C}}}^{ca}$ are significantly smaller than those of $\mu_{\mathrm{NO^M}}$. The CTM may underestimate the northward extent of thunderstorm activity, may have a chemical lifetime $\tau_{\mathrm{NO_X}}$ which is too short, or may advect continental air of a too low NO content. The latter probably explains part of the low $\overline{\mu_{\mathrm{NO^C}}}^{ca}$ values since it is a consequence of the convection scheme used here. The wind speeds of the advecting westerlies themselves are high enough, but μ_{NO} generally is low at 500 hPa within the entire PEM-West B region, as Figures A.1 and A.2 show.

region	flights	number of data points	agreement	discrepancy or comment
East Pacific	1,16	2253	medium-good	$\overline{\mu_{NO^C}}^{ca} \lesssim \mu_{NO^M}$
Guam	2-5	6826	structure: good	$\overline{\mu_{NO^C}}^{ca} \ll \mu_{NO^M}$
Indonesia	6,7	2730	medium-good	$p \leq 300$ hPa: $\overline{\mu_{NO^C}}^{ca} \ll \mu_{NO^M}$
Asian East Coast	8-11	5775	medium-poor	$\overline{\mu_{NO^C}}^{ca} \ll \mu_{NO^M}$ $\overline{\mu_{NO^C}}^{ca} \ll \mu_{NO^M}$
Japan	12-15	5736	good	$\overline{\mu_{NO^C}}^{ca} \lesssim \mu_{NO^M}$

Table 6.5: Evaluation of the comparison between regionally averaged vertical PEM-West B profiles of μ_{NO^M} and $\overline{\mu_{NO^C}}^{ca}$ (see Figure 6.10).

However, since the chemical lifetime τ_{NO_X} is only about half a day at 700 hPa and slightly less than one day at 500 hPa, high values of $\overline{\mu_{NO^C}}^{ca}$ cannot be expected far off the Asian coast, even when higher amounts of NO were injected upwind. The low value of τ_{NO_X} mainly reflects high OH concentrations.

The region Guam is dominated by weak easterlies or north-easterlies throughout the depth of the troposphere, at least in the CTM. Hence, $\overline{\mu_{NO^C}}^{ca}$ is very low there. The reason why μ_{NO^M} is higher than $\overline{\mu_{NO^C}}^{ca}$ by about a factor of 5 at all altitudes again probably is a consequence of the low chemical lifetime τ_{NO_X}, since local NO emissions by lightning discharges should be rare [*Orville and Henderson*, 1986; *Goodman and Christian*, 1993]. In addition, if τ_{NO_X} is assumed to be longer than in the CTM, then the different mid-tropospheric values of μ_{NO} measured in the regions Guam and Indonesia might be explainable by a different air mass history. The fact that in the former region the variability of the daily mean values of μ_{NO^C} is much larger than in the latter could indicate the existence of such variability.

6.3.5 Summary and Discussion of the Comparison Between Regionally Averaged Vertical Profiles

The most important point of the foregoing comparison is that in each individual region, at each altitude, and during each season covered by the four aircraft campaigns the CTM yields NO mixing ratios of the same order of magnitude as the measurements. This is a nontrivial result since the NO mixing ratios which occur in the troposphere extend over a range of more than 5 orders of magnitudes. Furthermore, the present CTM is a very simple model, much simpler than most of the models currently used. Even more important than its simplicity is the fact that the resolution of the CTM is very coarse. Strictly speaking the one-dimensional data sets of aricraft measurements used here are not sufficent to provide a reliable data base for testing model results which are extensively averaged over four dimensions, at least if distributions of a tracer as short-living as NO_X are investigated. Despite this, the regionally averaged vertical profiles based on CTM calculations are able to reproduce most of the dominant features of the corresponding profiles derived from aircraft measurements.

Although the broad agreement between aircraft measurements and model results is quite good with respect to the very different resolution of both data sets, there are considerable deviations in detail. Generally, the CTM tends to underestimate the NO mixing ratios measured during the four aircraft campaigns in the lower and mid-troposphere. This underestimate usually is up to a factor of 2-3, but reaches almost one order of magnitude in South America. In the upper troposphere, the reverse is true in most regions: the model calculated mixing ratios $\overline{\mu_{\mathrm{NO}^{\mathrm{C}}}}^{ca}$ are higher than the caluclated data $\mu_{\mathrm{NO}^{\mathrm{M}}}$ by about a factor of 2, except during PEM-West B where $\overline{\mu_{\mathrm{NO}^{\mathrm{C}}}}^{ca}$ underestimates $\mu_{\mathrm{NO}^{\mathrm{M}}}$ throughout the depth of the troposphere. In addition, large discrepancies between $\mu_{\mathrm{NO}^{\mathrm{M}}}$ and $\overline{\mu_{\mathrm{NO}^{\mathrm{C}}}}^{ca}$ occur when the measurements are affected by local events like bush-fires which are not captured by the CTM. Apart from those events, there are some possible minor and four major reasons of large deviations of $\overline{\mu_{\mathrm{NO}^{\mathrm{C}}}}^{ca}$ from $\mu_{\mathrm{NO}^{\mathrm{M}}}$. Minor effects may arise due to uncertainties of the measurement technique, due to the fact that $\overline{\mu_{\mathrm{NO}^{\mathrm{C}}}}^{ca}$ describes daily mean, not actual values of μ_{NO}, or due to the negection of $\mathrm{NO_X}$ produced by oxidation of $\mathrm{NH_3}$. The four possible major reasons are:

1. A missing or insufficiently parametrized source.
2. An unrealistic vertical tracer redistribution due to the convection scheme used here.
3. Suppression of synoptic- and smaller scale transport features because of the low model resolution.
4. Unrealistic chemical lifetimes of $\mathrm{NO_X}$.

All of these major reasons help to explain the large discrepancies between $\overline{\mu_{\mathrm{NO}^{\mathrm{C}}}}^{ca}$ and $\mu_{\mathrm{NO}^{\mathrm{M}}}$, at least partly. Which role each of these major reasons plays is dependent on which region and which season is considered. In most cases a combination of several of these major reasons may act.

A missing source cannot make large contributions to the total atmospheric burden of $\mathrm{NO_X}$ since otherwise the nitrate deposition measurements would not agree with corresponding calculated deposition rates. Such a comparison was made, but only for the American continent for which *Penner et al.* [1991] evaluated nitrate deposition measurements [*Kraus et al.*, 1996]. Despite this restriction, an additional source of tropospheric $\mathrm{NO_X}$ is not very likely, at least if the source is a non-chemical one. The role of PAN, a possible chemical source of tropospheric $\mathrm{NO_X}$ is discussed below. Much more important in this context is the fact that the temporal resolution of the emission scenarios used in the CTM to describe the sources microbial activity in soils and biomass burning is only one month. This resolution suppresses the high variability of their emission rates which arises due to the strong dependence on the actual weather and the actual soil humidity. To a smaller extent the same is true for the other sources also.

The lightning source parametrization is unrealistic to the same degree as the CTM's deep wet convection is unrealistic. The horizontal distribution of the lightning source has been fitted to observations, but the problem how these emissions have to be distributed vertically still exists. However, since the agreement between the vertical profiles of $\mu_{\mathrm{NO}^{\mathrm{M}}}$ and $\overline{\mu_{\mathrm{NO}^{\mathrm{C}}}}^{ca}$ is increased when the unphysical case is assumed that lightning emits, density-weighted, more NO in the lower than in the upper troposphere, it is more likely that not the emission profile of the lightning source is unrealistic, but the redistribution of these emissions by the present convection scheme. The assumption that the convective tracer redistribution is unrealistic is supported by the results of Chapter 4. Since in addition to the $\mathrm{NO_X}$ contribution from lightning discharges, the contributions from the surface sources are affected by the vertical tracer redistribution, this effect totals up to approximately a factor of 2.

Regionally, the low model resolution has a substantial effect, as during PEM-West A over Japan. Furthermore, the CTM's global-scale tracer transport could be affected by the lack of synoptic- and smaller scale eddy diffusion, an underestimate of variability and the resulting underestimate of horizontal as well as vertical mixing processes. The $^{222}\mathrm{Rn}$ studies of *Balkanski and Jacob* [1990]; *Balkanski et al.* [1992] point into that direction (see pages 45 and 46).

The chemical lifetime of $\mathrm{NO_X}$ is determined by the concentrations of OH and $\mathrm{O_3}$. Reaction with OH is the main chemical removal process of $\mathrm{NO_X}$ in the lower troposphere, whereas reaction with $\mathrm{O_3}$ is dominant in the upper troposphere. Hence, in order to explain the deviations of $\overline{\mu_{\mathrm{NO}^{\mathrm{C}}}}^{ca}$ from $\mu_{\mathrm{NO}^{\mathrm{C}}}$, the concentration of OH must be too high and that of $\mathrm{O_3}$ too low at the corresponding altitude in the CTM. Since *Spivakovsky et al.* [1990] proved the global total of their calculated OH to be realistic by a comparison with measurements of $\mathrm{CH_3CCl_3}$, only the regional or altitudinal distribution of this species can be wrong. At southern mid-latitudes, the mid-tropospheric OH concentrations might be overestimated over the Pacific.

CTM runs carried out with a nonlinear chemistry scheme and fields of OH and O_3 which are different from the ones used here give up to a factor of 2 lower values of μ_{NO} in the upper troposphere, but changes of only about 25% at mid-tropospheric levels [*Kuhn*, 1996]. In the lower troposphere, the largest zonal mean difference between both calculations occurs at 30-40°S, where the NO_X mixing ratios obtained by the nonlinear chemistry are more than 50% higher.

When the effect of PAN on tropospheric NO_X is estimated as it was done by *Moxim et al.* [1996], then the mid-tropospheric NO_X mixing ratios increase by less than a factor of 2 over remote oceanic regions and decrease by up to 25% over the continental source regions. Following *Kuhn* [1996], inclusion of PAN affects the global distribution of NO_X even less. He finds that with PAN the mid-tropospheric NO_X mixing ratio increases over oceans by 10-20% in January and by about 10% in July compared to runs without PAN. Over continents, this increase is 2-10%. However, the zonal mean PAN concentrations he obtains in the upper troposphere are about a factor of 2 lower than those calculated by *Singh et al.* [1995]. Main reason for this discrepancy is that *Singh et al.* include emission and transport of acetone. Based on a combination of upper tropospheric acetone measurements and model data, they postulate that up to 50% of the observed PAN concentrations may be formed as a result of the photolysis of acetone, mainly by production of peroxyacetyl radicals which react with NO_2. Additionally, the NO_X concentration is reduced since the acetone photolysis leads to an increase of OH radicals, but conversion into PAN by peroxyacetyl radicals is the dominant process. Altogether, the upper toposperic NO_X concentration decreases considerably if the acetone chemistry suggested by *Singh et al.* [1995] is assumed.

An additional source of uncertainties in the chemistry scheme used here is the fact that all photolysis rates describe clear sky conditions. However it is not clear whether inclusion of clouds increases or decreases the present NO_X mixing ratios in the lower and mid-troposphere where the majority of clouds occurs. On the one hand, lower values of J_{NO_2} decrease the the ratio NO/NO_X, but on the other hand the concentration of OH is decreased also. In addition, the conversion of NO_X into HNO_3 is slower at lower temperatures, i.e. below clouds.

6.4 Zonally Averaged Latitude-Altitude Cross Sections

A different aspect of the comparison between the NO mixing ratios measured during the four aircraft campaigns and the corresponding CTM results is the question of how good the model is able to reproduce the spatial structure of the observations. One way to answer this question is to consider zonally averaged fields of μ_{NO}. However, zonal averages must be interpreted carefully, because large differences might cancel as they occur, for example, between continental and oceanic air. Not only much of the information contained in the original data is lost by such cancelling, but in addition structures can be generated which are never observed.

A useful tool to judge whether averaged fields obtain most of the original large-scale structure is an analysis of variances [*Spiegel*, 1975; *Ehhalt et al.*, 1996]. For this purpose, the total number N of samples x of the field X is distributed among K boxes. Each of these boxes contains J_k individual samples. Hence, $\sum_{k=1}^{K} J_k = N$. The total variance, the in-box variance, and the in-between box variance are defined by:

$$V_{tot}(X) \equiv \frac{1}{N}\sum_{n=1}^{N}(x_n - \langle x\rangle)^2 , \tag{6.2}$$

$$V_{ib}(X) \equiv \frac{1}{N}\sum_{k=1}^{K}\sum_{j=1}^{J_k}(x_{k_j} - \langle x_k\rangle)^2 , \tag{6.3}$$

$$V_{bb}(X) \equiv \frac{1}{K}\sum_{k=1}^{K} J_k(\langle x_k\rangle - \langle x\rangle)^2 , \tag{6.4}$$

where $\langle x\rangle \equiv N^{-1}\sum_{n=1}^{N} x_n$ is the total mean value, x_{k_j} denotes the j-th sample in box k and $\langle x_k\rangle \equiv$

$J_k^{-1}\sum_{j=1}^{J_k} x_{k_j}$ is the mean value of the J_k samples x_{k_j} contained in box k. Since $V_{tot} = V_{ib} + V_{bb}$, the total variance can be divided into a contribution from the scatter of the individual values in each box around the box mean value and a contribution arising due to different box mean values. The in-box variance is a measure of the "noise" within individual boxes, i.e. of small-scale fluctuations, whereas the between-box variance measures the degree of large-scale structure contained in the entire data set. With increasing K, V_{ib} decreases and V_{bb} increases. Furthermore, high values of V_{bb} indicate that the data field is dominated by large-scale structures. Contrary, high values of V_{ib} occur when either the local fluctuations are high or in the case that data of different characteristics are averaged into one box.

In the following comparison between measured and calculated two-dimensional fields of NO mixing ratios the number of boxes K considered for each campaign is equal to the number of CTM grid boxes which are covered by the square extending from the most southern to most northern data point and from 850 hPa to 200 hPa. As before, the meridional and vertical resolution of a box are 8° and 50 hPa, respectively. Data obtained at a pressure higher than 850 hPa are neglected because of their high variability.

Table 6.6 gives the values of V_{tot}, V_{ib}, and V_{bb} as well as several other quantities derived from the data sets $\mu_{\mathrm{NO^M}}$, $\overline{\mu_{\mathrm{NO^C}}}^{ca}$, and the differences $\mu_{\mathrm{NO^M}} - \overline{\mu_{\mathrm{NO^C}}}^{ca}$ for each campaign. For STRATOZ III and TROPOZ II, the complete data sets additionally are divided into northbound and southbound subsets. This is done in order to take into account that rather different NO mixing ratios were measured during the corresponding parts of both campaigns, at least in the northern hemisphere. The variances given in Table 6.6 are normalized, i.e. before they are calculated, $\mu_{\mathrm{NO^M}}$ and $\overline{\mu_{\mathrm{NO^C}}}^{ca}$ are divided by their absolute mean values. This allows a direct comparison of the variances for the individual campaigns. Before the variances given in Table 6.6 are interpreted, first the corresponding zonally averaged fields of $\mu_{\mathrm{NO^M}}$ and $\overline{\mu_{\mathrm{NO^C}}}^{ca}$ are discussed briefly which are shown in Figures 6.11-6.13.

During STRATOZ III, the zonally averaged fields $\langle\mu_{\mathrm{NO^M}}\rangle_\lambda$ derived from the northbound and from the southbound flights are rather different, in contrast to the corresponding fields of $\langle\overline{\mu_{\mathrm{NO^C}}}^{ca}\rangle_\lambda$, as Figure 6.11 shows. The agreement between $\langle\mu_{\mathrm{NO^M}}\rangle_\lambda$ and $\langle\overline{\mu_{\mathrm{NO^C}}}^{ca}\rangle_\lambda$ is quite good for the northbound flights, but rather poor for the southbound flights, mainly because of high values of $\mu_{\mathrm{NO^M}}$ in the southern hemispheric lower troposphere. The CTM generally tends to underestimate the lower and mid-tropospheric NO mixing ratios. Reasons for this underestimate are discussed in detail in the previous section.

Figure 6.12 shows that $\langle\overline{\mu_{\mathrm{NO^C}}}^{ca}\rangle_\lambda$ is almost identical for the TROPOZ II northbound and southbound flights: NO mixing ratios higher than 100 pptv in the tropical upper troposphere, but significantly lower values everywhere else. For the southbound flights, $\langle\mu_{\mathrm{NO^M}}\rangle_\lambda$, is dominated by the extremely high values observed over Canada, whereas in the tropics and in the southern hemisphere only weak gradients occur. The same is true for the northbound flights throughout the entire sampling area.

During PEM-West A, the structure of $\langle\mu_{\mathrm{NO^M}}\rangle_\lambda$ and $\langle\overline{\mu_{\mathrm{NO^C}}}^{ca}\rangle_\lambda$ is similar, but $\langle\overline{\mu_{\mathrm{NO^C}}}^{ca}\rangle_\lambda$ has by more than a factor of 2 higher values in the upper troposphere around 30°N than $\langle\mu_{\mathrm{NO^M}}\rangle_\lambda$, as the upper panels of Figure 6.13 show. The local mid-tropospheric maxima of $\mu_{\mathrm{NO^M}}$ are a result of individual spikes (see the panels for the regions Japan and Hong Kong in Figure 6.9) which have been removed in the calculation of the variances given in Table 6.6.

The lower panels of Figure 6.13 show that during PEM-West B the lower and mid-tropospheric gradients of $\langle\mu_{\mathrm{NO^M}}\rangle_\lambda$ and $\langle\overline{\mu_{\mathrm{NO^C}}}^{ca}\rangle_\lambda$ are similarly low as during PEM-West A. In the upper troposphere, however, the results obtained for PEM-West A are reversed here: a significant peak around 30°N in the measured data, but no meridionally uniform values of $\overline{\mu_{\mathrm{NO^C}}}^{ca}$.

Table 6.6 shows that during all campaigns V_{tot} is larger for the measurement data than for the model calculation, as expected due to the different resolution of both data sets. The only exception are the TROPOZ II northbound flights, where V_{tot} is slightly larger for $\overline{\mu_{\mathrm{NO^C}}}^{ca}$. For these flights both the meridional and the altitudinal gradients of $\mu_{\mathrm{NO^M}}$ are weak. In the model, however, there is a clear peak of $\overline{\mu_{\mathrm{NO^C}}}^{ca}$ in the tropical upper troposphere (see the lower panels of Figure 6.12).

campaign	data set	data points N	absol. mean value $\langle\mu_{\mathrm{NO}}\rangle$	normal. total variance V_{tot}	normal. between-box var. V_{bb}	normal. in-box variance V_{ib}	fraction V_{bb}/V_{tot}	fraction V_{ib}/V_{tot}
STRATOZ III	meas.	2163	49.96	1.98	1.07	0.92	0.54	0.46
	calc.		61.63	1.30	1.19	0.12	0.91	0.09
	diff.		0.010	1.70	0.65	1.05	0.38	0.62
STRATOZ III Northbound	meas.	1342	54.11	2.06	1.19	0.89	0.57	0.43
	calc.		53.15	0.87	0.87	8.e-3	0.99	0.001
	diff.		0.010	1.36	0.49	0.87	0.36	0.64
STRATOZ III Southbound	meas.	821	43.17	1.63	1.22	0.43	0.74	0.26
	calc.		75.48	1.53	1.53	1.e-4	1.00	1.e-4
	diff.		0.011	1.42	0.99	0.42	0.70	0.30
TROPOZ II	meas.	2125	85.77	1.85	0.90	0.95	0.49	0.51
	calc.		43.63	1.33	1.24	0.08	0.94	0.06
	diff.		0.002	3.03	2.02	1.01	0.67	0.33
TROPOZ II Northbound	meas.	1023	77.88	1.11	0.61	0.50	0.55	0.45
	calc.		37.35	1.19	1.19	5.e-3	1.00	4.e-3
	diff.		0.003	1.54	1.03	0.51	0.67	0.33
TROPOZ II Southbound	meas.	1102	93.08	2.29	1.40	0.89	0.61	0.39
	calc.		49.47	1.33	1.28	0.05	0.97	0.03
	diff.		0.002	3.98	2.96	0.93	0.76	0.24
PEM-West A	meas.	2878	25.62	2.38	0.64	1.74	0.27	0.73
	calc.		55.60	0.86	0.76	0.10	0.88	0.12
	diff.		3.e-6	2.10	0.45	1.65	0.21	0.79
PEM-West B	meas.	20585	37.74	1.24	0.54	0.71	0.43	0.57
	calc.		22.50	0.53	0.37	0.17	0.71	0.29
	diff.		3.e-4	1.23	0.32	0.92	0.26	0.74

Table 6.6: Statistical data related to the zonally averaged values of the measured and calculated NO mixing ratios of each campaign. The abbreviations in the second column denote measurements ($\mu_{\mathrm{NO}^{\mathrm{M}}}$), CTM calculation ($\overline{\mu_{\mathrm{NO}^{\mathrm{C}}}}^{ca}$), and the difference $\mu_{\mathrm{NO}^{\mathrm{M}}} - \overline{\mu_{\mathrm{NO}^{\mathrm{C}}}}^{ca}$. The variances in colums 5-7 are defined in Equations (6.2)-(6.4). See text for discussion.

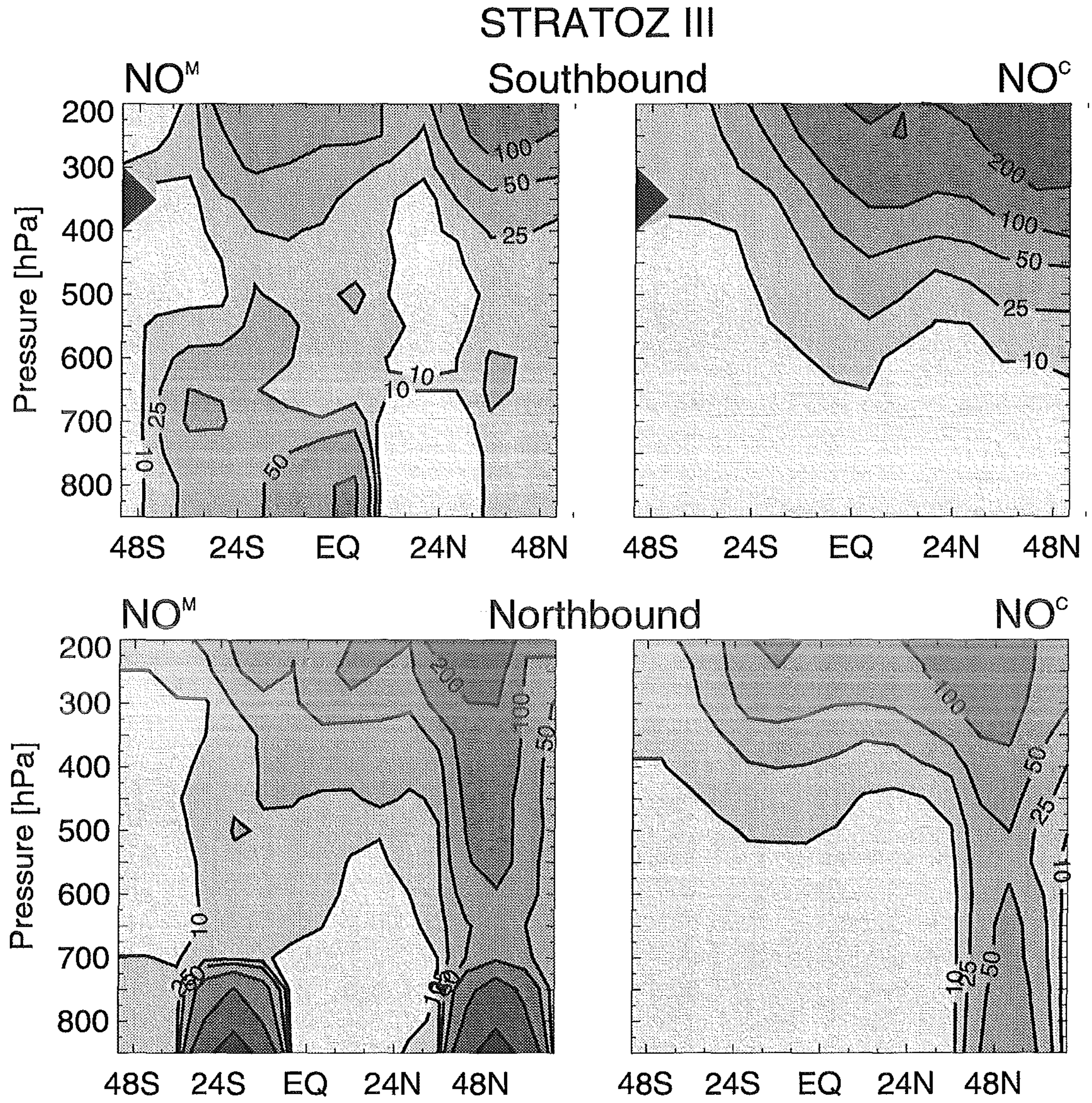

Figure 6.11: Zonally averaged values of the NO mixing ratios (left panels) observed during STRATOZ III, $\mu_{\mathrm{NO}^{\mathrm{M}}}$, and (right panels) temporal averages $\overline{\mu_{\mathrm{NO}^{\mathrm{C}}}}^{ca}$ calculated along the flight track. Data from the southbound and northbound flights are averaged separately in the upper and lower panels, respectively.

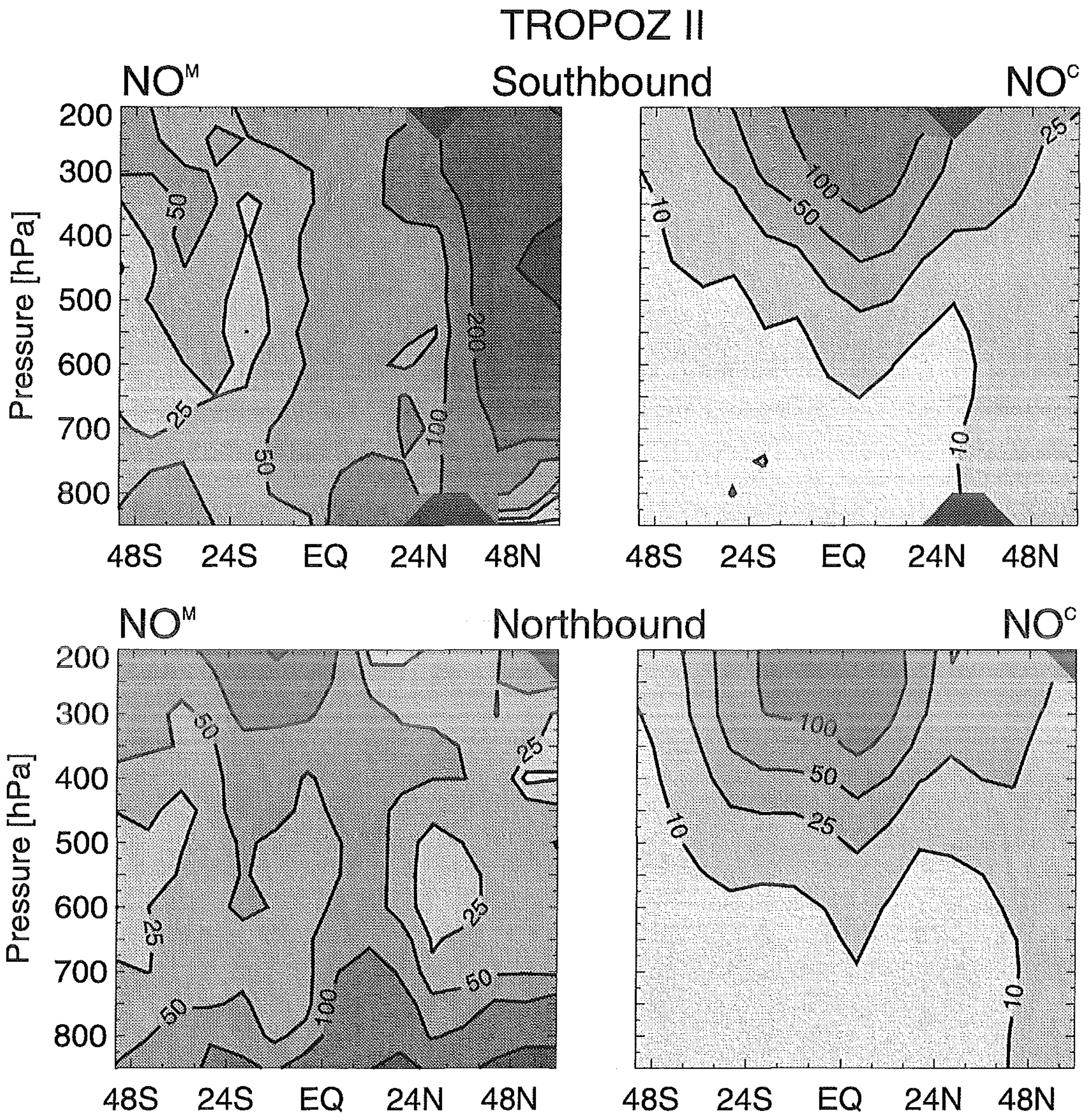

Figure 6.12: Zonally averaged values of the NO mixing ratios (left panels) observed during TROPOZ II $\mu_{\mathrm{NO^M}}$, and (right panels) temporal averages $\overline{\mu_{\mathrm{NO^C}}}^{ca}$ calculated along the flight track. Data from the southbound and northbound flights are averaged separately in the upper and lower panels, respectively.

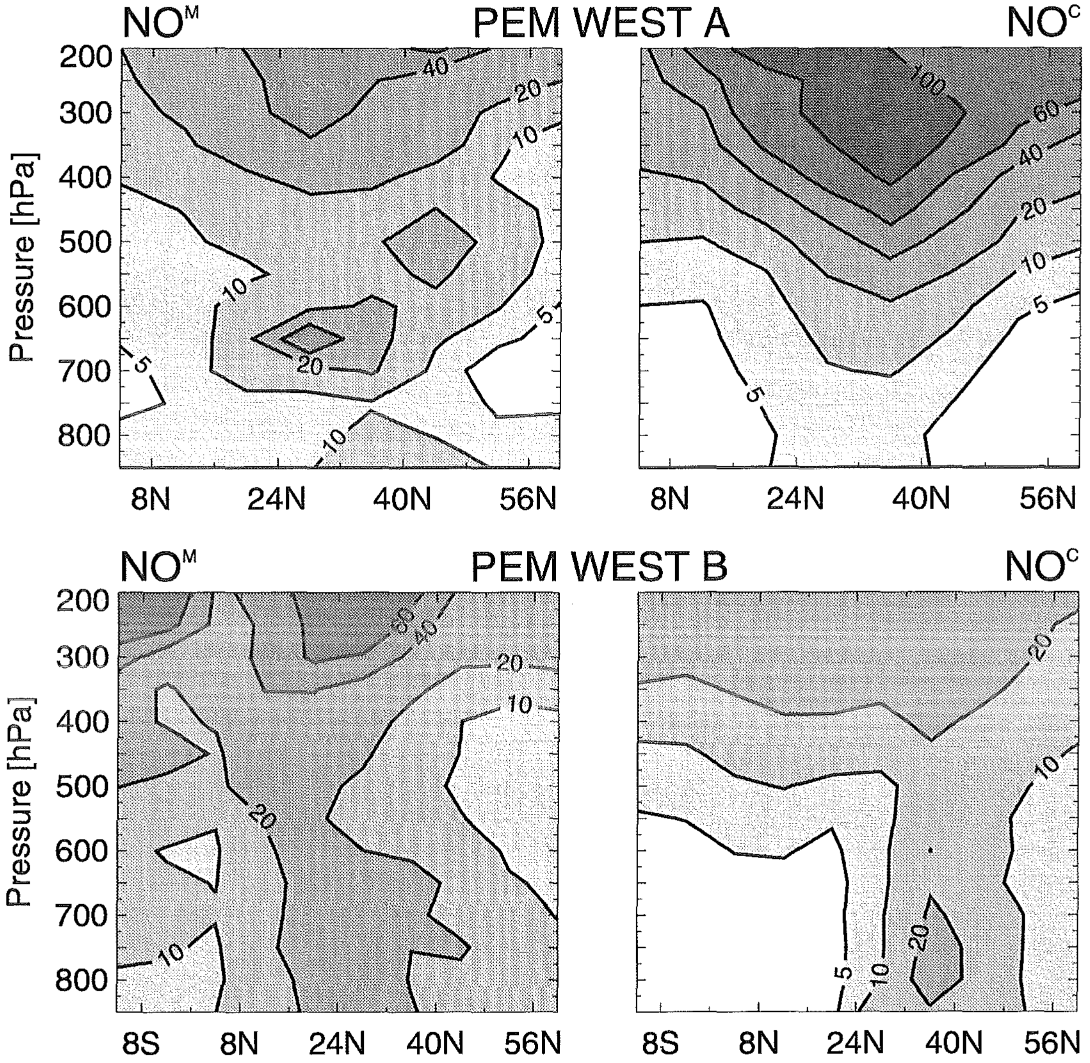

Figure 6.13: Zonally averaged values of the NO mixing ratios (left panels) observed during PEM-West, $\mu_{\mathrm{NO^M}}$, and (right panels) temporal averages $\overline{\mu_{\mathrm{NO^C}}}^{ca}$ calculated along the flight tracks. Upper and lower panels are data for PEM-West A and PEM-West B, respectively.

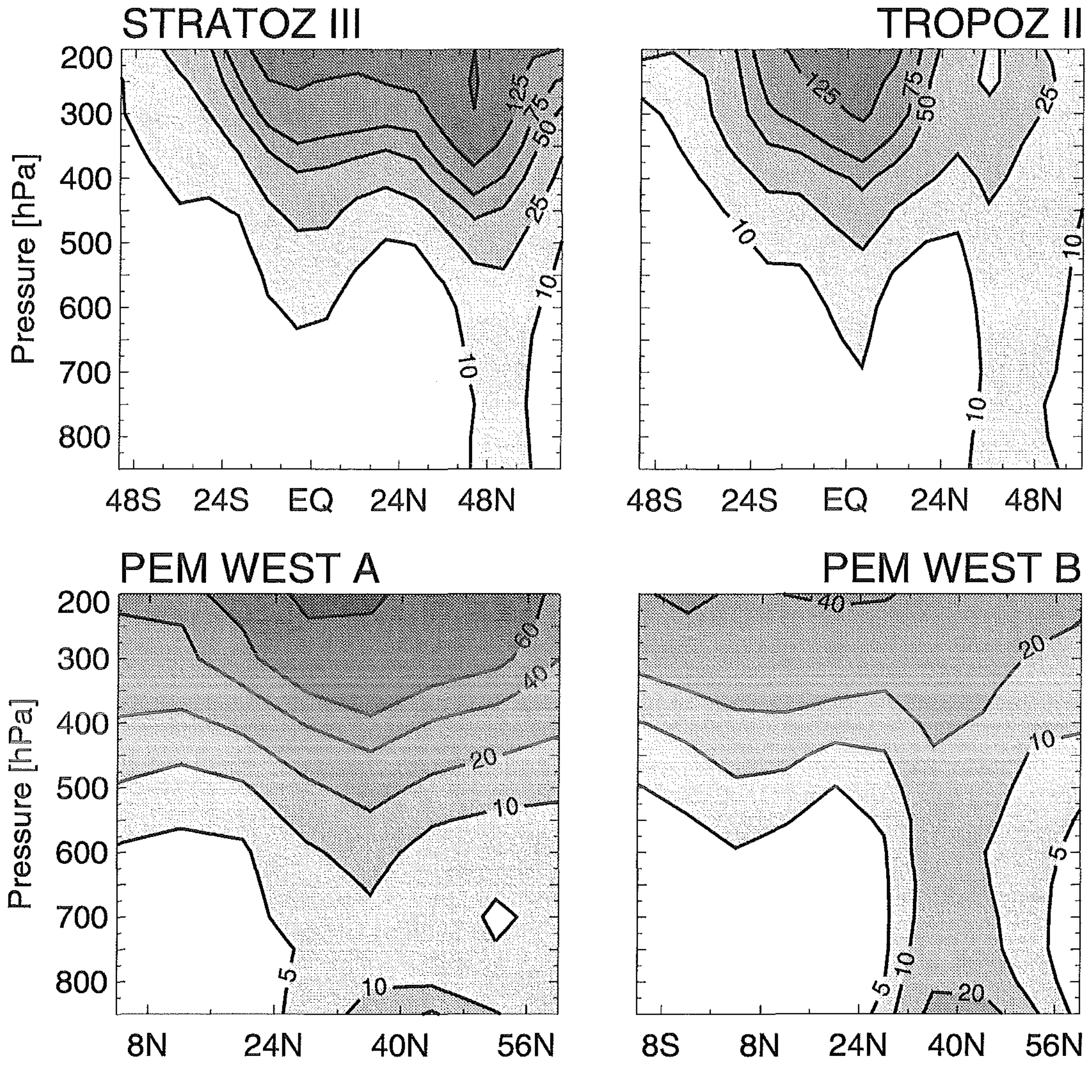

Figure 6.14: Zonal mean values of the NO mixing ratios calculated within the longitude-latitude square of (upper left panel) 85°W $\leq \lambda \leq$ 5°E, 56°S $\leq \varphi \leq$ 72°N during the time period of STRATOZ III, (upper right panel) 85°W $\leq \lambda \leq$ 5°E, 56°S $\leq \varphi \leq$ 64°N during the time period of TROPOZ II, (lower left panel) 105°E $\leq \lambda \leq$ 115°W, 0°N $\leq \varphi \leq$ 64°N during the time period of PEM-West A, and (lower right panel) 105°E $\leq \lambda \leq$ 115°W, 16°S $\leq \varphi \leq$ 64°N during the time period of PEM-West B.

The high fractions V_{bb}/V_{tot} indicate that the zonally averaged fields based on calculations, $\langle \overline{\mu_{\mathrm{NO^C}}}^{ca} \rangle_\lambda$, represent the structure of the entire calculated data set very well during all campaigns. In the worst case, PEM-West B, the between-box variation contributes still 71% to the total variation. For STRATOZ III and TROPOZ II hardly any in-box variation is left when northbound and southbound flights are treated separately.

In contrary, V_{bb}/V_{tot} calculated from the zonally averaged fields based on the measurements, $\langle \mu_{\mathrm{NO^M}} \rangle_\lambda$, is much smaller for all campaigns. For STRATOZ III and TROPOZ II, this term increases when the northbound and southbound parts of the campaigns are considered separately, because then the measurements made in more continental air are distinguished to some degree from the measurements in more oceanic air. Although local spikes have been removed in the calculation of the variances, 73% of the total variance associated with the PEM-West A measurements are a consequence of in-box variations. This high value is decreased only slightly when all data referring to longitudes east of 155°E are neglected. For PEM-West B, the measurements yield higher fractions V_{bb}/V_{tot} than for PEM-West A, but also in this case the small-scale fluctuations dominate over a large-scale structure. Here, however, V_{bb}/V_{tot} is as high as 76% when the data referring to longitudes $\lambda \geq 155°$E are neglected. This is the case since close to the Asian east coast the upper tropospheric values of $\mu_{\mathrm{NO^M}}$ are about a factor of 3 higher than those over the east Pacific. However, $\overline{\mu_{\mathrm{NO^C}}}^{ca}$ is low in the upper troposphere of the entire PEM-West B region and, hence, the agreement between $\langle \mu_{\mathrm{NO^M}} \rangle_\lambda$ and $\langle \overline{\mu_{\mathrm{NO^C}}}^{ca} \rangle_\lambda$ is worse when only data referring to $\lambda < 155°$E are considered.

A large value of V_{bb}/V_{tot} both for the measured and for the calculated data is necessary, but not sufficient for a small in-between box variance of the difference $\mu_{\mathrm{NO^M}} - \overline{\mu_{\mathrm{NO^C}}}^{ca}$. During TROPOZ II, the total variance of this difference is even larger than that of the measurements. This indicates that the structure of the zonal averages $\langle \overline{\mu_{\mathrm{NO^C}}}^{ca} \rangle_\lambda$ does not represent the structure of $\langle \mu_{\mathrm{NO^M}} \rangle_\lambda$, as Figure 6.12 shows also. For the other campaigns, the total variance of $\mu_{\mathrm{NO^M}}$ is larger than the corresponding variance of the difference $\mu_{\mathrm{NO^M}} - \overline{\mu_{\mathrm{NO^C}}}^{ca}$. Thus, at least some of the structure of $\langle \mu_{\mathrm{NO^M}} \rangle_\lambda$ is captured by $\langle \overline{\mu_{\mathrm{NO^C}}}^{ca} \rangle_\lambda$.

In summary, the analyzis of variances shows that the zonally averaged fields derived from the aircraft measurements are more or less strongly affected by local variations or by averaging over rather different values; large-scale structures are dominant only in the southbound flights of STRATOZ III. Therefore, the regionally averaged vertical profiles discussed in the previous section are a more suitable tool to gain insight into the structure of tropospheric NO mixing ratios than these zonal mean fields are. The most striking advantage of the vertical profile representation of the data is that the information provided about their variability is resolved at least one-dimensionally, whereas the variances defined in Equations (6.2)-(6.4) reduce the variability of the entire data set to a single figure.

It is mentioned finally that, despite the local large differences between the observed and calculated NO mixing ratios, the total mean value of all aircraft measurements made during one of the four campaigns at a pressure of 850 hPa or lower is 50 pptv and agrees excellently with the corresponding value obtained from the model calculation which is 46 pptv.

The global maps given in Figures A.1-A.4 indicate that the zonal variability of the calculated NO mixing ratio is rather low in the mid- and upper troposphere. Hence, it is not surprising that the zonal mean fields calculated for the entire domains shown in Figures 6.1 and 6.2 are very similar to the zonally averaged fields shown in Figures 6.11-6.13. Figure 6.14 shows these domain-average zonal mean fields which are determined from the NO mixing ratios of all grid columns belonging to the square extending from the most southern to the most northern and from the most western to the most eastern data point of the corresponding campaing. The high degree of similarity between calculations along the flight tracks on the one hand and domain-averages on the other hand occurs not only for PEM-West A and PEM-West B, but for STRATOZ III and TROPOZ II as well, although corresponding panels are not shown directly here. This implies that the zonal variability of the CTM is rather small. However, if it is assumed that the CTM is able to represent the real world, then this also implies that measurements within a latitude-altitude plane are sufficent to reveal the global structure of tropospheric NO$_X$ distributions. This would result in a considerable reduction of the efford required to determine these structures experimentally.

Chapter 7

Conclusion

Primary aim of this study was to provide global distributions of tropospheric NO_X. This aim was reached by implementing emission scenarios for the sources fossil fuel combustion, soil microbial activity, biomass burning, downward transport from the stratosphere, and aircraft emissions, as well as a simple chemistry scheme in a three-dimensional chemical tracer model. These fundamental elements of the present study could be adopted from previous investigations.

In addition, a parametrization of the NO production by lightning discharges was developed here. This parametrization bases on an empirical fit of the occurrence of deep wet convection in the model to observed lightning distributions. Relative lightning rates are determined thereby which are scaled according to an independent estimate of the global emission rate of this source. Since the conditions leading to a lightning discharge are highly variable and not well understood and, in addition, reliable measurements are sparse, both the horizontal distribution of global lightning occurrence and the estimate of the total emission rate are associated with an uncertainty of a factor of 2 at least. Even less is known about the vertical profile of NO emission. However, the exact profile of these emissions plays only a minor role since the resulting vertical distribution of NO_X is dominated by redistribution due to convection and by the vertical profile of the chemical lifetime of NO_X. Altogether, the NO production by lightning discharges is the most uncertain of all sources of tropospheric NO_X. This only will change if the results of additional measurements are available. Such measurements should focus in particular on the vertical profiles of NO emissions and lightning formation over tropical oceanic regions.

The global distribution of tropospheric NO_X is characterized by "C-shaped" vertical profiles with, over continents, mixing ratios of up to several ppbv in the boundary layer, about 50 pptv in the mid-troposphere, and up to 500 pptv in the upper troposphere. Over oceans, less than 10 pptv are calculated for the boundary layer and roughly 10 and 50 pptv for the mid- and upper troposphere, respectively. Fossil fuel combustion by far is the dominant source of NO_X north of 30°N up to about 300 hPa. At northern mid-latitudes between 200 and 300 hPa, aircraft emissions play a significant role, but only in winter, when deep convection is weak. Lightning discharges provide the vast majority of NO_X present in the tropical mid-troposphere. Only near the surface and in the upper troposphere there are additional, non-negligible contributions from the sources soil microbial activity and biomass burning. The southern hemispheric NO_X mixing ratios generally are low with lightning being the most important source of tropospheric NO_X. Only close to the South pole downward transport from the stratosphere is dominant.

Convection processes are substantial for the distribution of short-living tracers like NO_X. A comparison of ^{222}Rn distributions calculated by the CTM with corresponding distributions obtained from two other global models revealed that the convection scheme used in the present version of the CTM oversimplifies the effect of deep convection on the vertical distribution of such short-living tracers. In the tropics, the CTM underestimates the lower and mid-tropospheric content of tracer emitted at the surface by about a factor of 2, whereas the corresponding overestimate in the tropical upper troposphere is even larger. The same is true for mid-latitudes also, but to a lower degree since convection processes there are less dominant. Hence, the NO_X contributions calculated by the CTM from the surface sources probably have to be scaled by corresponding correction factors. To what extent NO_X from lightning discharges thereby also is affected is not yet fully understood. Additional CTM runs based on a modified convection scheme are necessary to answer this question. Contrary to the absolute contributions of the individual sources, their relative contributions are expected to be quite resistant against changes of the convection scheme.

The NO mixing ratios calculated by the CTM were compared in detail by corresponding measurements gained during four aircraft campaigns. Regionally averaged vertical profiles derived from both kinds of data turned out to be a more reliable tool for such a comparison than zonally averaged fields are. These vertical profiles show that throughout the depth of the troposphere and in all regions considered the CTM is able to reproduce the orders of magnitude of the observations. This is a nontrivial result since the tropospheric NO mixing ratios extend over a range of 5 orders of magnitude. Moreover, the broad characteristics of the vertical profiles' shape agree with the measurements in most regions. Finally, the total mean value of all aircraft measurements made at a pressure of 850 hPa or less agrees very well with the corresponding mean value derived from the model calculation.

However, an analysis of the regionally averaged vertical profiles confirmed the assumption that the CTM underestimates lower and mid-tropospheric NO mixing ratios, but overestimates the upper tropospheric ones. The reason for these discrepancies is not yet understood completely, but probably is a combination of several dynamical and chemical effects. The oversimplified convection scheme used here plays an important role, in particular in the tropics, as the comparison of ^{222}Rn distributions calculated by three different global models showed. Another possible reason for discrepancies between observed and calculated NO_X mixing ratios is the CTM's low temporal resolution of one month for the sources soil microbial activity and biomass burning, whereas in the real world the emission rates of these sources strongly depend on the actual weather conditions and the actual soil humidity and, hence, are highly variable.

In some regions the discrepancies between observed and calculated NO mixing ratios could be explained by the CTM's lack of dynamical variability. The region Japan during PEM-West A is an example of such a case where the low resolution of the model suppresses the formation of locally dominant flow structures. The low degree of variability in the CTM's wind fields probably leads to an underestimate of horizontal as well as vertical mixing processes in other regions as well.

Because of the very different resolution of the NO measurements on the one hand and the CTM calculation on the other hand it might be the case that the observed data sets evaluated here simply are not large enough to provide reliable mean values on the scale of the model resolution.

The chemical lifetime of NO_X also can explain the discrepancies occuring between the measured and the calculated NO mixing ratios under certain conditions. In general, however, the uncertainty of this lifetime due to uncertainties of the fields of OH and O_3 is only about a factor of 2. Larger differences between the observed and calculated NO mixing ratios could be explained in the lower part of the troposphere by an up to now unknown process like a recycling of NO_X from HNO_3 via heterogeneous processes on aerosol. Very recent results of *Hauglustaine et al.* [1996] point into that direction. In the lower and mid-troposphere, inclusion of a PAN chemistry does not change the NO_X mixing ratios by more than roughly 50%. In the upper troposphere, however, the NO_X concentrations calculated here are overestimated considerably when products of the photolysis of acetone indeed convert NO_X into PAN as efficient as suggested by *Singh et al.* [1995].

Acknowledgments

First, I want to thank Prof. M. Kerschgens who accepted the role of the first supervisor. I am grateful for his constructive critique which accelerated the process of writing down my results.

I am particularly indebted to Prof. D. H. Ehhalt who gave me the possibility to carry out this thesis in his institute. His readiness for numerous, intensive and encouraging discussions let me profit from both his enthusiasm and his deep knowledge of atmospheric chemistry. In addition to all the scientific stimulations I am very grateful for the freedom he granted with respect to my working times which I could adjust to my little son's sleeping rhythm.

Many of my daily questions were answered immediately by Dr. F. Rohrer. I want to thank him very much for this as well as for the patience he had in explaining the mysteries of chemistry to me. He used the same patience to insist on precisely formulated arguments in our numerous discussions. In addition, I am grateful for the effort he invested in making the CTM run on the KFA's CRAY, for solving other hard- and software problems, and for reading the draft of this thesis.

Furthermore, I want to thank Dr. E.-P. Röth for giving access and an introduction to his model which calculates photolysis rates of various species.

The model comparison of global Radon distributions only was possible because I. Köhler and Dr. R. Sausen (DLR Oberpfaffenhofen, Germany) as well as Dr. P. v. Velthoven (KNMI De Built, Netherlands) generously provided their results.

I am grateful also to Dr. E. Grobler and Dr. M. Kuhn (Forschungszentrum Jülich), Dr. A. Fink, Dr. M. Laube, and Dr. U. Ulbrich (University of Cologne), Prof. A. Hense, Prof. H. Kraus and Prof. H. Volland (University of Bonn), and Dr. H. Feichter and Dr. U. Schlese (Max-Planck-Institut for Meteorology, Hamburg) for helpful and encouraging discussions on individual aspects of this thesis.

Finally, I want to express my gratitude for my husband Martin and his parents for their encouragement to continue, their assistance in baby sitting, and their tolerance with me, in particular during the last few weeks. Without their help and without Zacharias being such an uncomplicated son this thesis would not be finished yet. I am additionally indebted to Martin for solving many technical problems with my computer at home and for critical comments on the draft of this thesis.

Appendix A

Monthly Mean Mixing Ratios of NO

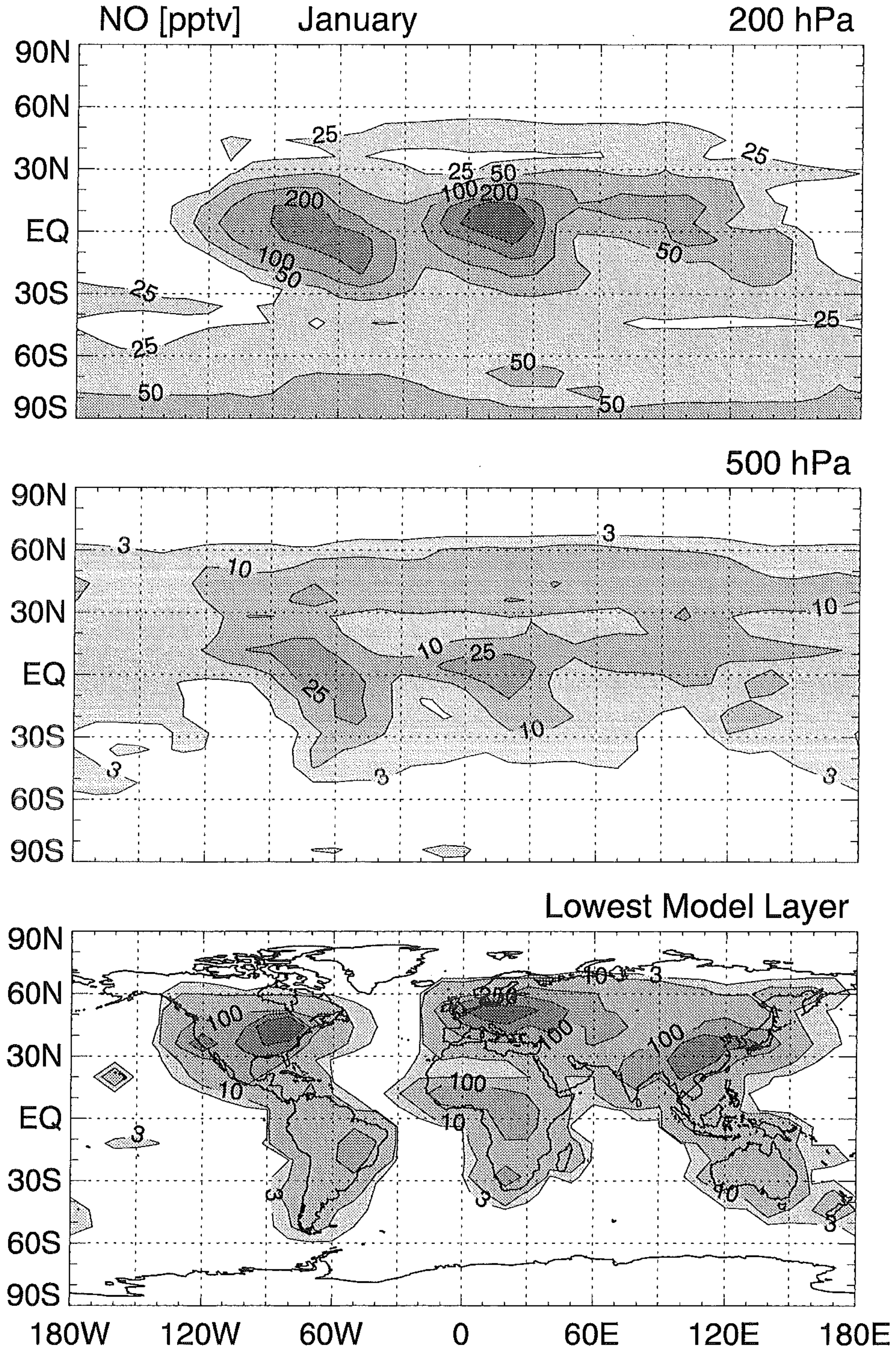

Figure A.1: January monthly mean distributions of NO mixing ratios $\overline{\mu_{\mathrm{NO}}}^m$, calculated with all sources included: (upper panel) 200 hPa level with contours at 25, 50, 100, 200, and 300 pptv, (middle panel) 500 hPa level with contours at 3, 10, 25, 50, and 75 pptv, and (lower panel) the lowest model layer with contours at 3, 10, 100, 250, and 500 pptv.

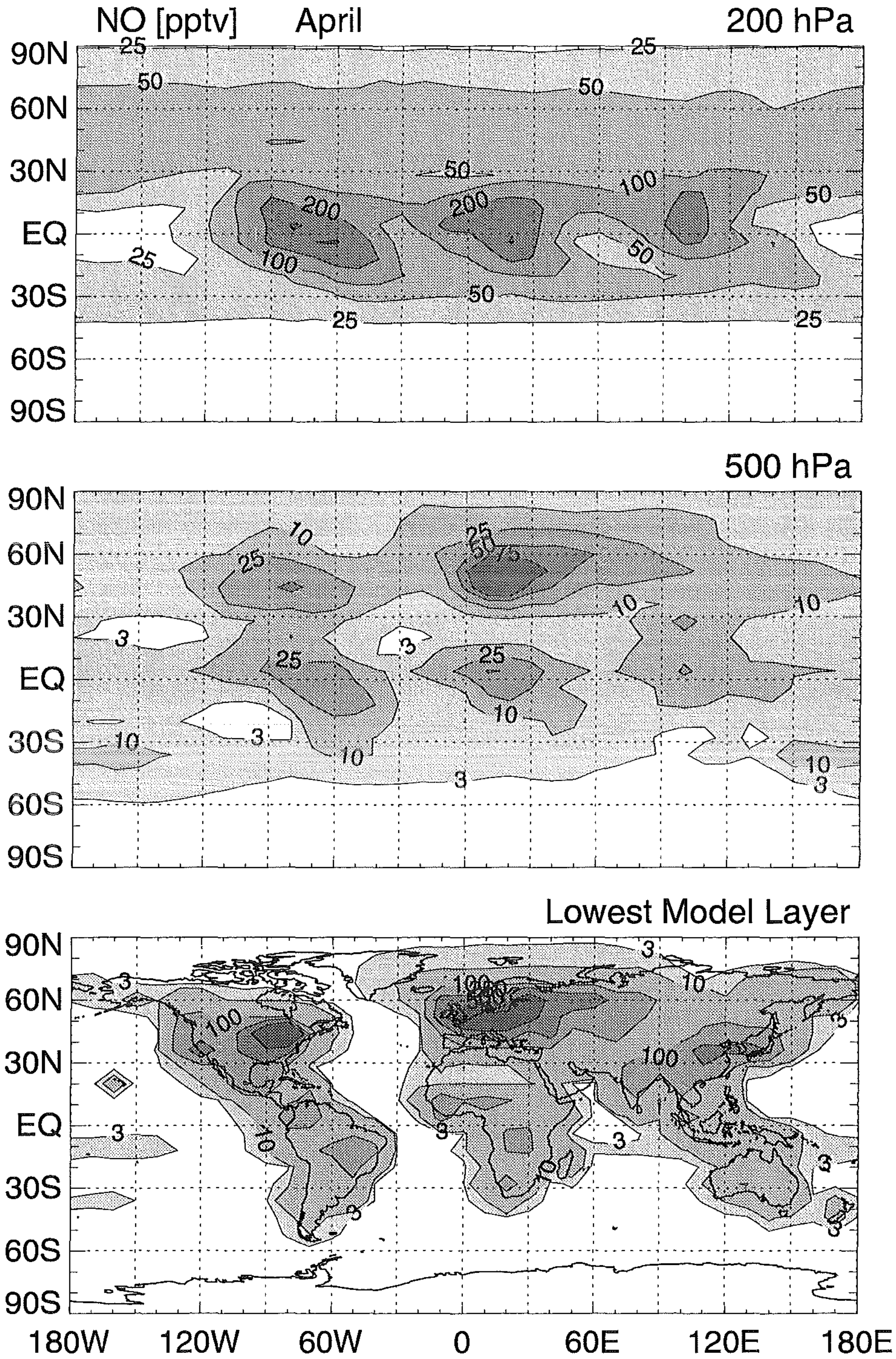

Figure A.2: April monthly mean distributions of NO mixing ratios $\overline{\mu_{\mathrm{NO}}}^m$, calculated with all sources included: (upper panel) 200 hPa level with contours at 25, 50, 100, 200, and 300 pptv, (middle panel) 500 hPa level with contours at 3, 10, 25, 50, and 75 pptv, and (lower panel) the lowest model layer with contours at 3, 10, 100, 250, and 500 pptv.

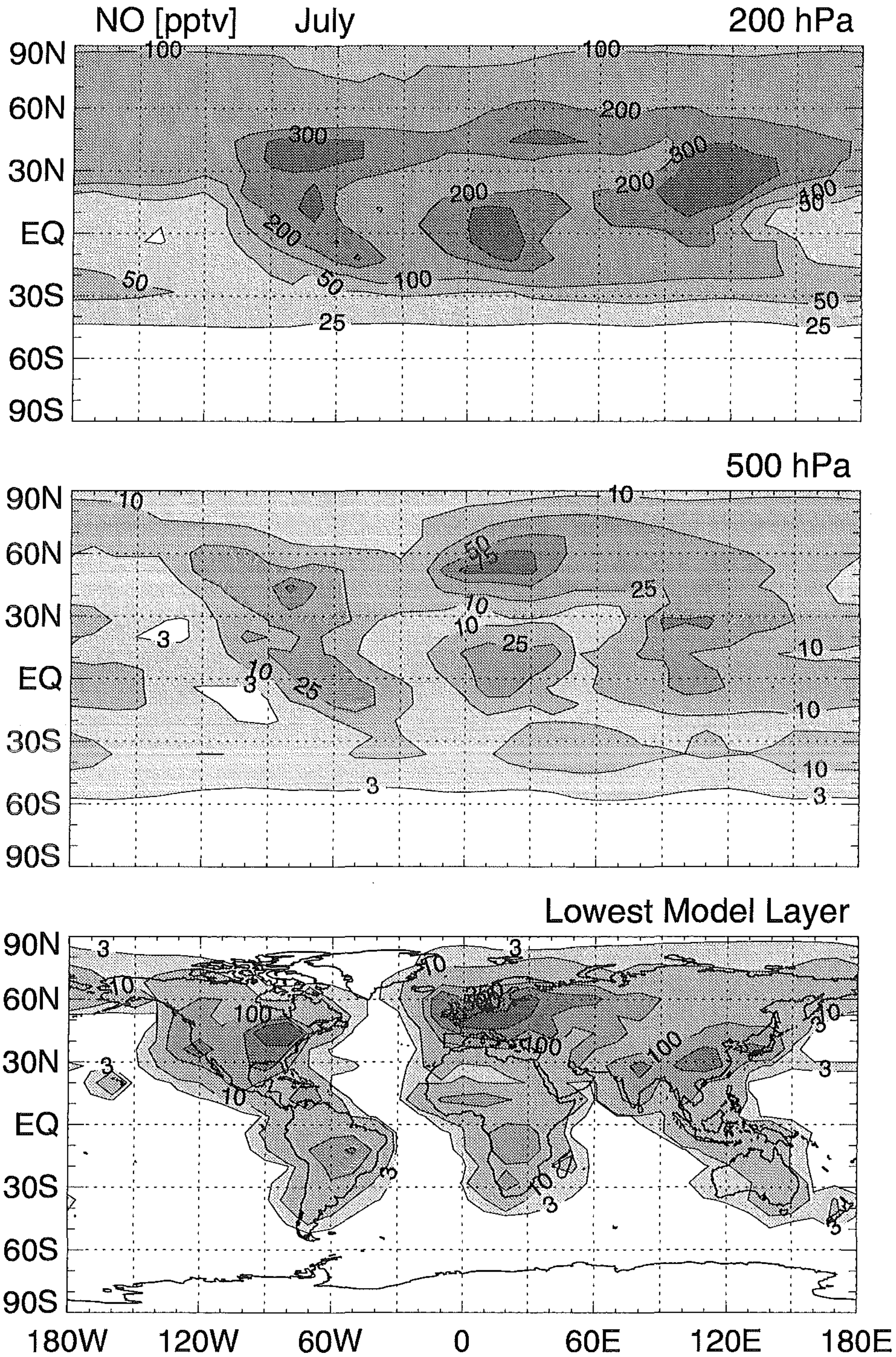

Figure A.3: July monthly mean distributions of NO mixing ratios $\overline{\mu_{\mathrm{NO}}}^{m}$, calculated with all sources included: (upper panel) 200 hPa level with contours at 25, 50, 100, 200, and 300 pptv, (middle panel) 500 hPa level with contours at 3, 10, 25, 50, and 75 pptv, and (lower panel) the lowest model layer with contours at 3, 10, 100, 250, and 500 pptv.

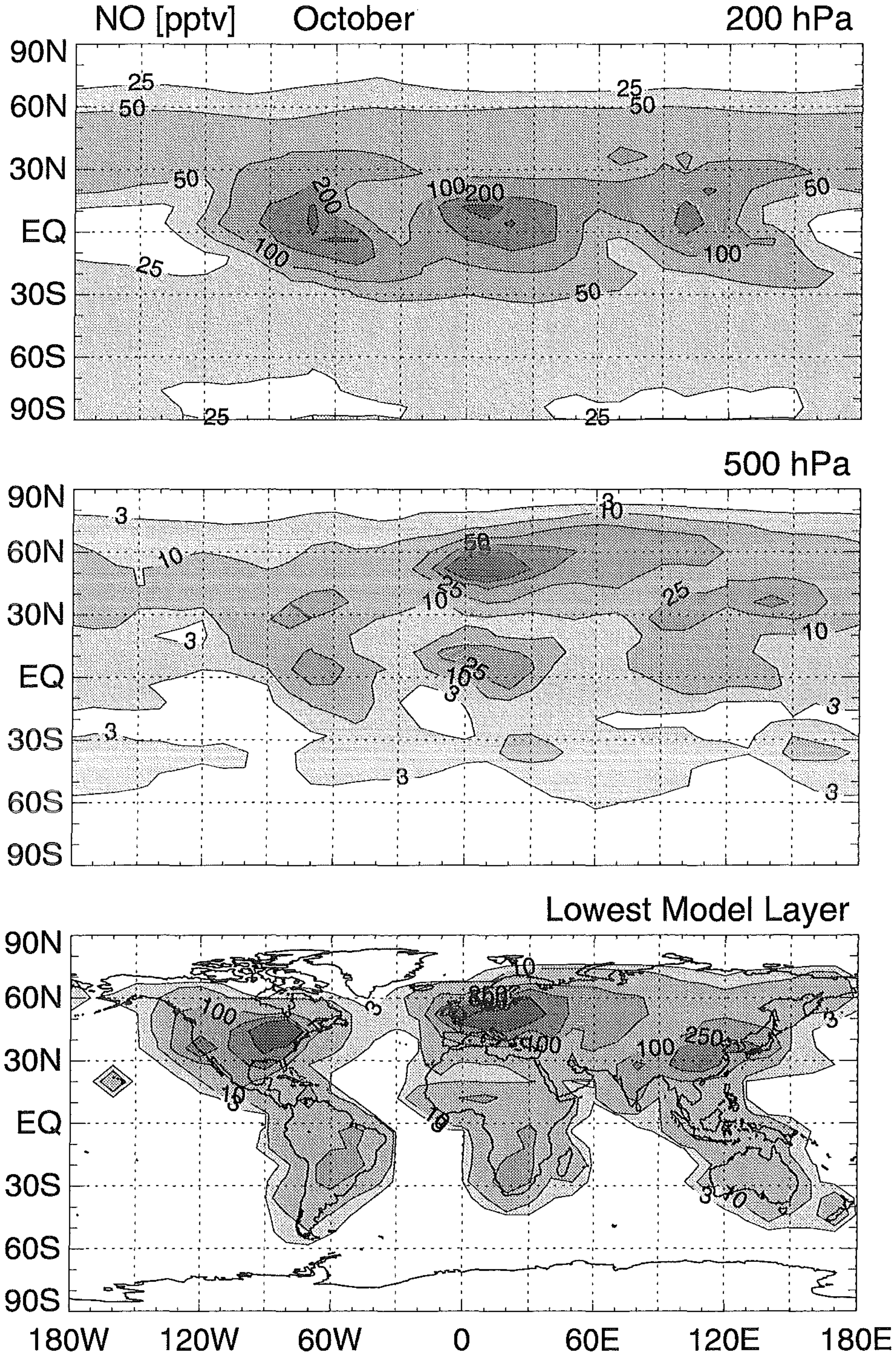

Figure A.4: October monthly mean distributions of NO mixing ratios $\overline{\mu_{\mathrm{NO}}}^m$, calculated with all sources included: (upper panel) 200 hPa level with contours at 25, 50, 100, 200, and 300 pptv, (middle panel) 500 hPa level with contours at 3, 10, 25, 50, and 75 pptv, and (lower panel) the lowest model layer with contours at 3, 10, 100, 250, and 500 pptv.

Appendix B

Maps of the Contributions from the Individual Sources

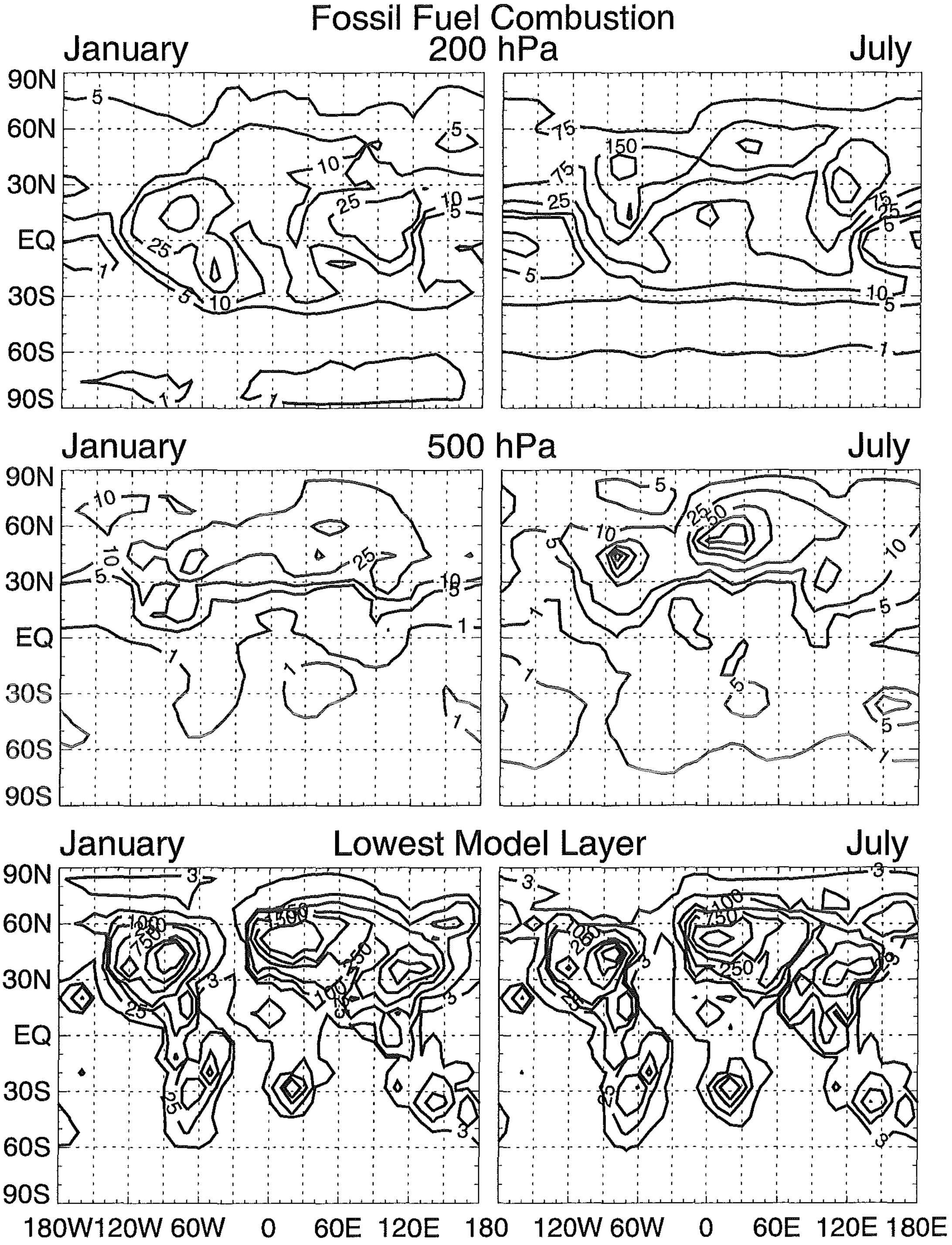

Figure B.1: January and July monthly mean values of NO_X mixing ratios calculated for the source fossil fuel combustion. (Upper panels) 200 hPa level with contours at 1, 5, 10, 25, 75, 150, and 250 pptv, (middle panels) 500 hPa level with contours at 1, 5, 10, 25, 50, 75, and 100 pptv, and (lower panels) the lowest model layer with contours at 3, 25, 100, 250, 750, 1500, and 3000 pptv.

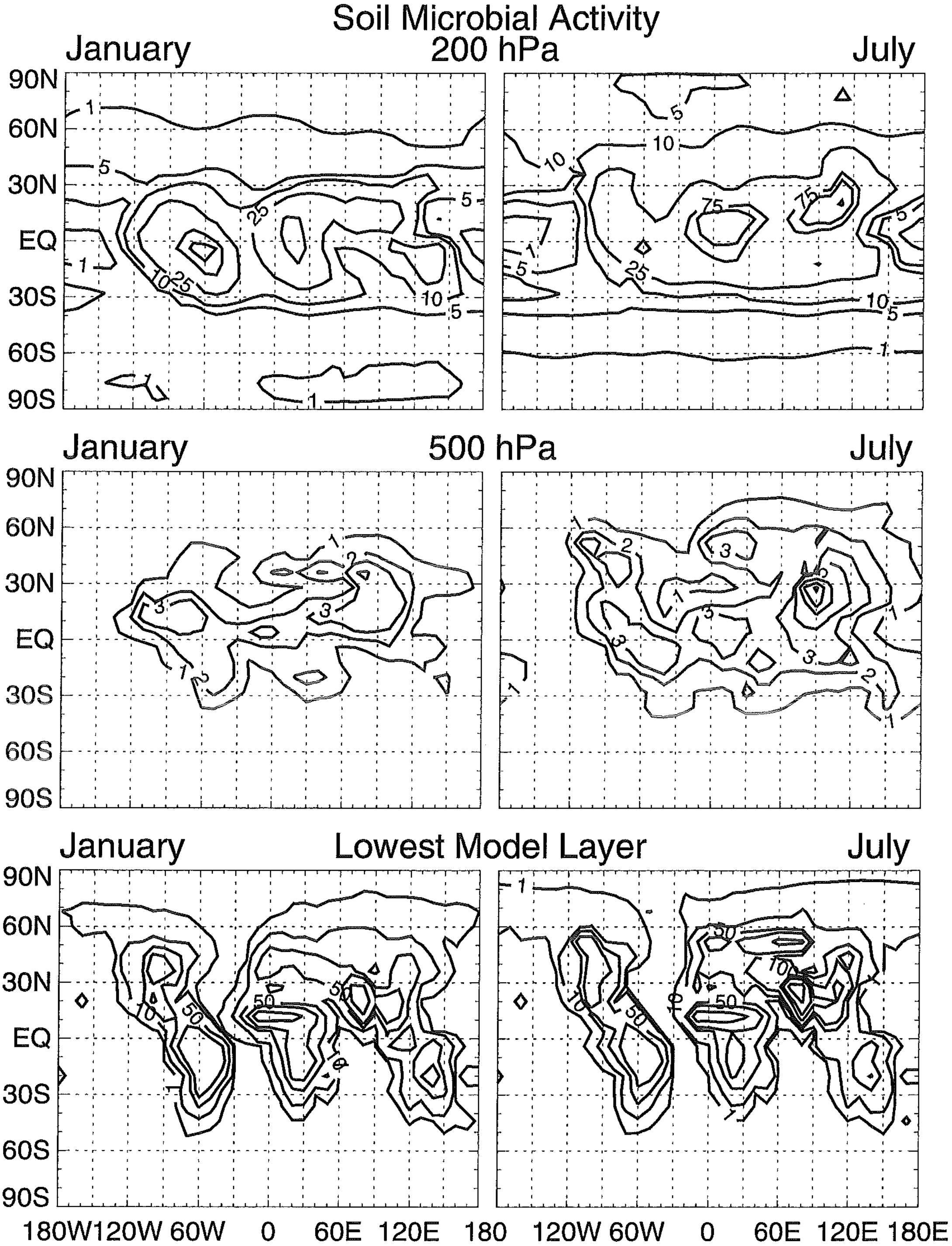

Figure B.2: January and July monthly mean values of NO_X mixing ratios calculated for the source soil microbial activity. (Upper panels) 200 hPa level with contours at 1, 5, 10, 25, 75, 100, and 150 pptv, (middle panels) 500 hPa level with contours at 1, 2, 3, 5, 10, 15, and 20 pptv, and (lower panels) the lowest model layer with contours at 1, 10, 50, 100, 200, 300, and 500 pptv.

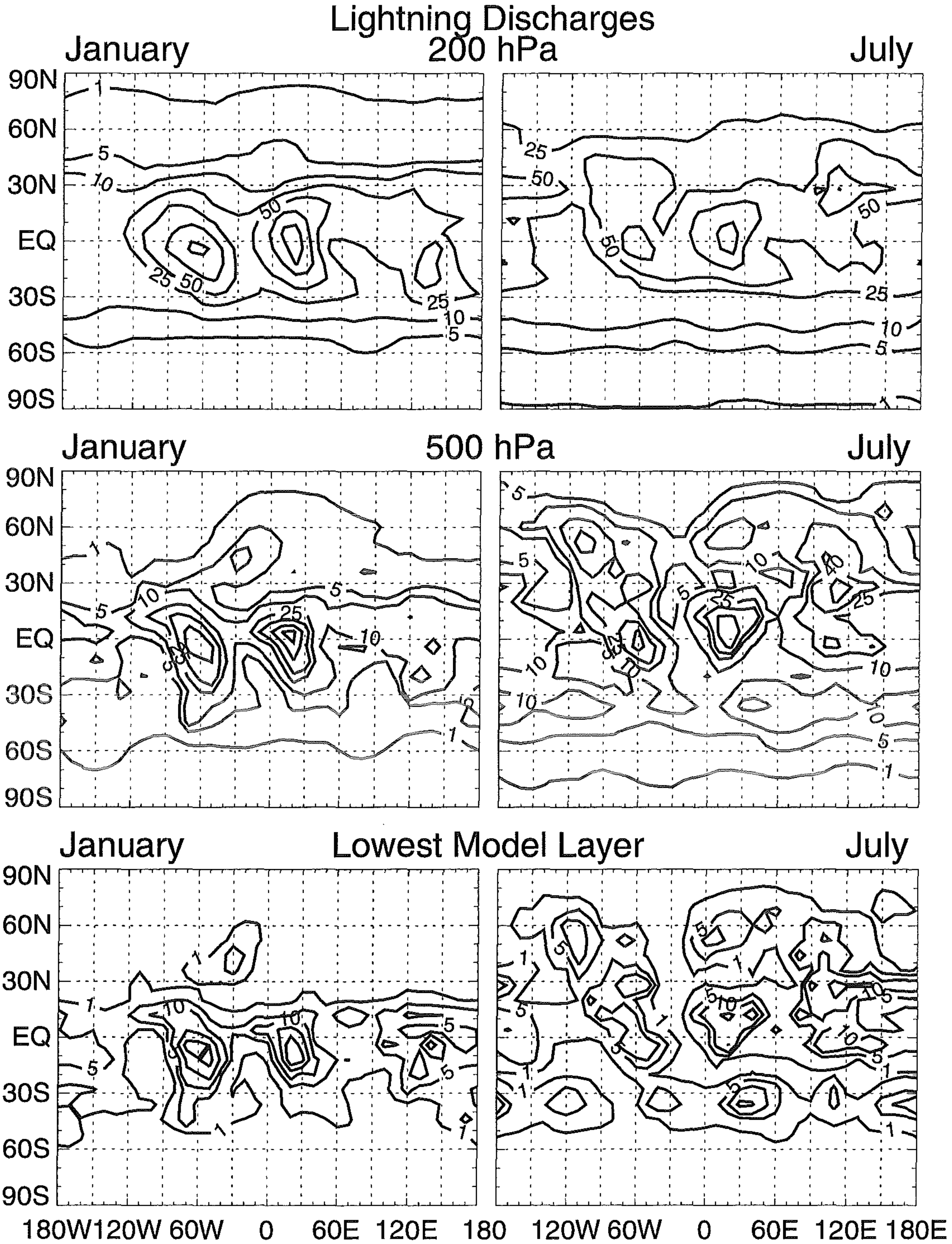

Figure B.3: January and July monthly mean values of NO_X mixing ratios calculated for the source lightning discharges. (Upper panels) 200 hPa level with contours at 1, 5, 10, 25, 50, 100, and 150 pptv, (middle panels) 500 hPa level with contours at 1, 5, 10, 25, 40, 60, and 80 pptv, and (lower panels) the lowest model layer with contours at 1, 5, 10, 20, and 30 pptv.

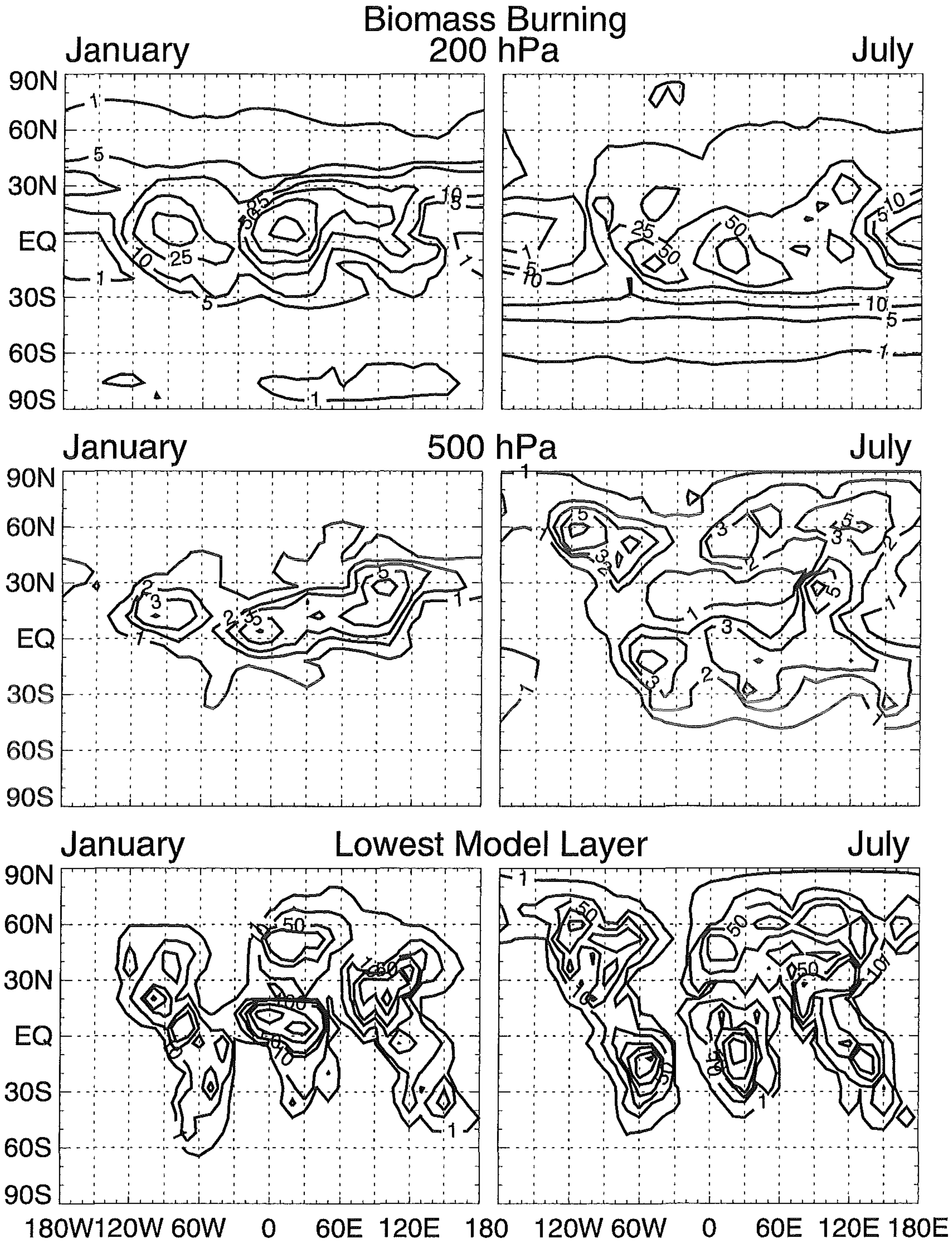
Biomass Burning

January 200 hPa July

January 500 hPa July

January Lowest Model Layer July

Figure B.4: January and July monthly mean values of NO_X mixing ratios calculated for the source biomass burning. (Upper panels) 200 hPa level with contours at 1, 5, 10, 25, 50, 100, and 250 pptv, (middle panels) 500 hPa level with contours at 1, 2, 3, 5, and 10 pptv, and (lower panels) the lowest model layer with contours at 1, 10, 50, 100, 250, 500, and 750 pptv.

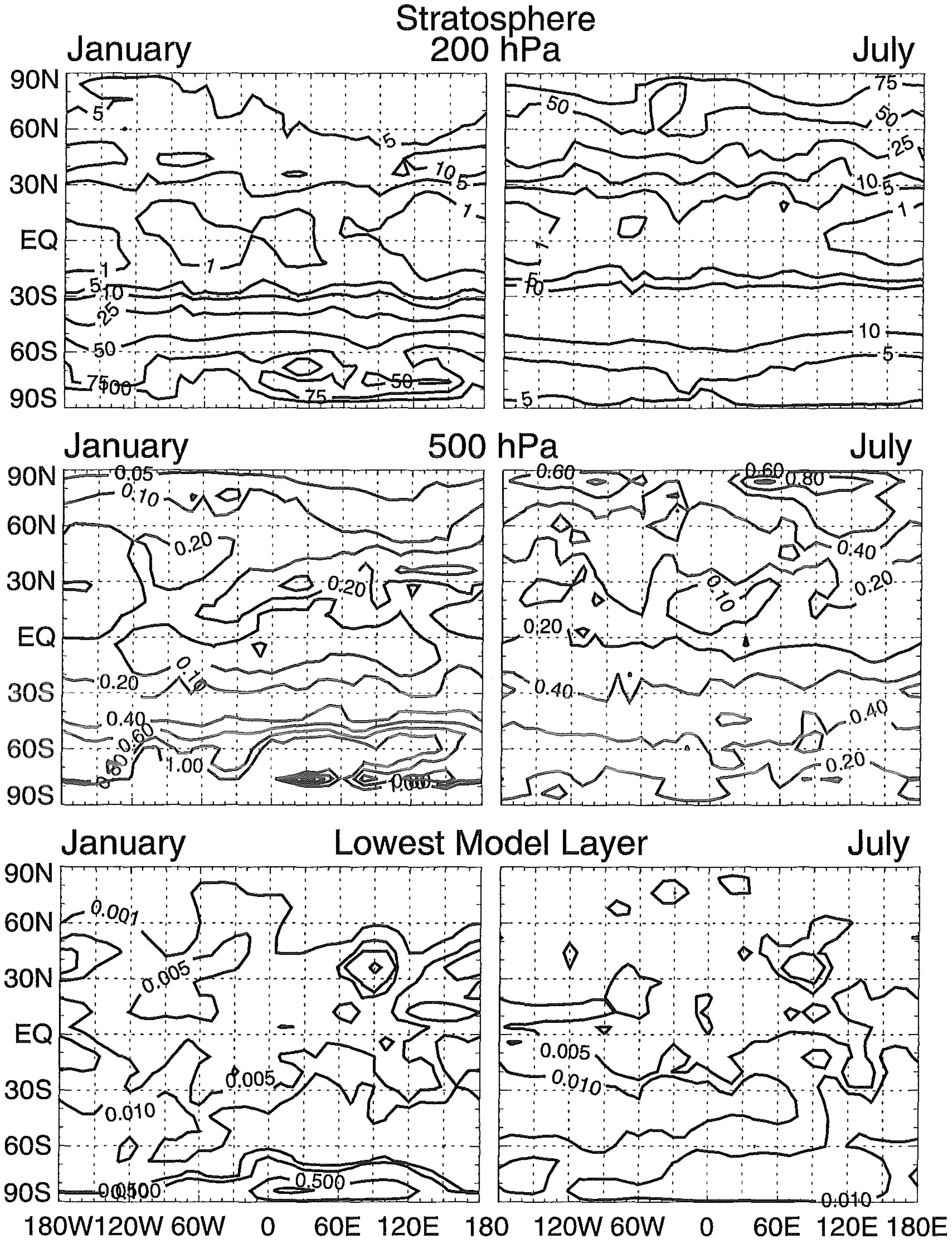

Figure B.5: January and July monthly mean values of NO_X mixing ratios calculated for the source NO_X transported downward from the stratosphere. (Upper panels) 200 hPa level with contours at 0, 1, 5, 10, 25, 50, 75, and 100 pptv, (middle panels) 500 hPa level with contours at 0.05, 0.1, 0.2, 0.4, 0.6, 0.8, and 1 pptv, and (lower panels) the lowest model layer with contours at 0.001, 0.005, 0.01, 0.05, 0.1, 0.5, and 1 pptv.

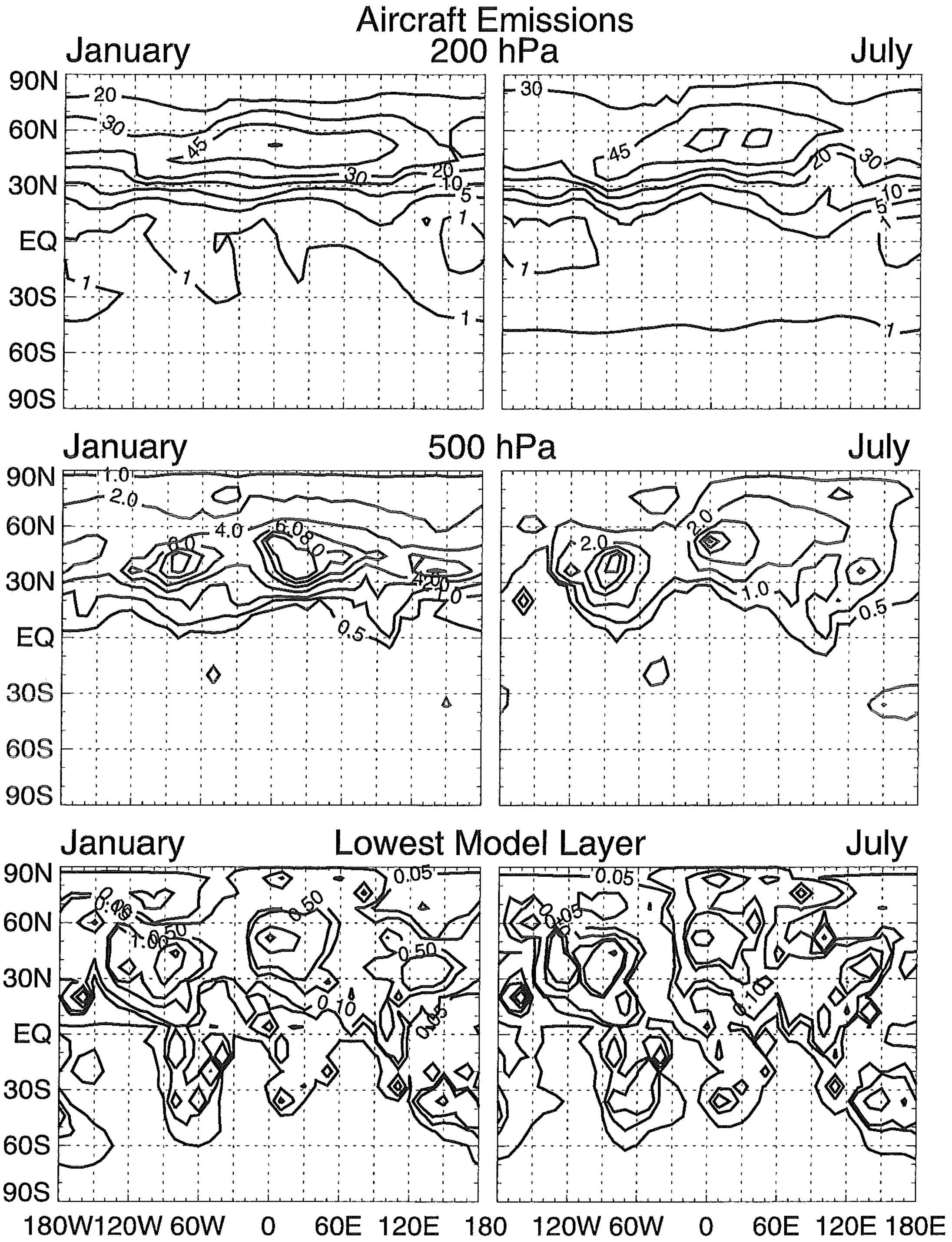

Figure B.6: January and July monthly mean values of NO$_X$ mixing ratios calculated for the source aircraft emissions. (Upper panels) 200 hPa level with contours at 1, 5, 10, 20, 30, 45, and 60 pptv, (middle panels) 500 hPa level with contours at 0.5, 1, 2, 4, 6, 8, and 10 pptv, and (lower panels) the lowest model layer with contours at 0.01, 0.05, 0.1, 0.5, 1, 5, and 10 pptv.

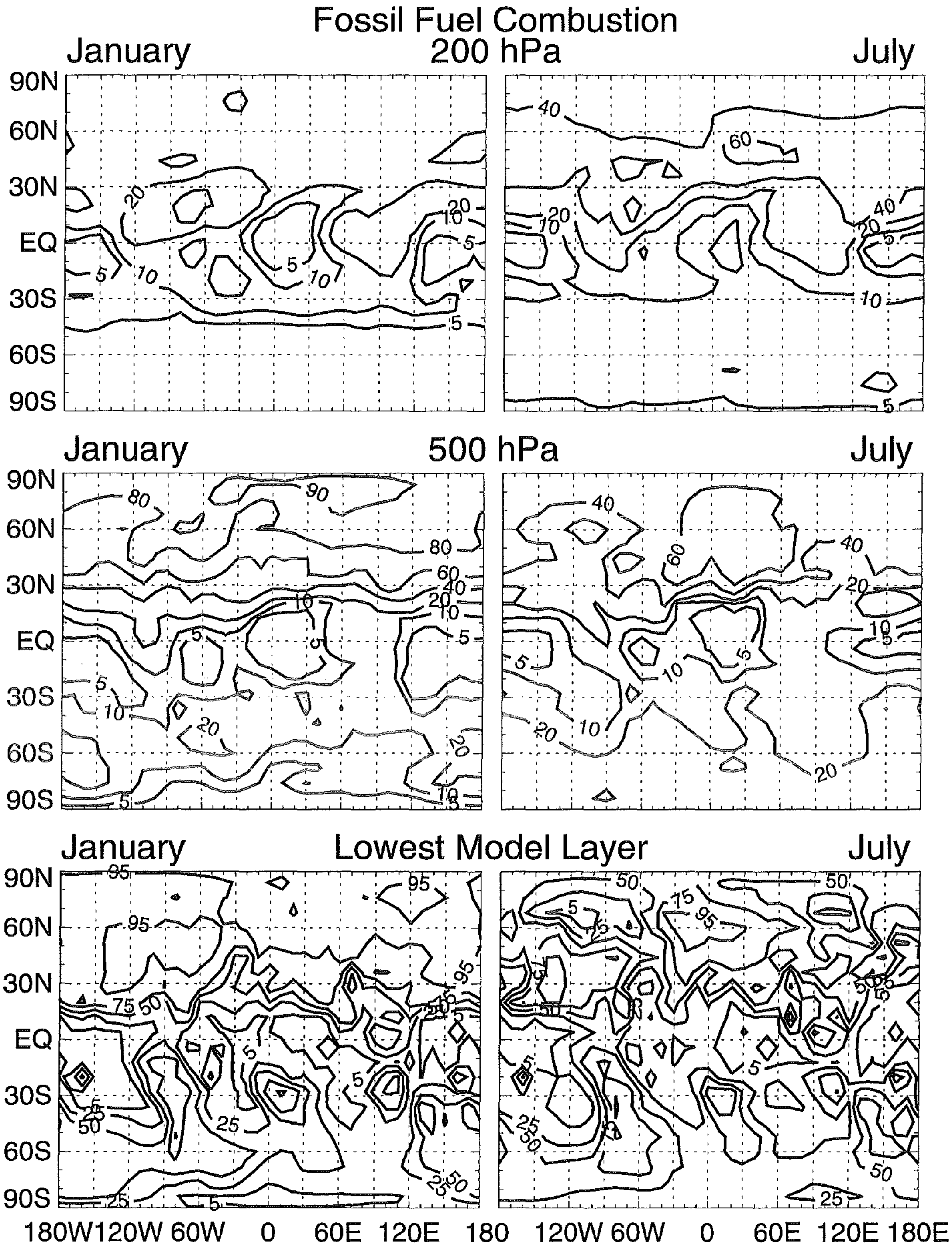

Figure B.7: January and July monthly mean values of the relative contribution from the source fossil fuel combustion. (Upper panels) 200 hPa level, (middle panels) 500 hPa level, and (lower panels) the lowest model layer. Contours are displayed at 5, 10, 20, 40, 60, 80, and 90% in the upper two panels and at 5, 25, 50, 75, and 95% in the lower panel.

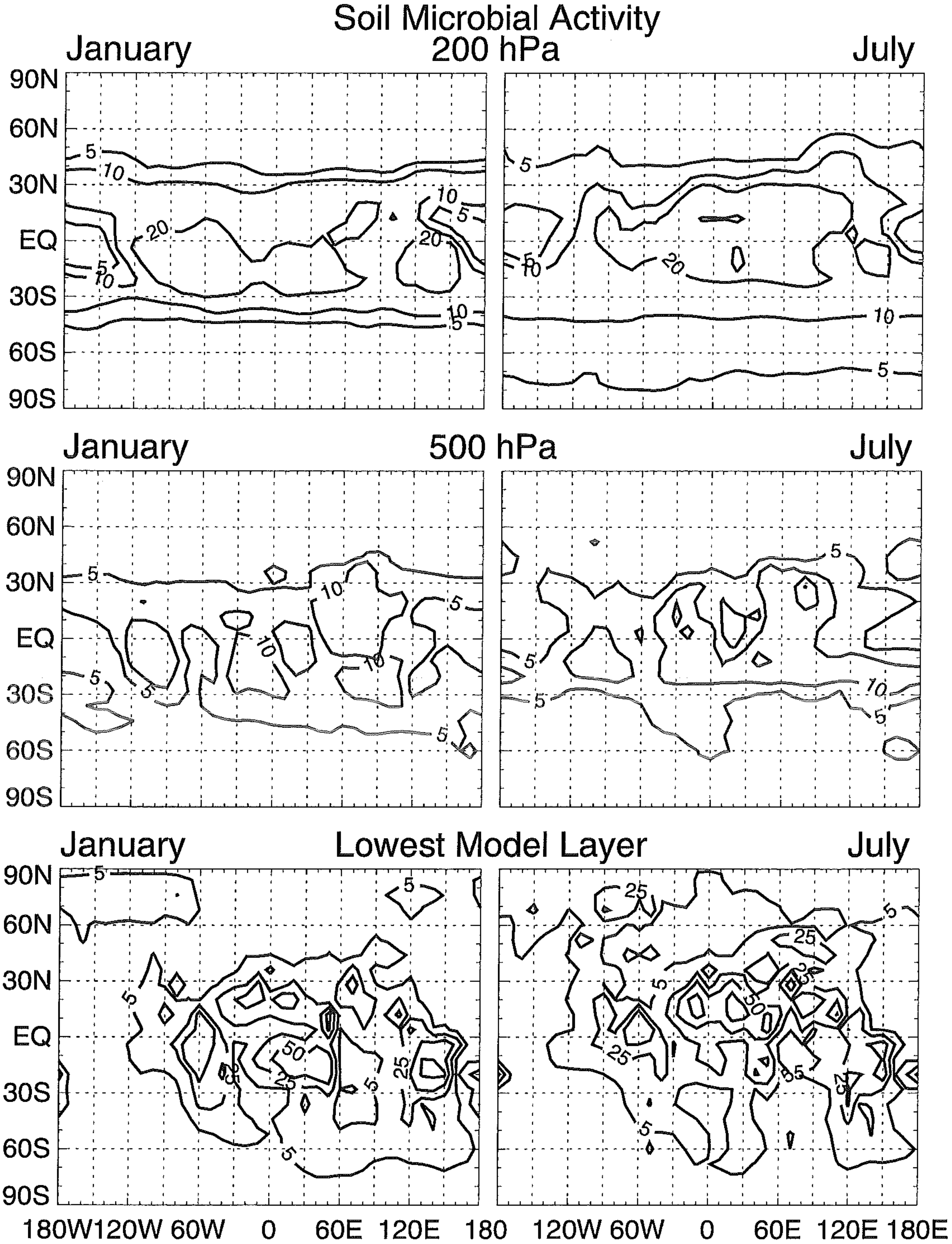

Figure B.8: January and July monthly mean values of the relative contribution from the source soil microbial acitivty. (Upper panels) 200 hPa level, (middle panels) 500 hPa level, and (lower panels) the lowest model layer. Contours are displayed at 5, 10, 20, 40, 60, 80, and 90% in the upper two panels and at 5, 25, 50, 75, and 95% in the lower panel.

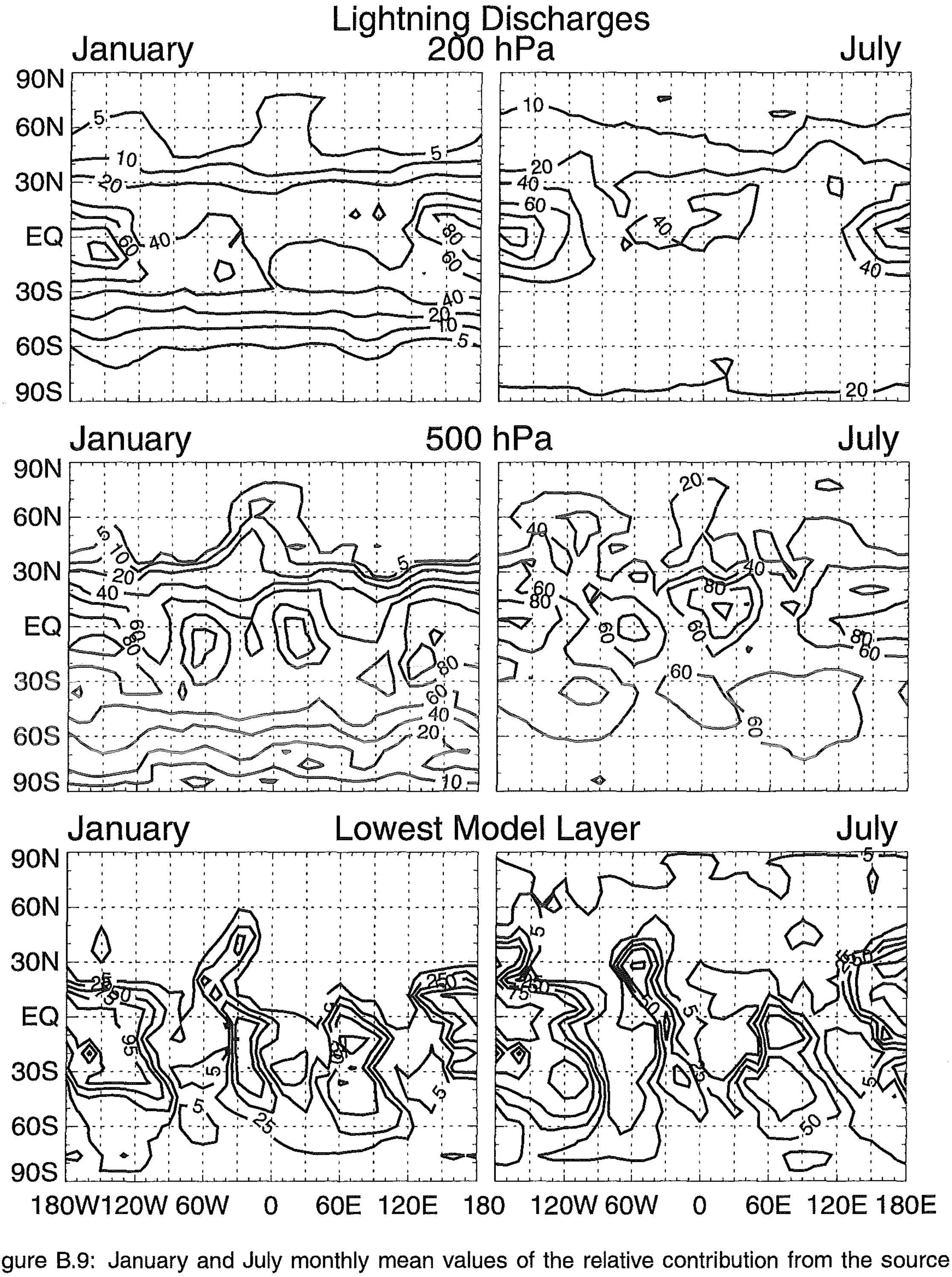

Figure B.9: January and July monthly mean values of the relative contribution from the source lightning discharges. (Upper panels) 200 hPa level, (middle panels) 500 hPa level, and (lower panels) the lowest model layer. Contours are displayed at 5, 10, 20, 40, 60, 80, and 90% in the upper two panels and at 5, 25, 50, 75, and 95% in the lower panel.

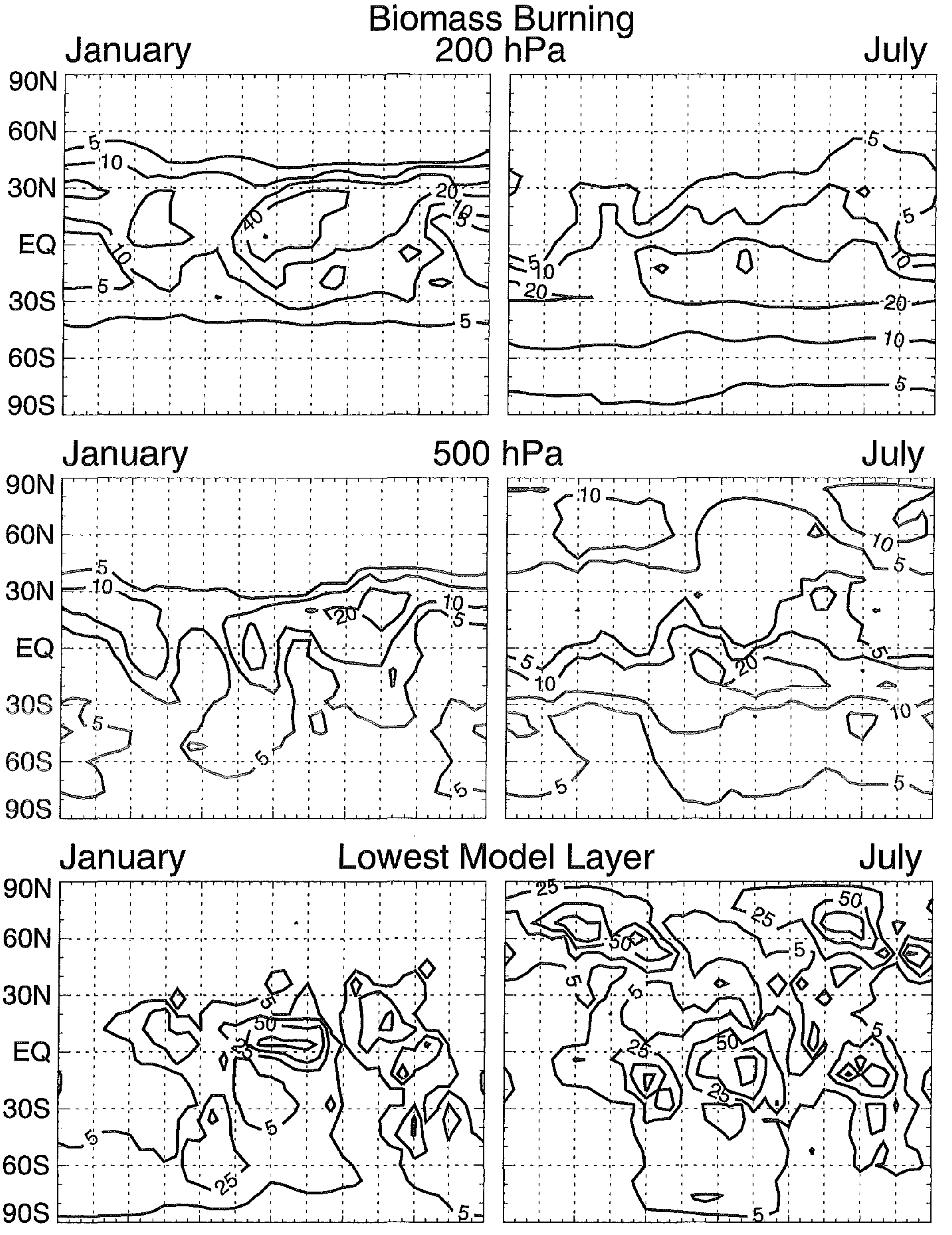

Figure B.10: January and July monthly mean values of the relative contribution from the source biomass burning. (Upper panels) 200 hPa level, (middle panels) 500 hPa level, and (lower panels) the lowest model layer. Contours are displayed at 5, 10, 20, 40, 60, 80, and 90% in the upper two panels and at 5, 25, 50, 75, and 95% in the lower panel.

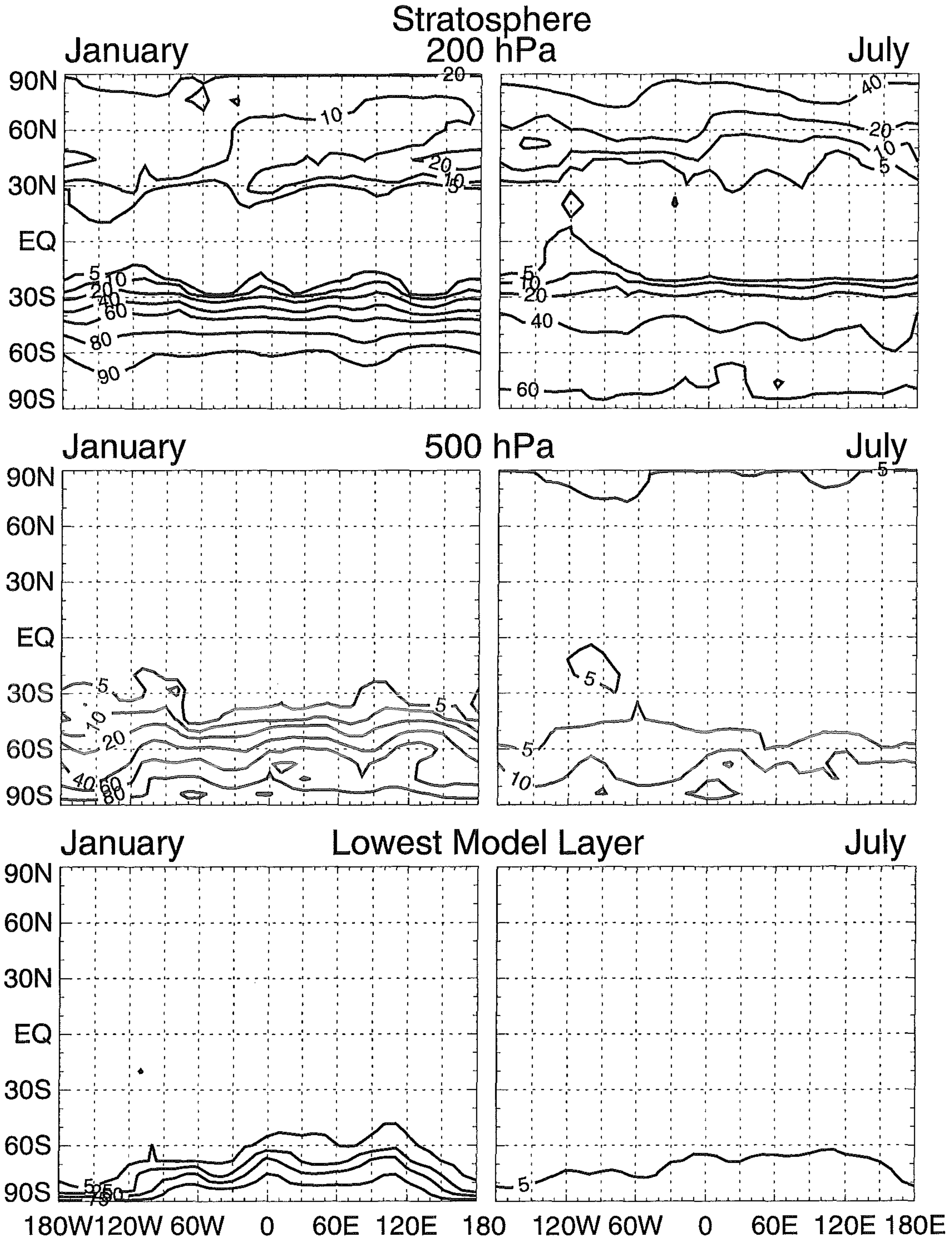

Figure B.11: January and July monthly mean values of the relative contribution from the source NO_X transported downward from the stratosphere. (Upper panels) 200 hPa level, (middle panels) 500 hPa level, and (lower panels) the lowest model layer. Contours are displayed at 5, 10, 20, 40, 60, 80, and 90% in the upper two panels and at 5, 25, 50, 75, and 95% in the lower panel.

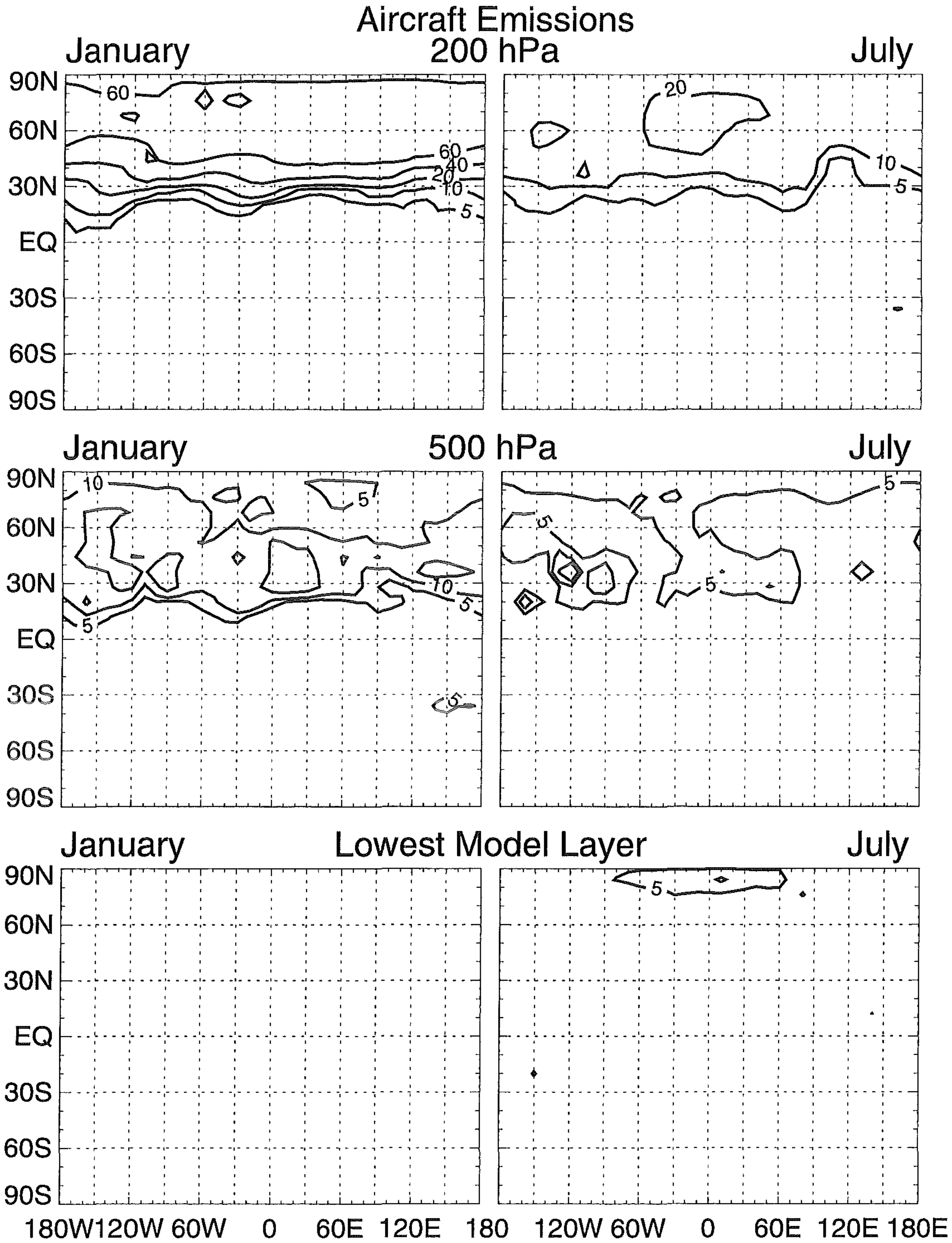

Figure B.12: January and July monthly mean values of the relative contribution from the source aircraft emissions. (Upper panels) 200 hPa level, (middle panels) 500 hPa level, and (lower panels) the lowest model layer. Contours are displayed at 5, 10, 20, 40, 60, 80, and 90% in the upper two panels and at 5, 25, 50, 75, and 95% in the lower panel.

Bibliography

AGU, American Geophysical Union, *J. Geophys. Res., 94.* 13,083-13,337, 1989.

AGU, American Geophysical Union, *J. Geophys. Res., 99.* 10,601-10,845, 1994.

AGU, American Geophysical Union, *J. Geophys. Res., 100.* 1463-1510, 1995.

AGU, American Geophysical Union, *J. Geophys. Res., 101.* 1641-2147, 1996.

Allen, D. J., R. B. Rood, A. M. Thompson, and R. D. Hudson, Three-dimensional ^{222}Rn calculations using assimilated meteorlolgical data and a convective mixing algorithm, *J. Geophys. Res.*, *101*, 6871–6881, 1996.

AMS, American Meteorological Society, Thunderstorm electrification and lightning, in *Monthly Weather Review, 122.* 1669-1946, 1994.

Bachmeier, A. S., R. E. Newell, M. C. Shipham, Y. Zhu, D. R. Blake, and E. V. Browell, PEM-West A: Meteorological overview, *J. Geophys. Res.*, *101*, 1655–1677, 1996.

Balkanski, Y. J., and D. J. Jacob, Transport of continental air to the subantarctic Indian Ocean, *Tellus*, *42B*, 62–75, 1990.

Balkanski, Y. J., D. J. Jacob, R. Arimoto, and K. A. Kritz, Distribution of ^{222}Rn over the North Pacific: Implications for continental influences, *J. Atmos. Chem.*, *14*, 353–374, 1992.

Biswas, K. R., and P. V. Hobbs, Lightning over the Gulf stream, *Geophys. Res. Lett.*, *17*, 941–943, 1990.

Borucki, W. J., and W. L. Chameides, Lightning: Estimates of the rates of energy dissipation and nitrogen fixation, *Reviews of Geophys. and Space Phys.*, *22*, 363–372, 1984.

Böttger, A., D. H. Ehhalt, and G. Gravenhorst, Atmosphärische Kreisläufe von Stickoxiden und Ammoniak, Tech. Rep. No. 1558, Forschungszentrum Jülich, Jülich, Germany, 1978.

Brasseur, G. P., J.-F. Müller, and C. Granier, Atmospheric impact of NO_X emissions by subsonic aircraft: A three-dimensional model study, *J. Geophys. Res.*, *101*, 1423–1428, 1996.

Broecker, W. S., Y. H. Li, and J. Cromwell, ^{226}Rn and ^{222}Rn; concentrations in Atlantic and Pacific Oceans, *Science*, *158*, 1307–1310, 1967.

Carroll, M. A., D. D. Montzka, G. Hübler, and K. Kelly, In situ measurements of NO_X in the airborne Arctic stratospheric expedition, *Geophys. Res. Lett.*, *17*, 493–496, 1990.

Chameides, W. L., The role of lightning in the chemistry of the atmosphere, in *The Earth's electric environment*, edited by E. P. Krider, and R. G. Roble, pp. 70–77. National Academic Press, Washington, DC, USA, 1986.

Chameides, W. L., D. H. Stedman, R. R. Dickerson, D. W. Rusch, and R. J. Cicerone, NO_X production in lightning, *J. Atmos. Sci.*, *34*, 143–149, 1977.

Chameides, W. L., D. D. Davis, J. Bradshaw, M. Rodgers, S. Sandholm, and D. B. Bai, An estimate of the NO_X production rate in electrified clouds based on NO observations from the GTE/CITE 1 fall 1983 field operation, *J. Geophys. Res.*, *92*, 2153–2156, 1987.

Collé, R., et al., An international intercomparison of marine atmospheric ^{222}Rn measurements in Bermuda, *J. Geophys. Res.*, *100*, 16,617–16,638, 1995.

Cotton, W. R., and R. A. Anthes, *Storm and cloud dynamics*. Academic Press, San Diego, CA, USA, 1989.

Crutzen, P. J., and P. H. Zimmermann, The changing photochemistry of the troposphere, *Tellus*, *43*, 136–151, 1991.

Dawson, G. A., Nitrogen fixation by lightning, *J. Atmos. Sci.*, *37*, 174–178, 1980.

DelGenio, A. D., and M.-S. Yao, Sensitivity of a global climate model to the specification of convective updraft and downdraft mass fluxes, *J. Atmos. Sci.*, *45*, 2641–2668, 1988.

DelGenio, A. D., and M.-S. Yao, Efficient cumulus parameterization for long-term climate studies: The GISS scheme, in *Cumulus Parameterization*, edited by K. Emanuel, and D. Raymond, vol. 24 of *Meteorological Monographs*, pp. 181–184. American Meteorolocical Society, Boston, MA, USA, 1992.

Dentener, F. J., and P. J. Crutzen, A three-dimensional model of the global ammonia cycle, *J. Atmos. Chem.*, *19*, 331–369, 1994.

Dignon, J., NO_X and SO_X from fossil fuels: A global distribution, *Atmos. Environ.*, *26A*, 1157–1163, 1992.

DKRZ, Deutsches Klimarechenzentrum, Modellbetreuungsgruppe, The ECHAM3 atmospheric general circulation model, Tech. Rep. No. 6, ISSN 0940-9327, Max-Planck-Institut für Meteorologie, Hamburg, Germany, 1992.

Dörr, H., Untersuchung des Gas- und Wasserhaushaltes in der ungesättigten Bodenschicht durch Messung von CO_2 und ^{222}Rn, Ph.D. thesis, Universität Heidelberg, Heidelberg, Germany, 1984.

Drapcho, D. L., D. Sisterson, and R. Kumar, Nitrogen fixation by lightning activity in a thunderstorm, *Atmos. Environ.*, *17*, 729–734, 1983.

Drummond, J. W., D. H. Ehhalt, and A. Volz, Measurements of nitric oxide between 0-12 km altitude and 67°n-60°s latitude obtained during stratoz iii, *J. Geophys. Res.*, *93*, 15,831–15,849, 1988.

Ehhalt, D. H., and J. W. Drummond, NO_X sources and the tropospheric distribution of NO_X during STRATOZ III, in *Tropospheric Ozone*, edited by I. S. A. Isaksen, pp. 217–237. D. Reidel, Dordrecht, The Netherlands, 1988.

Ehhalt, D. H., F. Rohrer, and A. Wahner, Sources and distribution of NO_X in the upper troposphere at northern mid-latitudes, *J. Geophys. Res.*, *97*, 3725–3738, 1992.

Ehhalt, D. H., F. Rohrer, and A. Wahner, The atmospheric distribution of NO, O_3, CO, and CH_4 above the North Atlantic based on the STRATOZ III flight, in *The Tropospheric Chemistry of Ozone in the Polar Regions*, edited by H. Niki, and K. H. Becker, vol. 17 of *NATO ASI Ser.*, pp. 171–187. Springer, Heidelberg, Germany, 1993.

Ehhalt, D. H., F. Rohrer, A. B. Kraus, M. J. Prather, D. R. Blake, and F. S. Rowland, On the significance of regional trace gas distributions as derived from aircraft campaigns in PEM West A and B, *J. Geophys. Res.*, submitted, 1996.

Fahey, D. W., S. R. Kawa, and K. R. Chan, Nitric oxide measurements in the Arctic winter stratosphere, *Geophys. Res. Lett.*, *17*, 489–492, 1990.

Feichter, J., and P. J. Crutzen, Parameterization of vertical tracer transport due to deep cumulus convection in a global transport model and its evaluation with ^{222}Rn measurements, *Tellus*, *42B*, 100–117, 1990.

Franzblau, E., and C. J. Popp, Nitrogen oxides produced from lightning, *J. Geophys. Res.*, *94*, 11,089–11,104, 1989.

Garstang, M., et al., Trace gas exchanges and convective transports over the Amazonian rain forest, *J. Geophys. Res.*, *93*, 1528–1550, 1988.

Genthon, C., and A. Armengaud, ^{222}Rn as a comparative tracer of transport and mixing in two general circulation models of the atmosphere, *J. Geophys. Res.*, *100*, 2849–2866, 1995.

Gesell, T. F., Background atmospheric ^{222}Rn concentrations outdoors and indoors: A review, *Health Physics*, *45*, 289–302, 1983.

Gilmore, F. R., The production of nitrogen oxides by low-altitude nuclear explosions, *J. Geophys. Res.*, *80*, 4553–4554, 1975.

Goodman, S. J., and H. J. Christian, Global observations of lightning, in *Atlas of satellite observations related to global change*, edited by R. J. Gurney, J. L. Foster, and C. L. Parkinson, pp. 191–222, Cambridge University Press, Cambridge, England, 1993.

Goodman, S. J., D. E. Buechler, and P. D. Wright, Lightning and precipitation history of a microburst-producing storm, *Geophys. Res. Lett.*, *15*, 1185–1188, 1988.

Grandt, C. E., Global thunderstorm monitoring by using the ionospheric propagation of VLF lighting pulses (sferics) with applications to climatology, Ph.D. thesis, Rheinische Friedrich-Wilhelms-Universität, Bonn, Germany, 1991.

Gregory, G. L., and A. D. Scott, Compendium of NASA data base for the global tropospheric expertiment's Pacific Exploratory Mission West-A, Tech. Rep. 110193, Langley Research Center, Hampton, VA, USA, 1995a.

Gregory, G. L., and A. D. Scott, Compendium of NASA data base for the global tropospheric expertiment's Pacific Exploratory Mission West-B, Tech. Rep. 110193, Langley Research Center, Hampton, VA, USA, 1995b.

Grobler, E. S., Experimentelle Untersuchungen zur Verteilung oxidierter Stickstoffverbindungen in der Troposphäre in Verbindung mit 3D-chemischen Transprotmodellrechnungen, Ph.D. thesis, Rheinische Friedrich-Wilhelms-Universität, Bonn, Germany, 1996.

Hansen, J., G. Russell, D. Rind, P. Stone, A. Lacis, S. Lebedeff, R. Ruedy, and L. Travis, Efficient three-dimensional global models for climate studies: Models I and II, *Mon. Weather Rev.*, *111*, 609–662, 1983.

Hauf, T., P. Schulte, R. Alheit, and H. Schlager, Rapid vertical trace gas transport by an isolated midlatitude thunderstorm, *J. Geophys. Res.*, *100*, 22,957–22,970, 1995.

Hauglustaine, D. A., B. A. Ridley, S. Solomon, P. G. Hess, and S. Madronich, HNO_3/NO_X ratio in the remote troposphere during MLOPEX 2: Evidence for nitric acid reduction on carbonaceous aerosols ?, *Geophys. Res. Lett.*, *23*, 2609–2612, 1996.

Heimann, M., The global atmospheric tracer model TM2, Tech. Rep. No. 10, ISSN 0940-9327, Max-Planck-Institut für Meteorologie, Hamburg, Germany, 1995.

Heimann, M., P. Monfray, and G. Polian, Modeling the long-range transport of ^{222}Rn to subantarctic and antarctic areas, *Tellus*, *42B*, 83–99, 1990.

Hill, R. D., R. G. Rinker, and H. D. Wilson, Atmospheric nitrogen fixation by lightning, *J. Atmos. Sci.*, *37*, 179–192, 1980.

Holton, J. R., *An Introduction to Dynamic Meteorology*, Int. Geophys. Ser. Academic Press, San Diego, CA, USA, 2nd edition edn., 1979.

IPCC, Intergovernmental Panel on Climate Change, *Climate Change 1994*. Cambridge University Press, Cambridge, UK, 1995.

Jacob, D. J., and M. J. Prather, ^{222}Rn as a test of convective transport in a general circulation model, *Tellus*, *42B*, 118-134, 1990.

Jacob, D. J., and S. C. Wofsy, Budgets of reactive nitrogen, hydrocarbons, and ozone over the Amazon forest during the wet season, *J. Geophys. Res.*, *95*, 16,737–16,754, 1990.

Jacob, D. J., M. J. Prather, S. C. Wofsy, and M. B. McElroy, Atmospheric distribution of ^{85}Kr simulated with a general circulation model, *J. Geophys. Res.*, *92*, 6614–6626, 1987.

Jacob, D. J., et al., Intercomparison of global atmoshperic transport models using ^{222}Rn and other short-lived tracers, *J. Atmos. Sci.*, submitted, 1996.

Jaeger, L., *Monatskarten des Niederschlags für die ganze Erde*, vol. 139. Deutscher Wetterdienst, Offenbach am Main, Germany, 1976.

Jorgensen, D. P., E. J. Zipser, and M. A. LeMone, Vertical motions in intense hurricanes, *J. Atmos. Sci.*, *42*, 839–856, 1985.

Kasibhatla, P. S., NO_y from sub-sonic aircraft emissions: A global three-dimensional model study, *Geophys. Res. Lett.*, *20*, 1707–1710, 1993.

Kasibhatla, P. S., H. Levy II, W. J. Moxim, and W. L. Chameides, The relative impact of stratospheric photochemical production on tropospheric NO_y levels: A model study, *J. Geophys. Res.*, *96*, 18,631–18,646, 1991.

Köhler, I., R. Sausen, and L. Gallardo Klenner, NO_X production by lightning, in *AERONOX The impact of* NO_X *emissions from aircraft upon the atmosphere at flight altitudes 8-15 km*, edited by U. Schumann, Final report to the commission of European Communities CEC contract EV5V-CT91-0044, chap. V 3.5, pp. 343–345. EC-DLR publication on research related to aeronatutics and environment, 1995.

Komhyr, W. D., S. J. Oltmans, P. R. Franchois, W. F. J. Evans, and W. A. Matthews, The latitudinal distribution of ozone to 35 km altitude from ECC ozonesonde observations 1985-1987, in *Ozone in the Atmosphere*, edited by R. D. Bojkov, and P. Fabian, Proceedings of the Quadrennial Ozone Symposium 1988 and Tropospheric Ozone Workshop, pp. 147–150. A. Deepak Publ., Hampton, VA, USA, 1989.

Kondo, Y., H. Ziereis, M. Koike, S. Kawakami, G. L. Gregory, G. W. Sachse, H. B. Singh, D. D. Davis, and J. T. Merrill, Reactive nitrogen over the Pacific ocean during PEM-West A, *J. Geophys. Res.*, *101*, 1809–1828, 1996.

Kotaki, M., and C. Katoh, The global distribution of thunderstorm activity observed by the ionosphere sounding satellite (ISS-b), *J. Atmos. Terr. Phys.*, *45*, 833–847, 1983.

Kowalczyk, M., and E. Bauer, Lightning as a source of NO_X in the troposphere, Tech. Rep. FAA-EE-82-4, U.S. Dep. of Transp., Alexandria, VA, USA, 1981.

Kraus, A. B., F. Rohrer, E. S. Grobler, and D. H. Ehhalt, The global tropospheric distribution of NO_X estimated by a three-dimensional chemical tracer model, *J. Geophys. Res.*, *101*, 18,587–18,604, 1996.

Krehbiel, P. R., M. Brook, R. L. Lhermitte, and C. L. Lennon, Lightning charge structure in thunderstorms, in *Proceedings in Atmospheric Electricity*, edited by L. H. Ruhnke, and J. Latham, pp. 408–410. A. Deepak Publ., Hampton, VA, USA, 1983.

Krider, E. P., Physics of lightning, in *The Earth's electric environment*, edited by E. P. Krider, and R. G. Roble, pp. 30–40. National Academic Press, Washington, DC, USA, 1986.

Krider, E. P., and R. G. Roble (eds.), *The Earth's electric environment*. National Academic Press, Washington, DC, USA, 1986.

Kritz, M. A., S. W. Rosner, K. K. Kelly, M. Loewenstein, and K. R. Chan, Radon measurements in the lower tripical stratosphere: Evidence for rapid vertical transport and dehydration of tropospheric air, *J. Geophys. Res.*, *98*, 8725–8736, 1993.

Kuhn, M., Untersuchungen zur troposphärischen Verteilung von Stickoxiden, Ozon, OH, Peroxiden, Aldehyden und PAN mit einem dreidimensionalen globalen Chemie- und Transportmodell, Ph.D. thesis, Universität zu Köln, Köln, Germany, 1996.

Kumar, P. P., G. K. Manohar, and S. S. Kandalogaokar, Global distribution of nitric oxide production by lightning and its seasonal variation, *J. Geophys. Res.*, *100*, 11,203–11,208, 1995.

Lambert, G., G. Polian, J. Sanak, B. Ardouin, B. Buisson, A. Jegou, and J.-C. Le Roulley, Cycle du radon et de ses descendants: Application à l'étude des échanges troposphére-stratosphére, *Ann. Geophys.*, *38*, 497–531, 1982.

Laube, M., personal communication, 1994.

Lawrence, M. G., W. L. Chameides, P. S. Kasibhatla, H. Levy, and W. Moxim, Lightning and atmospheric chemistry: The rate of atmospheric NO production, in *Handbook of atmospheric electrodynamics*, edited by H. Volland, vol. I, Atmospheric electricity, pp. 189–202. CRC Press, Boca Raton, FL, USA, 1995.

Lee, D., and E. S. Grobler, Microbial soil production, in *AERONOX The impact of* NO_X *emissions from aircraft upon the atmosphere at flight altitudes 8-15 km*, edited by U. Schumann, Final report to the commission of European Communities CEC contract EV5V-CT91-0044, chap. V 3.4, pp. 342–343. EC-DLR publication on research related to aeronatutics and environment, 1995.

LeMone, M. A., and E. J. Zipser, Cumulonimbus vertical velocity events in GATE. Part I: Diameter, intensity, and mass flux, *J. Atmos. Sci*, *37*, 2444–2457, 1980.

Levine, J. S., R. S. Rogowski, G. L. Gregory, W. E. Howell, and J. Fishman, Simultaneous measurements of NO_X, NO, and O_3 production in a laboratory discharge: Atmospheric implications, *Geophys. Res. Lett.*, *8*, 357–360, 1981.

Levy, H., and W. J. Moxim, Simulated global distribution and deposition of reactive nitrogen emitted by fossil fuel combustion, *Tellus*, *41B*, 256–271, 1989.

Levy, H., W. J. Moxim, and P. S. Kasibhatla, A global three-dimensional time-dependent lightning source of tropospheric NO_X, *J. Geophys. Res.*, submitted, 1996.

Liaw, Y. P., D. L. Sisterson, and N. L. Miller, Comparison of field, laboratory, and theoretical estimates of global nitrogen fixation by lightning, *J. Geophys. Res.*, *95*, 22,489–22,494, 1990.

Liljequist, G. H., and K. Cehak, *Allgemeine Meteorologie*. Vieweg, Braunschweig, Germany, 2nd edition edn., 1979.

Liu, S. C., J. R. McAfee, and R. J. Cicerone, ^{222}Rn and tropospheric vertical transport, *J. Geophys. Res.*, *89*, 7291–7297, 1984.

Logan, J. A., Nitrogen oxides in the troposphere: Global and regional budgets, *J. Geophys. Res.*, *88*, 10,785–10,807, 1983.

London, J., and S. C. Liu, Long-term tropospheric and lower stratospheric ozone variations from ozonesonde observations, *J. Atm. Terr. Phys.*, *54*, 599–625, 1992.

MacGorman, D. R., and D. W. Burgess, Positive cloud-to-ground lightning in tornadic storms and hailstorms, *Mon. Weather Rev.*, *122*, 1671–1697, 1994.

Mackerras, D., and M. Darveniza, Latitudinal variation of lightning occurrence characteristics, *Geophys. Res. Lett.*, *99*, 10,813–10,821, 1994.

Mahowald, N. M., P. J. Rasch, and R. G. Prinn, Cumulus parameterizations in chemical transport models, *J. Geophys. Res.*, *100*, 26,173–26,189, 1995.

Manabe, S., J. Smagorinsky, and R. F. Strickler, Simulated climatology of a general circulation model with a hydrologic cycle, *Mon. Weather Rev.*, *93*, 769–789, 1965.

Marenco, A., and F. Said, Meridional and vertical ozone distribution in the background troposphere (70°N-60°S; 0-12 km altitude) from scientific aircraft measurements during the STRATOZ III experiment (June 1984), *Atmos. Environ.*, *23*, 201–214, 1989.

Matthews, E., Global vegetation and land use: New high-resolution data bases for climate studies, *J. Clim. Appl. Meteorol.*, *22*, 474–487, 1983.

Merrill, J. T., Trajectory results and interpretation for PEM-West A, *J. Geophys. Res.*, *101*, 1679–1690, 1996.

Moxim, W. J., H. Levy, and P. S. Kasibhatla, Simulated global tropospheric PAN: Its transport and impact on NO_X, *J. Geophys. Res.*, *101*, 12,621–12,638, 1996.

Müller, J.-F., Geographical distribution and seasonal variation of surface emissions and deposition velocities of atmospheric trace gases, *J. Geophys. Res.*, *97*, 3787–3804, 1992.

Müller, J.-F., and G. Brasseur, IMAGES: A three-dimensional chemical transport model of the global troposphere, *J. Geophys. Res.*, *100*, 16,445–16,490, 1995.

Nielsen, K. E., R. A. Maddox, and S. V. Vasiloff, The evolution of cloud-to-ground lightning within a portion of the 10-11 June 1985 squall line, *Mon. Weather Rev.*, *122*, 1809–1817, 1994.

Noxon, J. F., Atmospheric nitrogen fixation by lightning, *Geophys. Res. Lett.*, *3*, 463–465, 1976.

Ogawa, T., Lightning currents, in *Handbook of atmospheric electrodynamics*, edited by H. Volland, vol. I, Atmospheric electricity, pp. 93–136. CRC Press, Boca Raton, FL, USA, 1995.

Orville, R. E., and R. W. Henderson, Global distribution of midnight lightning: September 1977 to August 1978, *Mon. Weather Rev.*, *114*, 2640–2653, 1986.

Orville, R. E., and D. W. Spencer, Global lightning flash frequency, *Mon. Weather Rev.*, *107*, 934–943, 1979.

Penner, J. E., C. S. Atherton, J. Dignon, S. J. Ghan, J. J. Walton, and S. Hameed, Tropospheric nitrogen: A three-dimensional study of sources, distributions, and deposition, *J. Geophys. Res.*, *96*, 959–990, 1991.

Petersen, W. A., and S. A. Rutledge, Some characteristics of cloud-to-ground lightning in tropical northern Australia, *J. Geophys. Res.*, *97*, 11,553–11,560, 1992.

Peyrous, R., and R.-M. Lapeyre, Gaseous products created by electrical discharges in the atmosphere and condensation nuclei resulting from gaseous phase reactions, *Atmos. Environ.*, *5*, 959–968, 1982.

Phillips, N. A., A coordinate system having some special advantages for numerical forecasting, *J. Meteorol.*, *14*, 184–185, 1957.

Pickering, K. E., A. M. Thompson, J. R. Scala, W.-K. Tao, and J. Simpson, Ozone production potential following convective redistribution of biomass burning emissions, *J. Atmos. Chem.*, *14*, 297–313, 1992.

Polian, G., Les transports atmosphériques dans l'hémisphère sud, et le bilan global du ^{222}Rn, Ph.D. thesis, Université Pierre and Marie Curie, Paris, France, 1984.

Prather, M. J., Numerical advection by conservation of second-order moments, *J. Geophys. Res.*, *91*, 6671–6681, 1986.

Prather, M. J., M. B. McElroy, S. C. Wofsy, G. Russell, and D. Rind, Chemistry of the global troposphere: Fluorocarbons as tracers of air motion, *J. Geophys. Res.*, *92*, 6579–6613, 1987.

Prentice, S. A., and D. Mackerras, The ratio of cloud to cloud-ground lighnting flashes in thunderstorms, *J. Appl. Meteorol.*, *16*, 545–550, 1977.

Price, C., and D. Rind, A simple lightning parameterization for calculating global lightning distributions, *J. Geophys. Res.*, *97*, 9919–9933, 1992.

Price, C., and D. Rind, What determines the cloud-to-ground lightning fraction in thunderstorms?, *Geophys. Res. Lett.*, *20*, 463–466, 1993.

Price, C., and D. Rind, Modeling global lightning distributions in a general circulation model, *Mon. Weather Rev.*, *122*, 1930–1939, 1994.

Proctor, D. E., Regions where lightning flashes began, *J. Geophys. Res.*, *96*, 5099–5112, 1991.

Pyle, J. A., et al., An overview of the EASOE campaign, *Geophys. Res. Lett.*, *21*, 1191–1194, 1994.

Ridley, B. A., J. E. Dye, J. G. Walega, J. Zheng, F. E. Grahek, and W. Rison, On the production of active nitrogen by thunderstorms over New Mexico, *J. Geophys. Res.*, *101*, 20,985–21,005, 1996.

Rind, D., and J. Lerner, Use of on-line tracers as a diagnostic tool in general circulation model development, 1: Horizontal and vertical transport in the troposphere, *J. Geophys. Res.*, *101*, 12,667–12,683, 1996.

Roeckner, E., et al., Simulation of the present-day climate with the ECHAM model: Impact of model physics and resolution, Tech. Rep. No. 93, ISSN 0937-1060, Max-Planck-Institut für Meteorologie, Hamburg, Germany, 1992.

Roelofs, G.-J., and J. Lelieveld, Distribution and budget of O_3 in the troposphere calculated with a chemistry general circulation model, *J. Geophys. Res.*, *100*, 20,983–20,998, 1995.

Roeth, E.-P., Description of a one-dimensional model of atmospheric chemistry, Tech. Rep. No. 2098, Forschungszentrum Jülich, Jülich, Germany, 1986.

Rohrer, F., D. Brüning, and D. H. Ehhalt, Tropospheric mixing ratios of NO obtained during TROPOZ II in the latitude region 67°N-56°S, *J. Geophys. Res.*, submitted, 1996.

Rossow, W. B., Clouds, in *Atlas of satellite observations related to global change*, edited by R. J. Gurney, J. L. Foster, and C. L. Parkinson, pp. 141–163. Cambridge University Press, Cambridge, England, 1993.

Rust, W. D., D. R. MacGorman, and R. T. Arnold, Postive cloud-to-ground lightning flashes in severe storms, *Geophys. Res. Lett.*, *8*, 791–794, 1981.

Rutledge, S. A., and W. A. Petersen, Vertical radar reflectivity structure and cloud-to-ground lightning in the stratiform region of MCSs: Further evidence for in situ charging in the stratiform region, *Mon. Weather Rev.*, *122*, 1760–1776, 1994.

Saunders, C. P. R., Thunderstorm electrification, in *Handbook of atmospheric electrodynamics*, edited by H. Volland, vol. I, Atmospheric electricity, pp. 61–92. CRC Press, Boca Raton, FL, USA, 1995.

Sausen, R., The atmospheric general circulation model ECHAM, in *AERONOX The impact of* NO_X *emissions from aircraft upon the atmosphere at flight altitudes 8-15 km*, edited by U. Schumann, Final report to the commission of European Communities CEC contract EV5V-CT91-0044, chap. V 4.9, pp. 359–360. EC-DLR publication on research related to aeronatutics and environment, 1995.

Seiler, W., and J. Fishman, The distribution of carbon monoxide and ozone in the free troposphere, *J. Geophys. Res.*, *86*, 7255–7265, 1981.

Singh, H. B., M. Kanakidou, P. J. Crutzen, and D. J. Jacob, High concentrations and photochemical fate of oxygenated hydrocarbons in the global troposphere, *Nature*, *378*, 50–54, 1995.

Smit, H. G. J., S. Gilge, and D. Kley, Ozone profiles over the Atlantic Ocean between 36°S and 52°N in March/April 1987 and September/October 1988, Tech. Rep. No. 2567, Forschungszentrum Jülich, Jülich, Germany, 1991.

Spiegel, M. R., *Theory and problems of probability and statistics*, Schaum's outline series. McGraw-Hill, New York, USA, 1975.

Spivakovsky, C. M., R. Yevich, J. A. Logan, S. C. Wofsy, M. B. McElroy, and M. J. Prather, Tropospheric OH in a three-dimensional chemical tracer model: An assessment based on observations of CH_3CCl_3, *J. Geophys. Res.*, *95*, 18,441–18,471, 1990.

Stark, M. S., J. T. H. Harrison, and C. Anastasi, Formation of nitrogen oxides by electrical discharges and implications for atmospheric lightning, *J. Geophys. Res.*, *96*, 6963–6969, 1996.

Stolzenburg, M., Observations of high ground flash densities of positive lightning in summertime thunderstorms, *Mon. Weather Rev.*, *122*, 1740–1750, 1994.

Stolzenburg, M., T. C. Marshall, W. D. Rust, and B. F. Smull, Horizontal distribution of electrical and meteorological conditions across the stratiform region of a mesoscale convective system, *Mon. Weather Rev.*, *122*, 1777–1797, 1994.

Takahashi, T., Near absence of lightning in torrential rainfall producing micronesian thunderstorms, *Geophys. Res. Lett.*, *17*, 2381–2384, 1990.

Tiedtke, M. A., A comprehensive mass flux scheme for cumulus parameterization in large-scale models, *Mon. Weather Rev.*, *117*, 1779–1800, 1989.

Tuck, A., personal communication, 1996.

Turekian, K. K., Y. Nozaki, and L. K. Benninger, Geochemistry of atmospheric radon and radon products, *Ann. Rev. Earth Planet. Sci.*, *5*, 227–255, 1977.

Turman, B. N., and B. C. Edgar, Global lightning distributions at dawn and dusk, *J. Geophys. Res.*, *87*, 1191–1206, 1982.

van Velthoven, P. F. J., and H. Kelder, Estimates of stratosphere-troposphere exchange: Sensitiviy to model formulation and horizontal resolution, *J. Geophys. Res.*, *101*, 1429–1434, 1996.

van Velthoven, P. F. J., and W. M. F. Wauben, The 3-D chemical transport model CTMK, in *AERONOX The impact of* NO_X *emissions from aircraft upon the atmosphere at flight altitudes 8-15 km*, edited by U. Schumann, Final report to the commission of European Communities CEC contract EV5V-CT91-0044, chap. V 4.5, p. 355. EC-DLR publication on research related to aeronatutics and environment, 1995.

Velders, G. J. M., L. C. J. Heijboer, and H. Kelder, The simulation of the transport of aircraft emissions by a three-dimensional global model, *Ann. Geophys.*, *12*, 385–393, 1992.

Volland, H., personal communication, 1994.

Volland, H. (ed.), *Handbook of atmospheric electrodynamics*, vol. I, Atmospheric electricity. CRC Press, Boca Raton, FL, USA, 1995.

Vonnegut, B., Some facts and speculations concerning the origin and role of thunderstorm electricity, *Meteorol. Monogr.*, *5*, 224–241, 1963.

Wang, C., P. J. Crutzen, V. Ramanathan, and S. F. Williams, The role of deep convective storm over the tropical Pacific Ocean in the redistribution of atmospheric chemical species, *J. Geophys. Res.*, *100*, 11,509–11,516, 1995.

Weller, R., R. Lilischkis, O. Schrems, R. Neuber, and O. Wessel, Vertical ozone distribution in the marine atmosphere over the central Atlantic Ocean (56°S-50°N), *J. Geophys. Res.*, *101*, 1387–1399, 1996.

Wilkening, M. H., and W. E. Clements, ^{222}Rn from the ocean surface, *J. Geophys. Res.*, *80*, 3828–3830, 1975.

Williams, E. J., G. L. Hutchinson, and F. C. Fehsenfeld, NO_X and N_2O emissions from soil, *Global Biogeochem. Cycles*, *6*, 351–388, 1992a.

Williams, E. R., Large-scale charge separation in thunderclouds, *J. Geophys. Res.*, *90*, 6013–6025, 1985.

Williams, E. R., The tripole structure of thunderstorms, *J. Geophys. Res.*, *94*, 13,151–13,167, 1989.

Williams, E. R., Meteorological aspects of thunderstorms, in *Handbook of atmospheric electrodynamics*, edited by H. Volland, vol. I, Atmospheric electricity, pp. 27–60. CRC Press, Boca Raton, FL, USA, 1995.

Williams, E. R., and S. J. Heckman, The local diurnal variation of cloud electrification and the global diurnal variation of negative charge on the earth, *J. Geophys. Res.*, *98*, 5221–5234, 1993.

Williams, E. R., M. E. Weber, and R. E. Orville, The relationship between lightning type and convection state of thunderclouds, *J. Geophys. Res.*, *94*, 13,213–13,220, 1989.

Williams, E. R., S. A. Rutledge, S. G. Geotis, N. Renno, E. Rasmussen, and T. Rickenbach, A radar and elictrical study of tropical "hot towers", *J. Atmos. Sci.*, *49*, 1386–1395, 1992b.

WMO, World Meteorological Organization, *World distribution of thunderstorm days.* WMO 21, TP. 6, Geneva, Switzerland, 1953 and supplement 1956.

WMO, World Meteorological Organization, *A preliminary cloudless standard atmosphere for radiation calculation.* WCP 112, TP. 24, Boulder, CO, USA, 1986.

WMO, World Meteorological Organization, *An intercomparison of the climates simulated by 14 atmospheric general circulation models.* CAS/JSC working group on numerical experimentation WCRP-58, WMO/TD-No. 425, Geneva, Switzerland, 1991.

WMO, World Meteorological Organization, *Scientific assessment of ozone depletion: 1994.* Global Ozone Research and Monitoring Project, Rep. Nr. 37, Geneva, Switzerland, 1995.

Wuebbles, D. J., D. Maiden, R. K. Seals, Jr., S. L. Baughcum, M. Metwally, and A. Mortlock, Emission scenarios development: Report of the emissions scenarios committee, in *The Atmospheric Effects of Stratospheric Aircraft: A Third Program Report*, edited by R.S.Stolarski, and H. Wesoky. NASA Reference Publication 1313, NASA Office of Space Sci. and Appl., Hampton, VA, USA, 1993.

Yienger, J. J., and H. Levy, Empirical model of global soil-biogenic NO_X emissions, *J. Geophys. Res.*, *100*, 11,447–11,464, 1995.

Zel'dovich, Y. B., and Y. P. Raizer, *Physics of shock waves and high-temperature hydrodynamic phenomena*, vol. 1. Academic Press, San Diego, CA, USA, 1966.

Zipser, E. J., Deep cumulonimbus cloud systems in the tropics with and without lightning, *Mon. Weather Rev.*, *122*, 1837–1851, 1994.

Zipser, E. J., and M. A. LeMone, Cumulonimbus vertical velocity events in GATE. Part II: Synthesis and model core structure, *J. Atmos. Sci.*, *37*, 2458–2469, 1980.

Forschungszentrum Jülich

Jül-3352
February 1997
ISSN 0944-2952